The Pennsylvania State University

The Graduate School

Department of Astronomy and Astrophysics

PRECISE RADIAL VELOCITIES IN THE NEAR INFRARED

A Dissertation in

Astronomy and Astrophysics

by

Stephen L. Redman

Submitted in Partial Fulfillment
of the Requirements
for the Degree of

Doctor of Philosophy

May 2011

The dissertation of Stephen L. Redman was reviewed and approved[1] by the following:

Lawrence Ramsey
Professor of Astronomy and Astrophysics
Head of the Department of Astronomy and Astrophysics
Dissertation Adviser
Chair of Committee

James Kasting
Distinguished Professor of Geosciences and Meteorology

Kevin Luhman
Assistant Professor of Astronomy and Astrophysics

Mercedes Richards
Professor of Astronomy and Astrophysics

Steinn Sigurdsson
Professor of Astronomy and Astrophysics

Alexander Wolszczan
Professor of Astronomy and Astrophysics

Jason Wright
Assistant Professor of Astronomy and Astrophysics

[1]Signatures on file in the Graduate School.

Abstract

Since the first detection of a planet outside our Solar System by Wolszczan & Frail (1992), over 500 exoplanets have been found to date[2], none of which resemble the Earth. Most of these planets were discovered by measuring the radial velocity (hereafter, RV) of the host star, which wobbles under the gravitational influence of any existing planetary companions. However, this method has yet to achieve the sub-m/s precision necessary to detect an Earth-mass planet in the Habitable Zone (the region around a star that can support liquid water; hereafter, HZ) (Kasting et al. 1993) around a Solar-type star. Even though Kepler (Borucki et al. 2010) has announced several Earth-sized HZ candidates, these targets will be exceptionally difficult to confirm with current astrophysical spectrographs (Borucki et al. 2011). The fastest way to discover and confirm potentially-habitable Earth-mass planets is to observe stars with lower masses - in particular, late M dwarfs.

While M dwarfs are readily abundant, comprising some 70% of the local stellar population, their low optical luminosity presents a formidable challenge to current optical RV instruments. By observing in the near-infrared (hereafter, NIR), where the flux from M dwarfs peaks, we can potentially reach low RV precisions with significantly less telescope time than would be required by a comparable optical instrument. However, NIR precision RV measurements are a relatively new idea and replete with challenges: IR arrays, unlike CCDs, are sensitive to the thermal background; modal noise is a bigger issue in the NIR than in the optical; and the NIR currently lacks the calibration sources like the very successful thorium-argon (hereafter, ThAr) hollow-cathode lamp and Iodine gas cell of the optical. The PSU Pathfinder (hereafter, Pathfinder) was designed to explore these technical issues with the intention of mitigating these problems for future NIR high-resolution spectrographs, such as the Habitable-Zone Planet Finder (HZPF) (Mahadevan et al. 2010), and forms the core of my dissertation.

I have investigated and quantified several aspects of making precision radial velocity measurements in the NIR using Pathfinder. Between 2006 and 2008, I made precise measurements of the Earth's rotational velocity with respect to the solar spectrum, with which we were able to achieve precisions of less than 10 m/s. In late 2008 and 2009, I worked on optimizing the spectrograph and reduction code in preparation for our first on-sky tests. I also began characterizing a new calibration source for the NIR, the emission spectrum of a uranium-neon hollow-cathode lamp. During 2010, Pathfinder saw first light at the Hobby-Eberly Telescope (hereafter, HET), where we observed almost a dozen radial velocity standard stars and bright planet-hosting stars. Using uranium-neon as a calibration source, we were able to achieve a precision of 20 m/s in the Y band. In collaboration with Colorado University and the National Institute for Standards and Technology (NIST), we fed Pathfinder with a laser frequency comb, and were able to

[2] `http://exoplanets.org/`, 2010-12-01

achieve precisions of less than 5 m/s in the H band. These are some of the highest-precision radial velocity measurements in the Y and H bands to date, and represent an enormous advancement in our ability to make precision measurements in the NIR.

Table of Contents

List of Tables

List of Figures

Acknowledgments

I would be remiss if I did not acknowledge those along the way who, through direct or indirect actions, helped me achieve my goals. First and foremost I need to thank my thesis advisor Larry, who taught me to measure what I care about, and that the devil is in the details. To my thesis committee members, who worked hard to ensure I was on the right path. To those who have worked on Pathfinder in the past: Leland Engel, Stephen Bongiorno, Sara Gettel, James Jenkins, Nick Vlajic, Stephanie Zonak, Nate Troupe, Arpita Roy, and Ryan Terrian. A special thanks to Suvrath Mahadevan and Chad Bender, who taught me how to attract the javalinas, and also how to properly reduce and analyze echelle data.

I must also thank Dr. Sara Heap, who supported me for two years through the GSRP, taught me to program in IDL, and led me to Dr. Gillian Nave, who helped me with all things FTS and uranium. To those who helped me program efficiently: Dr. Nikolai Piskunov, who was kind enough to answer my email questions about REDUCE, and Dr. Pat Broos, who never turned me away from his office when I had an IDL question. Without the advice of the latter, this thesis would have taken at least two more months.

To the entire staff at the HET, who made the conclusion of thesis possible, with a special thanks to Herman Kriel, Chevo Terrazas, and Steve Odewahn.

To my graduate companions and allies, Jason Young, Thomas Bentley, Stephen Bongiorno, Becky MaCauley, Sara Gettel, and the Revelation Blockade improv troupe, for their phenomenal ideas and the great memories we made.

My thanks to my mother and father, who patiently and lovingly supported me through this thesis, and all of my life. To my future in-laws, Gary and Ruth Sheetz, who have treated me like family since the beginning.

Finally, to my fianc'ee Lori, for her support, patience, and laughter through these past two years. I could not have completed this work without her encouragement, advice, and support.

The aim of argument, or of discussion, should not be victory, but progress.

–Joseph Joubert (1754 — 1824)

Chapter 1

Introduction

In this chapter, I will review some of the current techniques used in the search for the radial velocity signature of exoplanets, the limits to our understanding of exoplanets, and why late M dwarfs are an attractive target for near-infrared radial velocity searches. This chapter will conclude with the reasons why near-infrared precision radial velocity measurements are challenging, and why the PSU Pathfinder was an important testbed to explore these limitations.

1.1 The Radial Velocity Signature of Extrasolar Planets

A planet orbiting a star induces a reflex velocity in the latter, the velocity semi-amplitude of which is given by:

$$K = (\frac{2\pi G}{P})^{1/3} \frac{m \sin i}{(M+m)^{2/3}} \sqrt{1-e^2} \tag{1.1}$$

where P is the orbital period, M is the mass of the star, a is the semi-major axis of the relative orbit, e is the eccentricity, i is the inclination angle (such that the orbital plane is perpendicular to the plane of the sky when $i = 90°$), and m is the mass of the planet. Unless the inclination angle of the orbit can be determined through other means (*e.g.,* if the system is also a transiting planetary system), the measured mass of the planet will be a lower-limit, $m \sin i$. For Jupiter ($m = 318 M_\oplus$, $P = 11.8$ years) around the Sun, $K/sini$ is 12.5 m/s, and for the Earth ($m = 6 \times 10^2 4$ kg, $P = 3.15 \times 10^7$ s) it is 0.089 m/s:

$$K[m/s] = 0.089 \frac{m[M_\oplus] \sin i}{P^{1/3}[years] M^{2/3}[M_\odot]} \sqrt{1-e^2} \tag{1.2}$$

$$= 28.3 \frac{m[M_♃] \sin i}{P^{1/3}[years] M^{2/3}[M_\odot]} \sqrt{1-e^2} \tag{1.3}$$

For a typical R $\sim 50,000$ spectrograph in the optical, a 1 m/s shift translates to a shift of ≈ 0.001 pixels.

1.1.1 Early RV Searches for Exoplanets

One of the first claimed exoplanets was a 1.6 $M_♃$ companion to Barnard's Star, determined via astrometric measurements by van de Kamp (1963) with 25 years of photographic plates taken at the Sproul Observatory. These results were later refuted

by Gatewood & Eichhorn (1973), and a subsequent study by Hershey (1973) revealed that the apparent astrometric shifts measured by van de Kamp were correlated with physical adjustments to the objective lens over the history of the telescope.

The first systematic radial velocity search for exoplanets was conducted by Campbell & Walker (1979) using a hydrogen fluoride (HF) absorption cell. By passing the starlight through a pressure-controlled cell, they were able to achieve 15 m/s precision. The spectrum of HF produces a series of seven $3-0$ band R branch absorption lines spanning 100 Åaround 8715 Å. Despite 10 years of searches, they detected no planets (Campbell et al. 1991).

It is clear in retrospect that part of the failure of these first exoplanet searches was the small sample size, and the expectation that other systems would resemble the solar system. The first breakthrough was the discovery of a system of exoplanets orbiting the pulsar $B1257+12$ by Wolszczan & Frail (1992). This planet was discovered through studies of the slight variations in pulsar timing — the arrival of the pulses varied as it orbited the center of the mass of the system.

The second breakthrough was the discovery of 51 Peg by Mayor & Queloz (1995), the first of many hot Jupiters that would later dominate the early discoveries. Few people expected a Jupiter to be found so close to its parent star, a signal that could be detected with just a few days of observations — but see citet1952Obs....72..199S for an exception. The formation of such a planet posed a serious challenge to the planet formation theories of the day, and led to the theory by Boss (1997) that giant planets might form from gravitational instabilities. Since then, the proximity of these planets to their parent stars has been explained via migration, where the planet forms at much larger distances from the star, but migrates inward by exchanging angular momentum with disk material between it and the star (Alibert et al. 2005).

1.1.2 Spectral Information

Not all stellar spectra provide the same radial velocity precision. Changes in the position of deep, sharp absorption lines are easier to measure than the positions of shallow or broad absorption lines. The velocity precision provided by a single absorption line (whether a calibration line or a stellar line) is given by:

$$v_{rms} = \frac{kc\Delta\lambda}{\lambda D(S/N)} \tag{1.4}$$

where k is a constant of order 1 (depending on how the line position is determined), c is the speed of light, $\Delta\lambda$ is the width of the line, D is the strength of the line, and (S/N) is the signal-to-noise ratio of the spectrum (Campbell & Walker 1979; Brown 1990).

A perfect instrument is ultimately limited by both the number of photons it detects, as well as the line abundance of the chosen spectral region. The usefulness of absorption lines within a spectrum is quantified by the quality factor, Q (Bouchy et al. (2001) and Connes (1985)). Adopting the notation of Bouchy et al. (2001), Q is given by:

$$Q = \frac{\sqrt{\sum W(i)}}{\sqrt{\sum A_0(i)}} \tag{1.5}$$

where $A_0(i)$ is the measured flux values at each wavelength $\lambda(i)$, and $W(i)$ is an optimum weighting factor, given by:

$$W(i) = \frac{\lambda^2(i)(\partial A_0(i)/\partial\lambda(i))^2}{A_0(i) + \sigma_D^2} \tag{1.6}$$

where $\partial A_0(i)/\partial\lambda(i))^2$ is the slope of the spectrum at pixel i, and σ_D^2 is the detector noise. The quality factor determines the photon-limited uncertainty in the measured radial velocity:

$$\delta V_{RMS} = \frac{c}{Q(S/N)} \tag{1.7}$$

where S/N is the signal-to-noise ratio ($\sqrt{N_{e^-}}$ in the photon-limited case). The achievable precision is inversely proportional to the slope of the spectrum, so that the majority of the Doppler content is contained in the steepest part of the stellar spectrum. Line broadening (*e.g.,* from stellar rotation) decreases the Q factor, and thus increases this precision limitation.

1.1.3 Current Optical Calibration Sources

Simultaneous calibrations are essential when making precision radial velocity measurements. Changes in temperature and pressure in the optical path can alter the index of refraction of air and the measured radial velocity across the chip significantly. The temperature and pressure dependence of the index of refraction of air is given by Allen (1973):

$$n - 1 = (n_0 - 1)d(P,T) = (n_0 - 1)P\frac{1 + (1.049 - 0.0157T)10^{-6}P}{720.883(1 + 0.003661T)} \tag{1.8}$$

(for P in mmHg and T in $^\circ$ C). The index of refraction of air is wavelength-dependant:

$$10^6(n_0 - 1) = 64.328 + \frac{29498.1}{146 - \lambda^{-2}} + \frac{255.4}{41 - \lambda^{-2}} \tag{1.9}$$

where λ is in microns. The observed velocity change for a 1° change in the temperature leads to an observed velocity shift of $c\ (n_0 - 1)\ \Delta d(P,T) = 266$ m/s at 1 μ m, 760 mmHg, and 25° C. For these same conditions, a change in the pressure of 1 mmHg leads to an apparent velocity shift of $c\ (n_0 - 1)\ \Delta d(P,T) = 105$ m/s.

In practice, these artificial velocity shifts are complicated by the fluctuations of other instrument components, such as the evaporation of liquid nitrogen from the dewar, and thermal flexing of the detector. For instance, HARPS reports that they observe a 3 m/s/K shift with their vacuum-sealed spectrograph (Pepe & Lovis 2008).

For these reasons, simultaneous calibrations are essential for removing the effects of instrumental drift. In the optical, calibrations are typically made with an iodine (I_2) gas cell or a thorium argon (ThAr) emission lamp. Although historically astronomers have occasionally utilized other techniques (hydrogen fluoride gas cell, stabilized fabry perots, and laser frequency combs), none have (yet) been used as prevalently as I_2 and ThAr. These calibration sources are summarized below.

1.1.3.1 Iodine Gas Cell

The I_2 calibration technique was pioneered by Libbrecht (1988), who was searching for stellar oscillations in Procyon. It was later adopted for exoplanet radial velocity searches by Marcy & Butler (1992). The gas cell sits in the optical path of the stellar light, imposing hundreds of lines over the optical part of the spectrum (from 5000 to 6200 Å). By using an observed stellar spectrum and a previously-measured, high-resolution iodine spectrum, one can measure sub-pixel shifts by convolving the product of these two spectra with the spectral response function (SRF) and using a least-squares fit to measure the shifts of both the I_2 and the stellar spectra. This technique is particularly useful on slit spectrographs, which have varying SRFs depending on the precise location of the star on the slit. The model spectrum (through the I_2 cell) is:

$$I_{obs}(\lambda) = k(I_s(\lambda + \Delta\lambda_s)T_{I_2}(\lambda + \Delta\lambda_{I_2})) \otimes SRF \tag{1.10}$$

where k is a normalization factor. The spectral response function is modeled by a series of overlapping Gaussians, with the amplitudes set as free parameters.

The I_2 cell technique offers a number of significant advantages, the most important of which are the stability of the cell and the high line density. The latter of these allows one to model the SRF of the instrument over the ≈ 0.1 μm coverage of the Iodine cell. However, this calibration technique only provides precise wavelengths over a relatively small section of the optical spectrum.

1.1.3.2 ThAr Hollow Cathode Lamp

The second popular calibration technique for precision radial velocities in the optical is the ThAr lamp. In a fiber-fed instrument, the ThAr is fed through a separate fiber adjacent to the target (science) fiber to monitor minute spectrograph changes during observations. One of the major advantages of ThAr is its wavelength coverage; precise wavelengths for thorium lines are available between 250 and 4500 nm. Computationally, emission line spectra are much easier to analyze than I_2 gas spectra, since the ThAr spectrum is not mixed with the stellar spectrum. ThAr is implemented very successfully on the instrument HARPS (High Accuracy Radial-velocity Planet Searcher, Pepe et al. (2000)), which currently achieves 0.30 m/s precision in the short term, and 1—2 m/s in the long term (Pepe & Lovis 2008).

The precision of the ThAr technique suffers from numerous problems. Changes in the pressure of the lamp can cause wavelength shifts in some of the Ar lines (Whaling et al. 2002), making them unsuitable for calibration. Studies by HARPS found that the argon lines can drift by tens of m/s, while the thorium lines remain stable to the single

m/s level (Lovis et al. 2006). The orders-of-magnitude difference in intensity between the thorium and argon emission lines requires longer exposures to emphasize the abundant weak lines. Longer exposures are limited by the requirement not to saturate the strongest lines, which in turn can bleed into the adjacent stellar spectrum. Changes in the applied voltage can cause the widths of the lines to vary (Hatzes et al. 2008). ThAr lamps also have a limited lifetime, often lasting for only a few hundred hours at high currents (≈ 15 mA). Even when lamps are used intermittently, the spectra are known to change with age (Hatzes et al. 2010), so that some lines disappear, and others appear over time. Such changes make it difficult to link datasets absolutely. However, the shelf life of these lamps has no known limit; for this reason, HARPS uses a series of master ThAr lamps, which it only uses infrequently to ensure linkage between different epochs.

1.1.4 Rotational Velocity and Stellar Activity

As a Solar-type star ages, its rotational velocity diminishes as magnetized stellar winds transfer angular momentum away from the star. High rotation speeds are undesirable for precision RV measurements because at large $V \sin i$, rotational broadening of the lines significantly diminishes the photon-limited radial velocity precision of the spectra (see §1.1.2 and Bouchy et al. (2001)). $V \sin i$ is measured by cross-correlating target star with a slowly-rotating comparison star (Mohanty & Basri 2003), so slowly-rotating stars can easily be selected. Unfortunately, by selecting stars with low $V \sin i$, one inadvertently biases the sample towards stars with a low inclination (where the plane of the orbit is parallel to the sky). While some exoplanets may orbit perpendicular to the spin axis of their host stars, the formation of planets from the collapsed disk of the protostellar nebula suggest that most exoplanetary systems will exhibit a strong alignment between the spin and orbital planes. Therefore, by selecting stars with a low $V \sin i$, one also restricts the sample to systems where the radial velocity signal of any orbiting exoplanets is significantly diminished by the low inclination.

It should be noted that studies of the Rositter-McLaughlin Effect on transiting exoplanets have recently shown that several exoplanets have orbits that are not aligned with the spin axis of their host stars (Hébrard et al. 2008; Winn et al. 2011). Statistics remain small, but a recent paper on these planets by Winn et al. (2010) counted 8 out of 19 planets in misaligned orbits (where the spin-orbit angle is greater than 10°, with 3σ confidence), with a possible trend in the fraction of misaligned planets towards hotter stars.

Since young stars rotate faster, and younger stars are more magnetically active, $V \sin i$ is also an indicator of stellar activity, such as the formation of star spots. Star spots block fractions of the rotationally Doppler-shifted stellar surface, altering the integrated Doppler velocity of the stellar surface in a quasi-periodic manner (Saar & Donahue 1997). Even worse, these star spots can persist for many rotation periods, and they can persist at the same stellar longitudes.

There are several ways to avoid this false identification. First, if the observed stellar periodicity is due to star spots, these spots will also reduce the stellar flux with the same period, and therefore will appear in photometric data. This only works if the star spots are not visible for the entirety of the stellar rotation period. Second, the

existence of periodic starspots will produce an asymmetry in the line profiles, which can be identified using line bisectors (Hatzes 1999). Third, if new star spots appear at different stellar longitudes, the periodicity of the measured RV signal will remain the same, but there will be a phase shift relative to the first set of measurements. Fourth, the amplitude of the faux Doppler shift is proportional to the photometric contrast between the star spot and the rest of the stellar surface (Rockenfeller et al. 2006). At infrared wavelengths, this contrast is less, and so is the amplitude of the false Doppler shift. The last of these is critical to observations of young stars (Prato et al. 2008).

1.2 Current Exoplanet Knowledge

To date, 506 planets have been discovered orbiting other stars[1], most of which do not resemble the planets in the Solar system. The characteristics of exoplanets provides us with specific insights into the nature and formation of these other systems. Figure 1.1 shows a plot of exoplanet minimum mass ($m \sin i$) versus semi-major axis (a). For planets found using the RV method, there is a distinct lack of low-mass planets at large semi-major axes, as well as a lack of planets (of all masses) at large ($\approx$ 7 AU) orbital radii. Both of these discrepancies exist because of selection effects introduced by the radial velocity search method — the former because the reflex velocities induced by low-mass planets at large a are below or near the precision threshold of current technology, and the latter because planets at large a have correspondingly large orbital periods, exceeding the history of precision radial velocities around most stars. However, the desert of planets between 0.1 and 0.6 A.U. appears to be real, suggesting a unique formation mechanism for hot Jupiters. It should be noted, however, that Kepler does not see this desert among its first release of exoplanet candidates (Borucki & the Kepler Team 2010). This may be because these targets are *candidates* — the actual planets in the Kepler sample (when they are finally confirmed via RV measurements or transit timing variations) may provide a different distribution.

Recent estimates of $\eta_\oplus$ — the fraction of exoplanets that host an Earth-mass planet — continue to support the hypothesis that there exist plethora of lower-mass exoplanets that have yet to be detected. Figure 1.2 shows the data used to estimate the $\eta_\oplus$ around Solar-type stars, from Howard et al. (2010); the authors pin the fraction of Earths to be 23^{+16}_{-10}%. Kepler has independently estimated $\eta_\oplus$ to be 6.1% for Earth-mass planets (Borucki et al. 2011), noting that this value could decrease (as false positives are removed from the list of planet candidates). Of the Kepler candidates that have been released, the distribution of exoplanet radii increases as $1/R^2$, with most planets having radii less than that of Neptune (3.8 $R_\oplus$) (Borucki & the Kepler Team 2010). This is in strong contrast to the current radii distribution of confirmed transiting exoplanets, the majority of which are between 10 and 17 $R_\oplus$. Given that it is more difficult to detect these smaller planets, this result from Kepler strongly suggests that the fraction of small planets is much larger than the fraction of known small exoplanets.

[1]From `http://exoplanet.eu/`

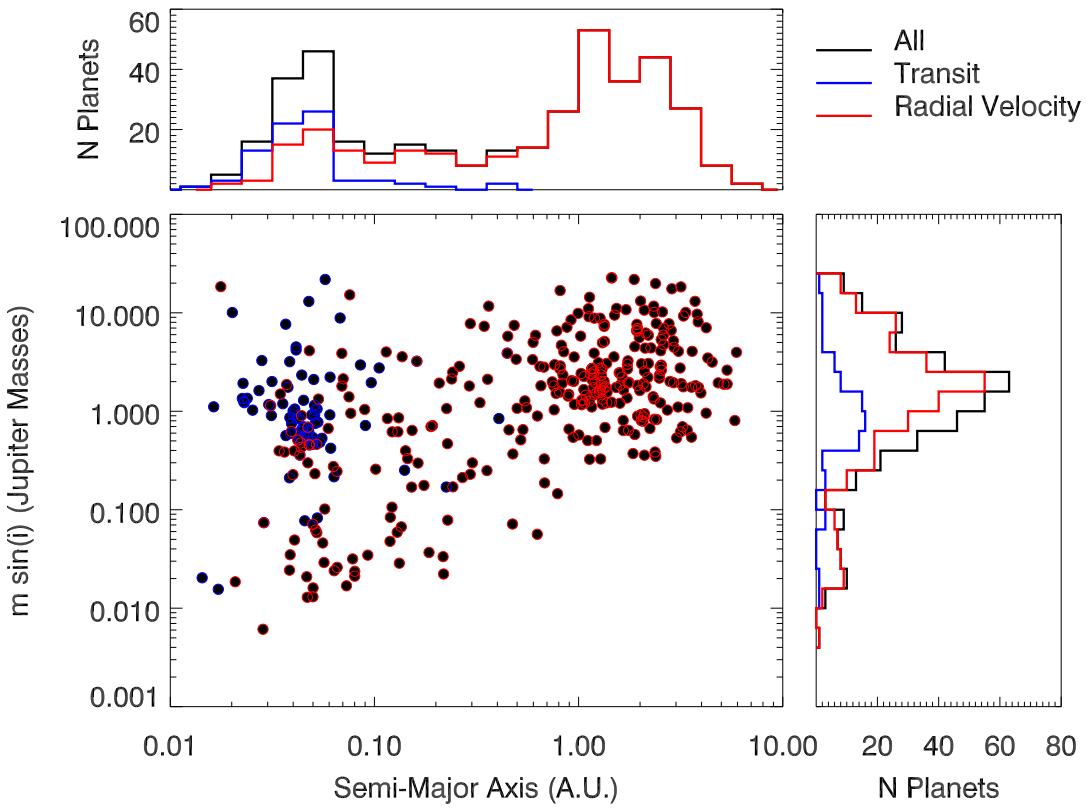

Fig. 1.1 Planetary mass ($m \sin i$) versus semi-major axis (a) for extrasolar planets detected via the radial velocity method (red circles) and the transit method (blue circles), from exoplanets.org. Histograms of each quantity are presented at the top and right-hand side of this figure as well (RV method = red, Transit = blue, All = black). Note the lack of low-mass planets at large orbital radii, as well as the lack of planets beyond ≈ 7 AU, each of which are forms of bias from the sensitivity and duration of the RV search technique, respectively.

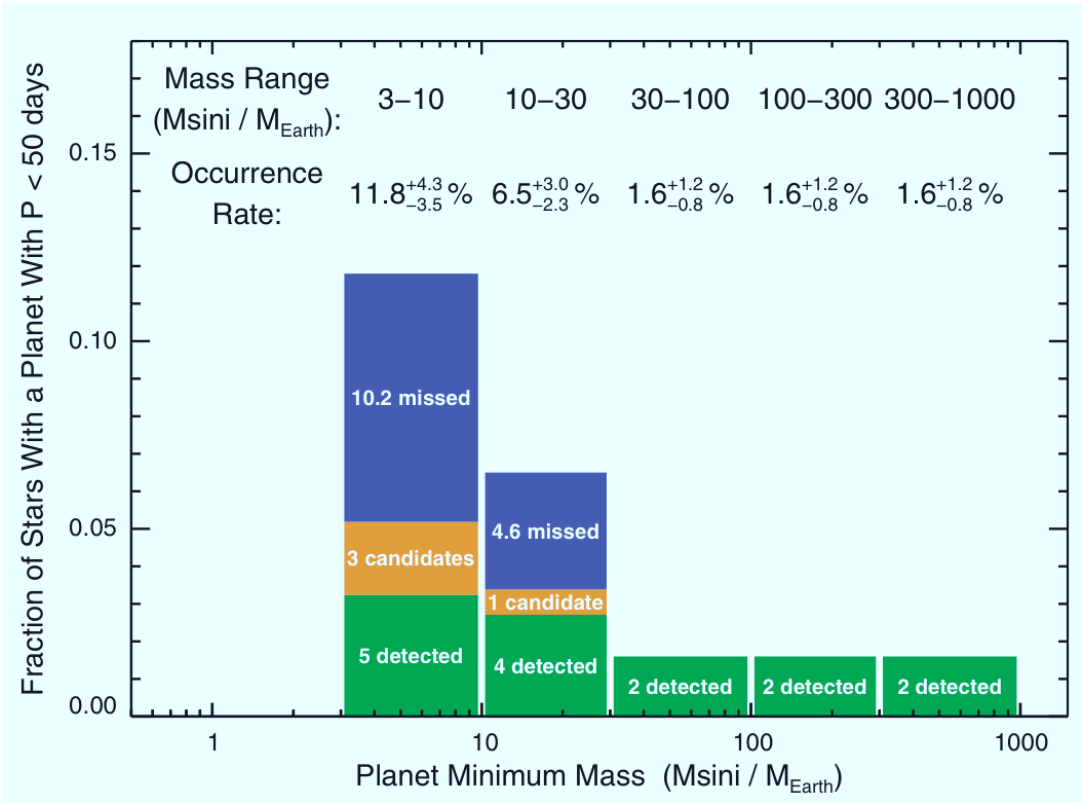

Fig. 1.2 The occurrence rate of Solar-type stars hosting planets with orbital periods less than 50 days, from Howard et al. (2010). Extrapolating to lower masses, the authors speculate that $\eta_\oplus$ is $23^{+16}_{-10}\%$ around Solar-type stars.

1.2.1 Planet Habitability

Life as we know it depends upon the presence of liquid water. This fundamental requirement limits the habitability of exoplanets to those bodies which orbit their stellar parent within the star's "Habitable Zone". The location of the Habitable Zone (hereafter, HZ) depends upon numerous factors, including the luminosity, size, and activity of the parent star, as well as the size, atmosphere, orbit, geology, and rotation of the planet. The HZ, as originally presented by Kasting et al. (1993), is shown in Figure 1.3.

The surface temperature of the exoplanet is what ultimately determines habitability. Neglecting the atmosphere, the equilibrium temperature of a planet (found by equating the emitted surface flux to the flux received by the parent star) is:

$$T_{eq} = (\frac{S(1-A)}{f\sigma})^{\frac{1}{4}} \tag{1.11}$$

where S is the stellar energy flux, A is the *Bond* albedo (the fraction of light reflected back into space), σ is the Stefan-Boltzmann constant, and f is a redistribution factor, the value of which depends upon the fraction of the surface over which the energy is distributed by winds or rotation. If the energy is redistributed over half the surface, $f = 2$; the whole surface, $f = 4$, and if the energy is not redistributed, the local temperature can be found by substituting $f = 1/\cos\theta$, where θ is the zenith angle (Selsis et al. 2007).

Equation 1.11 alone is insufficient for determining habitability, as the presence of an atmosphere will increase the actual surface temperature. In particular, the existence of greenhouse gases (such as H_2O and CO_2) will trap infrared light emitted from the surface of the planet. This effect keeps the Earth above the freezing point of water. Selsis et al (2007) demonstrated that T_{eq} must be below about 270 K, or the surface luminosity will tend toward the 300 W/m^2, known as the runaway greenhouse threshold.

The size of the planet is critical to the existence of a habitable world. If the planet is too small ($<\approx 0.5M\oplus$), the planet will not have enough mass to retain a sizable atmosphere. Additionally, small planets lack the necessary gravity to maintain geological activity, which is essential for recycling greenhouse gases such as CO_2 . At the other extreme, the core accretion model of planet formation predicts that large planetary cores ($>\approx 10M\oplus$) would accumulate hydrogen and helium from the protoplanetary disk, transforming into a gas giant (Mizuno 1980). While the surfaces of gas giants are inhospitable to life (due to their high surface pressures), large moons in orbit around gas giants in the HZ may support the existence of life (Williams et al. 1997).

The habitable zones of stars move as the stars age and grow brighter. This movement of the habitable zone further constricts the region around a star in which liquid water can exist for billions of years — the amount of time that is probably necessary for a planet to form intelligent life — to a region known as the continuous habitable zone (hereafter, CHZ). Here, M dwarfs have the advantage over G dwarfs, because their low mass slows down their stellar evolution. Kasting et al. (1993) estimate that the CHZ lasts for an order of magnitude longer around the M dwarf for this reason.

These conditions do not guarantee that a planet is habitable; environmental factors could render a planet uninhabitable. For example, high impact rates (as might be expected in a system that lacks an outer Jupiter and/or moon) on the surface could

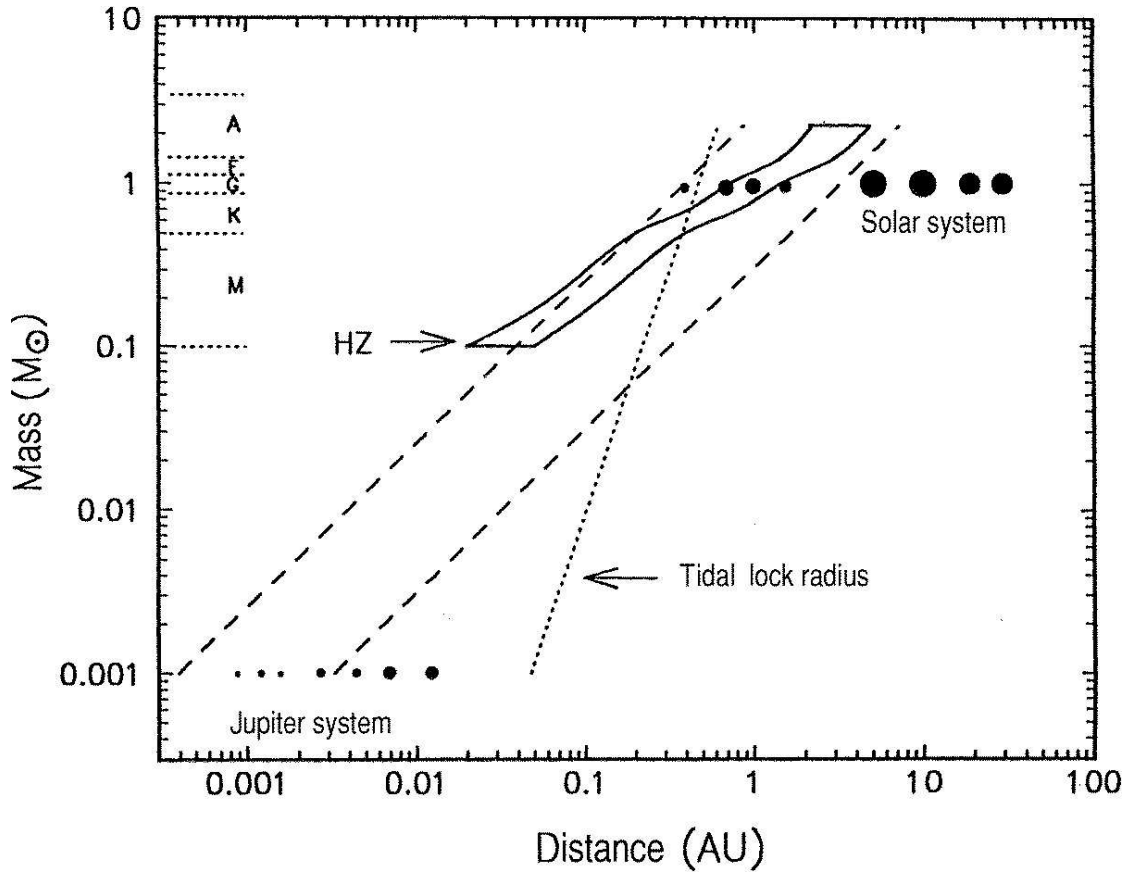

Fig. 1.3 The zero-age main sequence habitable zone, as published in Kasting et al. (1993). The stellar spectral type is indicated on the mass axis. The dotted line indicates the tidal locking radius after 4.5×10^9 years. Note that planets in the HZ around M dwarfs are within the tidal locking radius. Once thought to prevent life from arising on planets around these stars, Joshi et al. (1997); Joshi (2003) showed that winds on could effectively reduce the thermal gradient between the night and day sides of these planet.

severely depress attempts of life to arise on an otherwise habitable world (Wetherill 1994).

1.2.2 Exoplanet Atmospheres

The atmospheres of habitable exoplanets depend upon the existence of greenhouse gases, which keep the surface temperature above the freezing point of water. There are two primary greenhouse gases in the Earth's atmosphere: water vapor and carbon dioxide. The latter of these is regulated by two processes, which operate on different timescales. The fast timescale of CO_2 is an organic symbiosis between plants, which take in CO_2 and water and release O_2, and animals, which breath in O_2 and exhale CO_2. The slow timescale process is geological; carbonic acid falls with the rain water and mixes with silicates in the ground, which release calcium ions. These calcium ions flow into the oceans, where they are used by organisms to form shells. These shells fall down into the deep ocean when these organisms die, where some of the carbonate is preserved on the sea floor. The sea floor is subducted by the continental plates and heats up as it sinks below the crust. The carbonates are recombined into silicates and carbon dioxide, and the latter is released via volcanoes.

The long-term cycle (which takes about a half-million years to run once) depends upon plate tectonics, which is driven by the internal heat of planets. Planets with small masses lose their internal heat faster than large planets, so low-mass planets lose their ability to recycle the CO_2 early in their histories. This provides a lower-limit to the mass of a habitable planet, somewhere between 0.3 and $0.5M_\oplus$. Rocky planets with masses greater than $M_\oplus$ have thinner plates, and thus are more susceptible to plate tectonics (Valencia et al. 2007), although this result is controversial (Omerbashich 2008).

1.2.3 Tidal Locking and Synchronous Rotation

Planets in the habitable zone around M stars are tidally locked, in which one side of the planet permanently faces its parent star. The orbital distance at which tidal locking is important is difficult to estimate, but is approximated by the general form given by Peale (1977):

$$r_{lock} = 0.027(\frac{P_0 t}{Q})^{1/6} M^{1/3} \tag{1.12}$$

where P_0 is the original rotation period of the planet, t is the elapsed time, Q is a term that quantifies the plasticity of the planet (typically 100), and M is the mass of the star (all units are CGS).

Synchronous rotation was thought to be devastating to life as we know it, as temperatures on the near side rise above habitable levels, potentially evaporating the atmosphere, while the far side would suffer the opposite fate, with the atmosphere potentially freezing out and collapsing. However, recent simulations by Joshi et al. (1997) and Joshi (2003) indicate that these temperature extremes can be modulated by the planet's winds and greenhouse gases. Specifically, the collapse of the atmosphere can be avoided if advective currents (*e.g.,* planetary winds) move on a timescale that is smaller than the thermal relaxation timescale. The advective time scale is simply:

$$t_d = \Delta L / U \tag{1.13}$$

where ΔL is the distance between the night and day parts of the planet, and U is the atmospheric wind speed. The thermal relaxation time scale is given by Goody & Yung (1989):

$$t_r = \frac{c_p p_0}{\sigma g T_e^3} \tag{1.14}$$

where c_p is the specific heat of the atmospheric gas, p_0 is the surface pressure, σ is the Stefan-Boltzmann constant, g is the gravitational acceleration, and T_e is the effective emission temperature of the planet. For the Earth, $U \approx 10$ m/s, ΔL = 6378km $\times\pi$, $c_p = 1005$ J/kg K, $p_0 = 101325$ Pa, $\sigma = 5.67e-8$ J m^{-2} s^{-1} K^{-4}, $g = 9.8$ m/s^2, and $T_e = 250$ K, so that t_d is 23 days, while t_r is 136 days.

Not all planets orbiting within the tidal-locking distance of a parent star are necessarily tidally locked. Mercury rotates three times for every two orbits around the Sun. Such a spin/orbit resonance reduces the temperature gradient between the night and day sides of the planet, greatly reducing the chances of atmospheric collapse.

1.3 M Dwarfs as Exoplanet Host Stars

M dwarfs are both the least-massive and the most populous type of star in the Milky Way, comprising 72% of all stars within 10 pc [2]. These stars represent an important target for exoplanet searches for several reasons.

First, the radial velocity precision required to detect low-mass planets is inversely proportional to the mass of the star to the two-thirds power, making M dwarfs the most gravitationally-sensitive stars in the universe to any orbiting exoplanets. Additionally, since these stars have much lower luminosities than other stars, the habitable zone is much closer to these stars than around solar-type stars. These two factors mean that habitable Earth-mass planets around these stars exhibit an order-of-magnitude greater reflex velocity in their parent star than the Earth does around the Sun (see Figure 1.4).

Second, since M dwarfs evolve along the main sequence slowly, their habitable zone boundaries change slowly, allowing more time for life to evolve on any exoplanets therein. M dwarfs also have the longest lifetimes of all the stars, exceeding 10^{13} years for the least-massive stars (Laughlin et al. 1997).

Third, characterizing the population of exoplanets around M dwarfs constrains our models of planet formation. The frequency of planets is expected to increase sharply beyond the "snow line" — the radius at which ice condenses (Pollack et al. 1996). This radius is proportional to $\sqrt{L}$. Since the time needed to confirm the existence of a planet around a star is proportional to the planet's orbital period, the observation time needed to find planets beyond the snow line goes as $L^{3/4}$. In other words, a NIR radial velocity search can sample a planet orbiting at the snow line around an M dwarf about 100 times faster than the same around a solar-type star.

[2] RECONS `http://www.recons.org/`

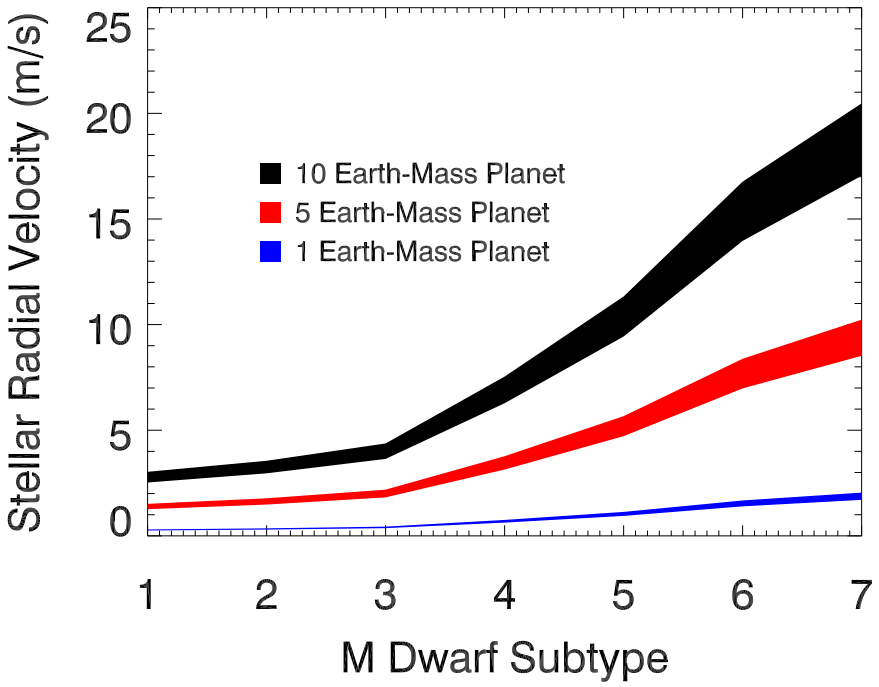

Fig. 1.4 The radial velocity precision required to detect potentially-habitable Earth- and Super Earth-mass planets in circular orbits around M dwarfs as a function of stellar subtype. The size of the Habitable Zone is indicated by the thickness of the lines, with the top of each line indicating the precision required to detect a planet on the inside of the HZ. Stellar masses and luminosities were acquired from Reid & Hawley (2005).

Fourth, M dwarfs with spectral types beyond M4 are difficult to attain with current optical planet searches, since these stars give off most of their flux in the NIR. Late M dwarfs have numerous molecular features, raising their spectral information content beyond that of their optical spectra.

The benefits of searches around M dwarfs were recognized in both the Exoplanet Community Report (Lawson et al. 2009) and the Exoplanet Task Force Report (Lunine et al. 2008), which recommend that developments in Doppler precision be extended to the NIR in an effort to reach sub-10 m/s precision, and that instruments that demonstrate these precision levels be fast-tracked, respectively.

1.3.1 Fundamental Parameters of M Dwarfs

Table 1.3.1 presents some of the fundamental parameters of M dwarfs. Historically, the stellar classification 'M' was based upon spectral features identified in low-resolution spectra. Initially, stars were only classified out to M2 Morgan et al. (1943). Johnson & Morgan (1953) classified dwarfs out to M5, after defining Barnard's star as such a star. The spectral classes beyond M7 were defined only twenty years ago by Kirkpatrick et al. (1991), using not only the strength of spectral features, but the spectrum's slope.

Because of the low temperature and high gravity of these stars, the atmospheres of M dwarfs support the formation of molecules. In the optical, the spectra are dominated by lines of titanium oxide (TiO) and vanadium oxide (VO), and in the infrared, the dominate features are steam and carbon monoxide (CO). The opacities of TiO and VO drive the flux towards the NIR, which give M dwarfs their characteristic spectral energy distribution peak in the infrared. Such a spectrum can be seen in Figure 1.5, which shows a composite spectrum of GJ 406 compiled by Pavlenko et al. (2006). This transition is illustrated in Figure 1.6 from McLean et al. (2003). This forest of lines produced by these absorption sources would be conducive to precision RV measurements, which rely upon a large number of stellar lines (see 1.1.2).

Even though M dwarfs have the low stellar masses, between ≈ 0.08 and 0.6 $M_\odot$ (Reid & Hawley 2005), their cumulative mass dominates the Milky Way. Since these stars are fully convective, they will burn their entire supply of hydrogen, which greatly extends their time on the main sequence (Laughlin et al. 1997). The evolution of M dwarfs on the HR diagram can be seen in Figure 1.7. Trillions of years from now, after all the earlier spectral types have faded away, the galactic luminosity will be dominated by contributions from evolved 0.2 $M_\odot$ G dwarfs such that the total luminosity will be $\approx 10^{10}$ $L_\odot$ (Adams & Laughlin 1997).

1.3.2 Rotation and Activity of M Dwarfs

As described in § 1.1.4, the rotation rate of stars slows as a star transfers angular momentum to the surrounding medium through magnetic braking. M dwarfs are no exception to this phenomenon, but it should be noted that the $v\sin i$ measurements of these stars tend to increase markedly beyond M4 (Jenkins et al. 2009). This is likely a change in the boundary between the partially radiative envelopes of early M dwarfs, and

Spectral type	V-I	Temperature (K)	Radius ($R/R_\odot$)	Mass ($M/M_\odot$)	Luminosity ($10^{-2}L/L_\odot$)	Gravity (log) ($g\ cm^{-2}s^{-1}$)	Prototype
M0	1.92	3800	0.62	0.60	7.2	4.65	GI 278C
M1	2.01	3600	0.49	0.49	3.5	4.75	GI 229A
M2	2.15	3400	0.44	0.44	2.3	4.8	GI 411
M3	2.46	3250	0.39	0.36	1.5	4.8	GI 725A
M4	2.78	3100	0.36	0.20	0.55	4.9	GI 699
M5	3.70	2800	0.20	0.14	0.22	5	GI 866AB
M6	4.06	2600	0.15	0.10	0.09	5.1	GI 406
M7	4.56	2500	0.12	≈ 0.09	0.05	5.2	GI 644C (VB 8)
M8	4.66	2400	0.11	≈ 0.08	0.03	5.2	GI 752B (VB 10)
M9	4.37	2300	0.08	≈ 0.075	0.015	5.4	LHS 2924

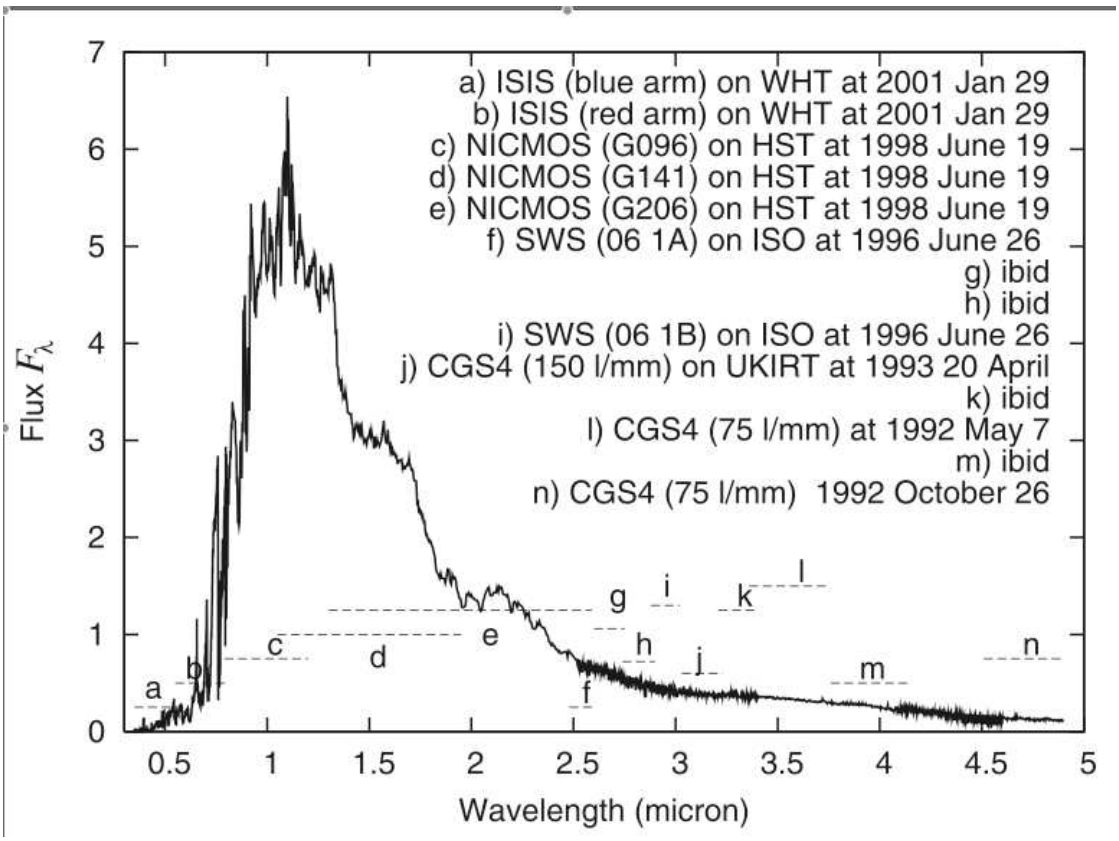

Fig. 1.5 The spectral energy distribution of M6V GJ406 from Pavlenko et al. (2006). Note the high NIR flux relative to the weak optical.

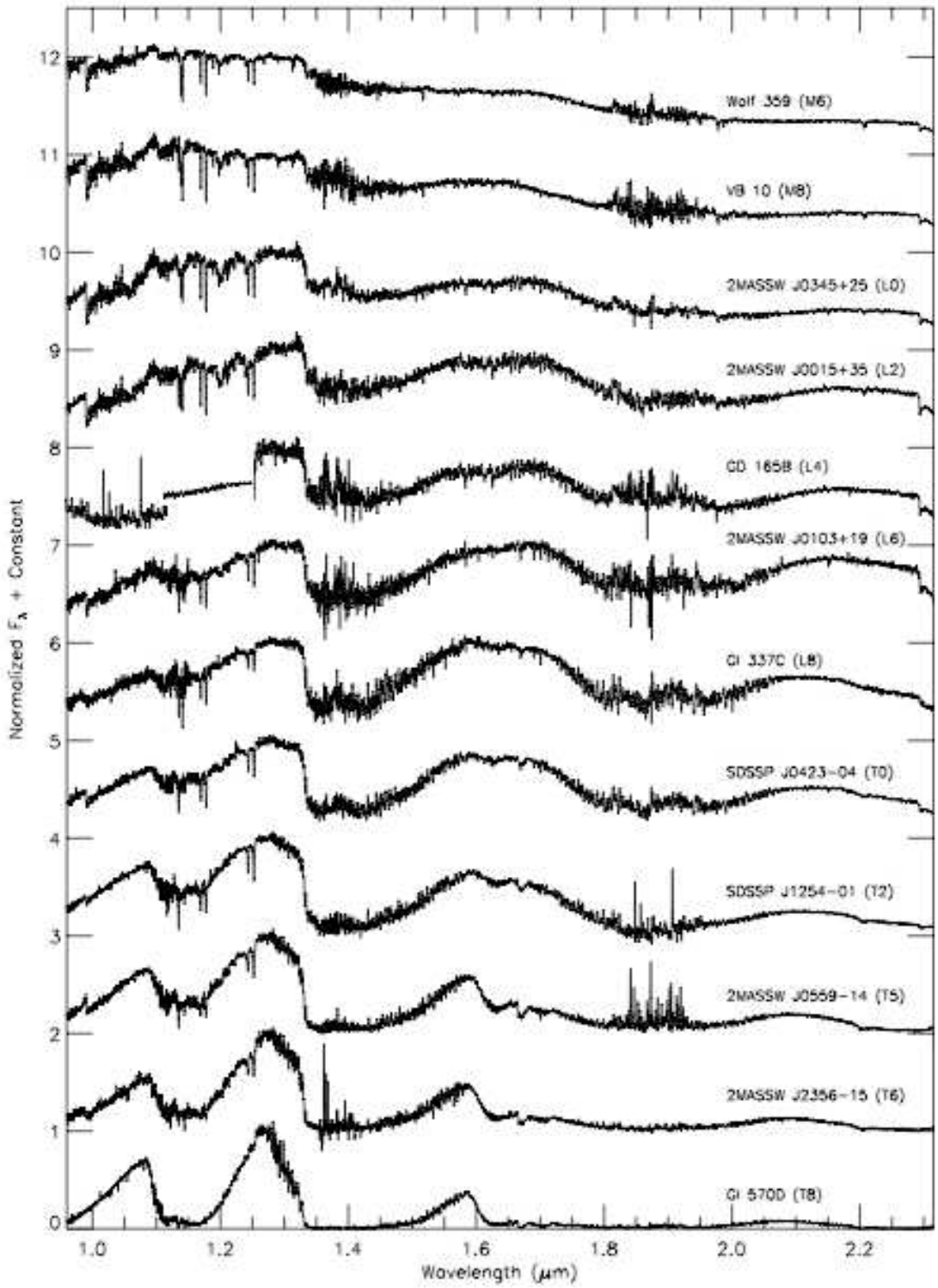

Fig. 1.6 M-, L-, and T-dwarf spectra from McLean et al. (2003), illustrating the deviation from blackbody spectra in these spectral types, where the light from these stars escapes through increasingly-narrower NIR bands.

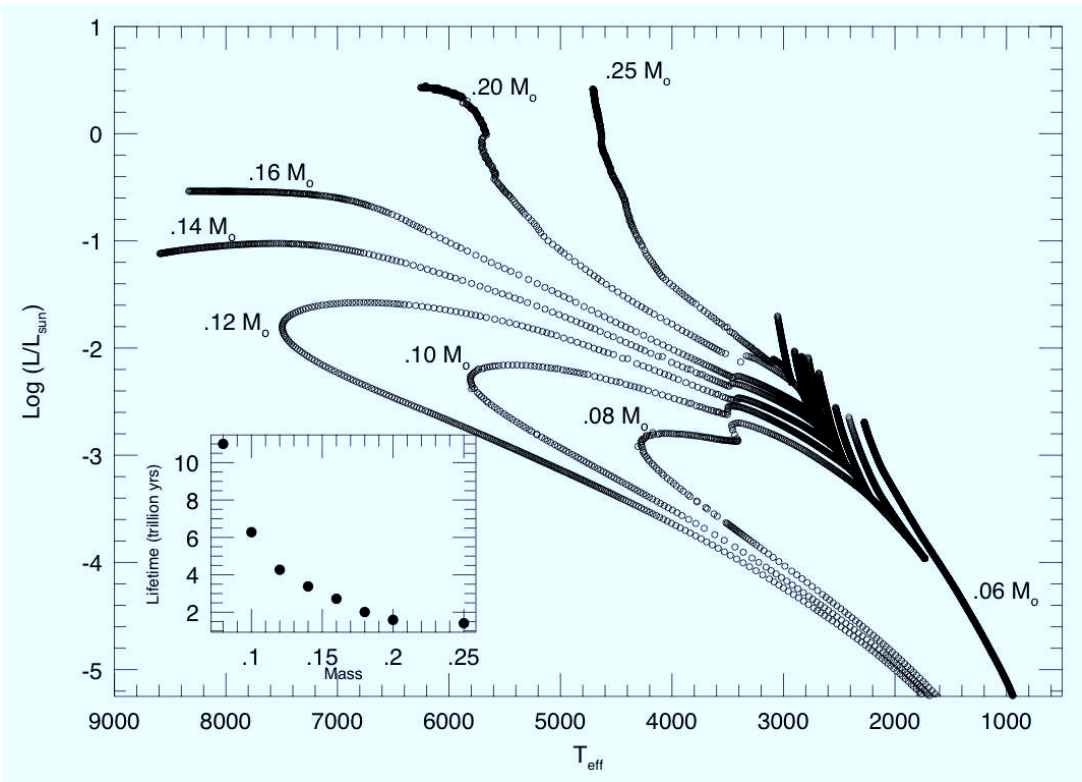

Fig. 1.7 The evolutionary tracks of M dwarfs on the H-R Diagram, as calculated by Laughlin et al. (1997). The inset graph indicates the expected main sequence lifetime for M dwarfs of different masses.

the fully convective late M dwarfs. These measurements suggest that late M dwarfs are less efficient at magnetic braking.

Curiously, M dwarfs lack the periodic signature of spots found in G and K dwarfs (Reid & Hawley 2005). This might be evidence that the spots on M dwarfs vary on short timescales, or they may be uniformly distributed on the surface. Additionally, the contrast between the stellar photosphere and spot is reduced by a factor of 3 to 4 in the NIR when compared to the optical (Rockenfeller et al. 2006). This suggests that NIR precision RV measurements may be able to avoid the brunt of the systematics from starspots.

Despite the lack of evidence for starspots, many late-type M dwarfs are active (as measured by their Hα equivalent width) — see Figure 1.8 from West et al. (2008). M dwarfs are well-known for their flaring activity, in which the star's blue and UV continuum emission rapidly increases by several orders of magnitude. These flares are followed by an increase in the observed soft X-ray flux (as the flares heat the corona).

1.3.3 The Search for Planets Around M Dwarfs

Given their dominant population in the local neighborhood, and the amplified radial velocity signal from orbiting Earth-mass planets, it is not surprising that current optical RV surveys (such as CPS, M2K, and HARPS) have found 18 planets around M Dwarfs to date [3]. This includes the multi-planet system GJ 581 (Mayor et al. 2009) which includes the claimed Earth-mass planet GJ581g in the HZ (Vogt et al. 2010). However, these surveys have been unable to explore late M dwarfs (> M4 or M5) because of their intrinsically low optical luminosities and the lack of suitable calibration sources in the NIR.

A histogram of the number of exoplanets discovered as a function of $m \sin i$ is shown at the top Fig. 1.1. The observed growth of the fraction of stars with planets towards lower planetary masses (see Figure 1.2) suggests that many low-mass planets remain undetected (Howard et al. 2010). Additionally, large fractions ($\approx 45\%$) of M dwarfs exhibit the infrared excess indicative of a circumstellar disk (Luhman et al. 2005), the existence of which is necessary for planet formation. All of this suggests that M dwarfs should be frequent hosts of planetary systems.

There are several mysteries regarding the population of known planets around M-dwarfs. For example, to date, only four systems with Jupiter-mass planets have been discovered around these stars. This may be due to a bias in the lack of M-dwarf observations, or in the short time since M-dwarf monitoring programs began, but the absence of hot Jupiters appears to be real (Endl et al. 2006). This result suggests that the stellar mass is linked to the size of the protoplanetary disk around these stars — *e.g.,* low-mass stars form low-mass planets (Laughlin et al. 2004). If we are to probe this hypothesized population of planets, we must continue to push our radial velocity techniques to lower precisions to test these planet formation theories.

The aforementioned study by Reiners et al. (2010) includes a comparison between the RV precisions achievable in the optical and the three closest NIR bands: the Y, J, and

[3] `http://exoplanet.eu`, 2010 12 01

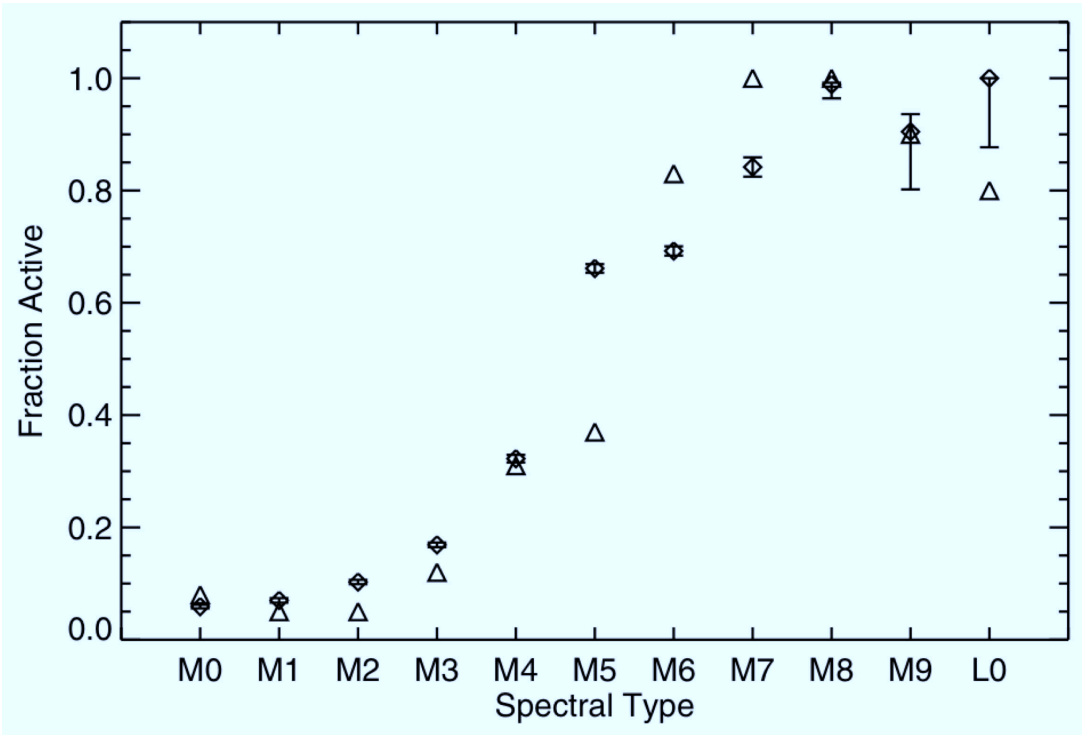

Fig. 1.8 M dwarf activity as a function of spectral type, based on the equivalent width of the Hα line, from West et al. (2008). Stellar activity increases strongly for late-type M dwarfs.

H bands. By comparing the information content (see § 1.1.2) of M3V, M6V, and M9V stars, as well as the current limitations of different calibration sources in these spectral ranges, they quantify the relative advantage of observing these stars in these different spectral ranges. They find that while the optical precision continues to dominate for early M dwarfs, around M4 or M5 and later it becomes more advantageous to observe these stars in the Y band. The J and H bands provide a precision advantage over the optical only for the very latest M dwarfs. This result confirms an unpublished study for the PRVS Pathfinder.

1.4 The Challenge of Near-Infrared Precision Radial Velocity Measurements

The NIR is replete with technological challenges that limit the currently-achievable precisions. The Pathfinder spectrograph was designed to explore some of these challenges, which are described in this subsection, and will be addressed throughout the remainder of the thesis.

1.4.1 Near-Infrared Calibration Sources

ThAr lamps offer significant line coverage well into the J-band — Kerber et al. (2008) presented a list of 2400 lines between 900 and 4500 nm — but bright argon lines dominate the spectrum in the NIR. Argon lines are much more sensitive to pressure shifts than the thorium lines (Whaling et al. 2002), and cannot be used for precision measurements (Lovis & Pepe 2007). There are undoubtedly many more ThAr lines in this spectral region, but the hollow cathode lamp in this study was purposely run at the same (low) current as on CRIRES, and so many of the fainter Th lines were undetectable.

A primary limitation to the utility of absorption cells (such as I_2 and HF) is their wavelength coverage. HF only covers a small ($\approx$ 100Å) range around 8715Å. The I_2 cell is effective only between ≈ 0.5 to 0.62μm (Marcy & Butler 1992), and cannot be used in the NIR. However, the utility of gas cells (which can be used on any telescope, as long as they can be inserted in the beam path) has encouraged many groups to design and test their own cells. ~ 5 m/s precision has been achieved by Bean et al. (2010) using an ammonia (NH_3) gas cell covering a small fraction of the K band. A variety of gas cells are being developed and tested by Valdivielso et al. (2010). Another possible solution for fiber-fed instruments is to feed flatfield light through a series of telecom gas cells and use this spectrum as a simultaneous calibration source through an adjacent fiber, as proposed by Mahadevan & Ge (2009). Such a spectrum would provide sharp absorption features over 120 nm of the H band.

1.4.2 Telluric Absorption

Ground-based observations outside the optical and radio bands are hindered by telluric lines. In the NIR, the Y, J, and H bands are separated by large spectral regions with numerous water, oxygen, and carbon dioxide bands (see Figure 1.9). While using these lines as calibration sources (or for measurements of the PSF) is a possibility for our work — *e.g.,* Gray & Brown (2006) — the precision obtained with these methods

is a few tens of m/s, which is above the level of precision we are trying to achieve. A crude technique for removing these lines involves observing a Telluric standard star contemporaneously with the target star, and dividing the stellar spectrum by the extracted Telluric spectrum. Unfortunately, Telluric lines — especially the water lines — vary rapidly and depend strongly upon the exact pointing of the telescope, both because different pointings are peering through different sections of the atmosphere, and because the velocities of these telluric features change due to winds as you look at higher zenith angles.

1.4.3 Modal Noise in Fibers

Modes can be thought of as electromagnetic plane waves entering a fiber at a specific angle and position, and exiting at a particular angle and position. The exit angles and positions of these modes depend upon microscopic imperfections in the fiber, and the exact position of the fiber, the latter of which changes by small amounts over the course of minutes while the telescope is tracking. This produces a speckled illumination pattern in the far field which, in turn, affects the illumination pattern of dispersed light upon the detector. If this illumination pattern does not remain constant between the flat field and science and/or calibration exposures, these changes will appear as increased noise in the extracted spectrum. An example of two different speckle patterns can be seen in the top two images of Figure 1.10.

The number of modes is given by Grupp (2003):

$$M = 2\pi^2 (\frac{r}{\lambda})^2 \sin^2 \arctan (\frac{1}{2\frac{f}{\#}}) \tag{1.15}$$

where r is the diameter of the fiber, λ is the wavelength of light, and $\frac{f}{\#}$ is the f-ratio. Noise from these modes is inversely proportional to the square root of the number of modes. Figure 1.11 shows the number of modes as a function of wavelength for a 100μm fiber with an f ratio of 4.5. The bottom plot shows the square root of the number of modes (which is proportional to the limiting S/N). While modal noise is less significant in the optical, it is essential to account for it in the NIR.

Fortunately, minimizing modal noise is, in theory, simple — the fibers must be vibrated near the output end (Baudrand & Walker 2001). By vibrating the fiber at a rate that is much faster than the exposure time, the speckle pattern is scrambled, averaging the contributions of the various modes. An example of a scrambled speckle pattern can be seen in the bottom image of Figure 1.10.

1.4.4 Persistence

HAWAII 1K arrays are known to exhibit residual excess dark current or "persistence" (Hodapp et al. 1992), a signal that remains on the array after the source has been removed or blocked. The latency of this dark current depends upon the level of exposure, with saturated elements exhibiting the greatest persistence. Studies by Campbell & Thompson (2006) on Indium Antimonide arrays suggest that persistence decays inversely with time, and that reading the array to eliminate persistence only increases its

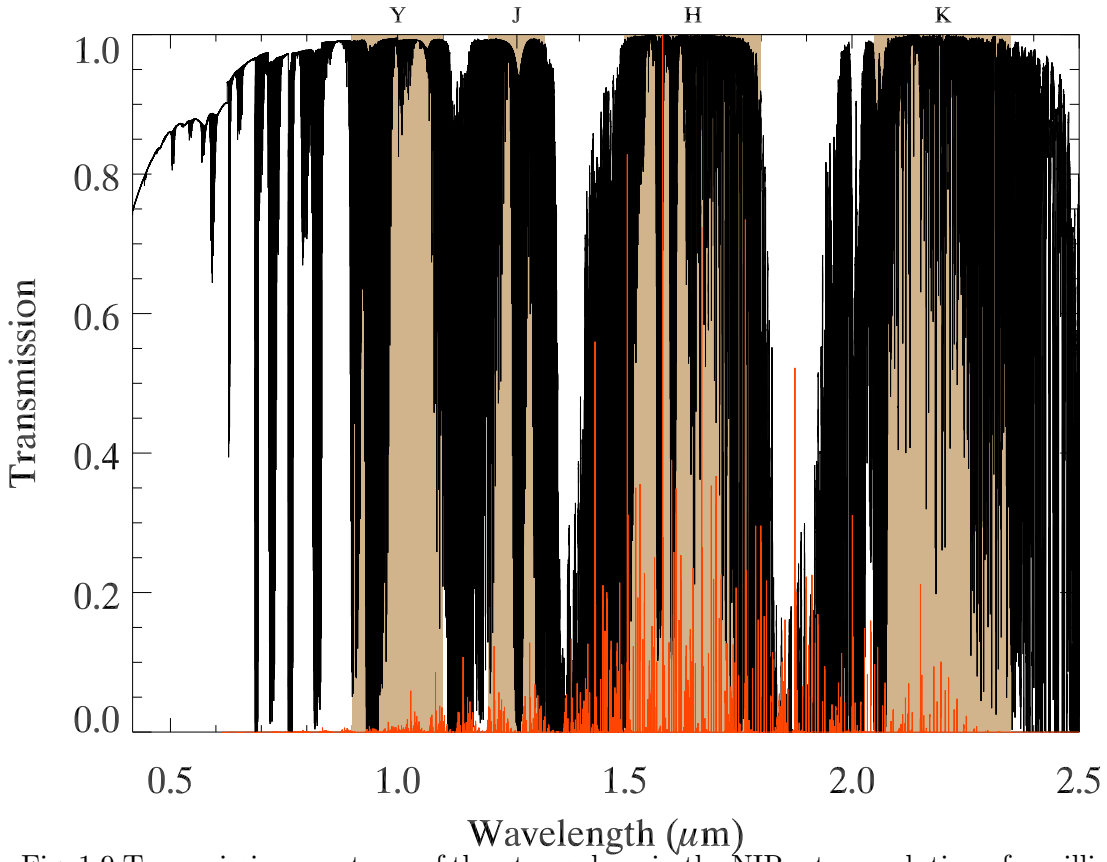

Fig. 1.9 Transmission spectrum of the atmosphere in the NIR, at a resolution of a million. The Y, J, H, and K bands are indicated by the shaded regions. The OH emission lines are indicated in orange. The relative lack of Telluric lines in the Y band is one of the reasons Pathfinder was designed for this region.

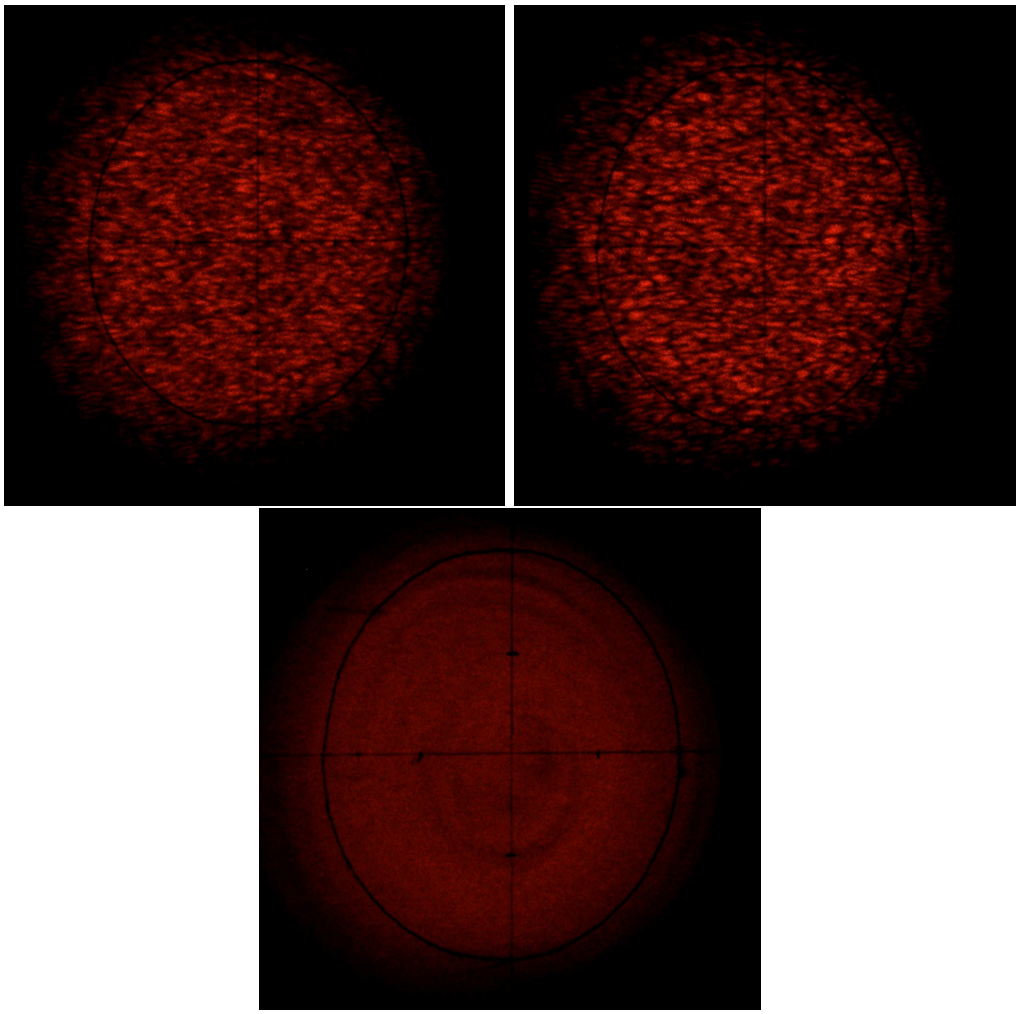

Fig. 1.10 The different modes of a HeNe laser through our fibers. If the speckle pattern were constant then modal noise would be ignorable. Unfortunately, microscopic and macroscopic changes to the fiber change the modes (top photos). The modes change slightly every 30 seconds or so. The solution in the optical is to vibrate the fiber, distributing the modes evenly in the radial direction (bottom photo). Agitating the fiber does not mix the modes in the radial direction.

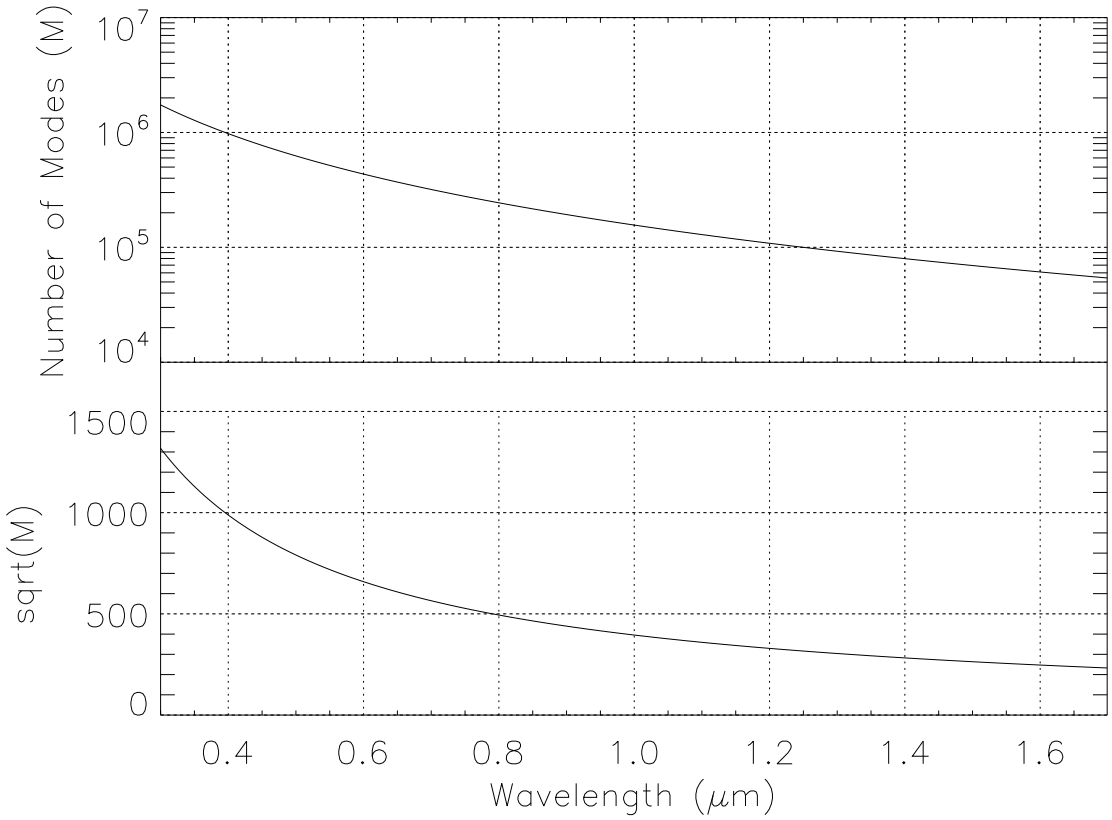

Fig. 1.11 The number of modes as a function of wavelength (top), and the square root of the number of modes (bottom; this quantity is proportional to the limiting S/N). Since there are many fewer modes in the NIR, it is more essential to mix these modes than it is in the optical.

influence, presumably by raising the temperature of the array. Tests by Hodapp et al. (1996) to reduce or eliminate charge persistence were also largely unsuccessful — the authors can only recommend avoiding element saturation. The physical mechanism for persistence is not certain, although tests by Smith et al. (2008) suggest that persistence is caused by the slow release of trapped charges, which leads to an imperfect reset.

1.5 Near-Infrared Precision Radial Velocities

In spite of the above-mentioned challenges, on-sky radial velocities in the NIR have improved dramatically in the previous three years. Blake et al. (2008) achieved 300 m/s precision with PHOENIX using Telluric Methane bands as a calibration source. Huélamo et al. (2008) achieved 35 m/s precision for TW Hya using CRIRES, rejecting a previously-proposed Jupiter-mass planet in that system. Blake et al. (2010) achieved 50 m/s precision in observations of a radial velocity standard M dwarf and 200 m/s precision on slowly-rotating L dwarfs using Telluric CH_4 features as a calibration source. Seifahrt & Käufl (2008) achieved a precision of 20 m/s over 5 hours on MS Vel. Figueira et al. (2010) achieved 6—10 m/s precision using CO_2 lines in the H band. Bean et al. (2010) achieved $\approx$ 5 m/s precision using an NH_3 gas cell in a small section of the K band with CRIRES.

1.5.1 Current NIR Instruments

Three NIR spectrographs are currently capable of making sub-100 m/s precision measurements in the NIR. The most precise operating infrared instrument on the planet is CRIRES (CRyogenic high-resolution InfraRed echelle Spectrograph) (Ulrich Käufl 2008) on the Very Large Telescope (VLT). Its high resolution ($\approx 10^5$) is limited only by its small simultaneous wavelength coverage ($\approx$ 10 nm on each of four detectors). It can cover wavelengths between 1 and 5 μm with 50 different grating settings. The most precise measurements that have been made with CRIRES to date are those of Bean et al. (2010), who achieved 5 m/s with an ammonia gas cell at 2.3 μm.

NIRSpec (Near-InfraRed Spectrograph) (McLean et al. 1998) on Keck II has a resolution of 25000 and a simultaneous coverage of 400 nm. CSHELL, the Crygenic eCHELLE spectrograph (Greene et al. 1993), on the NASA Infrared Telescope Facility (IRTF) has a resolution of 40000 between 1 and 5 μm, and simultaneous bandwidth of 30 nm. While high-precision measurements ($\approx$ 5 m/s) have been made with this instrument, these precisions are limited by the small bandwidth coverage and the S/N of the target, such that high precisions will only be achieved on the brightest M dwarfs.

TEDI (TripleSpec Exoplanet Discovery Instrument) (Edelstein et al. 2007) superimposes an unresolved comb on the stellar spectrum, and then passes the starlight through an interferometer. The stellar shifts are recoverable because the underlying comb spectrum is known. However, this technique has yet to demonstrate precisions below 50 m/s (Muirhead et al. 2011). Their use of Argon lines for calibration purposes is especially unfortunate, given that many of these lines are known to be unsuitable for precision RV work (Kerber et al. 2008).

1.5.2 Proposed NIR Instruments

The UKIRT Planet Finder (UPF) is another cross-dispersed echelle spectrograph based on the success of the Precision Radial Velocity Spectrometer (PRVS) Pathfinder (see Chapter 2). Unfortunately, UKIRT is currently scheduled to end operations in 2012, with no sign that the UPF will ever be constructed.

iSHELL (Immersion grating eCHELLE spectrograph) is the successor to cSHELL, and current plans do not include a fiber feed. The option for the inclusion of a gas cell is currently being discussed, but even so the silicon grating is ineffective in the Y band, and gas cells for the NIR are still in the testing phase. As a facility-class instrument with multiple settings, the stability of this instrument will be a serious concern.

CARMENES (Calar Alto high-Resolution search for M dwarfs with Exo-earths with Near-infrared and optical Echelle Spectrographs) will cover 950 to 1700 nm at a resolution of 85000 over 30 orders in a single exposure of two 2k by 2k arrays (Quirrenbach et al. 2010). This telescope will use either simultaneous ThAr exposures or a stabilized etalon (still in development) as a calibration source. Preliminary studies suggest, as we have also found in our Pathfinder, that the Y band is an optimal region to explore. CARMENES is expected to see first light in late 2013 or early 2014, and to begin its survey shortly thereafter.

The Habitable Zone Planet Finder (HZPF) is based upon the Precision Radial Velocity Spectrograph (PRVS), which won a Gemini instrument competition in 2006, but shortly thereafter was cancelled when the UK pulled its support from the facility. The design and requirements of the HZPF draws upon the research conducted as part of this dissertation. This proposed spectrograph would be a resolution 50000 with a precision of 3 m/s. Designed to observe late M dwarfs, which are inaccessible to current surveys, we most recently were awarded funding to obtain a HAWAII-2K array.

1.6 Conclusions

Late M dwarfs are promising targets for high-resolution,NIR spectrographs because they emit most of their light at NIR wavelengths. However, existing NIR spectrographs are too unstable for the high-precision needed for detecting Earth-mass planets around late M dwarfs. CARMENES and the HZPF have the capacity to conduct a survey of the nearest late M dwarfs. The following chapter describes my first experiments with the PSU Pathfinder — a high-resolution spectrograph designed to mitigate some of the risk associated with making precision radial velocity measurements in the NIR.

Chapter 2

The PSU Pathfinder: Solar Experiments

The Pathfinder was conceived as a way to to retire risk on the Precision Radial Velocity Spectrometer (PRVS), an instrument which successfully obtained approval and funding in 2006, but was cancelled after the UK pulled their support from Gemini (Jones et al. 2006). Between 2006 and 2008, we used the Pathfinder to measure precision RVs at the tens of m/s level by observing the rotation signal of the Earth via the solar spectrum. The amplitude of this signal is well-above the amplitude of the RV curves we hope to measure around late M dwarfs, but the precision of the theoretical earth rotation curve allowed us to carefully tune our instrument and observation technique.

2.1 Spectrograph

The spectrograph is constructed primarily with standard optical mounting hardware on an 8×2 foot optical bench, but the fiber input and the detector are mounted on custom-made units. This table is located in an interior lab that has controlled access to minimize temperature fluctuations. We did not have precision temperature monitoring hardware in place when the measurements discussed in this chapter were taken. However, recently-installed Lakeshore PT102 platinum resistance thermometers with a Lakeshore 218 monitor indicate ambient room temperature variations are typically 0.1 K over several hours, while spectrograph temperature variations are on the order of 0.05 K. The spectrograph, located in an interior room in Davey Laboratory on the Penn State campus, is fed by a single fiber optic cable whose input end is located on the roof of the building in one of the rooftop observatories.

2.1.1 Optical Design

We will adopt the notation of Schroeder (2000) in our description of the Pathfinder optical design. An optical layout of the system is displayed in Figure 2.1. The instrument has a straightforward in-plane configuration with an R2 echelle and a 100-mm collimated beam diameter. The echelle is operated at an unusually large θ angle of 11.66°, which is required to achieve the desired resolving power. The collimator is a simple 609 mm-focal length parabola. The collimated beam is dispersed by a gold-coated 31 lines/mm $\Theta_{\rm blaze} = 63.4^\circ$ R2 echelle on a 110×210 mm Zerodur substrate. Given that $\theta = 11.66^\circ$, the incident angle, $\alpha = \Theta_{\rm blaze} + \theta \approx 75^\circ$, produces a substantial vignetting of the collimated beam by the 200×100 mm ruled area of the grating. The effective collimated beam at the grating is 100 mm high and approximately 50 mm wide. The diffracted beam has an anamorphic magnification in the dispersion direction of ~ 2.3 that is cross-dispersed by a 150 lines mm^{-1}, $\Theta_{\rm blaze} = 2.15^\circ$ grating. The efficiency of this

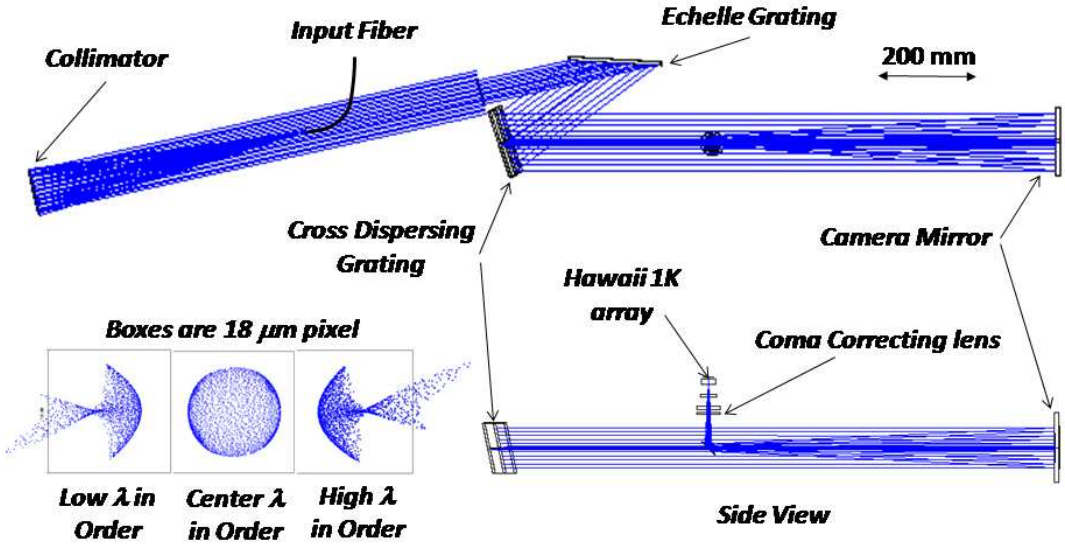

Fig. 2.1 The optical layout from a Zemax model of Pathfinder as well as the theoretical imaging performance, from Ramsey et al. (2008). The top of this figure is a top view in the plane of the echelle dispersion. The bottom right shows a side view from the cross disperser to the final focal plane. The bottom left shows the expected spots at the center and edges of an order centered on the HAWAII 1K array. The boxes are 18 μm^2 and are approximately the size of one pixel.

in-house (but far from optimal) cross disperser is low (∼20%) in the wavelength band (0.95-1.35 μm) of our initial observations.

The Pathfinder camera is, like the collimator, a simple Aluminum-coated, 154-mm diameter, 916-mm focal length parabola. A weak lens near the focus corrects much of the coma; this lens gives the camera an effective focal length of 800 mm. The camera beam is folded so as to allow the Dewar to be mounted vertically. This configuration allows the detector coolant (liquid nitrogen; hereafter, LN_2) to always cover the cold plate on which the detector is mounted.

Fig. 2.1 also shows the camera layout and spot diagram over the field of view of the detector in the focal plane. The effects of coma are controlled to about 1 pixel at the edges of the detector; this is of considerable importance as there are only about 2.5 detector pixels per resolution element. The variation of the spot shape over the camera field imposes a limit on the radial velocity precision achievable in our system due to the limited number of calibration lines. As this is essentially a variation with wavelength, fundamentally the quantity we are measuring, it can only be well compensated if there is a calibration line in close proximity. While limited, this implementation was judged sufficient for our initial tests.

2.1.2 Solar Feed

The signal required for our experiment is the integrated solar disk; this is obtained by imaging the Sun with a simple lens onto the input of a 6 mm liquid light guide, which scrambles the spatial information. An RG-850 filter was used to protect the liquid light guide from UV radiation. For the August 2006 run, the output of the liquid light guide was butted against a 100 μm blue-optimized (FV) optical fiber, which ran down to the lab on the lower floor. This fiber has poor transmission beyond 800 nm, but was adequate in the Y band for our tests.

In September 2006, we replaced the fiber with a 300 μm IR-optimized (FI) fiber, with a 2.5 mm ball lens glued to the input end. This ball lens afforded us a 10° field of view, so tracking errors would not compromise our ability to integrate the solar disk. Unfortunately, we found that the field of view was so large that light scattered by nearby clouds noticeably degraded the quality of our signal and so observations were only attempted when skies were mostly clear. Clouds that do not uniformly cover the Sun during an integration can lead to a significant solar rotation residual in the data as solar rotation is about 100 times greater than what we are trying to measure. In 2007, the ball lens was placed at the output of the liquid light guide.

2.1.3 Calibration System

Scientific measurements are only as good as the corresponding calibrations. In 2006, we used a series of pen lamps to provide us with a comparison spectrum to track our instrumental drift. This setup is pictured in Figure 2.2. Light from each of the four noble gas pen lamps (Kr, Ar Ne, and Xe) and the flat field lamp shines onto a pair of 200 μm fibers in ferrules. One fiber from each of these pairs is packed into a hexagon shape to form the calibration fiber bundle, and the other fiber from each of these pairs is combined with another 200 μm fiber from the solar feed to form a second fiber bundle.

This science fiber bundle is butted up against a 600 μm fiber which then leads to the splicer (see § 2.1.4). During science exposures, light from the pen lamps goes into both the calibration and the science fibers, while solar light is restricted to the science fibers.

While this setup provided us with simultaneous calibration in the science fiber, reductions were mired by the mixture of solar absorption lines and calibration emission lines. In practice, only one or two emission lines were useable in any given order. We were fortunate when emission lines did not blend with strong absorption lines.

In 2007, we used a "plus"-intersection, shown in Figure 2.3. During regular science exposures, solar light from the rooftop enters the intersection from the bottom of this image ("solar output" fiber), and enters the spectrograph via the "science input" fiber at the top of the image. Simultaneous ThAr light from the "calibration output" fiber enters the spectrograph via the "calibration input". Calibration light can also enter the science fiber when a flip mirror is inserted into the calibration beam path.

This intersection proved challenging in two particular ways: first, any mechanical settling in any of the lenses or FP-2s would result in a significant loss of throughput. However, as long as these components were sufficiently tightened, alignment remained adequate. Second, the flip mirror had to be aligned precisely in order to maintain calibration throughput to the science input fiber. The rotation of the flip mirror was not precisely controlled, making it especially difficult to align.

2.1.4 Feed Design

One of the challenges with a fiber-fed instrument is maximizing the light from the target while also maximizing the spectral resolution. The former is easier to achieve with larger-diameter fibers, while the latter encourages the use of small-diameter fibers. There are two ways to achieve both, with some loss of throughput. The first is to use a fiber slicer, where a hexagonal bundle of small-diameter fibers at the input are reconfigured at the output to form a pseudo-slit. In this case, throughput is limited by the packing problem at the input. The second is to use large-diameter fibers and then cover the output with a thin slit. Here there is also an obvious loss of throughput, but since the output is not uniformly distributed in the near-field (most of the light comes out at the center), the throughput loss is not as bad as it first appears. Both of these methods were utilized in our solar experiments.

For the 2006 August dataset, we used a fiber slicer for the object input (see the top of Figure 2.4). Our slicer used 100-μm core, 125-μm cladding diameter fibers; this yields a geometrical throughput of 49% after the Acrylate buffers are removed from the constituent fibers. The left panel of Fig. 2.4 displays the input of the seven slicer fibers, and the middle panel is the output of the slicer fibers formatted into a psuedo slit. The image of the pseudo slit was 70 pixels high on the detector. The two outermost fibers on each end of the slit are the calibration lamp feeds. A single fiber spacer is used to separate each calibration fiber from the seven object fibers. Initial measurements of the laser output indicated acceptable focal ratio degradation.

In October 2007, we implemented a configuration with 300 μm core fibers to maximize the throughput from the telescope and the calibration lamps. The object fiber is separated from the calibration fiber by a single fiber spacer (see right-hand image in

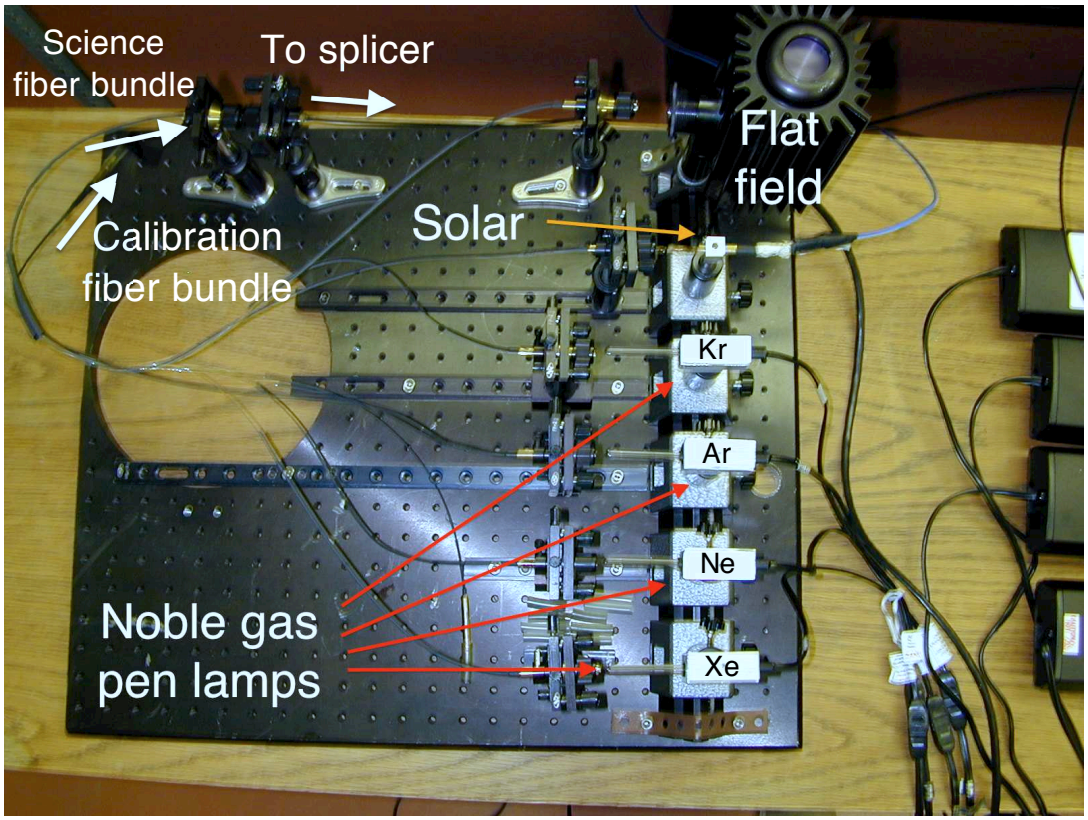

Fig. 2.2 An image of the calibration setup used in the 16 August 2006 run. Each ferrule for the pen lamps and flat field lamp have two 200 μm fibers, six of which are packed into a hexagon to form the calibration fiber bundle, and the others of which are joined with the solar feed to form the science fiber bundle, which leads to the fiber splicer. During science exposures, calibration light from the argon pen lamp and solar fibers are fed into a single 600 μm fiber via the science fiber bundle, which is then butted up against the fiber splicer bundle (see § 2.1.4). A second bundle leads to the two calibration fibers in the fiber splicer (this bundle does is not connected to the spectrograph in the above image, but can be seen hanging off to the side). When taking calibration exposures, the solar feed is blocked.

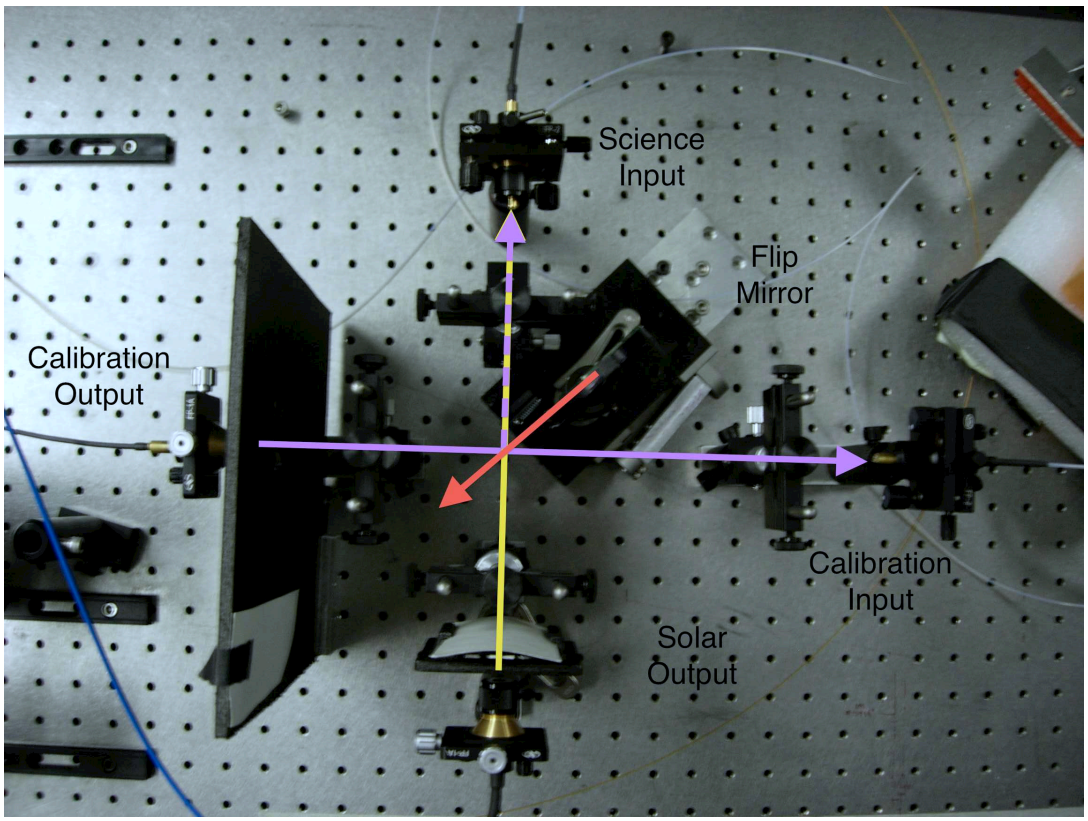

Fig. 2.3 An image of the calibration setup used in the 02 November 2007 run. During science exposures, calibration light from the ThAr and flat field lamps comes out the "calibration output" fiber on the left, and enters the "calibration input" fiber on the right (purple arrow). The fiber from the rooftop enters the setup from the "solar output" fiber at the bottom, and enters the "science input" fiber at the top of the image (yellow arrow). During calibration exposures (such as flats and ThAr exposures), the flip mirror slides into the middle of the "plus"-intersection (red arrow) and redirects the light from the calibration output into the science input fiber (dashed purple line). The fiber agitator can be seen in the upper-right of this photo.

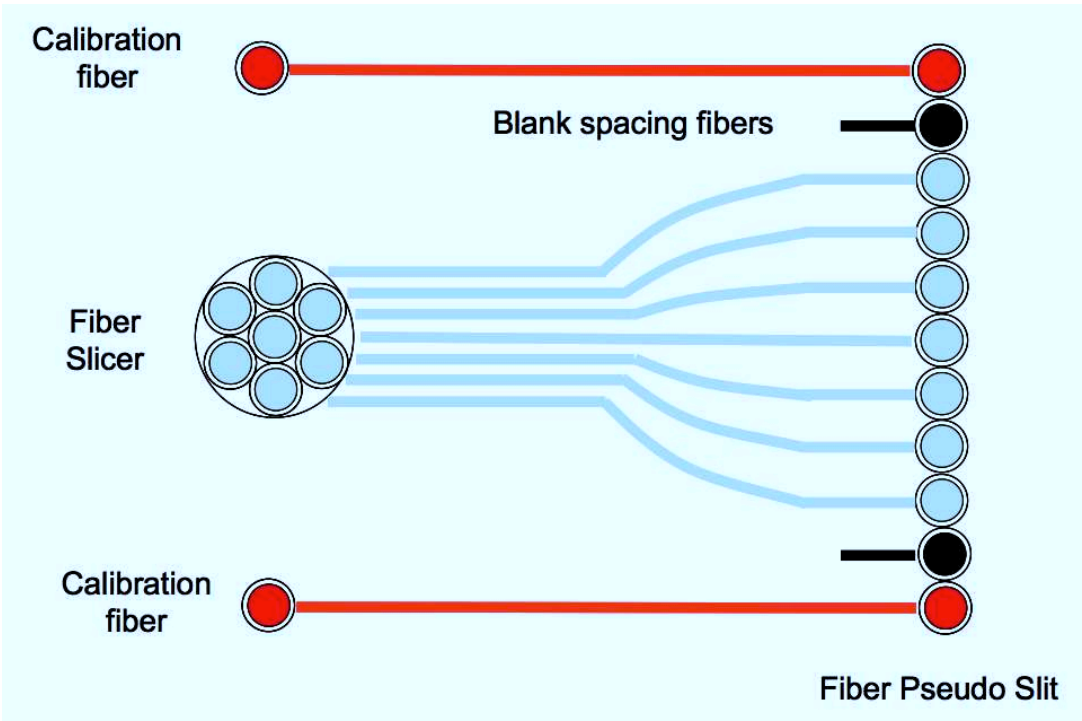

Fig. 2.4 **Top:** A diagram of the fiber slicer. Solar light from the telescope is aligned with the bundle of fibers shown on the left. The bundle is then reformed into the shape of a slit, shown on the right. **Bottom:** Photographs of the 2006 fiber slicer object input (left), fiber slicer pseudo slit with calibration fibers on each end (middle) for 2006 August data, and the fiber arrangement for 2007 November data with object, blank, and calibration fibers (right). The box in the 2007 November fiber arrangement shows the approximate location of a 100-μm slit.

Fig. 2.4). To achieve our desired resolution the output end of the new input fiber cable was butted up against a 100 μm slit on a 6-mm diameter stainless steel plate. The image of a single fiber in this setup was 24 pixels thick on the detector. In both instrument setups, we vibrated the fibers to minimize the effects of modal noise (Baudrand & Walker 2001).

2.1.5 Control System

The echelle and cross-disperser gratings are mounted on rotational stages and the camera is mounted on a linear stage. All three stages are driven with a DC servo motor with incremental encoder position feedback. A Newport ESP 300 motion controller with an RS232 interface to a PC are used for setting and tracking positions. Although we would prefer not to change the positions of the optics, the small size of the detector compared to the area covered by the spectral range of interest requires precision control of both the echelle and cross disperser. The ability to establish and adjust focus with a precision control system is also highly desirable, although in practice the focus rarely needs adjustment. The focus was never adjusted during a run.

2.1.6 Detector and Dewar System

Pathfinder's detector is a HAWAII 1K (1024 pix^2) science-grade array (Hodapp et al. 1996) provided through IR Labs in Tucson Arizona and uses a SDSU Gen II controller. The Dewar is cooled with LN_2. Inside the Dewar radiation shield a filter holder is mounted to the same cooling block as the detector. The temperature is continuously monitored and is typically 82.3 K. The thermal background is suppressed with 12.5-mm PK50 plate that attenuates radiation beyond 2 μm and a short-pass filter with a cut-off at 1.8 μm that has transmission less than 10^{-3} out to 3 μm. In operation the detector has a gain of 6.1 e^-/ADU and a read noise of 20 e^-. The bias voltage has been optimized to maximize well capacity or dynamic pixel range. We use single destructive readouts. Tests have shown that the linearity of the array is within 1% of linear for ADU counts below 3×10^4, which is our operational range. The effect of pixel-to-pixel variation of quantum efficiency, which is about 6.7% in our array, is reduced by averaging over the height of the spectrograph slit and by dividing by the flat-field spectra. As in any precision measurement, high S/N flat fields are crucial. The optical design yields a spectroscopic resolution of 50,000 with 2.5 pixels per resolution element ($\sim$2.5 km/s/pixel). At 1.0 μm approximately 44% of the Free Spectral Range (FSR) in an echelle order is covered by the detector; this value decreases to 33% at 1.6 μm.

HAWAII 1K arrays are known to exhibit residual excess dark current or "persistence" (Hodapp et al. 1992), a signal that remains on the array after the source has been removed or blocked. The latency of this dark current depends upon the level of exposure, with saturated elements exhibiting the greatest persistence. Studies by Campbell & Thompson (2006) on Indium Antimonide arrays suggest that persistence decays as 1/time, and that reading the array to eliminate persistence current only increases its influence, presumably by raising the temperature of the array. Tests by Hodapp et al. (1996) to reduce or eliminate charge persistence were also largely unsuccessful — the

authors can only recommend avoiding element saturation. Our tests with the Pathfinder indicate that persistence in the array is about 1%.

For reasons that are still not well understood, our detector exhibits higher-than-expected counts in the first few images of a given sequence. These counts decrease precipitously over the next 7 images, a function which is independent of exposure time except at the longest exposures ($\approx$ 45 minutes). We refer to this drop in the counts of successive exposures as "the ramp-down effect" throughout this dissertation. An example figure showing the ramp-down effect for different exposures lengths can be seen in Figure 2.5.

To avoid these higher counts (which are essentially a background and hence a source of noise), we modified our experiments by disregarding the first few exposures of any particular time sequence. Note that every time the exposure length was changed, a new set of ramp-down exposures had to be taken. We also tried taking a series of 1-second exposures ("clearing frames") to minimize the effect of this ramp down — they failed to do so, but these clearing frames do help clear the array when it saturates.

2.1.7 Y-Band Spectra

The appearance of this spectral region on the detector can be seen in Figures 2.6 and 2.7, which shows spectral orders 49 through 56 (bottom to top, respectively) at the two different epochs described above. In Fig. 2.6 from 2006, light from an argon pen lamp was fed into the spectrograph through both the calibration fibers and the science fiber pseduo-slit. While this form afforded us a large solar throughput, the sheer lack of calibration lines provided a fundamental limitation to the achievable precision. In Fig. 2.7 from 2007, light from a ThAr hollow cathode was fed into a separate 300 μm fiber, separated from the main science fiber by another 300 μm fiber. In both cases, the vignetting of the detector by the dewar window is clearly visible.

2.2 Observations

On 02 November 2007, we acquired three runs of 300 successive 10-second exposures with simultaneous solar and calibration spectra (in separate fibers). Our program concentrated in the Y band, which offered several orders with relatively few telluric lines, strong solar lines, and numerous emission line sources for monitoring instrumental drift. This region of the spectrum, between 1.03μm and 1.10μm, can be seen in Figure 2.8.

2.3 Data Reduction and Analysis

To reduce these data, I used a variety of IRAF[1], including APALL and APSCATTER for the echelle reduction, and FXCOR (Fitzpatrick 1993) for the cross-correlation routines. During the reduction, I analyzed regions that were free of telluric contamination, and cross-correlated the individual spectra relative to the exposure with the highest S/N. For the cross-correlation routine, I used all identifiable ThAr and solar lines.

[1] http://iraf.noao.edu/

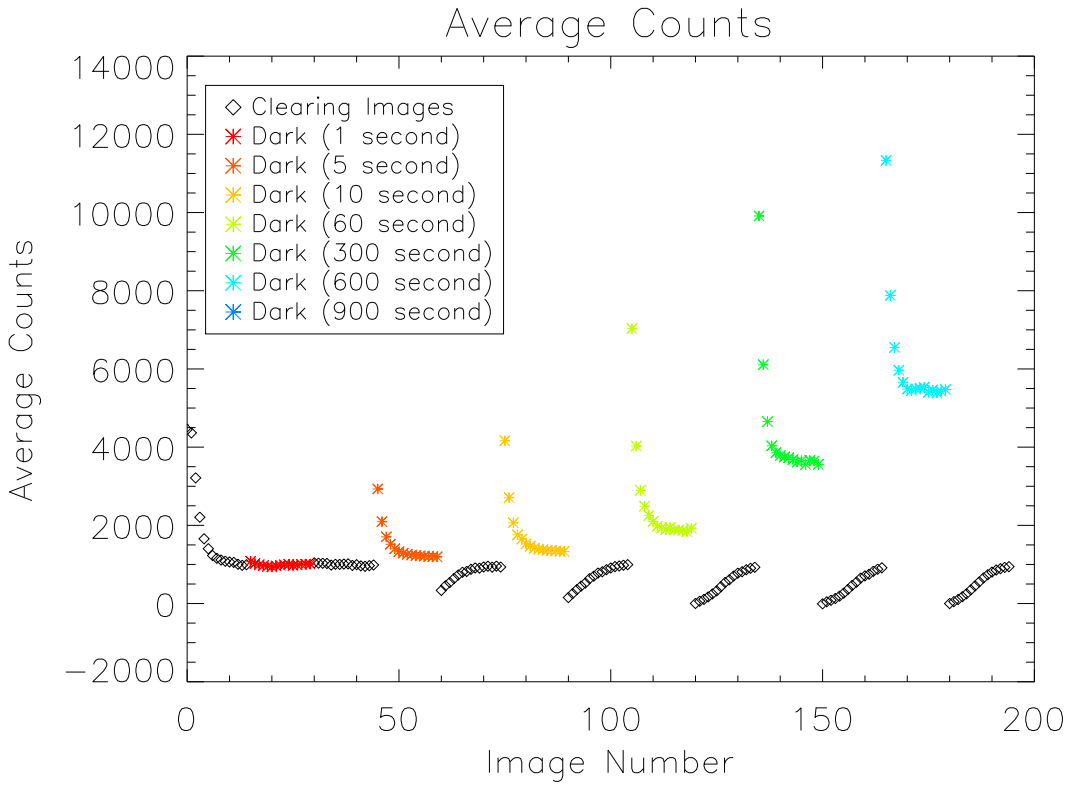

Fig. 2.5 The first few exposures in a series of constant exposure length show a drop in average counts before leveling off. This ramp down is independent of exposure length (except at exposures longer than ≈ 45 minutes — not shown). "Clearing frames" are a series of 1-second exposures that we thought might reduce the effect of the ramp down. They only help if the clearing frames are the same exposure length as the subsequent exposures — and therefore are useless for preventing the ramp down effect. However, clearing frames are essential for clearing the array after saturating the detector.

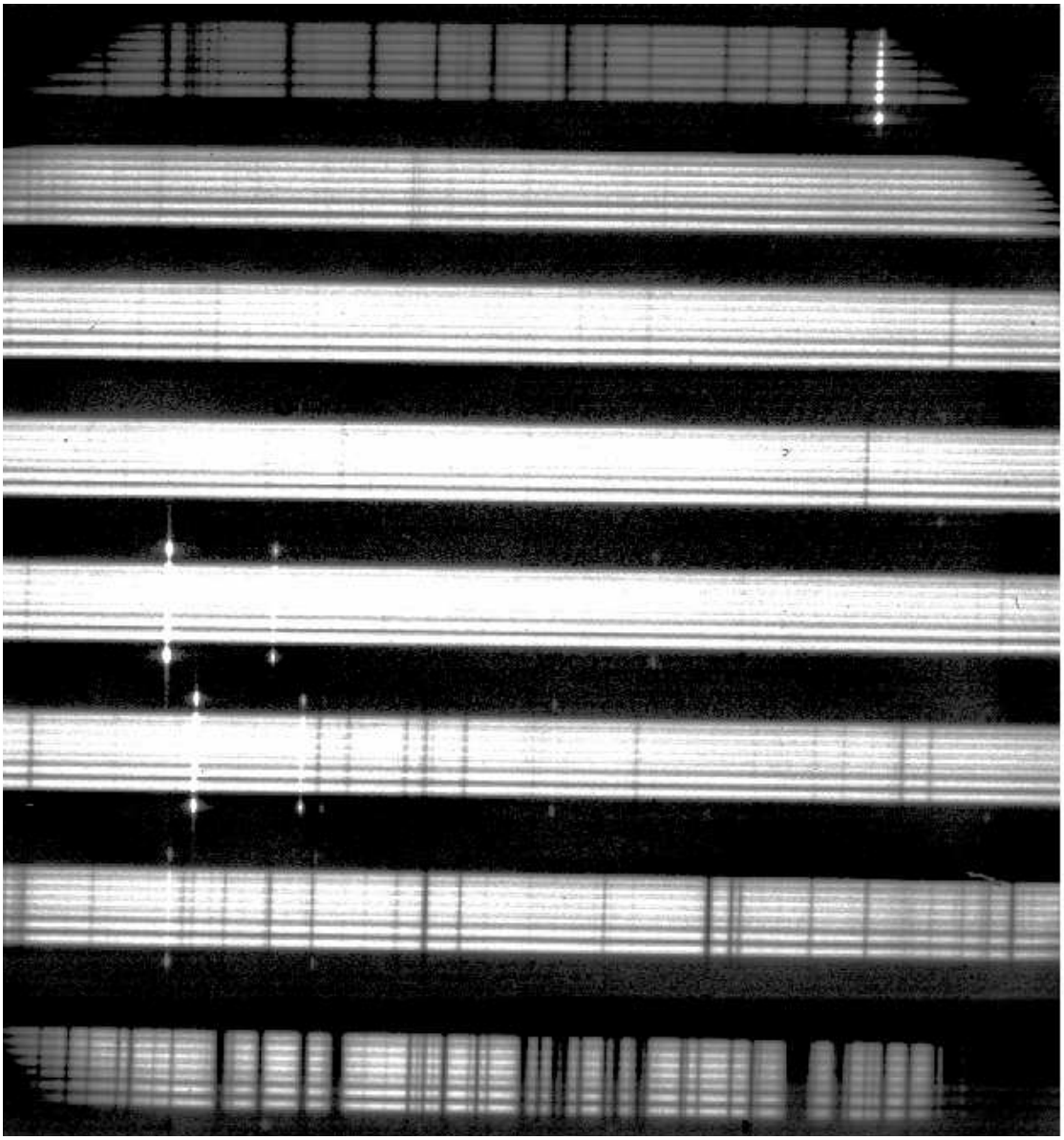

Fig. 2.6 Orders 49 (bottom) through 56 (top) of the Y-band, as seen on the Pathfinder HAWAII 1K array in 2006. In this fiber setup, we fed light from an argon pen lamp through both the calibration and the science fibers along with the solar light. Note the strong telluric lines in order 49 and 56. In this setup, the science fiber pseudo slit was 70 pixels thick.

Fig. 2.7 Orders 49 (bottom) through 56 (top) of the Y-band, as seen on the Pathfinder HAWAII 1K array in 2007. In this fiber setup, we fed light from a ThAr hollow cathode lamp through a calibration fiber, separated from the 300 μm solar fiber by another 300 μm fiber. Note the strong telluric features in orders 49 and 56. In this setup, the science fiber was 24 pixels thick. This setup also afforded us many additional calibration lines. A faint streak can be seen in the lower-righthand side of this figure, caused by reflections of bright argon lines within the spectrograph.

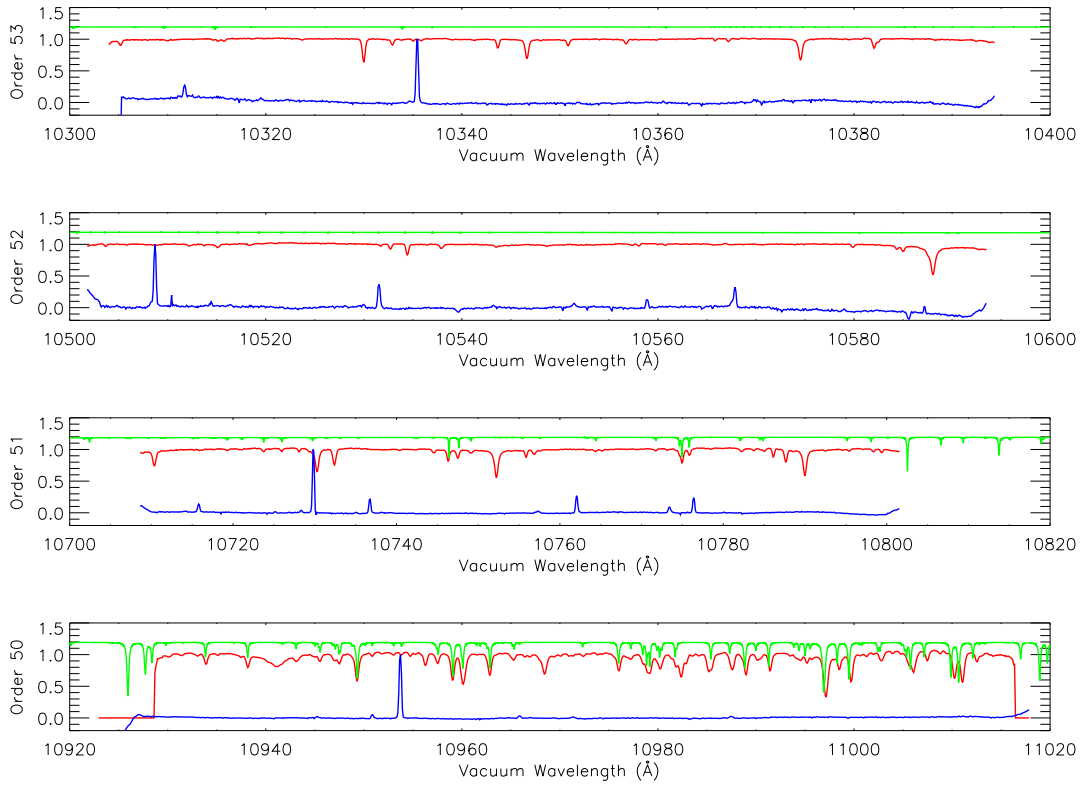

Fig. 2.8 The spectral region used for the observations on 02 November 2007. The region above, spanning orders 50 (bottom) through 53 (top) show the model telluric spectrum in green, the observed solar and telluric spectrum in red, and the ThAr emission-line reference spectrum, divided by a factor of 10, in blue. The significant misalignment between the telluric and observed solar/telluric spectrum in Order 50 at the long wavelength end is due to the large uncertainty in the dispersion solution of this order, which contains about 5 ThAr lines.

The calibration and science spectra were cross-correlated against the exposure with the highest-S/N solar spectrum. The resulting sub-pixel shifts of both the instrument drift (via argon emission lines) and the instrument drift plus Earth's rotation (via the solar spectrum) taken on 16 August 2006 are plotted in Figure 2.9. Here, a drift of a single pixel corresponds to a shift in velocity of 2.4 km/s. Ideally, the difference between the two measurements is the Earth's rotation velocity. The large drift is largely due to small temperature and pressure changes in the spectrograph room, as described in § 1.1.3. The gaps in the solar data indicate times when the Sun was covered by clouds.

2.3.1 Theoretical Earth Rotation Curve

The Earth's rotation curve relative to the Sun is dependent upon the exact coordinates of the observer and the Sun's location in the sky. While the former can be obtained from a GPS device, the deviation of the Earth's shape from a perfect sphere contributes a ≈ 0.5 m/s difference in the local radial velocity amplitude. The Earth's rotational velocity amplitude is given by:

$$v_{max} = 2\pi\rho/P_{\oplus} \tag{2.1}$$

where the period of the Earth's rotation, $P_{\oplus}$, is 23 hours, 56 minutes, and 4.096 seconds, and ρ is the distance of State College from the Earth's center. For a perfect sphere, this only depends upon the latitude of the observer and the radius of the sphere. The geodetic (common) latitude (ϕ_{gd}) of State College is 40.7981111° , the equatorial radius of the Earth is 6378137 m (a), and the sixth floor of Davey is $371.9m$ above sea level, so the maximum velocity is:

$$\begin{aligned} v_{max} &= 2\pi\rho/P_{\oplus} && (2.2)\\ &= 2\pi(a+h)\cos\phi_{gd}/P_{\oplus} && (2.3)\\ &= 2\pi(6378137m + 371.9m)\cos 40.7981111^{\circ}/(86164.096s) && (2.4)\\ &= 352.1m/s && (2.5) \end{aligned}$$

Since the Earth is not a perfect sphere, the velocity amplitude is modified by the ellipticity of the Earth's surface. The Earth's radius at the poles (b) is 6356752 m, so the distance between State College and the Earth's center is actually closer to (from the Astronomical Almanac, K11-K12):

$$\rho' = (a * C + h) * \cos(\phi_{gd})/\cos(\phi_{gc}) \tag{2.6}$$

where the geocentric latitude ϕ_{gc} is given by:

$$\begin{aligned} \phi_{gc} &= \arctan((\frac{b}{a})^2 \tan\phi_{gd}) && (2.7)\\ &= \arctan((\frac{6356752}{6378137})^2 \tan 40.7981111^{\circ}) && (2.8)\\ &= 40.60784^{\circ} && (2.9) \end{aligned}$$

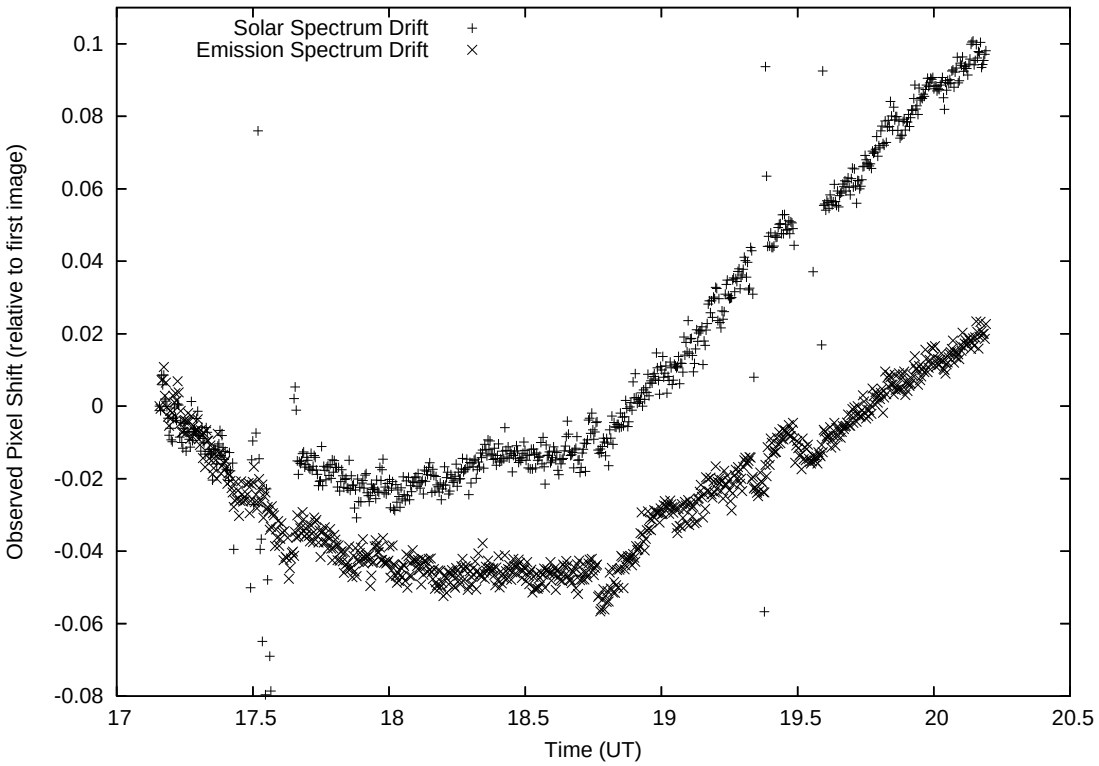

Fig. 2.9 The measured pixel drift for both the instrument and the sun, from the cross-correlation of spectral order 51 of data taken 16 August 2006, from Ramsey et al. (2008). A drift of one pixel corresponds to a change in velocity of 2.4 km/s. The difference between the two is the measured rotation of the Earth. Breaks in the solar drift correspond to the presence of clouds.

and where C is given by:

$$\begin{aligned} C &= \sqrt{\cos(\phi_{gd})^2 + (b/a)^2 * \sin(\phi_{gd})^2} && (2.10) \\ &= \sqrt{\cos(40.7981111^\circ)^2 + (6356752/6378137)^2 * \sin(40.7981111^\circ)^2} && (2.11) \\ &= 0.9985700 && (2.12) \end{aligned}$$

Thus, ρ' is:

$$\begin{aligned} \rho' &= (6378137 \times 0.9985700) * \cos(40.7981111^\circ)/\cos(40.60784^\circ) && (2.13) \\ &= 6350847m && (2.14) \end{aligned}$$

and v'_{max} is:

$$\begin{aligned} v'_{max} &= 2\pi\rho' \cos(\phi_{gc})/P_\oplus && (2.15) \\ &= 2\pi(6350847m + 371.9m)(\cos 40.60784^\circ)/(86164.096s) && (2.16) \\ &= 351.6m/s && (2.17) \end{aligned}$$

The Sun's coordinates can be calculated from the following procedure[2]. According to the authors, these coordinates are good to 1 arcminute between 1800 and 2200 AD. The right ascension and declination of the Sun are given by:

$$\begin{aligned} \tan \mathrm{RA}_\odot &= \cos e \sin L / \cos L && (2.18) \\ \sin \delta_\odot &= \sin e \sin L && (2.19) \end{aligned}$$

where e is the mean obliquity of the ecliptic ($e = 23.439 - 0.00000036D$, D being the number of days since 2000 January 1.5 — $D = JD - 2451545.0$) and L is:

$$L = q + 1.915 \sin g + 0.020 \sin 2g \qquad (2.20)$$

where q and g are:

$$\begin{aligned} g &= 357.529 + 0.98560028D && (2.21) \\ q &= 280.459 + 0.98564736D && (2.22) \end{aligned}$$

The equation of time is the difference between the true solar time and the mean solar time (based upon uniform motion along the celestial equator). The former depends upon both the eccentricity of the Earth and the obliquity of the ecliptic. The difference

[2]from `http://www.usno.navy.mil/USNO/astronomical-applications/astronomical-information-center/approx-solar`

between these two times ranges between -14 and 16 minutes, and is thus essential to consider when measuring the Sun's position in the sky to the precision of a few m/s. The equation of time changes from year-to-year, but updated values of the coefficients can be found in the Astronomical Almanac. For 2009, for example, the equation of time ϵ was:

$$\epsilon = -108.5 \sin L + 596.0 \sin 2L + 4.5 \sin 3L - \tag{2.23}$$

$$12.7 \sin 4L - 428.2 \cos L - 2.1 \cos 2L + 19.3 \cos 3L \tag{2.24}$$

where L is the mean Longitude of the Sun (corrected for aberrations):

$$L = 297^\circ\, 791 + 0.985647d \tag{2.25}$$

where d is the number of days since January 0 2009 at 0^h UT.

The local transit time of the Sun is then given by:

$$t_{transit} = t_{UT} + \epsilon - 687.073333 \tag{2.26}$$

where the constant is the temporal distance of State College from the center of the Eastern time zone.

The radial velocity curve of the Earth's rotation around the Sun is given by:

$$rv(t) = v'_{max} \cos(\delta_\odot) \cos(\phi_{gc}) \sin(t/P) \tag{2.27}$$

where P is the Earth's rotation period and $\delta_\odot$ is the declination of the Sun.

2.4 2006 and 2007 Results

The results from the 16 August 2006 and 02 November 2007 experiments are presented in Figure 2.10. The top panel shows the measured relative radial velocity of the Earth on these two days, along with the theoretical Earth rotation curves on each of those days. The data have been binned into clusters of five, so that each point is the average over $\approx$ 70 seconds. The bottom panel shows the residuals (observed – theoretical). The $\approx$ 1-hour gaps between runs in 2007 are times during which flat, dark, and calibration images were obtained. The relatively large scatter in the first run of 2007 is due to the misalignment of the telescope, and corresponds to large changes in the flux of each exposure as a function of time, as shown in Figure 2.11.

The binned residuals of the 2006 observations are 11.6 m/s, and 14.5, 4.0, and 5.9 m/s for each of the three 2007 runs, respectively. These residuals are less than an order of magnitude away from the photon-limited velocity precision for this spectrum. The combined Q factor for orders 51—53 is about 4000, and the counts in each pixel average about 6250, so the photon-limited precision is $3e8/(4000 * \sqrt{3 * 1024 * 150000 * 6})$, or about 1.5 m/s.

The root-mean-squared (RMS) values of the three 02 November 2007 runs are given in Figure 2.12, where we have plotted the measured RMS values for different bin sizes (N), along with the $\sqrt{N}$ functions that would be expected if the data were free of

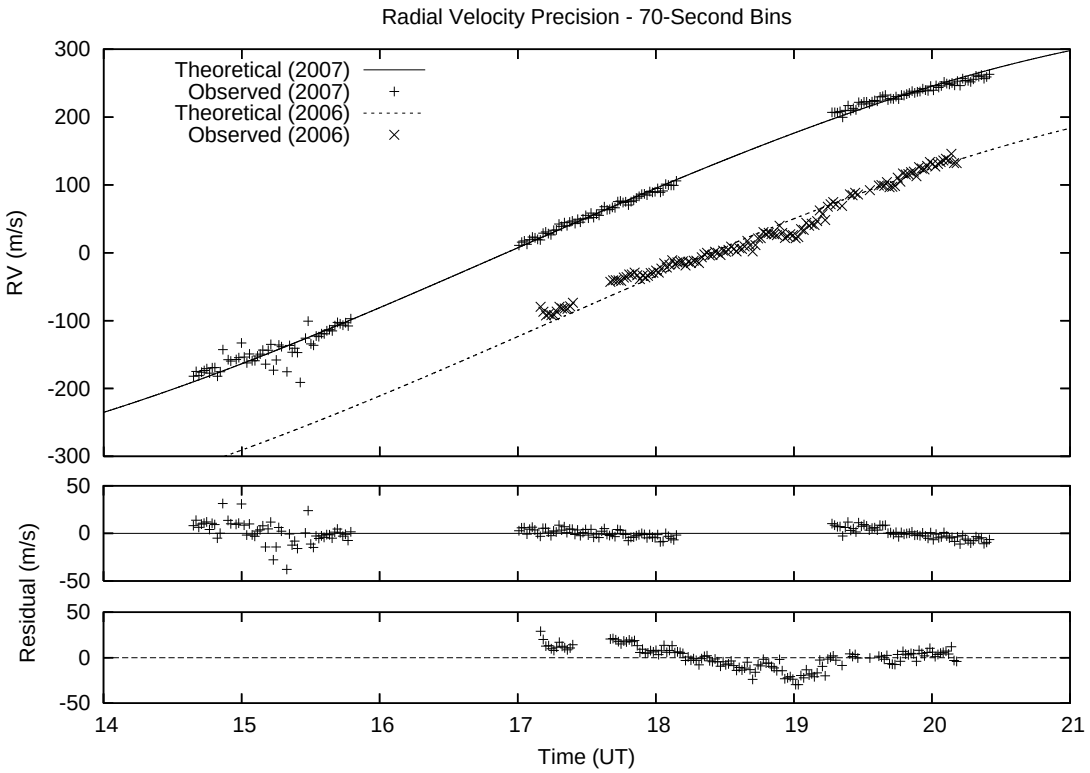

Fig. 2.10 **Top:** The observed (pluses, exes) and theoretical (solid line, dashed line) Earth rotation curves for observations made on 02 November 2007 and 16 August 2006, respectively, from Ramsey et al. (2008). **Bottom:** The residuals (observed – theoretical). All data have been binned so that each point represents the average relative velocity of five data points. The source of the trends in the residuals is not well understood.

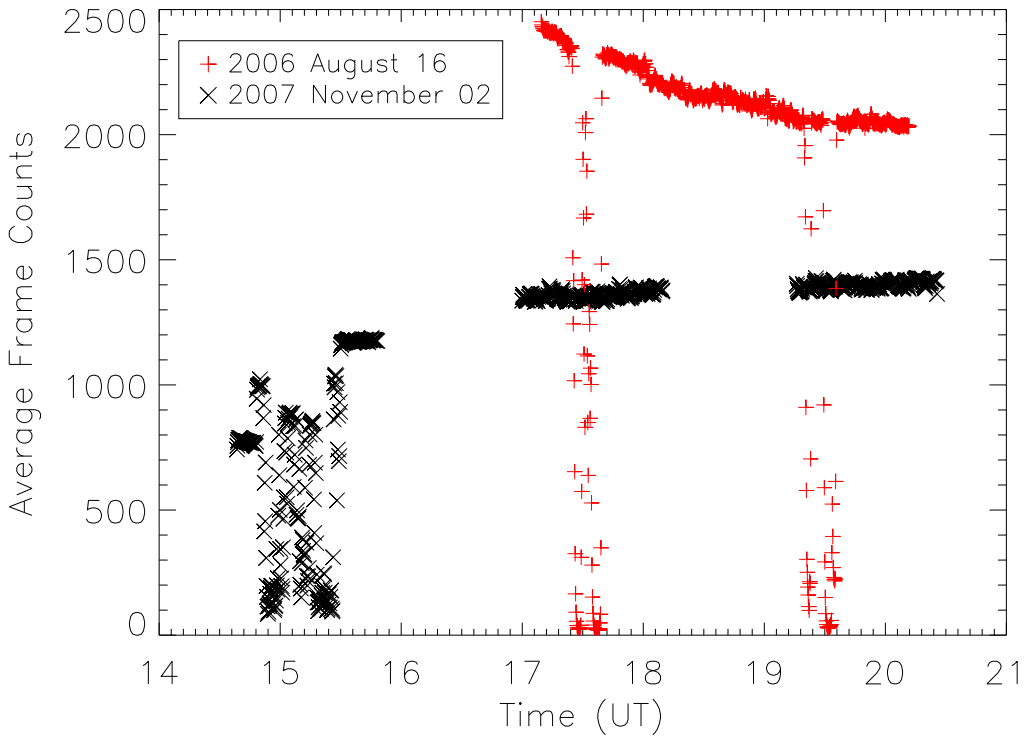

Fig. 2.11 The average pixel count for exposures in 2006 and 2007, after dark-subtraction and setting all bad pixels to zero. Clouds are responsible for the large drops in flux in the 2006 August 16 data set, and the drift of the telescope out of alignment is responsible for the large drops in flux seen in the first run of the 2007 November 02 data.

systematic trends. The source of these trends, visible in the bottom panel of Fig. 2.10, is not yet understood. We hypothesize that these results were limited both by the lack of calibration lines, as well as the lack of deep spectral lines.

2.5 Summary

Perhaps the most important result from the Pathfinder experiments is the result that we were able to achieve 7 m/s precision despite all of the challenges expected in the near-infrared. We selected a spectral region that was relatively free of telluric absorption and agitated the fiber input to reduce the effects of modal noise. The effects of persistence do not appear to be serious enough to limit our precision at the 10 m/s level, although they are a suspected source of the slow drift we see in the residuals of the 2007 November 02 runs.

Based on these initial Pathfinder experiments, we learned that the number of calibration lines present in the hollow cathode lamp is a primary limitation in the achievable precision. Since this calibration source is the sole source of removing the instrumental drifts, which are orders of magnitude larger than the source radial velocities, a source with a large number of evenly-illuminated calibration lines is essential to properly measuring the dispersion solution consistently. This result led us to search for calibration sources that over a greater density of lines, and in the next chapter I will discuss our calibration source of choice — a uranium neon hollow-cathode lamp.

The fiber slicer proved to be an exceptional challenge, both to obtain and to reduce. In particular, aligning the solar output to the fiber bundle resulted in a significant loss of throughput. It was also very challenging to make the switch between illuminating the fiber bundle with Solar and calibration light in a consistent manner. When it came to reducing the data, we made no attempt to calibrate the individual fibers in the pseudo slit; rather, the flux over the entire pseudo slit was extracted as a single aperture. While this approach yielded results with a large flux, it also hid the fact that imperfections in the alignment in the fibers of the pseudo-slit would diminish our resolution.

These tests shaped our future HET runs dramatically. Our understanding of modal noise and the thermal background greatly improved during the summer of 2009. The limitations imposed by our reduction software led us to new reduction tools to help control and understand our systematics (see Chapter 4).

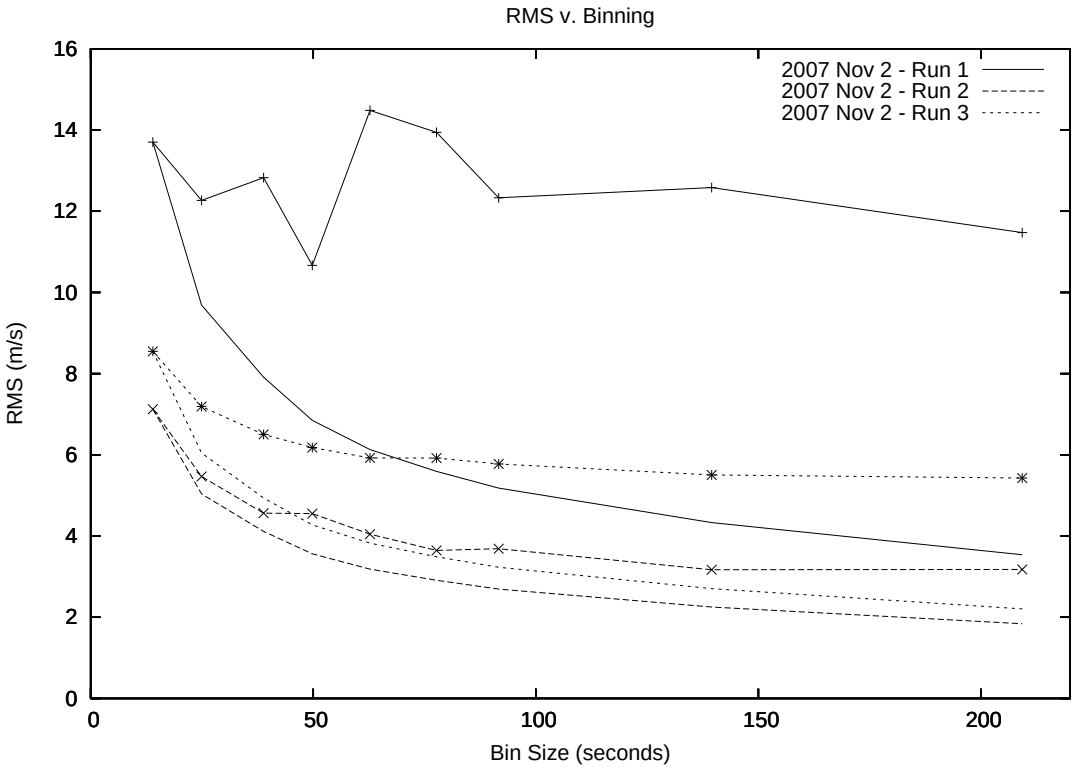

Fig. 2.12 The observed RMS values for different amounts of binning for each of the three runs of 02 November 2007 (points with lines), along with the theoretical $\sqrt{N}$ curves (lines without points), which we would expect if there were no systematic errors in the observations. From Ramsey et al. (2008)

Chapter 3

UNe as a Calibration Source

The history of exoplanet searches in the NIR has been brief, and therefore it is no surprise that the calibration sources used to make precision radial velocities in this spectral region have yet to be fully explored. To date, the most popular calibration sources in the visible have been Thorium Argon (ThAr) for fiber-fed spectrographs, and Iodine (I_2) cells for direct-feed spectrographs. Unfortunately, neither is ideal for NIR observations. Argon has many bright lines in the NIR, and there are comparatively few Thorium lines. Iodine provides well-understood absorption lines over a small piece of the optical spectrum, from about 500 to 650 nm. Therefore, I have spent some time exploring alternative calibration sources, including pen light sources such as neon (Ne), argon (Ar), xenon (Xe), and krypton (Kr), as well as other hollow cathode sources, such as thorium neon (ThNe), uranium argon (UAr), and uranium neon (UNe).

Three hollow cathode lamps are compared in Figure 3.1: Th/Ar, U/Ar, and U/Ne. All of these lamps were run at 14 mA through the same optical components, and all three images are median-averages of twenty-five 25-second exposures. Thus, common lines between the top two images are argon lines, and common lines between the bottom and top-right images are uranium lines. Argon lines in the NIR are much brighter than neon lines, and thus produce much larger quantities of scattered light and multiplexer crosstalk. Neon is a much better fill gas to use in the NIR for this reason.

The idea that uranium might be an excellent calibration source in the NIR was first suggested by Engleman (2003), who noted a high density of lines in the uranium spectrum. More recently, Gettel (2008) found that the uranium spectrum was about twice as dense as thorium around 900 nm. From atomic physics, these results are not entirely surprising: a higher atomic number means that uranium atoms have more high-level electron orbits that can give rise to low-energy transitions. Uranium shares many of the characteristics that make thorium such a good calibration source. Both are heavy elements, have zero nuclear spin, a long half life, and many lines. Only thorium is a mononucleide (has only one natural isotope), but the isotopic ratio of uranium is dominated by uranium-238 (99.275%), with smaller fractions of ^{235}U (0.720%) and ^{234}U (0.005%) [1]. The electronic transitions of different isotopes will be slightly offset from the transitions of the dominant isotope.

There are two historical uranium line lists; Palmer et al. (1980) provided uranium identifications for bright uranium lines up through 11000 cm^{-1} (9091 Å), and Conway & Worden (1984) compiled a list of uranium lines between 1.8 and 5.5 μm. In early 2010, I began working with Dr. Gillian Nave and Dr. James Lawler to measure uranium wavelengths in the gap between 0.9 and 1.8 μm.

[1] http://physics.nist.gov/PhysRefData/Handbook/Tables/uraniumtable1.htm

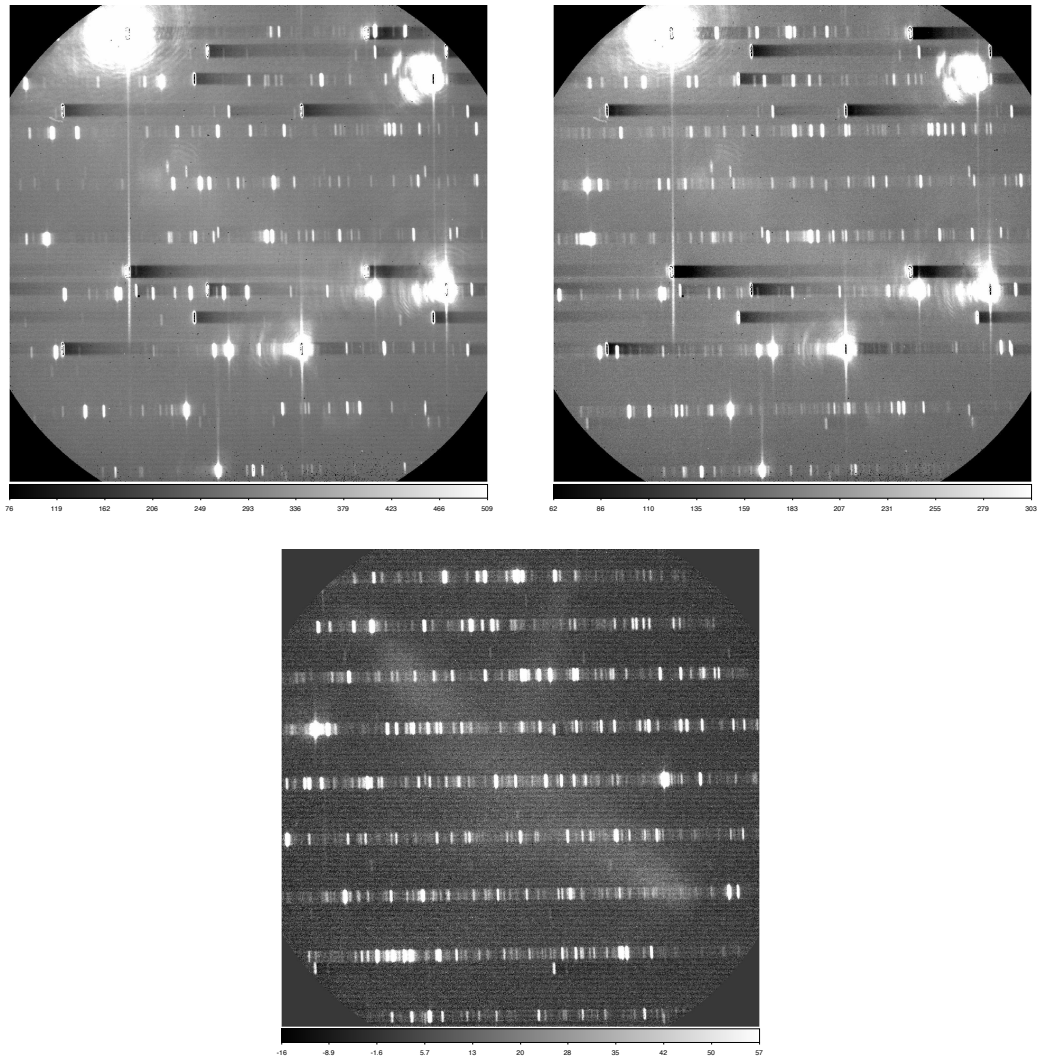

Fig. 3.1 Y-band observations with the Pathfinder spectrograph of Th/Ar (top-left), U/Ar (top-right) and U/Ne (bottom). All lamps were run at 14 mA through the same optical alignment, and all three images are the median-average of twenty-five 25-second exposures. Thus, lines common between the top exposures are argon, etc. Note the much higher background present in the Ar images; bright argon lines mask out the fainter actinides. Multiplexer cross-talk is responsible for the negative images of bright lines in adjacent quadrants. Neon provides a much cleaner image; the faint scattered light pattern in the U/Ne exposure is from three relatively bright neon lines in spectral orders not present on the array.

3.1 NSO Uranium Observations

High-current uranium lamps are not readily available for FTS measurements, and so we utilized archival data taken with the 1-m FTS on Kitt Peak between 1979 and 2002. These data are publicly available on the National Solar Observatory (NSO) website[2]. Since echelle spectrographs can detect fainter lines than are visible in an FTS (at the same lamp currents), we were particularly interested in measuring the wavenumbers of the faintest uranium lines, which are only visible in high-current FTS data. We found two high-current U/Ar FTS spectra that covered the J and H bands, and another medium-current U/Ne FTS spectrum that covered the Y band. We also selected two low-current U/Ne FTS observations to check for plasma shifts.

These data and their attributes are summarized in Table 3.1. The first column of the table is the spectrum number (shorthand which is used throughout the text). The second column is the name of the archive data file (the first six digits indicate the year, month, and day of the observations, respectively, and the last three indicate the spectrum number of that day). The third column is the species (either uranium neon or uranium argon). Column four is the current the lamp was run at, in mA. The wavenumber range of the observation is given in the next two columns. Column seven is the wavenumber correction factor applied to each spectrum, and column eight is the standard error of the mean in that factor (both divided by 10^{-7} for readability).

Table 3.1 NSO FTS Observations

Spectrum Number	Archive Filename	Species	Current (mA)	Wavenumber (cm^{-1}) Start	End	κ ($/10^{-7}$)	$\delta\kappa$ ($/10^{-7}$)
SP1	020227.023	U/Ar	26	3900	14400	2.16	0.05
SP2	020227.024	U/Ar	26	4100	14400	2.13	0.05
SP3	790221.005	U/Ne	75	8300	22200	−4.63	0.08
SP4	820520.003	U/Ar	169	1800	9300	−6.51	0.06
SP5	801214.005	U/Ar	300	2400	9500	−15.10	0.06

Uranium-argon and uranium-neon and FTS spectra from the NSO Archive. Throughout the text, these spectra are referred to by their spectrum number. Their archive filename is the name of the file on the NSO website. The species in these observations are either uranium and argon or uranium and neon. SP1 and SP2 are low-current observations that are close to the current of our hollow-cathode lamps. SP3 was the brightest U/Ne spectrum we used (and also the only high-current spectrum with coverage in the Y band), and SP4 and SP5 are both high-current spectra that cover the J and H bands. The wavenumber correction factor κ and uncertainty therein $\delta\kappa$ are measured from comparisons to fiducial calibations.

[2] `http://diglib.nso.edu/nso\_user.html`

These data were reduced and analyzed using the interactive computer program XGREMLIN, an X-windows implementation of Brault's GREMLIN program (Brault & Abrams 1989) developed by Griesmann (Nave et al. 1997). The earlier uranium interferograms (SP3, SP4, and SP5) were taken with unequal numbers of points on each side of the zero path difference and the line profiles in the corresponding spectra have large, antisymmteric imaginary parts. Such spectra require careful phase correction in order to ensure that none of the imaginary part of the line profile is rotated into the real part, causing asymmetric line shapes (Learner et al. 1995). We re-transformed SP4 and SP5 from the original interferograms in order to confirm that the phase correction was done correctly. In all cases, the residual phase errors were less than 20 mrad, corresponding to a maximum wavenumber shift of 0.0003 cm^{-1} (15 m/s at 6000 cm^{-1}).

A small continuum is observed in some our spectra in the region above 1.5 μm. When present, this continuum was subtracted. All lines with a signal-to-noise threshold of 20 were then identified in the spectrum. Voigt profiles were fitted to these lines to obtain the wavenumber, peak intensity, line width, and Voigt lineshape parameters. Since spectrum SP3 was taken in air, all wavenumbers in this spectrum were converted to vacuum wavenumbers using the pressure, temperature, and humidity values from the spectrum headers. The correction factor was based on the formulae of Edlén (1966). We estimate residual errors in the wavenumbers from this correction to be $<$ 0.0004 cm-1 (20 m/s at 6000 cm^{-1}).

The wavenumber scale of a FTS is linear and is defined by the control laser (usually HeNe, wavenumber 15798.0025 cm^{-1}) used to measure the optical path difference in the interferometer. However, differences in the optical path through the FTS between the laser and the source result in a small stretching or compression of the wavenumber scale. This effect can be corrected by measuring the wavenumbers of standard lines throughout the spectrum and comparing them to their indepently-determined wavenumbers. The difference between these two provides a multiplicative wavenumber correction factor κ defined as: $\kappa = 1 - \sigma_{obs}/\sigma_{std}$ where σ_{obs} is the wavenumber of the line observed in the spectrum and σ_{std} is the wavenumber of the standard.

Wavenumber standards for the calibration of our spectra were taken from three different references: Ar I lines are from Whaling et al. (2002) measured using FT spectrometry, Ne lines from Sansonetti et al. (2004) measured using FT spectrometry, and eight U lines from Degraffenreid & Sansonetti (2002) measured using laser spectroscopy. The Ar I wavenumbers of Whaling et al. (2002) have been shown to be too large by 6.7 parts in 10^8 by Sansonetti (2007), and were appropriately corrected. Wavenumbers of Ar I lines are also susceptible to plasma shifts, but Kerber et al. (2008) showed that these shifts are less than 0.0003 cm^{-1} for Ar I lines with upper levels less than 115 000 cm^{-1}. We thus calibrated spectra SP1, SP2, SP4 and SP5 with Ar I lines with upper levels below 115 000 cm^{-1} using wavenumbers taken from Whaling et al. (2002).

The uranium lines of Degraffenreid & Sansonetti (2002) appear in spectra SP1, SP2 and SP3, but cover a small wavenumber range between 13269 cm^{-1} and 14391 cm^{-1}. The calibration of SP1 and SP2 using these lines agrees with the calibration using Ar I lines within 7 parts in 10^8, which is within the joint uncertainties for spectrum SP2. Spectrum SP3 contains the uranium lines of Degraffenreid & Sansonetti (2002) and neon lines of Sansonetti et al. (2004). The calibration using uranium differs from that

using neon by about 1 part in 10^7, significantly more than the joint uncertainties of 2 parts in 10^8. Calibration using the eight uranium lines of Degraffenreid & Sansonetti (2002) also gives wavenumbers of other uranium lines that agree with those measured in spectra SP1 and SP2 within the joint uncertainties (See Figure 3.2). The neon standards also show a slope in the correction factor of about 2 parts in 10^7 between 9000 cm^{-1} and 14000 cm^{-1}. Since we observe similar slopes on other uranium/neon spectra we studied during selection of the five spectra we have chosen for this work, we believe this slope is present in the neon lines of Sansonetti et al. (2004) and not in spectrum SP3.

3.2 Line List Construction

After adjusting each spectrum with the wavenumber correction factors from Table 3.1, we re-measured the wavenumbers of any features above a S/N of 20. This line list was first matched to known argon lines from Whaling et al. (2002) and neon lines from Sansonetti et al. (2004) within 0.01 cm^{-1}. To identify the uranium lines, we first calculated the expected wavenumbers from Ritz energy levels (the theoretical energy levels, based on observed lines and atomic physics), taken from the database of actinides[3], which are based upon Blaise & Radziemski (1976) and Blaise et al. (1994). All non-noble gas lines were compared to these energy level transitions using the same 0.01 cm^{-1} window function.

A second, independent reduction was carried out by Jim Lawler. He examined lines individually, and kept them only if they (1) appeared in at least two spectra, (2) had a good S/N ratio, and (3) were symmetric and had a consistent width. Numerical integrals were used to determine the center-of-gravity wavenumber. In regions where our independent reductions overlapped, our wavenumbers (within 0.01 cm^{-1}) were averaged with equal weighting. 97% of these lines were within 0.002 cm^{-1} of each other (10 m/s at 6000 cm^{-1}).

I went through each spectrum individually to check and make sure each feature identified by XGremlin was indeed a line and not a ghost or ringing. Some of these spurious features were expurgated by removing lines with widths greater than three standard deviations from fits to the uranium line widths. An example of this is given in Figure 3.3. This technique likely eliminates blended uranium lines, but this is perfectly in line with the goals of the final line list, since these blended lines cannot be used for precise wavelength calibration.

In a given spectrum, the uncertainty of a line's wavenumber (δ_{SPX}) is the sum in quadrature of (1) the one-standard deviation uncertainty in the wavenumber correction factor (δ_κ) and (2) the one-standard deviation uncertainty in the line position (δ_{LC}):

$$\delta_{SPX} = \sqrt{\delta_\kappa^2 + \delta_{LC}^2} \tag{3.1}$$

where δ_κ is given by:

$$\delta_\kappa = \sigma * (\delta\kappa/(1-\kappa)) \tag{3.2}$$

[3] `http://www.lac.u-psud.fr/Database/Tab-energy/Uranium/U-el-dir.html`

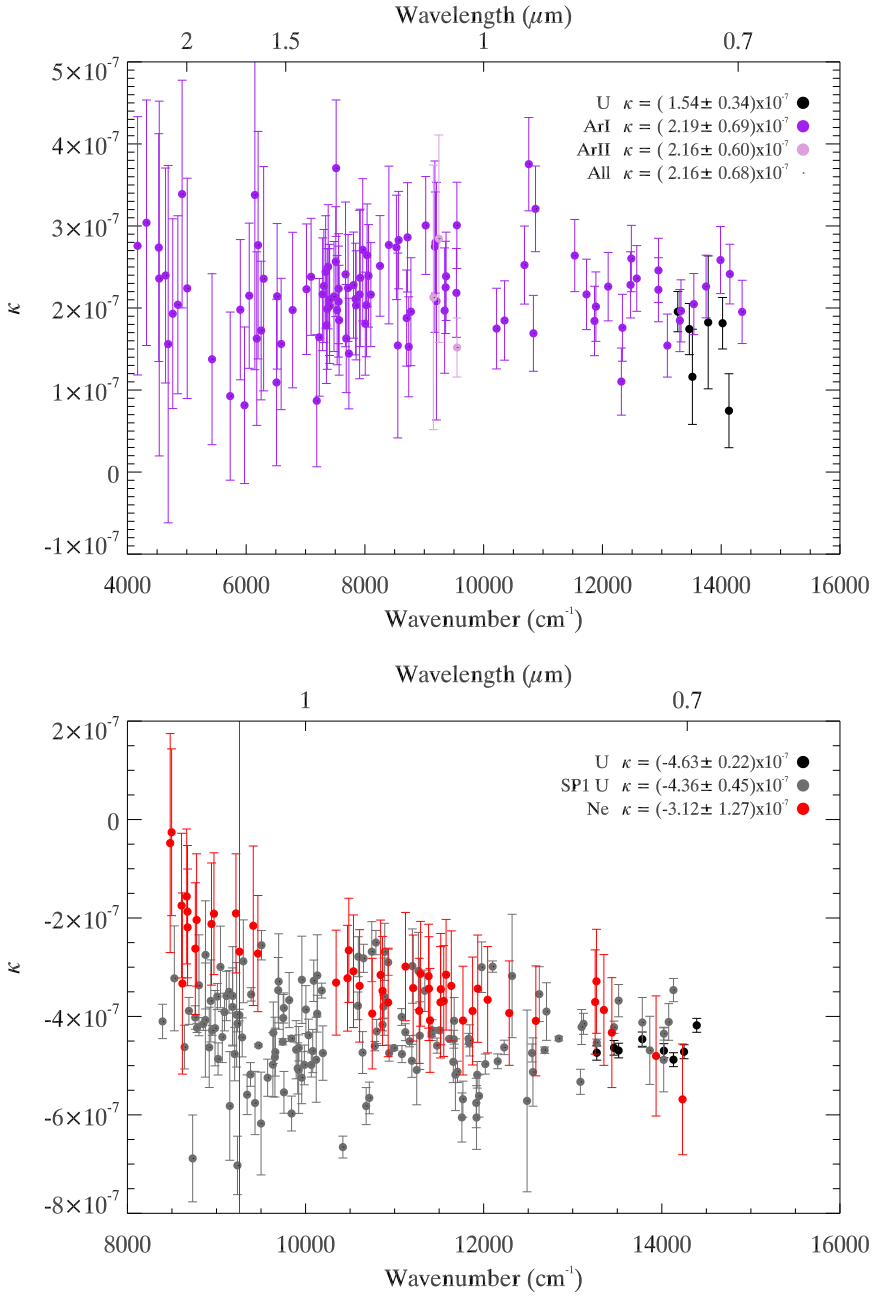

Fig. 3.2 **Top:** An example of the calculation of the wavenumber correction factor, using fiducials established by Whaling et al. (2002); Sansonetti (2007) (ArI and ArII lines) and Degraffenreid & Sansonetti (2002) (U lines). The robust mean includes only points that lie within three standard deviations of the mean κ. **Bottom:** The same, but for SP3 (U/Ne). The neon standards come from Sansonetti et al. (2004). The slope in the neon standards (emphasized here when compared to the uranium wavenumbers of spectrum SP1) suggests to us that something is wrong with these standards; for this reason, we used only the uranium standards of Degraffenreid & Sansonetti (2002) to determine the wavenumber correction factor in our analysis of spectrum SP3.

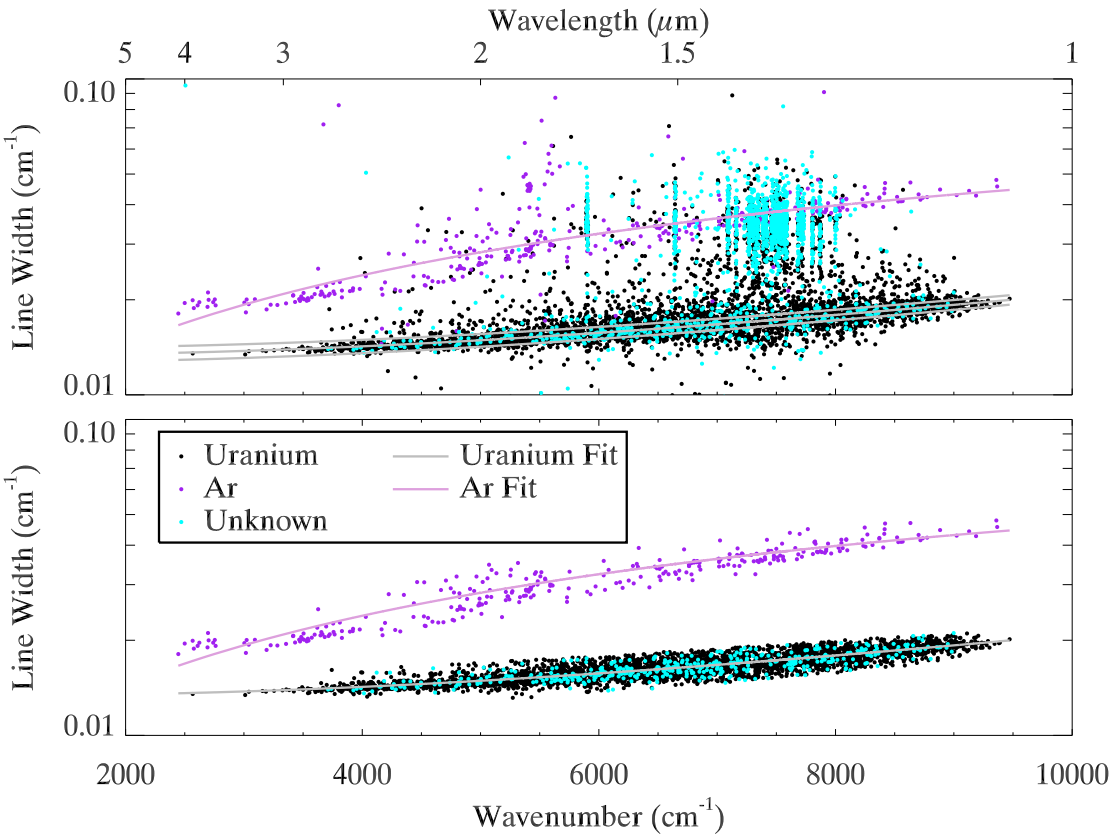

Fig. 3.3 A diagnostic plot showing how we first culled blended lines and spurious features in SP5. **Top:** Both the uranium and argon line widths distributions were fit with a polynomial. **Bottom:** All lines that fell more than three standard deviations from these fits were eliminated from the final distribution. The gray lines above and below the fit to the uranium line widths represent one standard deviation from the polynomial fit. The many wide unknown lines between 6000 and 8000 cm^{-1} were found around bright Argon lines, and resembled the peaks of sinc functions, but could not be eliminated in the usual manner by convolving the spectrum with a Gaussian. This technique should also cull blended uranium lines from our list.

and δ_{LC} is the one-standard deviation uncertainty in the line center:

$$\delta_{LC} = \frac{W}{SNR} \tag{3.3}$$

Here W is the line width, and SNR is the signal-to-noise ratio of the line (Davis et al. 2001). When a line was found in multiple spectra, these spectrum-specific uncertainties were added in quadrature:

$$\delta = \sqrt{\delta_{SPX}^2 + \delta_{SPY}^2} \tag{3.4}$$

3.3 Uranium Line List Results

The complete table of uranium lines is several hundred pages long, and is presented in (Redman et al. in preparationa). A short selection of the complete list is presented in Table 3.2. The first column is the average wavenumber, in cm^{-1}. The second column is the single standard deviation uncertainty in the wavenumber measurement, in 10^{-3} cm^{-1}. Since none of our spectra covered the entire wavelength range of interest, the third column lists the signal-to-noise ratio (SNR) of SP5 up through 9000 cm^{-1}, and the SNR of SP3 thereafter. The fourth column provides the species identification, and ionization state for uranium lines. A **?** in this column indicates that the line does not fall within 0.01 cm^{-1} of a known uranium Ritz energy level transition. It is very likely that these lines are uranium, however, based solely upon the similar line widths. The next four columns are the upper and lower energy levels for uranium transitions, according to the known energy levels. The ninth column is the difference between the Ritz energy level transition (calculated from the theoretical energy levels) and the observed wavenumber of the line. A **b** or bf B in the last column denotes a blend.

The sheer density of uranium lines in the NIR means both that there are a large number of uranium lines in any desired section of the spectrum, but also that there are a great many blends at "high" spectral resolutions of 50000. In an effort to guide the reader in using such lines, we have provided two notes in the table. First, lines marked with a lower-case **b** are lines that are blended at the resolution of the FTS. Second, we re-analyzed SP4 and SP5, identifying all suspected lines with a SNR > 10 in the same manner as before. Most of these are likely to be real lines, but since their larger uncertainty makes them unsuitable for wavelength calibration we have chosen not to include them in our final line list. However, we have marked lines in our list (at SNR > 20) that are within 2×10^{-3} cm^{-1} of other lines found in the SNR > 10 list, which would be unresolved at a resolution of 50000. These lines are marked in our list with a capital **B**, and should be avoided when making high-precision measurements. The reader should note that there are pairs of resolved lines in our list that will appear blended at these resolutions, but because they are resolved by the FTS, they have not been marked as blends in our final line list.

The physical conditions of the plasma inside the hollow cathode lamp can shift the spectral lines systematically. Such shifts are found by comparing data taken under a variety of conditions. We compared the lines from our low-current observations (SP1 and SP2) to the lines of our highest-current observation (SP5). No systematic plasma

Table 3.2 Sample of the Uranium Line List

$<\sigma>$ cm^{-1}	δ 10^{-3} cm^{-1}	SNR	Species	Upper cm^{-1}	Upper J	Lower cm^{-1}	Lower J	$\sigma_{Ritz} - <\sigma>$ 10^{-3} cm^{-1}	Notes
6313.6678	0.5	98	UI	20139	5	13825	4	0.2	B
6313.9554	0.2	147	UI	25462	6	19148	5	-0.4	B
6315.6544	0.3	113	UI	24906	6	18591	6	-1.4	B
6315.7848	0.3	63	UI	25458	7	19142	8	-0.8	B
6316.3444	0.9	28	UI	22891	3	16575	2	0.6	B
6316.5207	0.2	244	UI	18260	2	11943	3	-0.7	
6317.2294	0.5	35	UI	27938	5	21620	5	-2.4	
6317.5659	0.1	1303	UI	19885	7	13567	7	3.1	B
6319.0169	0.7	28	UII	23700	5/2	17381	7/2	-0.9	
6320.6746	0.4	437	Ar						
6321.0401	0.7	86	?						B
6321.5049	0.2	91	UI	24433	6	18111	6	2.1	B
6322.3856	0.5	32	UI	26781	3	20458	4	-0.6	B
6322.9182	1.0	85	UII	18136	15/2	11813	13/2	-2.2	
			UI	25096	3	18773	3	2.8	
6323.9207	0.5	47	UI	27440	4	21116	5	9.3	B
6324.7255	0.4	104	UI	24581	8	18256	7	0.5	B
6327.6904	0.4	47	UI	26287	6	19959	5	-1.4	B
6328.9785	1.1	29	UII	16211	9/2	9882	9/2	2.5	
6329.2833	0.5	101	UI	25626	9	19297	9	2.7	
6329.9371	0.2	127	UI	23432	5	17102	6	-0.1	
6330.1286	0.8	152	Ar						
6331.2853	0.3	96	UI	21766	6	15435	6	1.7	
			UII	24857	11/2	18526	9/2	1.7	
6332.5423	1.0	34	UII	20932	11/2	14599	13/2	-0.3	B
6332.8846	0.5	58	?						B

A small example of the uranium line list, from (Redman et al. in preparationa). The classifications are given for UI and UII lines, as are the wavenumber differences from the Ritz wavenumbers. Lines unassociated with known uranium level transitions are identified as a **?**. These lines, if they are real, are very likely to be uranium lines, based upon their narrow line widths. Notes indicate lines blended at the resolution of the FTS (**b**), lines blended with nearby suspected lines (unpublished) at a resolution of 50000 (**B**).

shifts were observed at the 10^{-3} cm^{-1} level (see Figure 3.4). In total, we identified 6853 UI lines and 756 UII lines. 749 lines remain unidentified, but are likely to be UI or UII, based on their narrow line widths.

3.4 Comparison with Other Uranium and Thorium Line Lists

Our line list overlaps two historical line lists. Palmer et al. (1980) provides uranium wavenumbers between 11000 cm^{-1} and 12000 cm^{-1}, and Conway & Worden (1984) covers the same between 2500 cm^{-1} and 5500 cm^{-1}. Comparisons between our wavenumbers are shown in Figure 3.5. The wavenumbers of Palmer et al. (1980) are systematically 0.00077 cm^{-1} (38 m/s at 6000 cm^{-1}) greater than ours. The comparison to Conway & Worden (1984) shows a much larger scatter, which is due in part to the order-of-magnitude lower precision. Even so, our measurements agree to within $(1.29 \pm 0.62) \times 10^{-3}$ cm^{-1} (64 m/s at 6000 cm^{-1}). It is not surprising that these line lists are systematically off, since these authors did not calibrate their spectra with standard lines, and only corrected their wavenumber scale for the refractive index of air and the finite aperture of the FTS.

The top plot in Figure 3.6 shows a histogram comparing the population density of uranium lines from this work and thorium lines from Kerber et al. (2008). Note that the lamp of the latter was run at 20 mA, much less than the lamp currents of the FTS uranium observations we utilized for our uranium line list, so many more thorium lines (which would be observable with a high-resolution echelle spectrograph) undoubtedly exist in the NIR that have not yet been published. The difference in quantity between this line list and Kerber's excellent Th/Ar work is quantified in Table 3.3. The bottom plot in Figure 3.6 shows a comparison between the number of neon and argon lines in the same spectral region (bottom). As shown in Fig. 3.1, not only are the neon lines less numerous, they are also of a comparable brightness to the actinides.

Table 3.3 Thorium and Uranium Line Quantities in Astrophysical Bands of the NIR

Band	Wavelength Range (μm)	N_{Th}	N_U
Y	0.9 — 1.1	437	1851
J	1.2 — 1.35	265	862
H	1.5 — 1.65	94	745
K	2.0 — 2.4	71	398
L	3.0 — 4.0	18	7
M	4.5 — 5.3	4	0

A comparison between the number of thorium lines found by Kerber et al. (2008) and the number of uranium lines found in this work. Lines without identifications from this work (indicated with a **?** symbol in the line list) are not accounted for in this table. Note that this is not a comparison between the true number of lines that these two sources provide in these regions, but rather a snapshot of the current number of known lines.

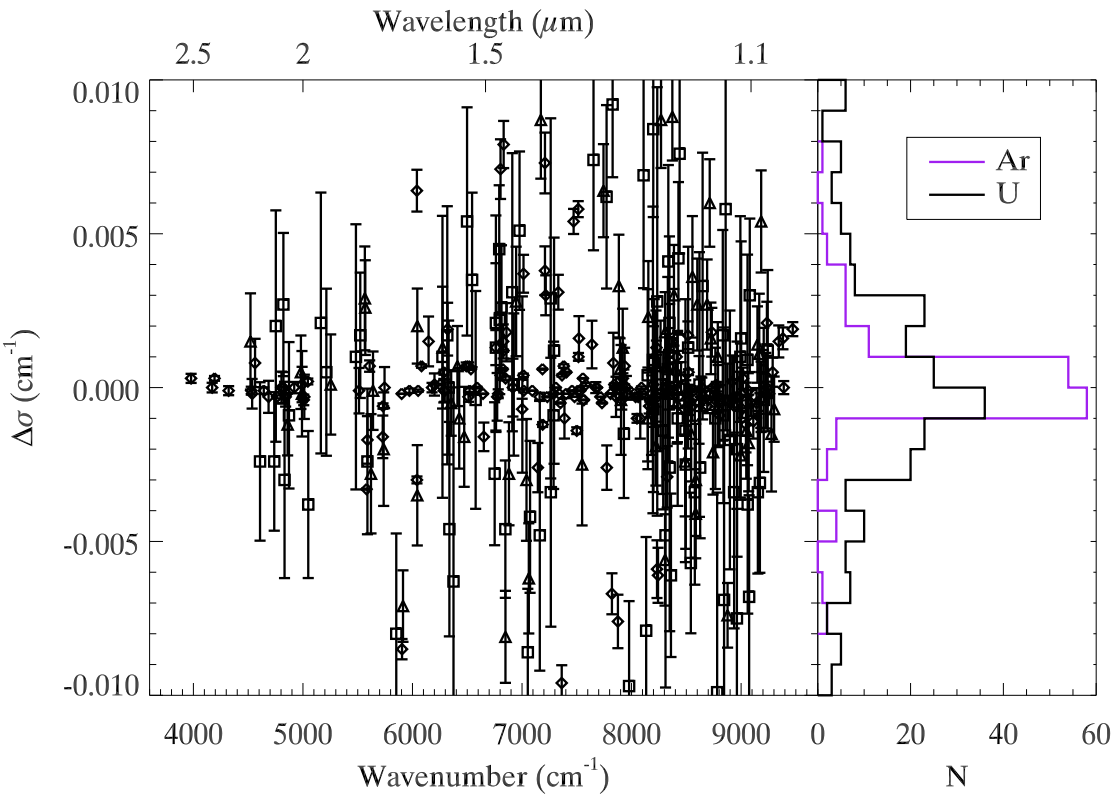

Fig. 3.4 The wavenumber difference (in milikaysers) between our highest-current spectrum (SP5, 300 mA) and our lowest-current spectrum (SP1, 26 mA). The uncertainties are indicated by the symbols (circles indicate $\delta \leq 0.001$ cm^{-1} (50 m/s at 6000 cm^{-1}), triangles indicate 0.001 cm^{-1} $< \delta \leq 0.002$ cm^{-1}, and squares indicate $\delta > 0.002$ cm^{-1}). The difference and one standard deviation for the argon and uranium lines is $(0.28 \pm 2.16) \times 10^{-3}$ cm^{-1} (14 m/s at 6000 cm^{-1}) and $(-0.37 \pm 3.47) \times 10^{-3}$ cm^{-1}, respectively.

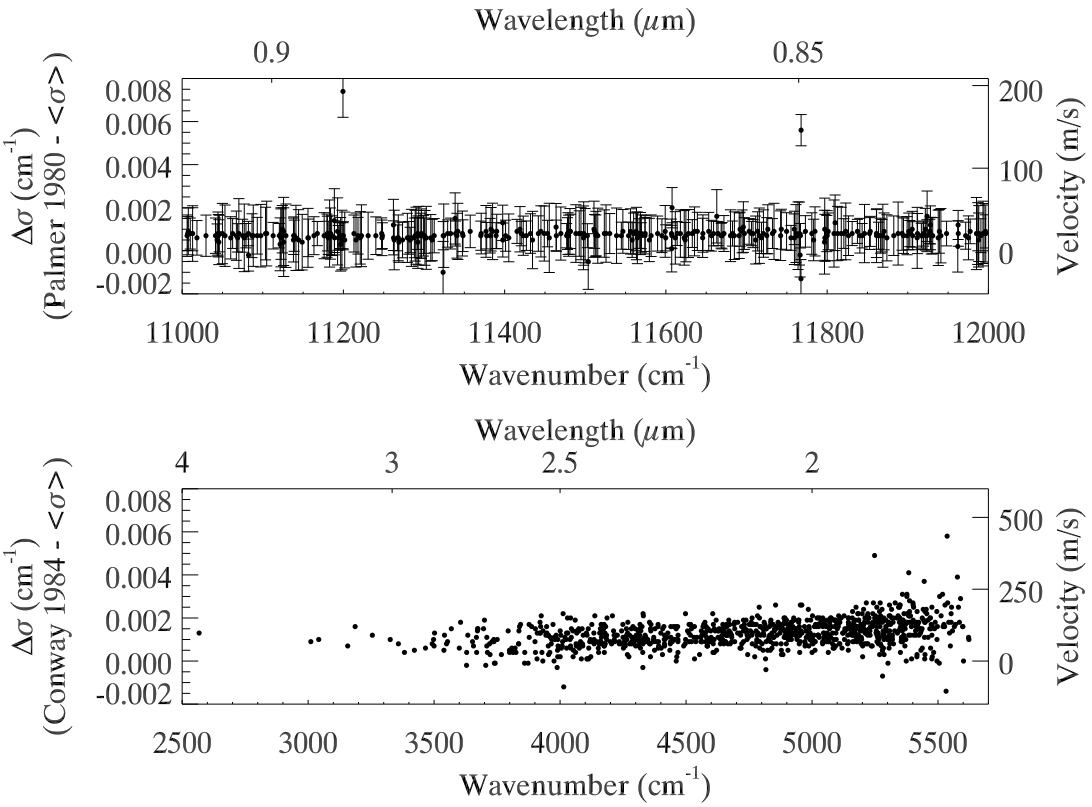

Fig. 3.5 Comparisons to historical uranium line lists. **Top:** A comparison to the lines of Palmer et al. (1980), from (Redman et al. in preparationa). The average and single standard deviation of this separation is $(0.77 \pm 0.52)\times10^{-3}$ cm^{-1} . **Bottom:** A comparison to the lines of Conway & Worden (1984). The average and standard deviation of this separation is $(1.29 \pm 0.63)\times10^{-3}$ cm^{-1}. Error bars in each are the sum in quadrature of our uncertainties and the uncertainties of the aforementioned authors. In the case of Conway & Worden (1984), we have omitted the error bars for readability; the average error bar in this case is ±0.001 cm^{-1}.

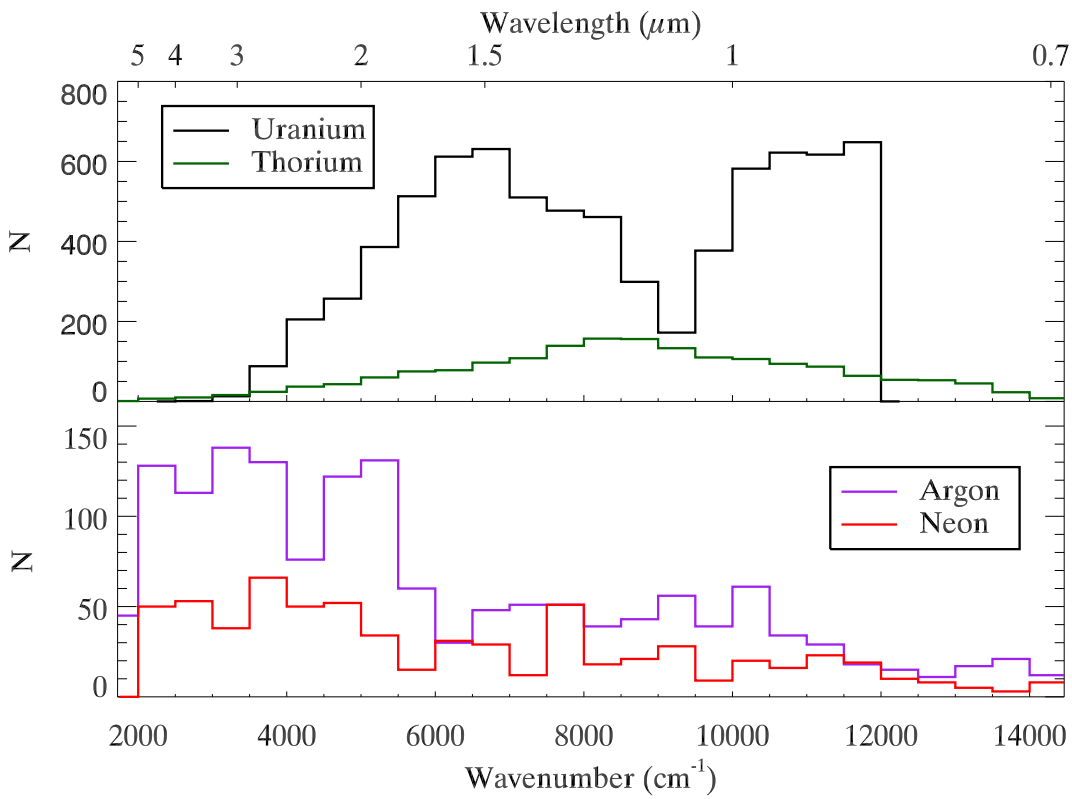

Fig. 3.6 **Top:** Histograms of the uranium (this work) and thorium (Kerber et al. 2008) lines in the NIR. The large gap in the number of uranium lines around 9000 cm^{-1} is from a gap in sensitivity between the spectra in our sample. **Bottom:** The same, but for argon (Whaling et al. 2002; Sansonetti 2007) and neon standards (Sansonetti et al. 2004).

3.5 The UNe / Frequency Comb Pathfinder Atlas

3.5.1 The Fiber-Fed NIR Pathfinder Spectrograph

Pathfinder (see Chapter 2), in its H band configuration has three optical fibers (one stellar fiber connected to the HET and two calibration fibers) that can simultaneously be illuminated. These fibers were polished and assembled into a vertical slit on site at the HET, and some physical offset is present in alignment, which we are able to quantify. Figure 3.7 shows an image obtained of these fibers configured into a pseudo-slit, and re-imaged onto a 100-μm slit. Due to an imperfect alignment of the slit with respect to the fiber pseudo-slit, the fibers are offset from each other by a constant amount. To measure this separation, we fed frequency comb light through the fibers, and independently fit dispersion solutions to the spectrum of each fiber. From the difference in dispersion solutions, we have determined that these fibers are offset by $\sim 1000 - 1100$ m/s (see Figure 3.8). We speculate that the ~ 30 m/s spread in the measurements is caused by fiber modal noise altering the illumination pattern of the comb lines (Hunter & Ramsey 1992), and that the top and bottom order separation is different than the central one due to the presence of optical distortions leading to PSF asymmetries. Note that the uncertainty in the fiber offset is small enough that it does not prevent us from comparing the FTS spectrum to our comb-calibrated spectrum.

3.5.2 The NIST/CU H-Band Frequency Comb

The construction and use of the NIST/CU frequency comb was not explicitly part of my thesis, but the frequency comb played a significant role in the calibration of our August HET run, and therefore deserves some attention. This section is based upon Redman et al. (in preparationb), with particular thanks to Gabe Ycas for his clarifications.

Laser frequency combs (hereafter, LFCs) are the best calibration sources for high-precision spectroscopy (Murphy et al. 2007; Osterman et al. 2007; Braje et al. 2008) because their frequencies are tied to atomic clocks (precise to approximately 1 part in 10^{14}) and because they produce a dense forest of uniformly-spaced, approximately equal intensity calibration lines (Hall 2006; Hänsch 2006). Only recently have they been utilized for astronomical research — Steinmetz et al. (2008) was the first to couple a comb to starlight at the Vacuum Tower (solar) Telescope. Optical combs are being tested by many groups around the world, including the HARPS, TRES, and HARPS-N (HARPS North) spectrographs (Li et al. 2008; Szentgyorgyi et al. 2008; Wilken et al. 2010). The Colorado University (CU) and NIST team have focused on the development of a NIR laser frequency comb (Quinlan et al. 2010) for the same purpose as Pathfinder — to find Earth-mass planets in the HZs of M dwarfs. They have cleverly utilized existing telecom H-band components to minimize the financial requirements of their comb.

The LFC lines are most commonly produced with a passively mode-locked laser (MLL), which emits a train of narrow (< 1 MHz) lines equally-spaced in frequency ($\sim 0.1 - 1$ GHz). These pulses are too dense to be resolved by astronomical grating spectrographs, so the mode density much be reduced using a Fabry-Perot etalon (Quinlan et al. 2010; Chen et al. 2008; Steinmetz et al. 2009; Braje et al. 2008; Kirchner et al.

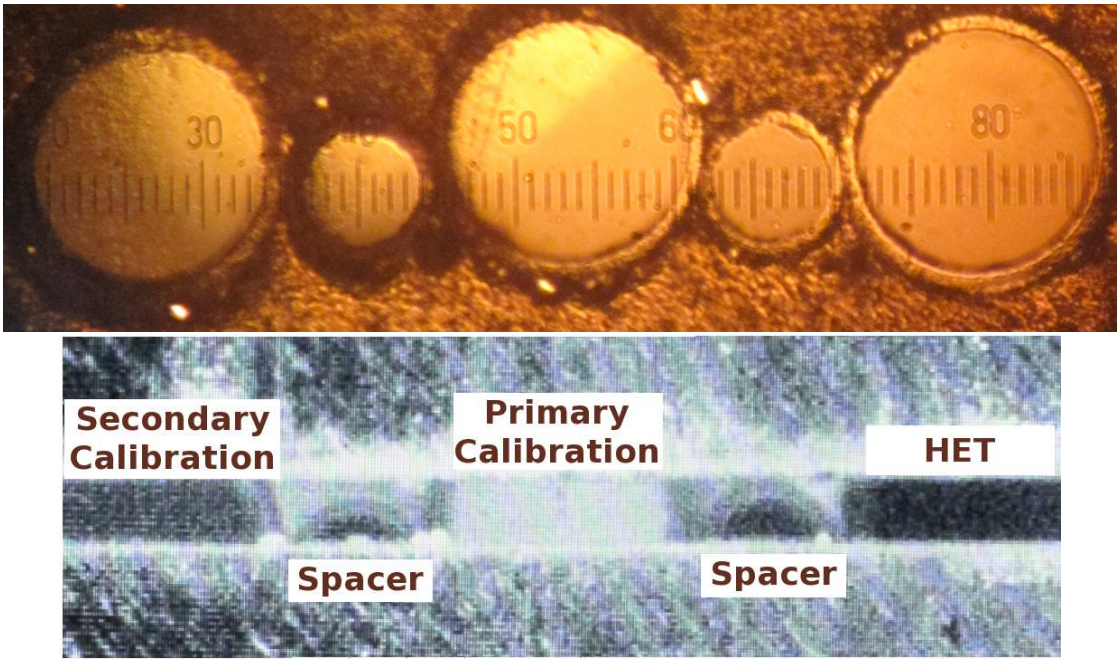

Fig. 3.7 **Top:** The three 300-μm fibers, separated by 125-μm (outer diameter) fibers that acted as spacers for the larger fibers. This fiber pseudo-slit was assembled and polished on-site. From left to right, these are the secondary calibration, primary calibration, and science (stellar) fibers. **Bottom:** The same fibers, re-imaged onto a 100-μm slit. In this image, the primary calibration fiber is transmitting light. The slit was aligned to optimize the orientation of the primary calibration and HET fibers.

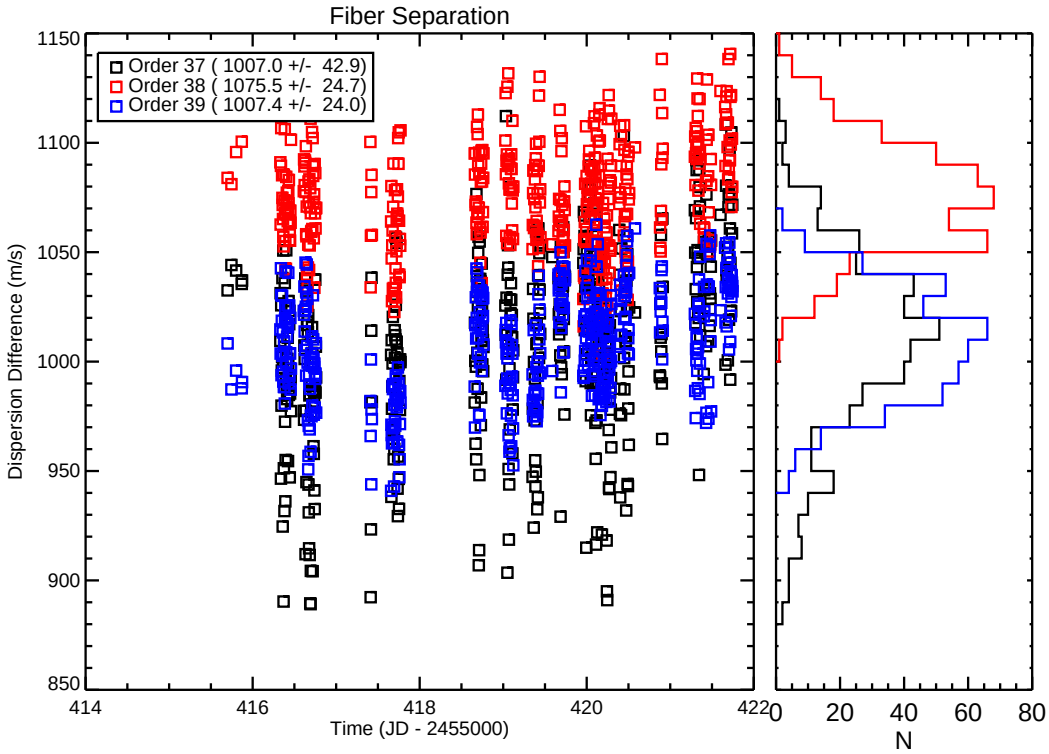

Fig. 3.8 The separation between the frequency comb and U/Ne calibration fibers for three different echelle orders, as measured by simultaneous frequency comb-frequency comb spectra over several days. The separation quoted in the legend is a robust mean (neglecting all points more than three standard deviations from the mean), and the uncertainty is a standard deviation of that robust distribution.

2009; Sizer 1989). When the etalon's free spectral range is set to a multiple (n) of the MLL's repetition rate (f_{rep}), the mode spacing is expanded to $n \times f_{rep}$.

The CU/NIST H-band LFC uses a 250-MHz passively mode-locked Erbium fiber laser, which is frequency stabilized by locking both f_{rep} and the carrier-envelope offset frequency f_{ceo} to a rubidium atomic clock that is corrected on longer time scales by GPS. This configuration generates comb lines at frequencies given by:

$$f_{\mathrm{n}} = f_{\mathrm{rep}} \times n + f_{\mathrm{ceo}}, \tag{3.5}$$

The spectrum of these comb lines were centered at 1550 nm, with a bandwidth of 70 nm. The accuracies of these lines are better than 1 part in 10^{11} (Quinlan et al. 2010). A diagram of the frequency comb can be seen in Figure 3.9. In these experiments, the mode spacing was increased using two Fabry-Pérot filter cavities, one before the MLL, and another after the optical amplifiers. The lengths of the cavities were actively locked using piezo-electric actuators for maximum transition of one set of 25-GHz spaced comb modes. After filtering, the 25-GHz comb is broadened by a highly-nonlinear fiber, and transmitted via a single-mode fiber to a integrating sphere, which was intended to minimize modal noise in the comb light. The final comb equation was then:

$$f_m = (n_0 + 100n) \times f_{\mathrm{rep}} + f_{\mathrm{ceo}}, \tag{3.6}$$

where n_0 is the index of one comb mode transmitted through the filter cavity, measured using a wavemeter.

3.6 Experimental Design and Observations

The data for this atlas were collected as part of a commissioning run at the HET with a frequency comb from NIST and the University of Colorado that we have described above. Light from the frequency comb was fed through an integrating sphere into the primary calibration fiber, while uranium-neon light was fed simultaneously through the secondary calibration fiber. We ran a Photron U/Ne hollow cathode lamp (Part number P863, Serial Number HGL0170) continuously at 14 mA. At each grating setting, we obtained ten 30-second U/Ne and frequency-comb images and five 30-second flat field images. All exposures were the same length so that we could take exposures continuously. The flat field exposures were taken with neutral density filters in front of each fiber, which had to be removed during the U/Ne/comb exposures. During these exchanges, a shutter in front of the fiber output in the pathfinder experiment was closed to minimize the effects of persistence in our images. The frequency comb was monitored continuously to ensure its stability.

3.7 Analysis

3.7.1 Data Reduction

We constructed a median-averaged flat field frame and a median-average U/Ne/comb image for each grating setting, both of which were dark-subtracted. We used subroutines

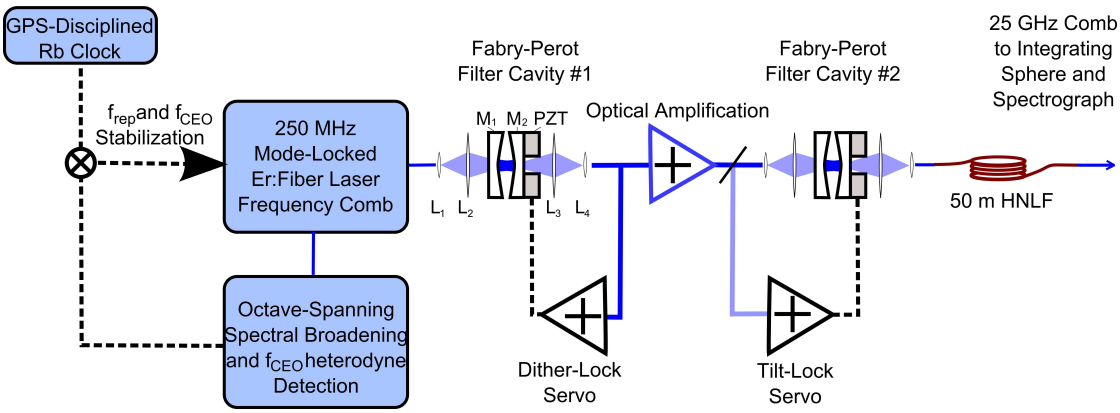

Fig. 3.9 Schematic of the 25 GHz frequency comb used at the HET in 2010 August, drawn by Gabe Ycas, and reprinted here from Redman et al. (in preparationb). A 250 MHz mode-locked erbium fiber laser is frequency controlled by locking both the repetition (f_{rep}) and the carrier-envelope offset (f_{CEO})frequencies. Light from the 250 MHz frequency comb is coupled into a 25 GHz FSR Fabry-Pérot cavity comprised of M_1 and M_2 with lenses L_1-L_4 matching the modes of the transmission fiber to the cavities. A piezoelectric actuator controlled by a servo is used to actively lock the cavity length to the frequency comb. The 25 GHz comb is optically amplified, filtered again in an identical Fabry-Pérot cavity, and then spectrally broadened in highly nonlinear fiber (HNLF). Standard single-mode fiber delivers the broadened 25 GHz comb to the spectrograph, where it is launched into an integrating sphere to minimize the modal noise.

from REDUCE (Piskunov & Valenti 2002) to model and normalize our master flats, subtract scattered light from the U/Ne/comb images, and (non-optimally) extract the U/Ne and comb spectra. After wavelength calibrating the spectra (see § 3.7.2), the U/Ne and comb spectra at each grating setting were resampled, merged, and averaged to produce a continuous spectrum from 14540 to 16380 Å. Outside of this range, the comb lines were too faint to identify. Our mean effective signal-to-noise of isolated uranium lines (which does not account for the effects of modal noise) was ~ 1026, while the median S/N of these same uranium lines is ~ 34.

3.7.2 Wavelength Calibration

Wavelength identification was conducted by manually identifying the comb lines specific to a given grating setting and fitting the comb peaks with Gaussians using MPFIT routines (Markwardt 2009) in IDL. Unlike a hollow-cathode emission spectrum, frequency comb lines are evenly spaced and identical in appearance. Because n_0, $f_{\rm rep}$, and $f_{\rm ceo}$ are known, one can determine n by feeding a single fiber with both comb light and a calibration with a well-known spectrum. In our case, since we know the fibers are separated by less than a pixel, while the comb lines are separated by ~ 25 pixels, we used bright (but not saturated) neon lines from the adjacent fiber (such as those marked on Fig. 3.10) to determine the index of the nearest comb lines and thereby determining the index (and frequency) for all lines in that order. The dispersion solution was iteratively fit with a third-order polynomial, ignoring outliers that fell more than three standard deviations from the mean residual to avoid the influence of cosmic rays. Note that the determination of n, which we are basing on the wavelengths of neon, requires much less precision (by two orders of magnitude) than our later comparison between the FTS uranium wavelengths and the comb-based uranium wavelengths. All wavelengths presented in this paper are vacuum wavelengths.

3.7.3 Line Identifications

Details of our uranium line measurement techniques can be found in Redman et al (2011), but are summarized here for completeness. Uranium lines were identified first as 10-σ deviations above the noise floor of historical FTS observations of U/Ar and U/Ne, taken from the Kitt Peak National Solar Observatory archive[4]. Spectral "ghosts" are common in FTS spectra, but their wavelengths are dependent upon the precise scanning parameters, so we restricted our compiled list to lines that were common to two high-current (300 and 169 mA) lamp FTS observations. Although these observations were taken at currents much higher than the typical currents of hollow-cathode lamps (5-15 mA), we found no evidence of plasma shifts (shifts in the wavelength due to slight changes in the energy levels of very hot gases). Uranium lines were readily discernible from Noble gas lines, the latter of which have much larger line widths. These archive lab data are sometimes of dubious quality; therefore, blended or artificial lines were rejected first automatically and then manually. Using a mixture of published and unpublished[5]

[4] `http://diglib.nso.edu/nso\_user.html`

[5] `http://www.lac.u-psud.fr/Database/Tab-energy/Uranium/U-el-dir.html` 2010 12 03

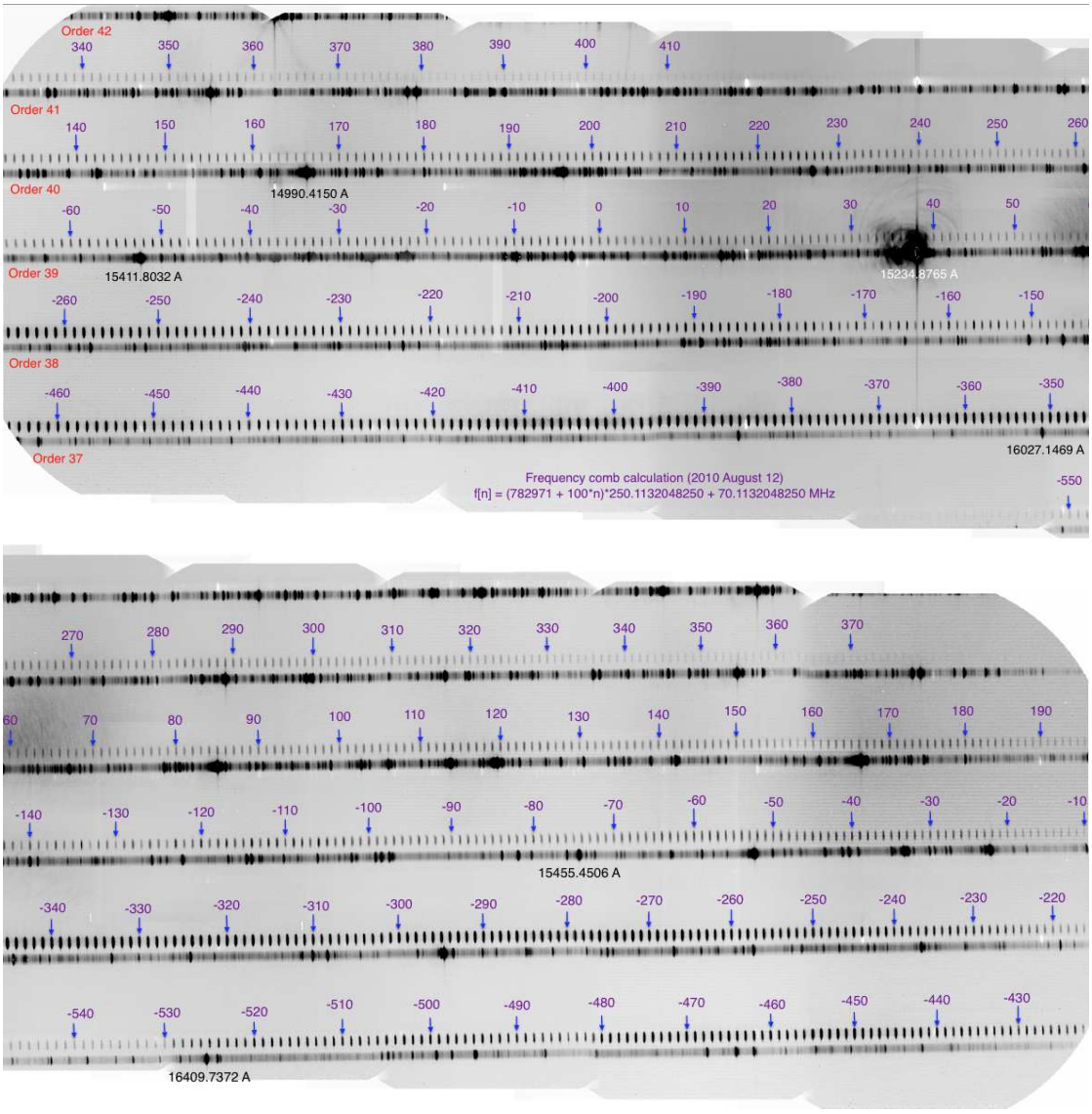

Fig. 3.10 A map of uranium-neon, taken with the Pathfinder spectrograph, and presented in two parts. The orders are indicated in red in the top half of the figure. The purple integers indicate the frequency comb index of the indicated line, which can be used with the frequency comb calculation (written in the top half of this plot) to calculate the frequency of any given comb line. Six bright neon lines have been indicated throughout using the neon line list of Salomana & Sansonetti (2004). For example, the bright neon line on the right of the top half of the map has a wavenumber of 6563.8865 cm^{-1}, and a vacuum wavelength of 15234.8765 Å.

uranium Ritz energy levels (Blaise & Radziemski 1976; Blaise et al. 1994), we matched the remaining lines to theoretical transitions. In this manner, we were able to classify over seven thousand uranium lines between 1 and 2 μm. Neon lines were taken from Salomana & Sansonetti (2004).

3.8 Uranium Neon Atlas Results

We have identified the strongest emission lines in the spectrum of a U/Ne hollow cathode lamp in the H band and present species identifications and precise wavelengths to aid in wavelength calibration of spectrographs using such lamps. An annotated map of U/Ne in the H band can be seen in Figure 3.10. The blackbody radiation of the hollow cathode lamp is visible as a faint continuum throughout the U/Ne spectrum while this continuum is not present in the frequency comb spectrum because the comb is not a thermal source.

The wavelengths of uranium lines from the FTS spectra and the neon lines from Sansonetti et al. (2004) in the H band are presented in the Appendix. A more precise and complete table of uranium lines covering the Y, J, and H bands is currently under preparation and will be published in Redman et al. (2011).

We wish to highlight some important features of in the U/Ne spectrum:

1. There is a uranium line that falls within 0.06 Å of a known neon line at 15110.5791 Å. The uranium line is based upon its existence in U/Ar spectra. It is not clear which source dominates this particular line from this spectrum alone.

2. Several blends are readily apparent throughout the spectrum, and confirmed both by the FTS spectra and the Pathfinder spectrum. Most notable are the pair of uranium lines at 16341 Å.

3. There are several unidentified bright lines throughout the spectrum (*e.g.,* the lines near 14645.0061, $\sim$ 15552, and 15907.3867 Å). Some of these are lines are strongly suspected to be uranium lines from yet-unknown uranium energy levels (in particular the lines at 14645.0061 and 15907.3867), as they have the same line width as other uranium lines, and were identified in at least two FTS uranium spectra. Others might be contamination in our hollow cathode lamp.

The difference between the uranium line peaks derived from the Pathfinder spectrum and the FTS-derived wavelengths are very small. Figure 3.11 shows a scatter plot of the uranium line peak differences, ignoring points that are more than three standard deviations from the mean uncertainty. The trimmed mean and single standard deviation is -0.00033 ± 0.028Å ($\sim 0.0042 \pm 0.35$ pixels, 6.4 ± 540 m/s).

We discovered in retrospect that the dewar temperature warmed 1.8 K exponentially over the course of this experiment, and the background counts in a 30-second dark correspondingly rose from $\sim$ 3000 electrons to $\sim$ 8000 electrons (see Figure 3.12). This was not completely U/Nexpected: this experiment took place at the very end of our run, and the dewar had only been partially filled the previous day in preparation for disassembling the spectrograph just a few hours after we finished.

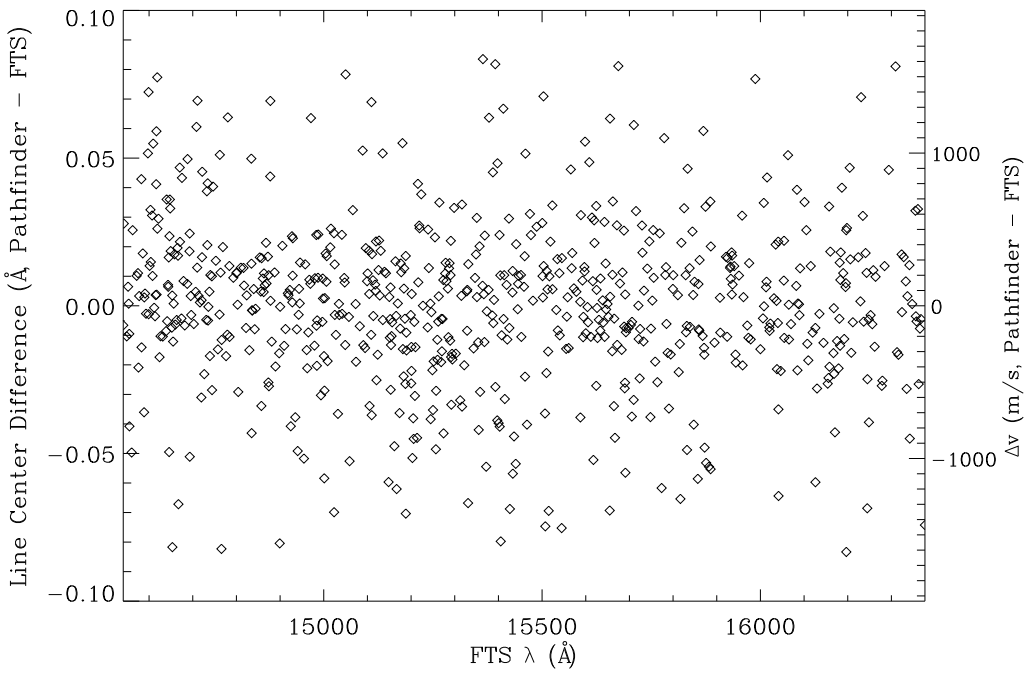

Fig. 3.11 The difference between the uranium peaks derived from the comb-calibrated Pathfinder spectra and the FTS-derived wavelengths, as a function of the FTS wavelengths, ignoring all points with differences more than three standard deviations from the mean difference. The trimmed mean and single standard deviation of these offsets is 0.00033 ± 0.028Å. Velocity differences are an approximation in this plot, using the central wavelength, 15500Å.

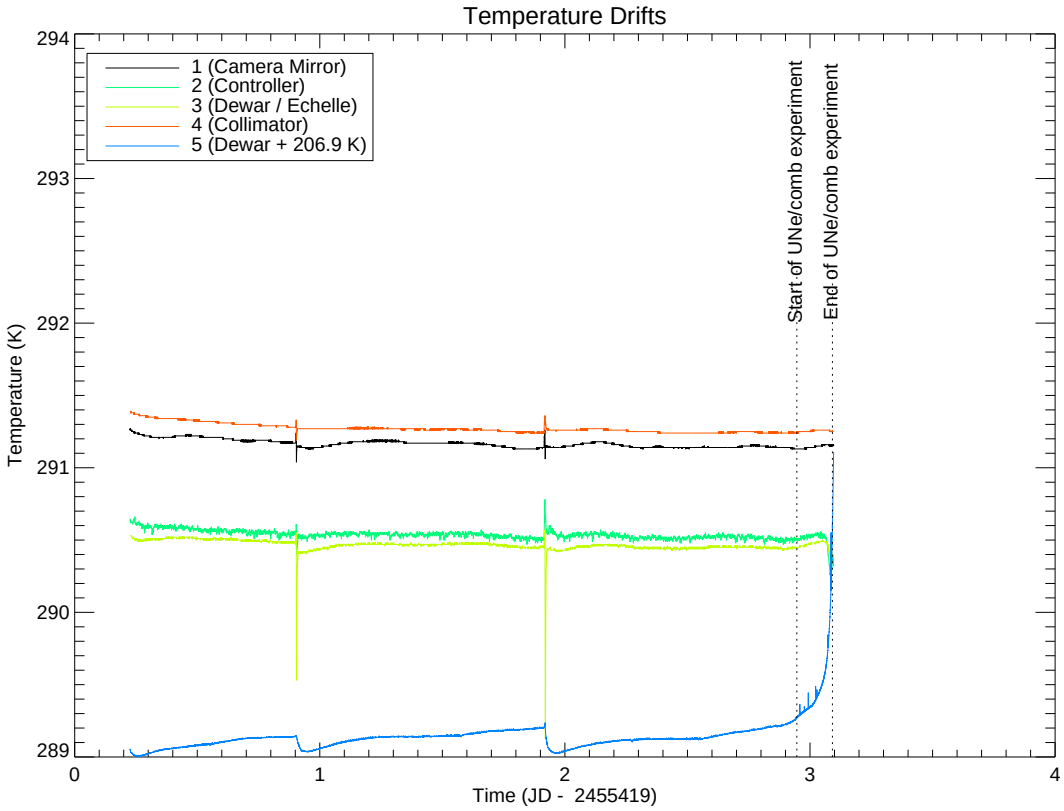

Fig. 3.12 The change in temperature of the dewar in the days leading up to the U/Ne and comb experiment. In preparation for dismantling the spectrograph, we had only partially filled the dewar the day before. The dewar temperature rose correspondingly. The small spikes in the dewar temperature during this time period are due to radio frequency interference from the walkie-talkies we used to communicate the filter and source changes.

Chapter 4

The PSU Pathfinder: HET Experiments

After the success of Pathfinder on the Sun (see Chapter 2), we secured 30 hours of observing time at the HET over three trimesters to perform on-sky experiments. The first two of these experiments were Y-band observations of radial velocity standards and bright planet-hosting stars, with a uranium-neon hollow cathode lamp as our calibration source, and the third was an H-band experiment with a frequency comb.

The spectrograph at the HET is shown in Figure 4.1, and a description of the light path through the spectrograph is given in the figure caption. The input fibers from the calibration bench were FIP 300/330/370 fibers from PolyMicro[1], with 195-μm (outer diameter) spacer fibers. The fiber slicer is shown in Fig. 3.7, where the top picture shows the three fibers and the spacer fibers, and the bottom picture shows the same set of fibers, covered with a 100-μm slit. This setup is very similar to the fiber setup we used for our Solar experiments (see Fig. 2.4).

In the interim between our Solar observations and these HET runs, we made several upgrades to both our hardware and our analysis software. These changes are detailed in the next two sections.

4.1 Hardware Upgrades

Pathfinder was constructed with parts scavenged from other experiments, which in some cases were sub-optimal for observations in the NIR. While throughput was not really a concern during our solar observations at Davey labs (where we were observing the brightest NIR object in the sky), we knew that we would not be successful in our on-sky observations with the same equipment. Therefore, it was essential that we upgraded our gratings to improve our efficiency and filters, and moved Pathfinder to a thermally-isolated location at the HET, where we could be sure the instrument would be less sensitive to thermal creep.

4.1.1 Grating Upgrades

We upgraded the echelle from the JCAM grating, which was an R2 ($\theta = 63.4^\circ$), 31 lines/mm, 110 $\times$ 210 mm gold-coated echelle, to an R3 ($\theta = 71.5^\circ$), 31 lines/mm, 128 $\times$ 254 mm gold-coated echelle. We upgraded the cross-disperser from a $\Theta_{\rm blaze} = 2.15^\circ$ aluminum grating to a $\Theta_{\rm blaze} = 1.25^\circ$ gold grating. Gold has a greater reflectivity than aluminum in the NIR, and the larger echelle with its higher blaze angle greatly increased our efficiency.

[1]Product specs can be found here: `http://www.polymicro.com/productpdfs/FI_12-04.pdf`

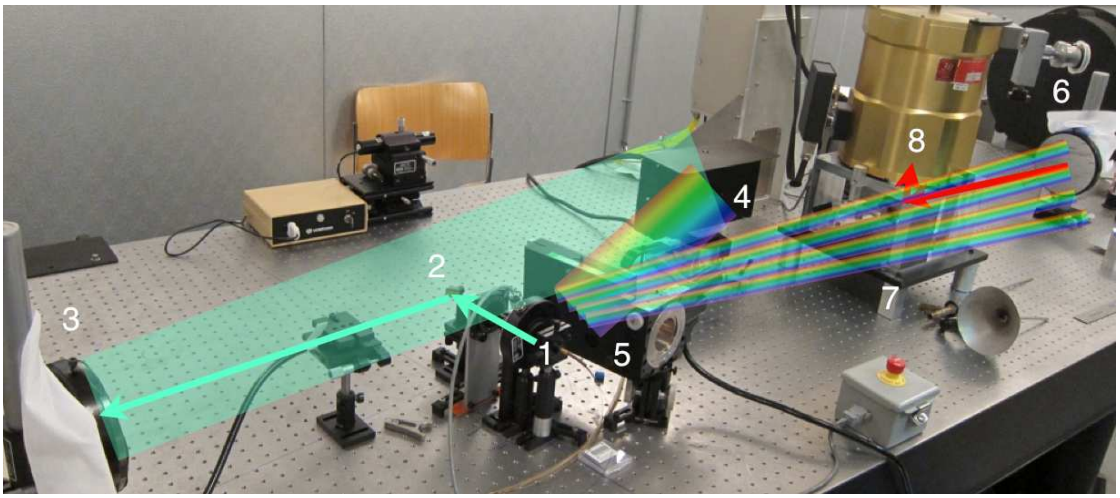

Fig. 4.1 An image of the PSU Pathfinder on the bench at the HET. Light from the HET and the calibration system is fiber-fed into a slit mechanism (1), bounces off a gold fold mirror (2), reflects off the collimating mirror (3), is dispersed off the grating (covered, 4), is cross-dispersed off the cross disperser (5), reflects off the camera mirror (6), and reflects off a gold mirror (not visible, 7) into the Dewar, where approximately 0.2% of the light from the telescope lands on the detector (8). This layout is very similar to the optical diagram shown in Figure 2.1, except in the latter case the fiber input mechanism is at the location of the above-pictured gold mirror (2).

4.1.2 Filters

As a warm infrared spectrograph, the PSU Pathfinder is particularly susceptible to the thermal background of the room, the bench, and the spectrograph itself. Since we have no cold shutter, this noise source shows up as increased counts in all of our frames, which limit the achievable S/N. The proper selection of filters must block this thermal radiation and not emit any thermal radiation themselves. By placing the filters inside of the Dewar and in close proximity to the liquid nitrogen reservoir (see Figure 4.2), we were able to keep our filters cold, and successfully observe with our warm instrument. We carefully selected a combination of filters that would provide the best possible thermal blocking, without compromising our throughput and the Y and/or H bands.

To first order, the transmission of filters can be determined from company specs. However, these do not always cover the wavelength range of interest. In particular, since we are interested in minimizing the thermal background, we need filters which exhibit a transmission of less than 10^{-5} beyond our observing region. To second order, the combined transmission of the thermal background with various filter combinations can be estimated from the dark counts at a variety of exposure times. Figure 4.3 shows the average number of electrons per pixel per second for four of these filter combinations. For reasons that are not clear to us, the detector shows an excess of counts in shorter exposures; we have partially corrected for this effect by subtracting the average counts in a one-second exposure from each of the points in this Figure.

We noticed that the dark counts rose unexpectedly high with certain filter combinations. In particular, there was a large rise in dark counts when the PK50 was replaced by the Barr-1300, and initially we suspected that this was due to pinhole flaws in the filter. Since swapping the filters requires warming opening, and cooling dewar, exposing the array to dust, the risk of physical damage, and delamination, these swaps are prohibitively risky. A much more efficient and safe way to identify the source of these increased counts is to characterize the filters individually, using a spectrophotometer. We carefully transported the filters to the Material Research Institute at PSU, where their absorptions were measured between 300 and 3300 nm with a Perkin-Elmer Lambda 950 Spectrophotometer[2] (PE950). This double-beam, double-monochromator, ratio-recording spectrophotometer is sensitive between 180 and 3300 nm. By placing a filter in one of the beam paths, and comparing the transmission to the unblocked beam, you can measure transmission curves to a sensitivity of tens of thousandths of an absorbance unit (a transmission of 10^{-5}). Figure 4.4 shows the spectrophotometer (left) and the 50-mm thick PK50 filter in one of the beam paths (right). The transmission curves of these filters are shown in Figure 4.5. The PE950 is not a perfect measuring device, and when the detector or transmission filters internal to the PE950 were swapped, the transmission spectrum sometimes exhibited false readings. The most prominent false reading in Fig. 4.5 is sudden drop in transmission of the Y/J/H band Omega filter at 1650 nm.

These results suggest that the detector is sensitive beyond the expected cutoff of 2.5 μm. By the time we had tracked down this problem and ordered a custom filter, we

[2] `http://las.perkinelmer.com/Catalog/ProductInfoPage.htm?ProductId=L950`

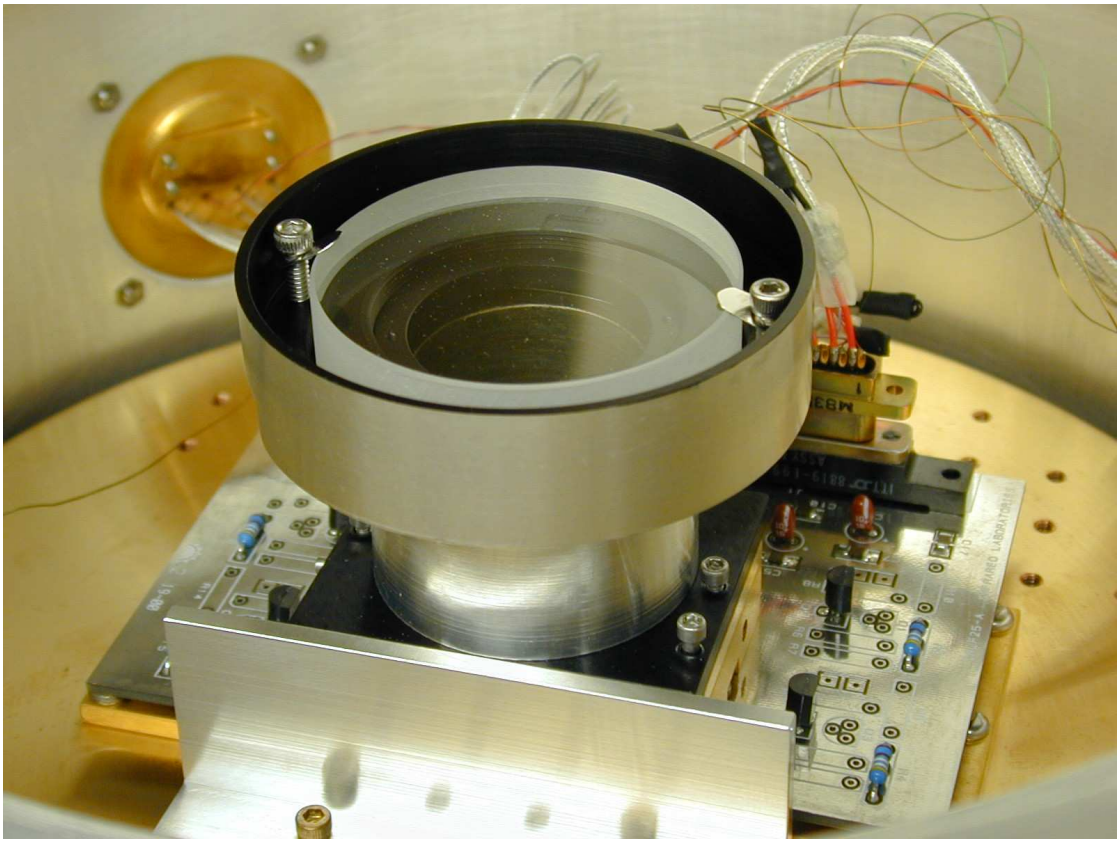

Fig. 4.2 The filter holder inside the Pathfinder dewar, with the PK50 filter visible at the top. The detector is directly beneath the filter holder, and the detector electronics are clearly visible. The detector electronics are mounted to the liquid nitrogen reservoir. The temperature sensor resided beneath the lip of the filter holder throughout the HET observations.

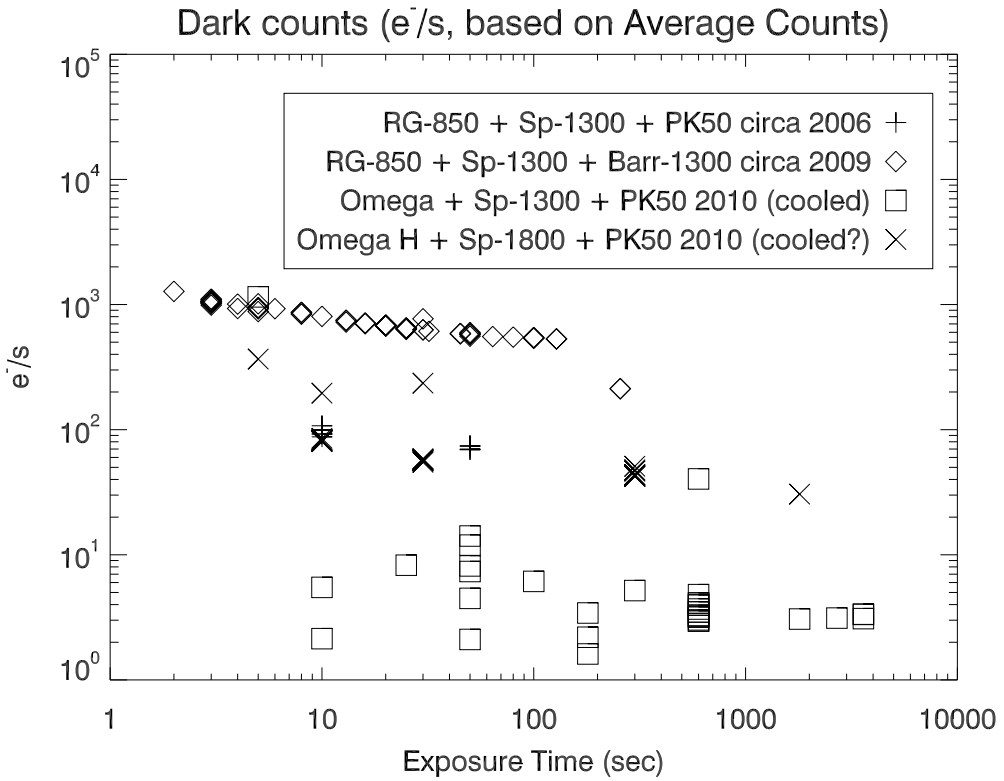

Fig. 4.3 The dark counts for a variety of filter sets. Note, in particular, the increased counts when the PK50 filter was replaced by the Barr-1300 (pluses vs. diamonds). The rise in counts between the (Omega, Spectragon-1300, and PK50) and the (Omega H, Spectragon-1800, and PK50) was expected based on the increased sensitivitiy to the thermal background in the H band that passes through the latter combination of filters.

Fig. 4.4 **Left:** The Perkin-Elmer Lambda 950 Spectrophotometer at the Penn State Material Research Institute. **Right:** A 50-mm thick chunk of PK50 glass in one of the double-beam paths. Light enters from the left, passes through the filter, and onto the detectors on the right (not pictured). The apertures for the comparison beam can be seen in the background.

only had a few days to settle on a filter combination to use at the HET. For the Y band, we ended up using a custom filter from Omega, the PK50, and the Spectragon-1300. It's possible that the Spectragon-1300 was unnecessary, but only in retrospect did we discover that it took more than 24 hours for the filters to cool down. Nonetheless, our chosen filter combination yielded a mere 3 e^-/second, an improvement of more than two orders of magnitude over the RG-850, Spectragon-1300 and Barr-1300 combination.

This result is crucial to the development of future NIR spectrographs. Avoiding the thermal background beyond 2.5 μm can either be accomplished by selecting a HAWAII array that cuts off at 1.7 μm, or by using a combination of filters that provide orders-of-magnitude suppression beyond 2.5 μm. Finding such glass is a difficult process. PK50 is no longer produced, but Ryan Terrian has tracked down an alternative, KZESN5, which exhibits nearly the similar spectrum as PK50.

4.1.3 Temperature Stability

One of the major sources of detector and spectrograph instability during our tests at Davey was the changing temperature of the spectrograph room. While these motions are in theory tracked by our calibration lines, larger drifts are more susceptible to sub-pixel and pixel-sized uncertainties, such as non-uniform pixel sensitivities and inadequate flatfielding. Larger drifts also require that the dispersion solution be pinned down across the entire array to a few mÅ. When we installed the PSU Pathfinder at the HET, it was placed inside an insulated chamber, which, even without temperature control, greatly improved our thermal stability. What we did not know until we were on-site was that the temperature of the spectrograph room (which houses three spectrographs — the HRS, MRS, and PSU Pathfinder) was being adjusted manually to stabilize the

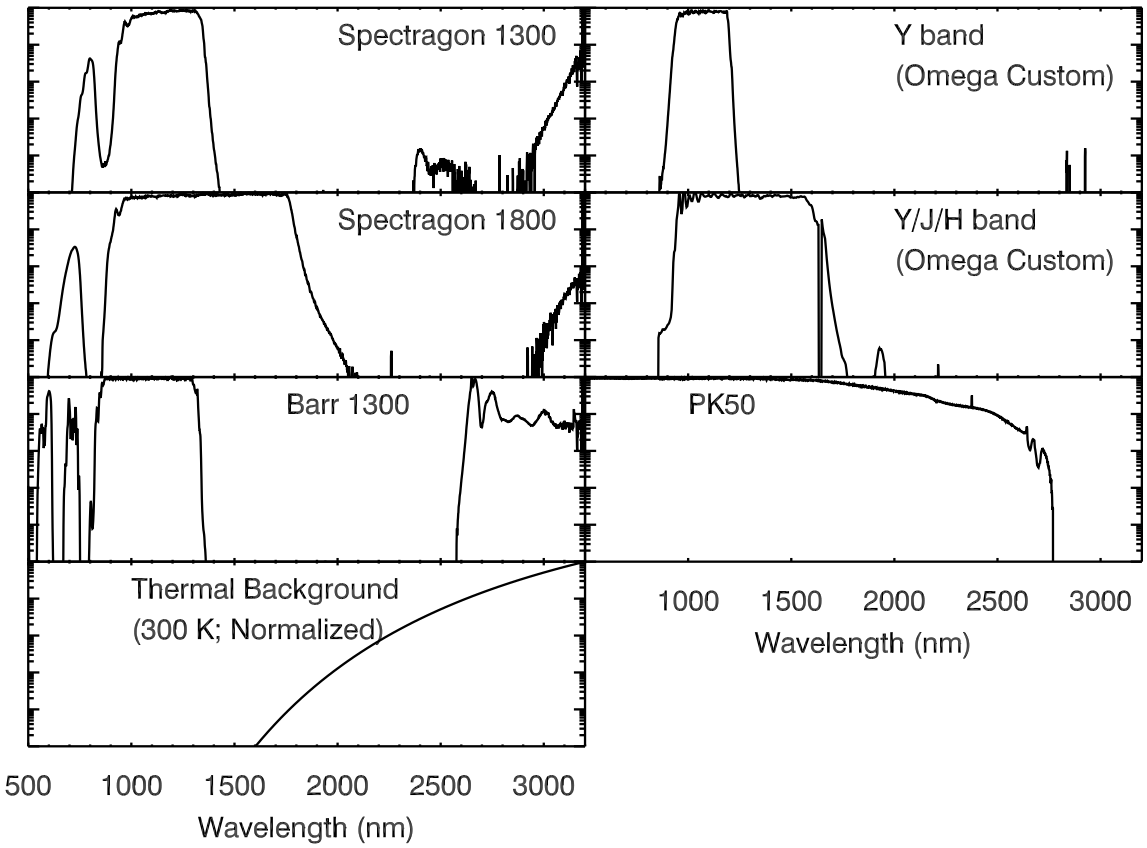

Fig. 4.5 Transmission spectra from six different filters and the thermal background (as indicated) between 500 and 3200 nm. The y-axis of each plot runs from 10^{-5} to 1. Some of these spectral features are due to scanning flaws in the Perkin-Elmer Lambda 950. One notable flaw is the deep gash in the Y/J/H Band Omega Custom filter, which corresponds to a filter change. Note that the Spectragon and Barr filters are all significanty transparent beyond 2.5 μm, where the thermal background is most prominent. We hypothesize that the PK50 was essential in reducing the thermal background beyond 2.8 microns.

temperature of the HRS enclosure. The HRS enclosure varied depending on the use of the instruments within the enclosure, and these adjustments adversely affected the MRS enclosure's temperature. Figure 4.6 shows some of the temperature drifts we experienced while at the HET in May of 2010, including one of the above-mentioned temperature adjustments.

This figure also shows the thermal impact of the controller, which is usually a heat source for the enclosure even though it is water-cooled. At one point during our experiments, our connection to the controller died, and we ceased to read data, which caused the enclosure temperature to drop significantly. Also visible in this Figure are the Dewar fill times, indicated by the large temperature drops measured by the probe near the Dewar approximately every 24 hours. It is not obvious to us why the temperature probe inside the Dewar also recorded a drop in temperature upon being filled, since the Dewar was never empty.

4.1.4 Modal Noise

We have conducted several experiments with the Pathfinder in each of the three NIR bands of interest (the Y, J, and H bands). The top panel in Figure 4.7 shows the extracted flatfield spectra in a single order of the Y band first without (top) and then with (bottom) agitation, and both normalized by a flatfield spectrum with approximately twice the S/N. The modal noise is readily apparent as low-frequency oscillations in the unagitated flatfield. Another way to present this same information is with a power spectrum, as seen in the bottom panel of the same Figure. Vibrating the fiber provides nearly an order-of-magnitude improvement in the low-frequency noise.

Modal noise also greatly impacted our frequency comb calibrations. One of our first indications that agitation was unsuccessful at mixing the modes was the scatter in the measured fiber separation between Fibers 2 and 3 (see Figure 3.8). Figure 4.8 shows some of the strongest evidence that the agitator was insufficient at mixing the modes in the H band. Each of the lines in these plots represent the flatfield spectrum extracted from a single order in the H band. Each spectrum has been divided by the median-averaged agitated flatfield frame. In the top panel of this plot, every flatfield shows the same modal noise pattern (indicating that the modal distribution was not changing during these exposures, but was not the same during the agitated frames), while in the bottom panel of this plot, there are three spectra that show clear modal noise - spectra 20, 21, and 32.

Figure 4.9 shows an example of the ratio of successive exposures with comb light through all three fibers. When modes are successfully mixed, they do not vary visibly from exposure to exposure, and the image ratios look uniform. The fiber from the HET exhibits this optimal modal mixing. The other two fibers, both calibration fibers, show significant structure in the image ratios, indicating insufficient modal mixing. Modal noise turned out to be one of the primary limitations in our August observations. This modal noise distorts the measured dispersion solution of the individual calibration and science frames, increasing the RMS residuals of these dispersion solutions. Figure 4.10 shows the RMS residuals of the dispersion solutions in each of the three fibers, over the course of the August 2010 observations.

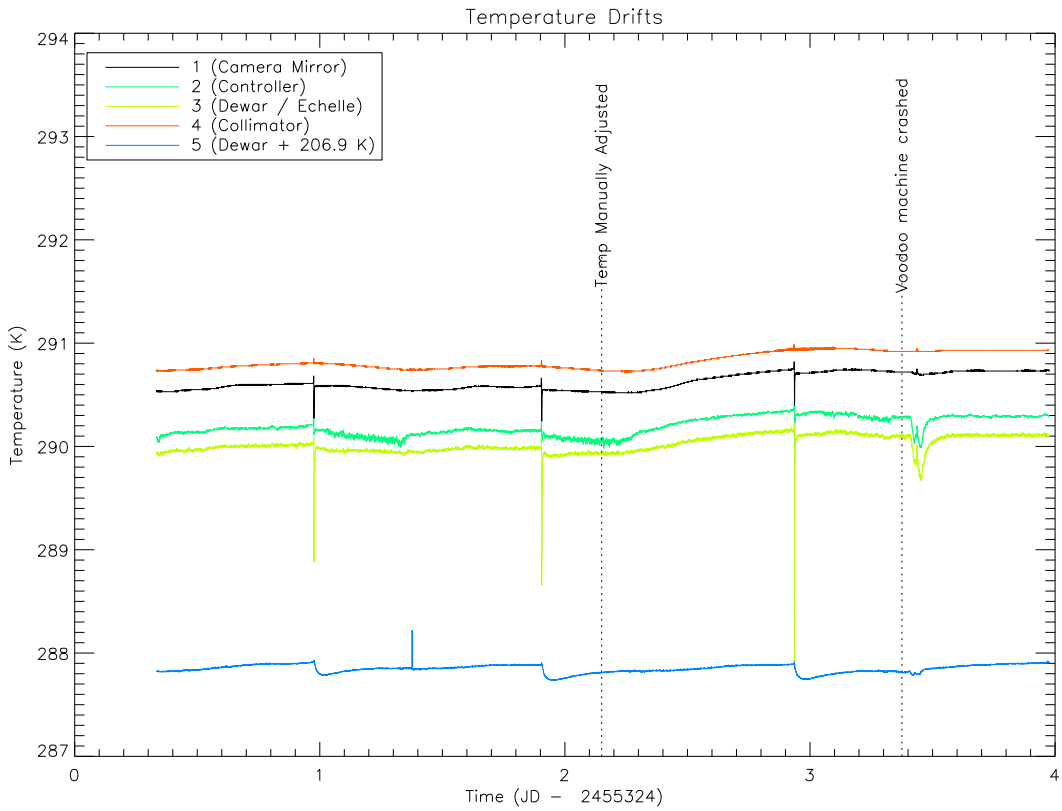

Fig. 4.6 The temperature drift of the MRS enclosure, which housed the PSU Pathfinder during part of our 2010 May observation run at the HET. Four temperature probes were placed throughout the enclosure to record thermal fluctuations at the optical components of the spectrograph: the camera mirror, collimator, echelle, and controller. A temperature probe inside the Dewar recorded the temperature of the filter holder. In this plot, the Dewar temperature has been offset by a constant amount so that it is visible on the same scale as the other four probes. The dewar fills, which occurred each morning after our observations, are indicated by sudden temperature drops at the camera mirror and echelle. Unbeknownst to us beforehand, the temperature of the HRS enclosure was being adjusted by changing the temperature of the spectrograph room. One such temperature adjustment is indicated near JD 2455326, and the subsequent rise in the enclosure temperature several hours later is readily visible. The controller also provides a source of heat for the enclosure, as is readily apparent by the sudden drop in temperature after the Voodoo computer crashed around JD 2455327.4.

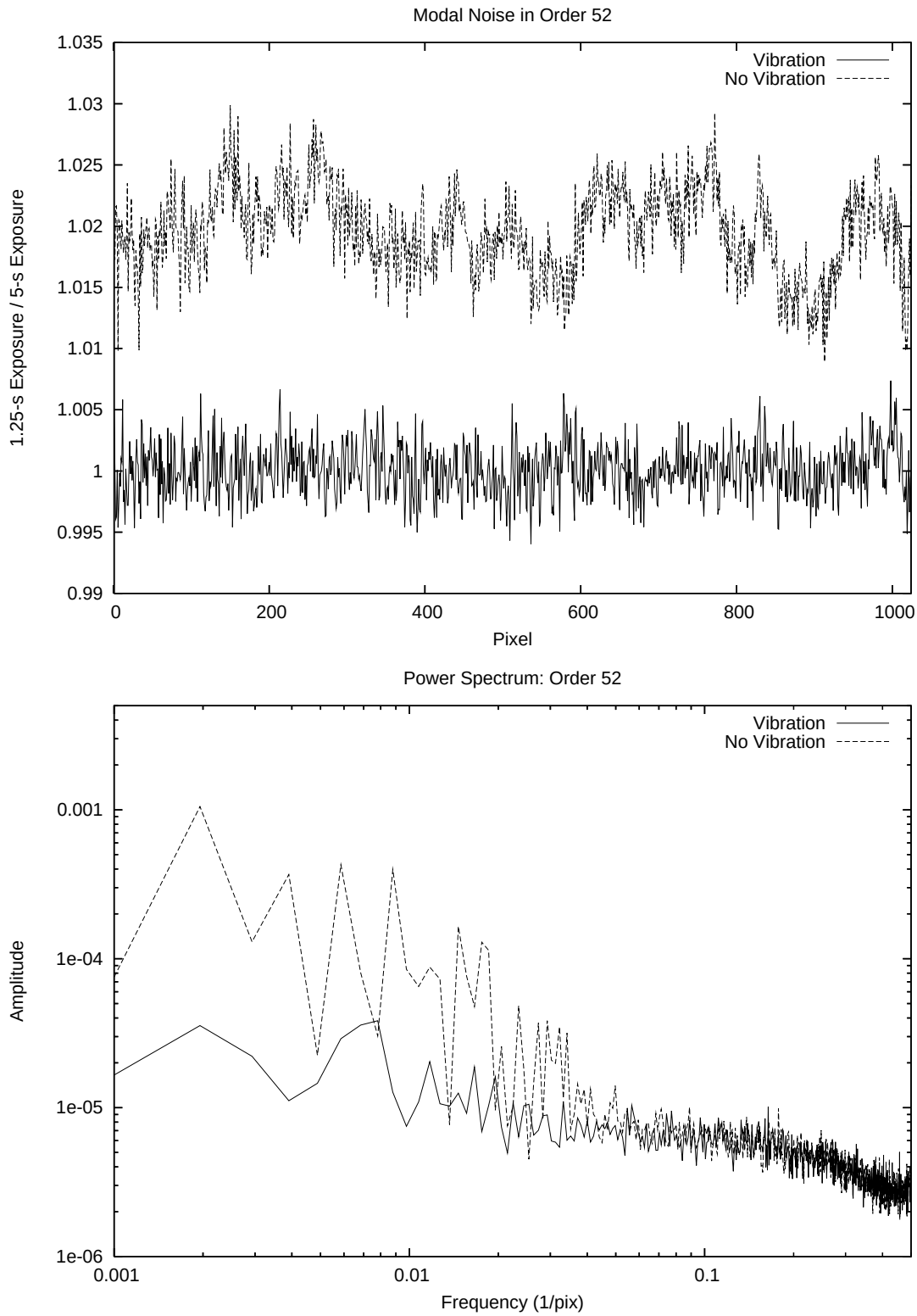

Fig. 4.7 Modal noise in the Y-band. **Top:** The ratio of a 1.25-second exposure and a 5-second exposure, with and without vibration. **Bottom:** The power spectrum of the spectra, with and without vibration. Vibrating the fiber reduces the low-frequency noise by about an order of magnitude.

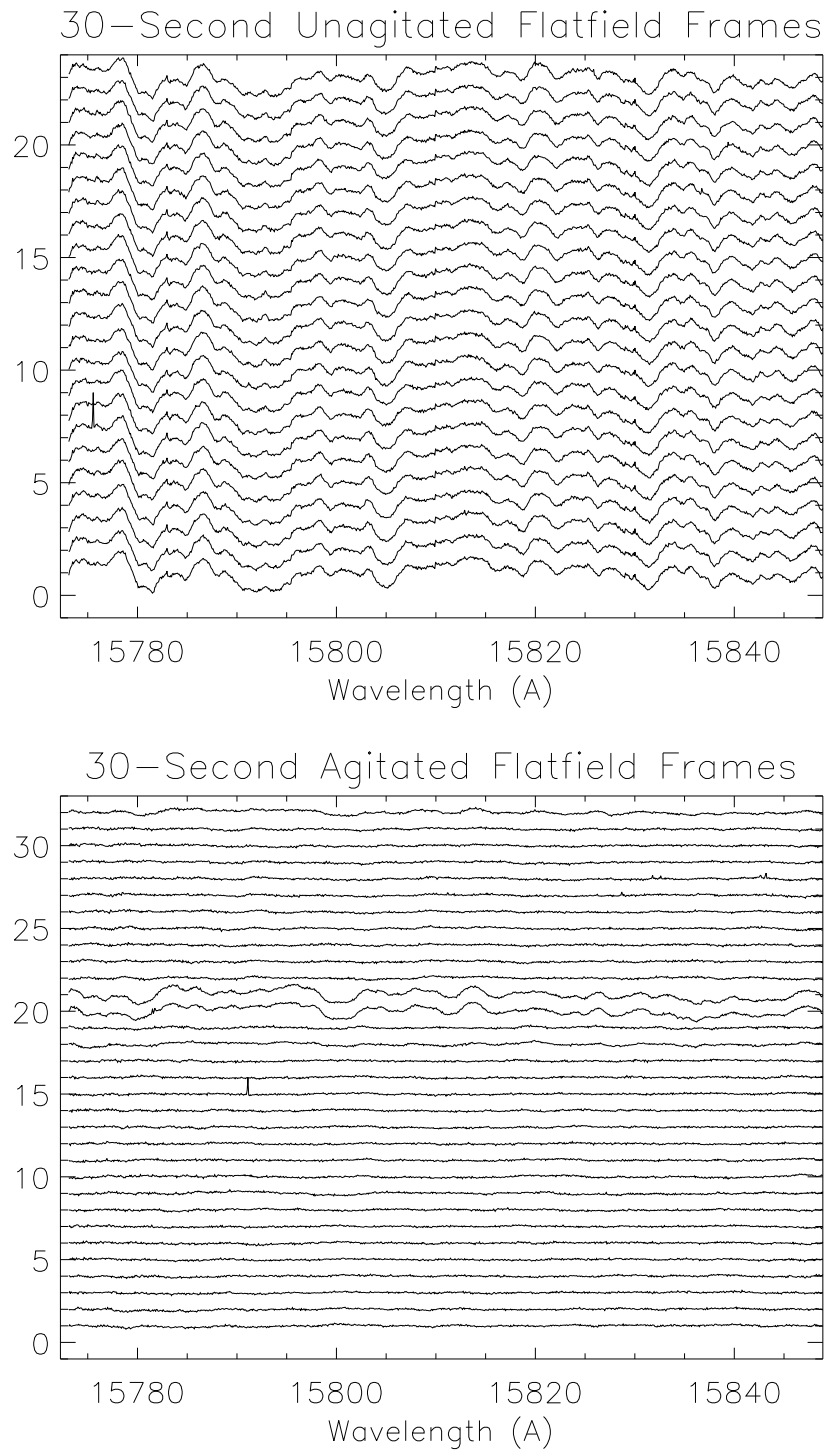

Fig. 4.8 Waterfall plots of successive unagitated (top) and agitated (bottom) flatfield frames in the H band. Time increases in the vertical dimension. All frames were divided by the median-averaged agitated flatfield spectrum, which why most agitated frames show no modal noise. However, the fact that at least three of the agitated frames (images 20, 21, and 32) show modal noise is strong evidence that the agitator was insufficient at uniformly mixing the modes.

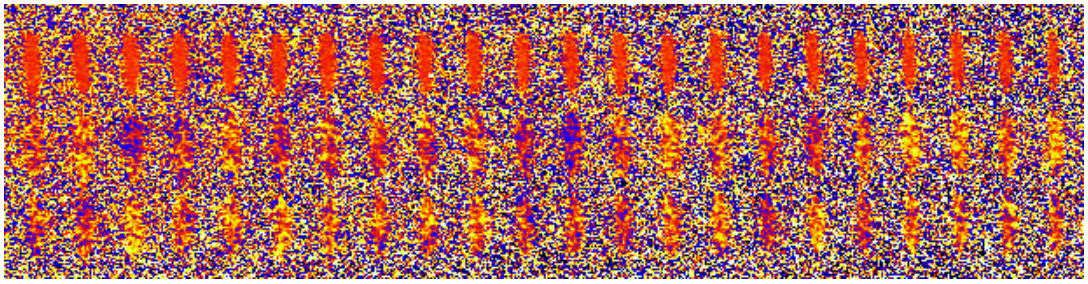

Fig. 4.9 The ratio of successive exposures of frequency comb light through all three fibers. Modal noise is readily apparent in both the calibration fibers (bottom fibers), but not in the light from the HET fiber. The insufficient modal mixing of these calibration fibers was one of the primary limitations to the achievable precision during our August observations.

4.2 Software Upgrades

Our improvements to the Pathfinder were not just hardware-based, but also software-based. Some of these software fixes — such as our attempts to mitigate the mutliplexer crosstalk — were pieces of software designed to mitigate hardware flaws. In our 2006 and 2007 runs, we relied upon IRAF to dark-subtract, normalize, extract, wavelength-calibrate, and cross-correlate our spectra. While we obtained reasonable results with the runs highlighted in Chapter 2, the black-box nature of IRAF left us without the necessary tools to understand the origins of our systematics.

In 2008, I was supported by a NASA GSRP Fellowship under the auspices of Dr. Sally Heap, who taught me how to program in IDL. This programming language provides many advantages over FORTRAN77, most notably array manipulation, and an extensive library of pre-written functions and programs relevant specifically to astronomers. In addition, Piskunov & Valenti (2002) have written an excellent echelle reduction package (REDUCE), which provide automated echelle order identification, optimal extraction for continuous and semi-continuous spectra, and code that is easy to debug and edit.

4.2.1 Model Spectrograph

A computational model spectrograph that provides the user with an image of the expected observed spectrum given a set of pre-determined parameters saves the user a great deal of time and frustration when bringing the spectrograph up for the first time since a new installation. In an effort to expedite our work at the HET, I designed an IDL model spectrograph based on Larry Ramsey's spectrograph Excel spreadsheet program, which was used for the design of the MRS and PRVS.

For the discussion below, I adopt the notation of Schroeder (2000). σ is the inverse of the number of lines per millimeter on a given grating. Θ_B is the blaze angle.

For the echelle:

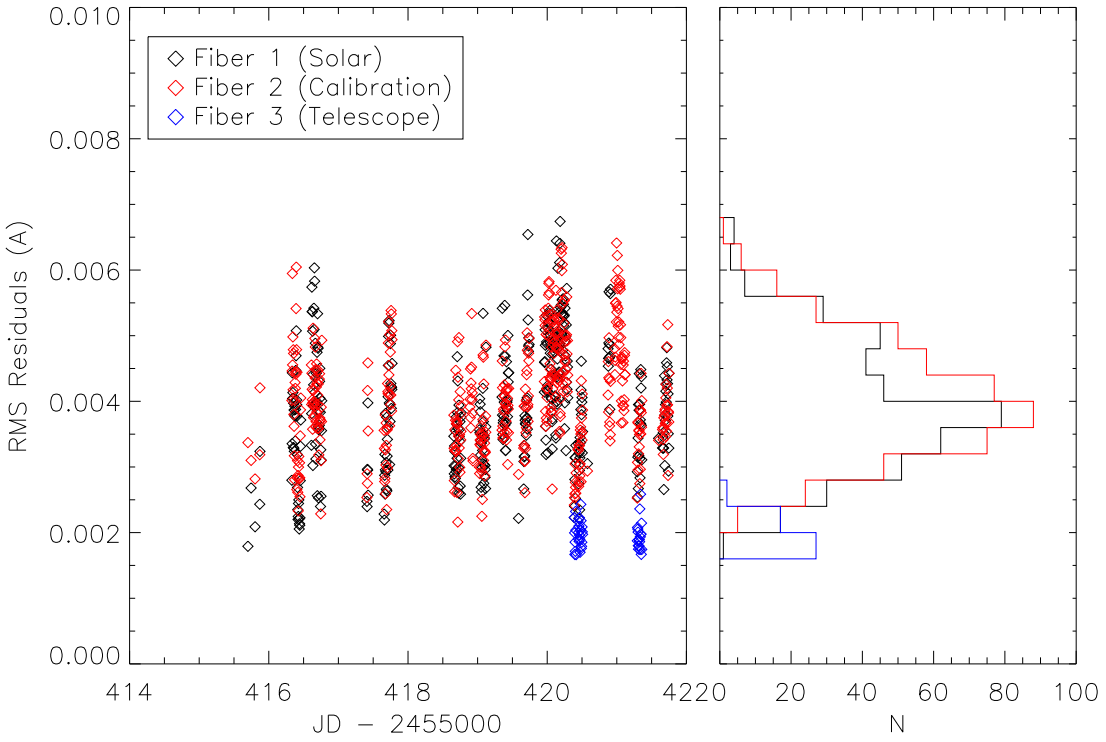

Fig. 4.10 The dispersion solution RMS residuals for the comb exposures through each of the three fibers over the course of the HET H-band observations. These residuals were calculated after correcting for the various detector flaws discussed in this chapter, including the irregularly-spacing of the pixels discussed in § 4.2.9. The increased residuals in fibers 1 and 2 are due to the additional modal noise in those fibers. This was a strong indication that these fiber were not fed correctly.

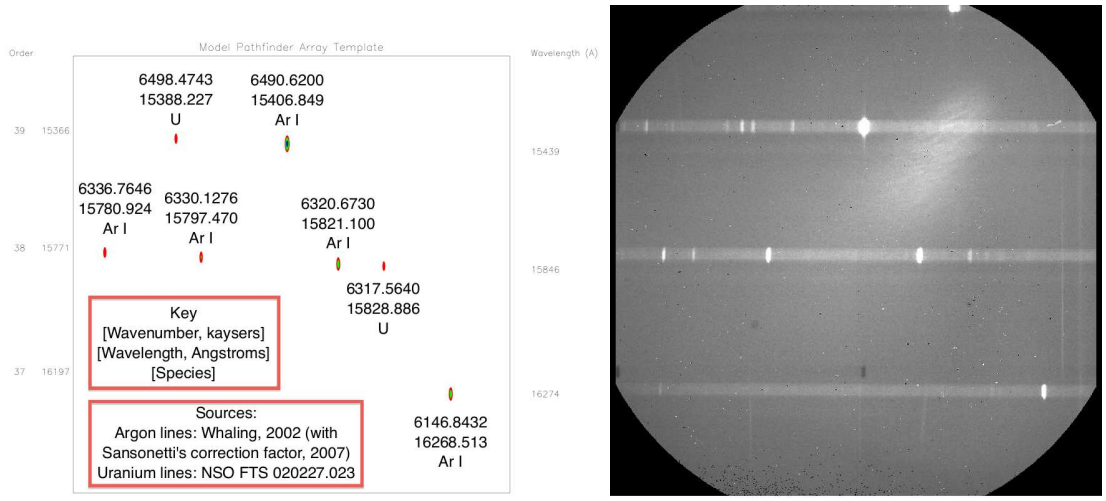

Fig. 4.11 A model image showing the expected location of uranium and argon lines on the detector, and the confirmation of that model. The figure on the left shows the model image of UAr spectra in the region selected for the HET Frequency Comb tests of August of 2010, and the figure on the right shows a Pathfinder image of the same region. Note that the model image required an FTS-identified spectrum with a similar current (in this case, 26 mA).

$$\sigma_{ech} = (31.6046)^{-1} \tag{4.1}$$
$$\Theta_{B,ech} = 71.5^{\circ} \tag{4.2}$$
$$\theta_{ech} = 5.5^{\circ} \tag{4.3}$$
$$\gamma_{ech} = 0.^{\circ} \tag{4.4}$$

and for the cross-disperser:

$$\sigma_{xd} = (150)^{-1} \tag{4.5}$$
$$\Theta_{B,xd} = 5.4657^{\circ} \tag{4.6}$$
$$\theta_{xd} = 0.^{\circ} \tag{4.7}$$
$$\gamma_{xd} = 11.^{\circ} \tag{4.8}$$

The angle of the echelle is denoted as $\delta\alpha_{ech}$, so that α_{ech} is $\Theta_{B,ech} + \delta\alpha_{ech} + \theta_{ech}$, and β_{ech} is $\alpha_{ech} - 2. \times \theta_{ech}$. The anamorphic magnification is:

$$r_{ech} = \cos(\alpha_{ech})/\cos(\beta_{ech}) \tag{4.9}$$

The central order coming off the echelle is:

$$m_{ech} = \sigma_{ech} \times \cos(\gamma_{ech}) \times (\sin(\beta_{ech}) + \sin(\alpha_{ech}))/\lambda_{cen,ech} \tag{4.10}$$

where $\lambda_{cen,ech}$ is an input. The central wavelength coming off the cross-disperser is:

$$\lambda_{cen,xd} = \sigma_{ech} \times \cos(\gamma_{ech}) \times (\sin(\beta_{ech}) + \sin(\alpha_{ech}))/m_{ech} \tag{4.11}$$

Thus, β_{xd} is:

$$\beta_{xd} = \arcsin(\lambda_{cen,xd}/(2 \times \sigma_{xd} \times \cos(\gamma_{xd})) \tag{4.12}$$

The central blaze wavelength (λ_{bl}) is given by:

$$\lambda_{bl} = \sigma_{ech} \times \cos(\gamma_{ech}) \times (\sin(\beta_{ech}) + \sin(\alpha_{ech})) \tag{4.13}$$

The angular coverage on the array is given by:

$$\delta = \arctan(0.5 \times n \times pitch/f_{cam}) \tag{4.14}$$

where n is the number of pixels (1024 in the case of Pathfinder), f_{cam} is the focal length of the camera mirror, and *pitch* is the size of a pixel — 18μm in our case. The wavelength coverage of the first order is bound by $\lambda_{\mathrm{low,1}}$ and $\lambda_{\mathrm{high,1}}$:

$$\lambda_{\mathrm{low,1}} = \sigma_{\mathrm{ech}} \cos(\gamma_{ech}) \times (\sin(\beta_{ech} - \delta) + \sin(\alpha_{ech})) \tag{4.15}$$

$$\lambda_{\mathrm{high,1}} = \sigma_{\mathrm{ech}} \cos(\gamma_{ech}) \times (\sin(\beta_{ech} + \delta) + \sin(\alpha_{ech})) \tag{4.16}$$

From here, the range of each other order on the detector can be found via the grating equation:

$$\lambda_{\mathrm{low,m}} = \lambda_{\mathrm{low,1}}/m \tag{4.17}$$

$$\lambda_{\mathrm{high,m}} = \lambda_{\mathrm{high,1}}/m \tag{4.18}$$

This model also takes a calibration line list of wavelengths and intensities and plots the expected visual layout of the Pathfinder spectrum. Figure 4.11 demonstrates the merits of this program. In this Figure, the model spectrum is seen on the left-hand side, showing the expected locations of the brightest Uranium and Argon lines from a 26-mA FTS observation. The image on the righthand side verifies the model.

4.2.2 Multiplexer Crosstalk

When our detector is read out, each quadrant is read simultaneously. Since all four quadrants are powered by the same bias power supply, a bright feature in one quadrant (such as an emission line) will produce a deficit of counts in the other three quadrants. While this problem could be solved by proving a separate power supply for each quadrant, this would require rewiring the detector and modifying the dewar. Therefore, we sought to partially correct the problem in software.

In order to reduce these, I subtracted 1% of each quadrant from each other quadrant. The results of this technique can be seen in the two images in Figure 4.12. The image on the left is a CDS-subtracted frame with two bright flat field orders at the top of the array, and clear negative images in the bottom half of the array. This frame also has two fainter UNe spectra (each appearing below the flatfield frames), but they make no significant contribution to the multiplexer crosstalk. The image on the right has been subtracted in the above-mentioned manner. Note the reduction in the contrast between the multiplexer crosstalk and the thermal background.

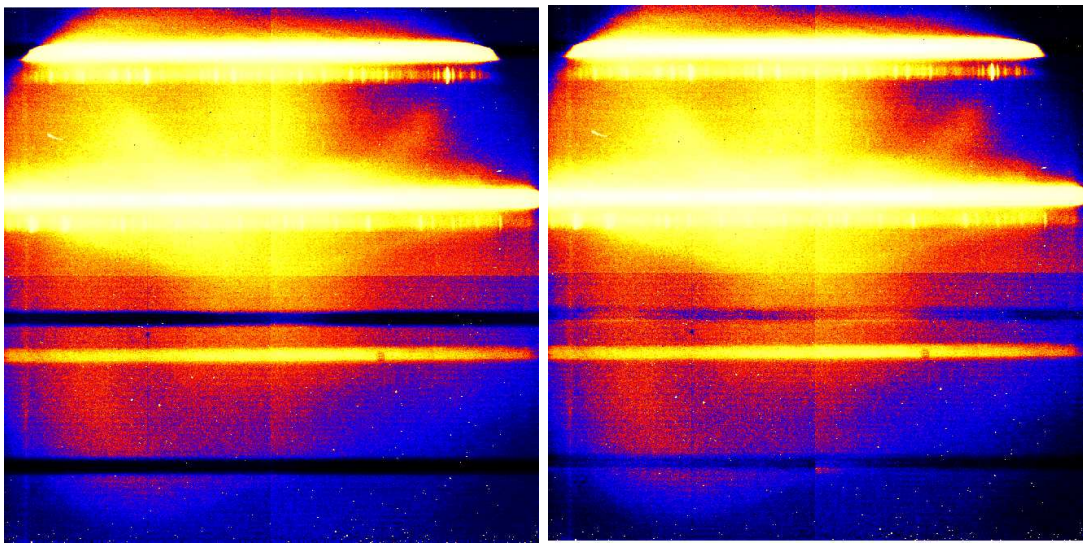

Fig. 4.12 Multiplexer crosstalk is visible on the detector when a bright feature draws current from wells in adjacent quadrants, reducing the apparent number of counts in those pixels. The top half of each image shows two bright flatfield orders; the multiplexer crosstalk appears as dark bands in the bottom half of each image. To mitigate this problem, 1% of each quadrant is subtracted from the other three quadrants. The result of this subtraction is shown in the righthand figure.

4.2.3 Bad Pixels

"Bad" pixels are those which do not act like "good" pixels — pixels that, for whatever reason, do not count photons linearly over the desired performance range. This definition allows for the inclusion of "hot" or "cold" pixels, which can provide useful scientific information, as long as they are linear and do not saturate. Principal component analysis (hereafter, PCA) provides a very useful way for distinguishing the performance of good and bad pixels. This technique utilizes the fact that the measured values in normal pixels will be correlated along a principal axis, with abnormal pixels lying farther away from this axis. Different noise sources will lie perpendicular to this

principle axis. Detail on this technique can be found in López-Alonso et al. (2002), but an outline is provided below.

The crux of this analysis is that pixel "goodness" is measured by two parameters, both related to the principal component of the data. Consider a series of N images, with M pixels each, such that the series of values measured by a given pixel can be arranged in a matrix F: F_1, F_2, ..., F_N. The covariance matrix of these data frames is S:

$$S = \frac{1}{M-1}\bar{F}^T\bar{F} \tag{4.19}$$

where $\bar{F}$ is the matrix F where each frame has been reduced by its mean value. Diagonalizing this matrix provides a set of N eigenvectors:

$$(S - \lambda I)E = 0 \tag{4.20}$$

where I is the N by N unity matrix, E is the set of eigenvectors (arranged as an N by N matrix), and λ is the set of N eigenvalues. The principle components are then given by:

$$Y = \bar{F}E \tag{4.21}$$

The distance between a pixel β and the data mean is defined by the Mahalanobis distance D^2_β:

$$D^2_\beta = Y_\beta S_Y^{-1} Y_\beta^T \tag{4.22}$$

Pixels with large Mahalanobis distances are those that demonstrate aberrantly low or high values consistently.

A pixel that always provides the same value will lie along a unitary vector, denoted by López-Alonso et al. (2002) as e_{sp} $(= \frac{1}{\sqrt{N}}(1, 1, ...1, 1))$. Likewise, a pixel that provides only random values will (with a large enough sample) lie perpendicular to this vector. Therefore, the second dimension by which to measure the goodness of a pixel is given by the cosine of the angle between the unitary vector and a vector pointing from the main pixel to the pixel value in the frames, F_β:

$$\cos[e_{sp}, (F_\beta - \mu)] \tag{4.23}$$

These two quantities ($\cos(\theta)$ and D^2_β) plotted against each other provide maps like those seen in Figure 4.13. The top-left plot in this Figure shows the expected distribution for a pair of normal random distributions. Since these values are completely random, the Mahalanobis distance is clearly defined. The top-right plot of this Figure shows the values from eight normal random distributions; the distribution clearly trends away from $\cos(\theta) = 1$ or -1 (pixels having the same value in all eight images). The bottom plots show the PCA analysis from real Pathfinder dark frames. The bottom-right plot is of six 10-second darks — note the dead pixels that cluster at $\cos(\theta) = 1$. The bottom-left plot shows the PCA analysis of three Pathfinder exposures of different lengths (10, 30, and 300 seconds). In this plot, the dead pixels show values away from $\cos(\theta) = 1$ and

-1 because of multi-plexer cross-talk. However, it's important to note that analyzing exposures of different lengths highlights a slightly different population of bad pixels.

One of the great advantages of this technique of identifying bad pixels is the resulting eigenimages, such as those shown in Figure 4.14. Since all images in these sets are linear combinations of these eigenimages, certain noise sources can be isolated from these eigenimages. For example, for the eigenimages shown in Figure 4.14, the third clearly shows the electronic noise that was present in many of our HET observations. In principle, one could recombine these eigenimages, giving zero weight to those with specific sources of noise, to produce cleaner dark frames.

4.2.4 Scattered Light

Standard scattered light removal algorithms calculate two-dimensional fits to the background. This type of algorithm works well for smooth backgrounds, but fails on irregularly-shaped discontinuities, such as multiplexer crosstalk. With the Pathfinder instrument, we had the advantage of being able to obtain all of our calibration sources independently — and thus we had the ability to create precise scattered-light masks between the orders.

For each calibration type (emission line and flat field), I produced median-averaged images and masked over the orders with linear fits to the spatial flux on either side of the order. For each science frame, I used these masks in combination with the IDL AMOEBA routine to calculate the optimal linear combination of the appropriate masks (depending upon the sources in the given image), as well as a constant factor for any raised background (such as that from the ramp-down effect). AMOEBA is a typical downhill simplex method (Nelder & Mead 1965) for computing the minimum of a multi-dimensional function[3]. Specifically, I minimized:

$$f(A, B, C) =< |A| - b \times B - c \times C - d > \tag{4.24}$$

where A is the starting (masked) image, B is the calibration image, C is the flat field image, and b, c, and d are the modified parameters. In order to avoid cosmic rays, the algorithm was limited to pixels that were less than a standard deviation from the mean pixel value of the starting image.

A demonstration of this algorithm can be seen in Figure 4.15, showing a dark-subtracted frame, the scattered light model for this particular image, and the difference between the two. This algorithm is particularly good at eliminating multiplexer crosstalk from different fibers and scattered light from bright Argon lines in nearby fields. It is *not* particularly good at getting rid of multiplexer crosstalk from the *same* order, or from the same fiber in different orders (since the multiplexer crosstalk is present in both the model image and the science frame).

Since the flux of the target and/or the calibration source can vary (*e.g.,* during exposures that are < 600 s), this algorithm must be run on each frame independently. This is computationally intensive, but partially eased by choosing starting parameters

[3] `http://star.pst.qub.ac.uk/idl/AMOEBA.html`

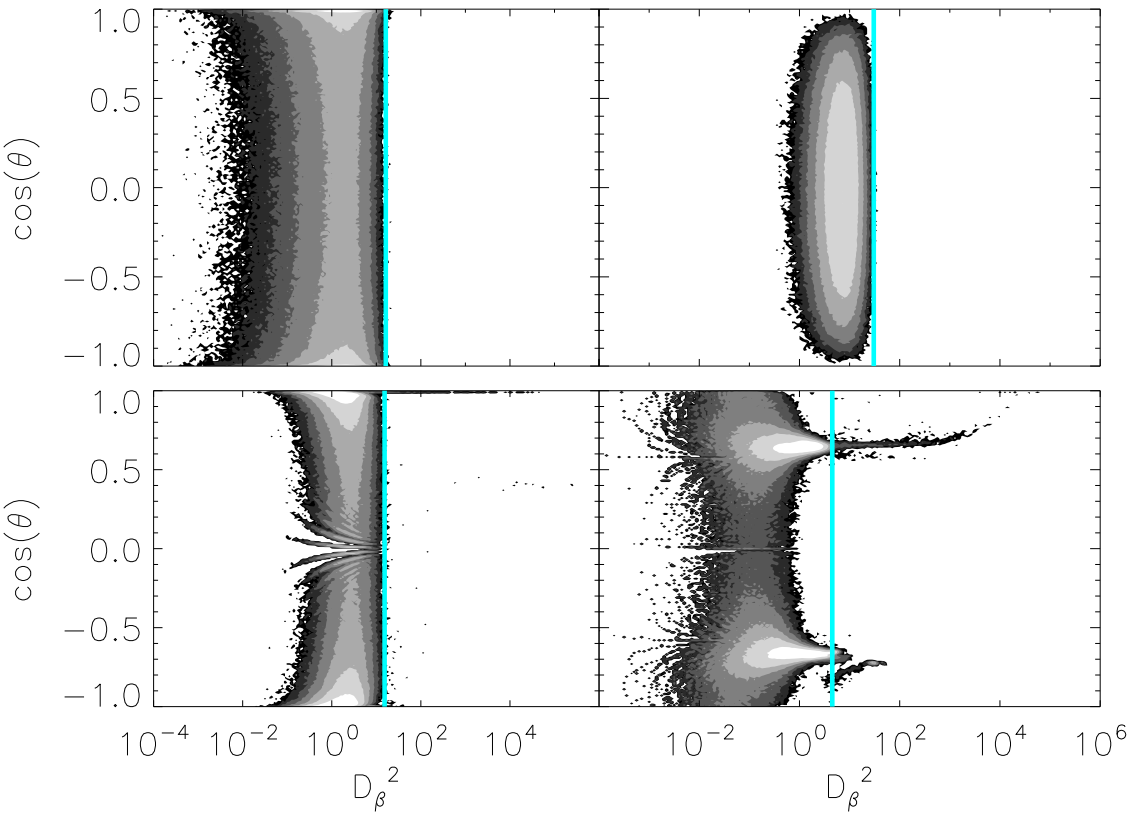

Fig. 4.13 Bad pixel analysis, for a pair of random normal distributions (top-left), a 10-, 30-, and 300-second dark frame from the same set of experiments (top-right), and six 10-second darks from the PSU Pathfinder experiments at the HET (bottom). All pixels that are 7σ from the mean Mahalanobis distance are considered bad pixels. This threshold is marked with a blue vertical line in each of the above plots. The discrete structures in the bottom-left figure near $\cos\theta = 0$ are due to the integer nature of the array. The population of pixels at $\cos\theta = 1$ in the same image are dead pixels (which always have same value). This population of pixels is pulled down in the top-right image because of multiplexer crosstalk (images of different exposure lengths contaminate these bad pixels in a manner that varies with exposure length).

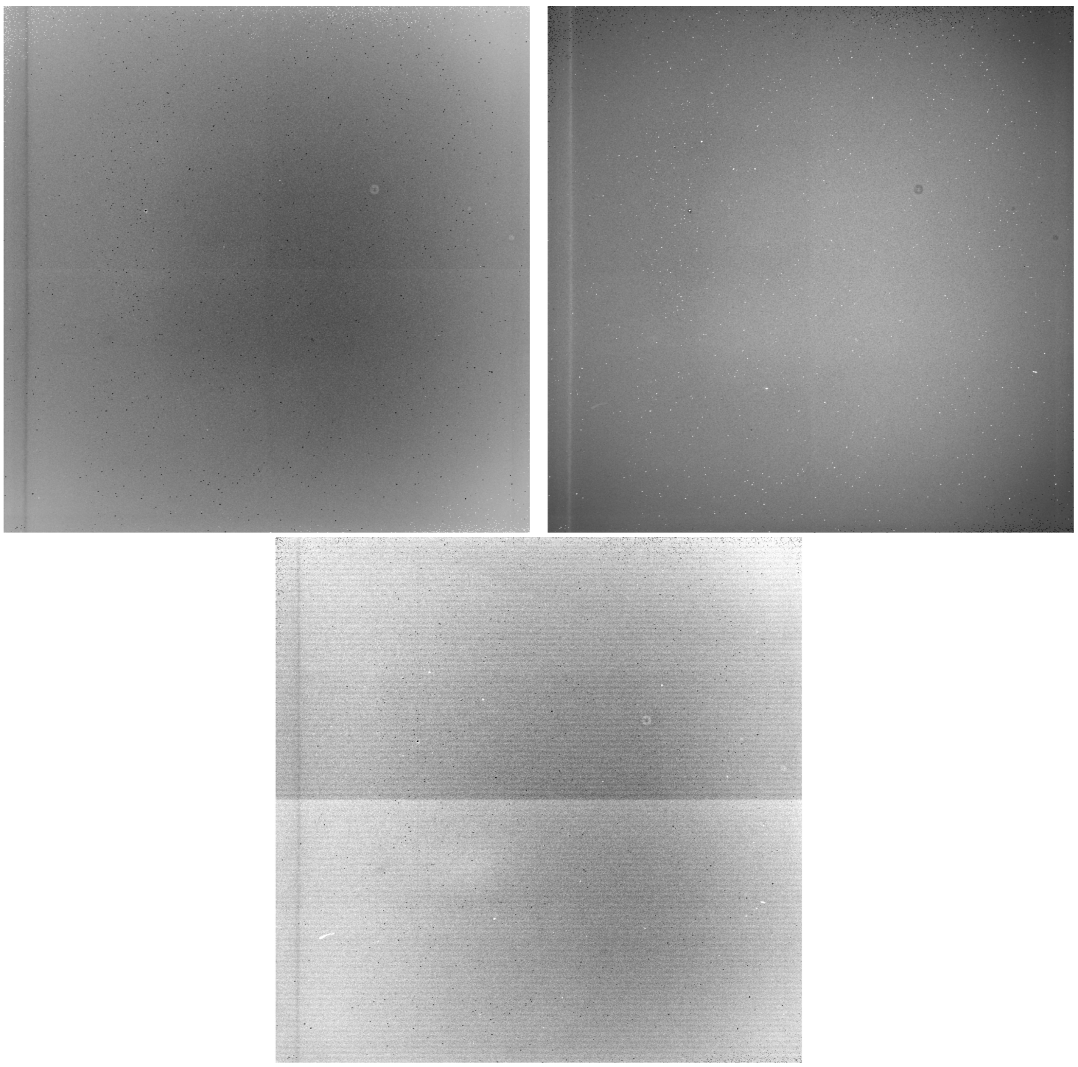

Fig. 4.14 The H-band eigenimages of the PCA analysis of three exposures of different lengths. Each of the three original images is a linear combination of these three images. The second eigenimage resembles the thermal background distribution, and the third eigenimage shows a noise structure seen in all of our HET observations.

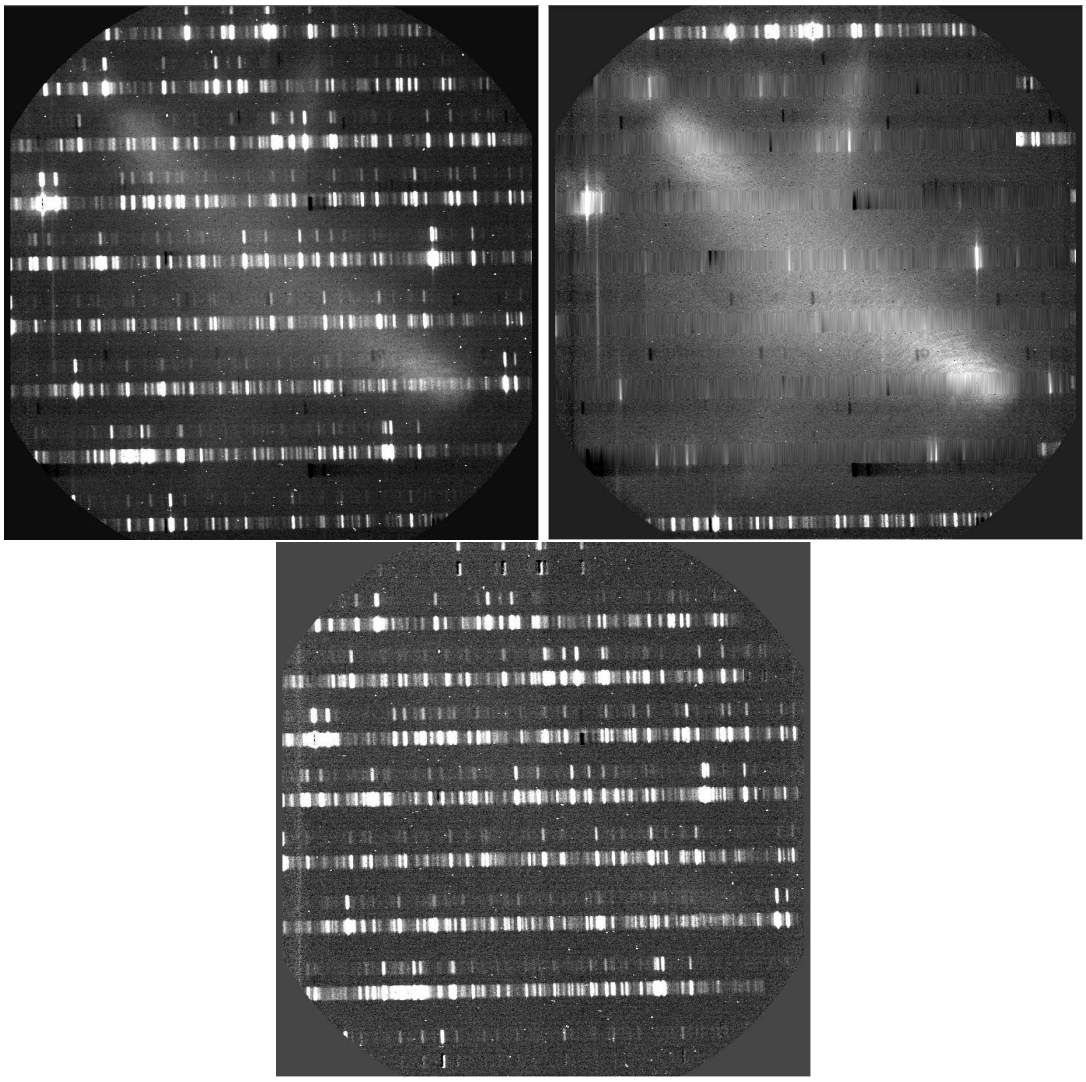

Fig. 4.15 A demonstration of the scattered-light removal algorithm. UNe light is seen here through two fibers (HET science fiber and calibration fiber). In the upper-left, scattered light from off-frame bright Neon lines throw light over the entire array. Upper-right, the scattered light map. Lower left, after the scattered light removal. Notice that this algorithm is particularly good at getting rid of multiplexer crosstalk, but only from other fibers. The emission lines at the top and bottom of the array are considered scattered light because the aperture-identification algorithm has trouble with the orders closest to the edges of the array.

that are close to the expected minimum. For example, good guesses for the above parameters are $b \approx 1.0$, $c \approx 0.1$, and $d \approx 500$.

4.2.5 Dispersion Solution

The wavelength calibration of spectra is one of the most critical steps of data reduction. In an effort to get away from the black box that is IRAF, I wrote an IDL program to calculate the dispersion solution. This routine relies upon an approximate correspondence table relating particular pixels of a given order to specific wavelengths, but is otherwise automated. For each calibration line, the calibration spectrum is searched within 15 pixels for a peak. This peak is fit with a Gaussian function, which is less susceptible to modal noise than a parabolic fit (since Gaussians can fit the background). The dispersion solution is found by fitting these pixel peaks and their corresponding wavelengths with a 4th-order polynomial. An iterative trimmed mean algorithm throws out outliers until all residuals lie within three standard deviations of each other. Figure 4.16 shows an example of this analysis — note the three frequency comb lines that were ignored in the final dispersion solution. Typical residuals to the dispersion solution are 0.005 Å(0.07 pixels, 100 m/s). Figure 4.17 shows fits to the dispersion solution with different order polynomials.

4.2.6 Spectral Extraction

The excellent echelle data reduction package by Piskunov & Valenti (2002) provides an optimal-extraction algorithm, which removes cosmic rays and other detector flaws (Horne 1986). This algorithm calculates the slit function — an average profile of a single order perpendicular to the dispersion direction — to identify outliers (*e.g.,* cosmic rays) and replace them with appropriate values. As would be expected, this algorithm fails when the source does not exhibit a continuous spectrum (*e.g.,* emission lamps, laser frequency combs), and when the defect is consistent across the aperture (*e.g.,* the faint streak seen in the lower-righthand side of Fig. 2.7). Note that, since cosmic rays cannot be easily removed from emission or comb spectra, it is all the more important to carefully assess changes in the apparent position of these spectral features, and to ignore their impact on the dispersion solution when they shift (see § 4.2.5).

4.2.7 Mitigating the Impact of Telluric Features

As discussed in § 1.4.2, telluric spectral features obscure the stellar spectrum and can shift the centers of lines as they change depth and the stellar spectrum is Doppler shifted across the relatively motionless atmospheric spectrum. Regions with telluric lines are not easily avoided in the NIR, especially beyond the Y band. Observations of telluric standard stars (which have featureless continua) and subsequent division of extracted spectrum only works well if the telluric standard star is at the same zenith angle, and is obscured by turbulent atmospheric cells of the same size and composition as those in the direction of the stellar target.

A more sophisticated technique developed by Chad Bender involves fitting the observed stellar spectrum with a model Telluric spectrum, with the abundance of each

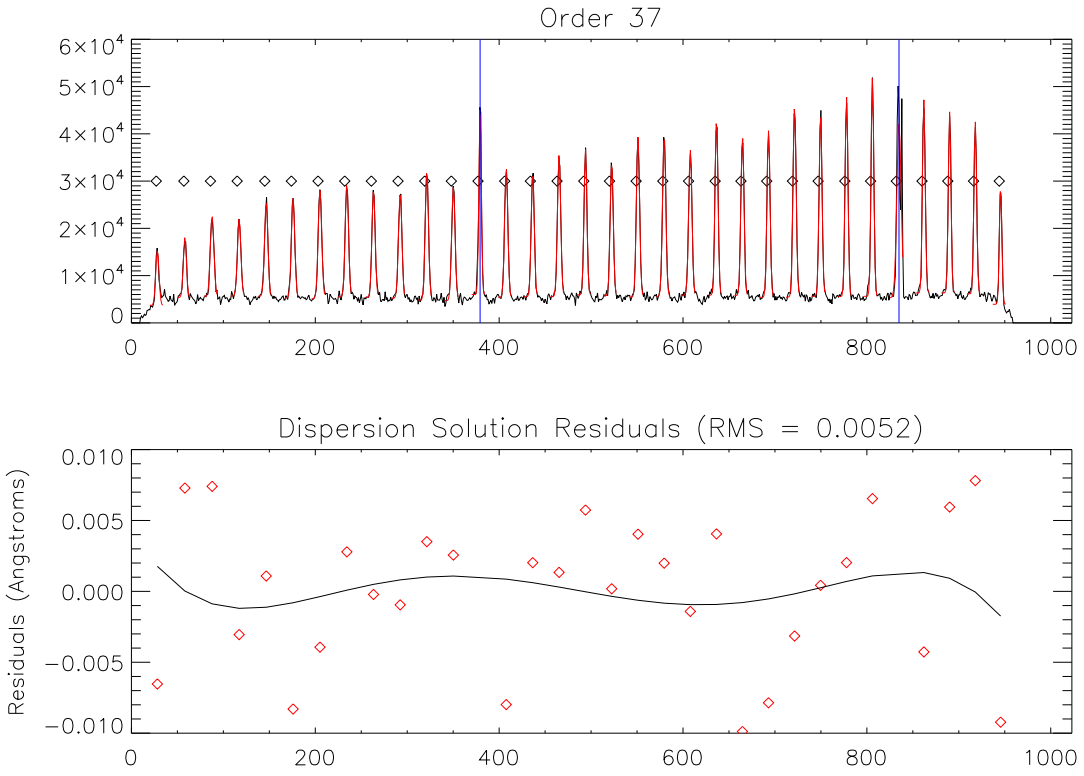

Fig. 4.16 A demonstration of the wavelength calibration algorithm. The peak of each frequency comb line is fit with a Gaussian function (top, in red). The dispersion solution is fit with a fourth-order polynomial. The residuals of the fit to the dispersion solution are shown in the bottom plot. The residuals are fit with a fifth-order polynomial. Any points that fall more than three standard deviations from the mean residual are disregarded in the final fit. Those lines that have been disregarded are highlighted in the top plot by blue lines. Note the cosmic ray that appears in the frequency comb line near pixel 835. Residuals on the order of 0.005 Å are typical of the fit to the dispersion solution of the frequency comb spectra. The dispersion solution algorithm is the same for the Uranium-Neon calibration lines, although the residuals are typically a bit worse.

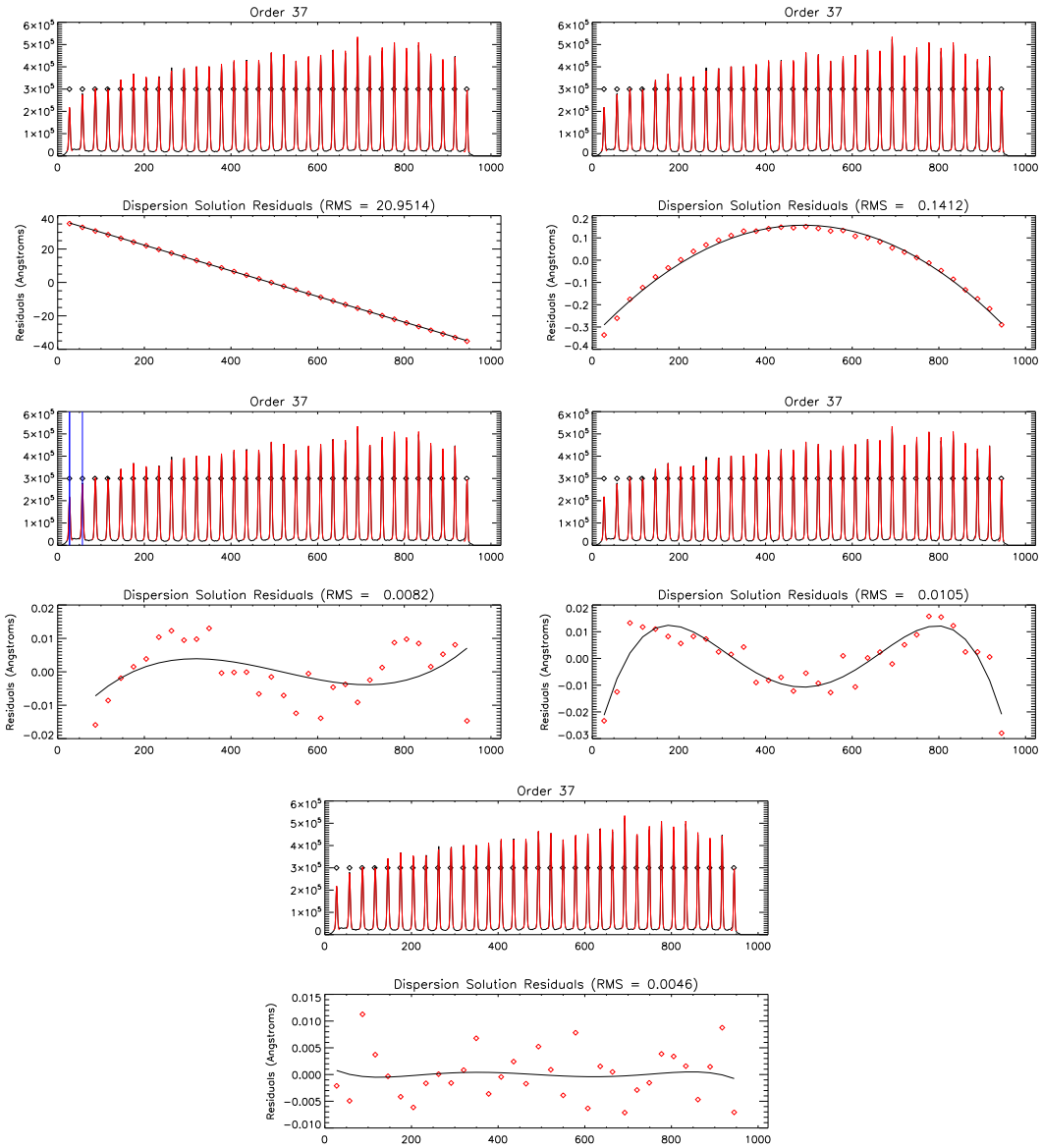

Fig. 4.17 Fits to the dispersion solution residuals of different polynomial orders. From left-to-right, top-to-bottom: 0th order, 1st order, 2nd order, 3rd order, 4th order. As described in Fig. 4.16, the blue vertical lines indicate lines that were not used in the fit to the dispersion solution.

molecule set as a free parameter. Details of this technique can be found in Bender (in preparation). An example of this technique, showing a comparison between the continuum-normalized spectrum, the telluric model of the spectrum, and the telluric-corrected spectrum of η Cas taken in 2010 August can be seen in Figure 4.18. This telluric correction was conducted by Brandon Botzer.

4.2.8 Cross Correlation

The process of measuring sub-pixel shifts involves cross-correlating two vectors at different velocity separations, and then fitting the cross-correlation with a polynomial or gaussian function. The peak (or minimum, depending upon the precise nature of the cross-correlation) of that function, where its derivative is equal to zero, gives a measure of the sub-pixel peak of the velocity correlation.

The analysis described in Chapter 2 involved the cross-correlating subsequent spectra in pixel space, and then converting the measured pixel shift of the thorium-argon and solar spectra to a velocity based on the dispersion of the spectra. This technique is less precise than the techniques described below, but these were largely inaccessible because of the lack of calibration lines, which were not sufficient in number to provide an accurate dispersion solution in our early Pathfinder experiments.

A more precise cross-correlation technique involves interpolating a higher-resolution template spectrum at a variety of different velocities, resampling the template spectrum to match the observed spectrum, and cross-correlating this spectrum with the observed spectra at each of these velocities. This technique requires a model spectrum with a reasonable match of stellar features to the observed stellar target. If such a template is not available, one of the observed spectra can be used, but this makes the interpolation particularly erroneous, since it is exceptionally difficult to conserve flux while interpolating spectra — especially at the precisions required for this work.

If the dispersion solutions are well-defined, and the wavelengths of the stellar spectral lines are well-known (either from a model spectrum or from the solar spectrum), then an even better technique is to cross-correlate the observed spectrum with a precisely-defined binary mask. This mask has a value of unity at each wavelength except where there are stellar lines — there, the mask has values that are proportional to the expected depth of the stellar lines. This mask is shifted in velocity space at a variety of velocities, and the cross-correlation values at each velocity are the product of the mask and the stellar spectrum. Thus, the minimum of the cross-correlation occurs where the mask is most well-aligned to the stellar spectrum. An example diagnostic image from this technique is shown in Figure 4.19. One of the primary advantages of this technique is that it doesn't require any re-interpolation of the observed spectrum. We obtained our best radial velocity measurements using this technique, and implemented it in all three of our HET runs.

4.2.9 Detector Irregularities

The frequency comb is a phenomenal ruler by which to not only measure precision radial velocities, but detector imperfections. For example, HARPS recently used a frequency comb to uncover previously unknown discontinuities in its dispersion solution

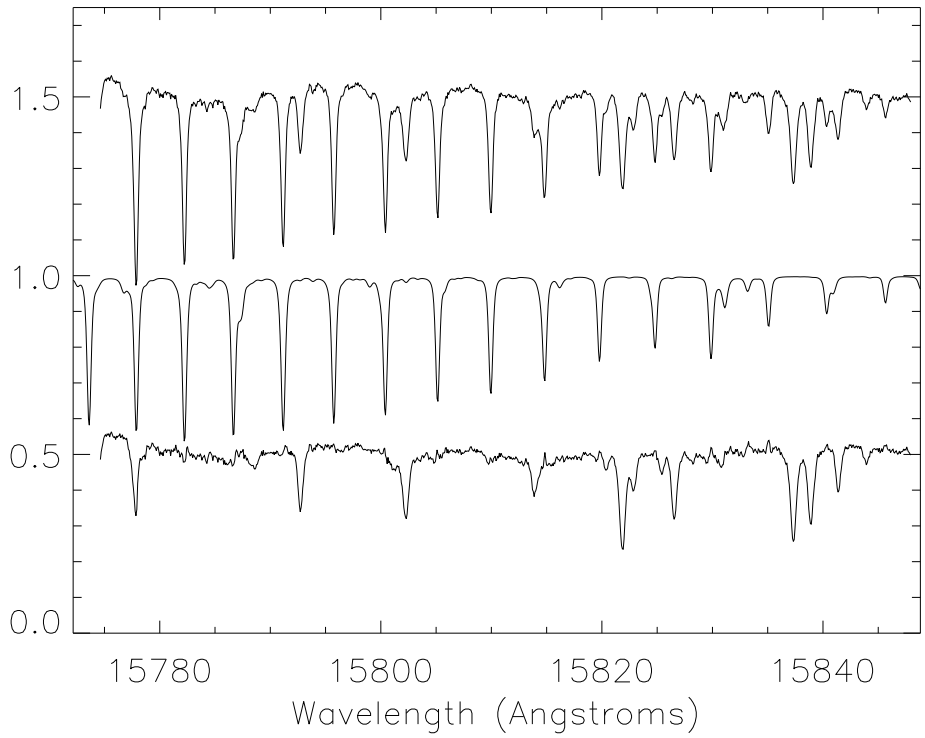

Fig. 4.18 An example of the telluric correction with TERRASpec. The top spectrum is a continuum-normalized spectrum of order 38 of η Cas, which contains many deep CO_2 lines and a few H_2O telluric lines. The middle spectrum is the model of the telluric spectrum, and the bottom is the η Cas spectrum after removing the telluric model.

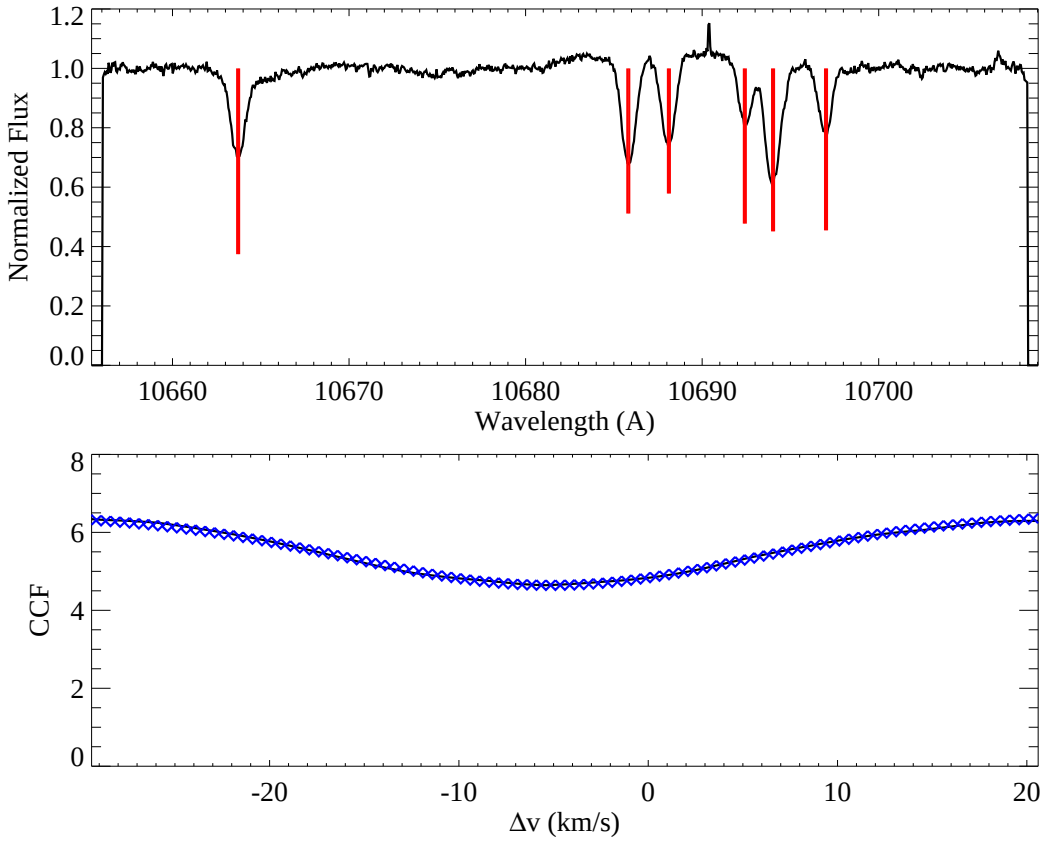

Fig. 4.19 An example of the cross-correlation mask technique. The top plot shows the spectrum of τ Boo, and the mask lines (in red) at the CCF minimum. The CCF in the bottom plot shows the product of the mask and the observed spectrum at different velocity intervals.

from the misalignment of adjacent segments of the CCD (Wilken et al. 2010). We were pleasantly surprised to discover that we were able to uncover a systematic flaw in our detector in a similar manner.

As described in § 4.2.5, the dispersion solution of the calibration source is determined by a fourth-order polynomial fit to the known wavelengths of the calibration lines as a function of their peak pixel location. Residuals of the sort seen in Fig. 4.15 are commonly seen in my diagnostic plots, and for several months I believed the scatter to originate entirely from the modal noise of the comb spectra (see Fig. 4.9). However, we were surprised to find that these residuals are, to a certain extent, systematic. Figure 4.20 shows the mean residual of each comb line in each fiber and each order during the August 2010 run. Each color corresponds to a different fiber, and the residuals are fit with cubic splines of the same colors. The residuals and errors are enlarged by a factor of 3000 for easy visualization. All of the comb wavelengths in every dispersion solution were corrected on an order-by-order basis using these spline fits. After re-calculating the dispersion solutions, the mean residuals fall much closer to the expected values, and are shown in the right plot of Fig. 4.20.

These sub-pixel offsets (which, at their peak, deviate from the expected position by an 1/8 of a pixel) are a mechanical defect. Most likely, these deformations originate in the shape of the array, possibly from undergoing numerous stresses from thermal cycling. It is unlikely the indium bumps are responsible for the observed deformation, since the positions of the indium bumps would likely be random relative to their expected locations, whereas the observed deviations are systematic and gradual.

4.3 Throughput

The throughput of the Pathfinder can be estimated from our Tau Boo observations. We observed 15000 electrons per pixel on our best night. With a dispersion at 1 micron of approximately 19 pixels/Å, and a spatial thickness of approximately 25 pixels, we collected ($15000 \times 19 \times 25 =$) 7125000 e^- in 600 seconds, or 11875 e^-/sec. At Y of 0, we would expect 300 counts/cm^2/s/Å, so for τ Boo (with a Y magnitude of 3.8) shining on the 9.2 m HET mirror that is 60% effective, we would expect to collect ($300 \times 2.54^{-3.8} \times \pi(920/2)^2 =$) 3.5×10^6 photons/second. This yields a throughput of 0.34%. Suvrath has also estimated the throughput from the instrument efficiency. If we estimate 20% for the slit, 95% for the collimator, 20% for the echelle, 70% for the cross disperser, 95% for the camera mirror, 98% for the gold fold mirror, 30% for the filters, and 50% for the IR array, we get approximately the same throughput: 0.37%.

4.4 HET On-Sky Tests

For our on-sky tests at the HET, we selected a mixture of RV standard stars, stars with known planets, and a late M dwarf. The complete list of targets are presented in Table 4.4. Horizontal lines roughly divide the targets chosen for the three trimesters of 2010, with the exception of τ Boötes (which was also observed in the second trimester), and σ Draconis (which was also observed during the third trimester). Stellar spectral

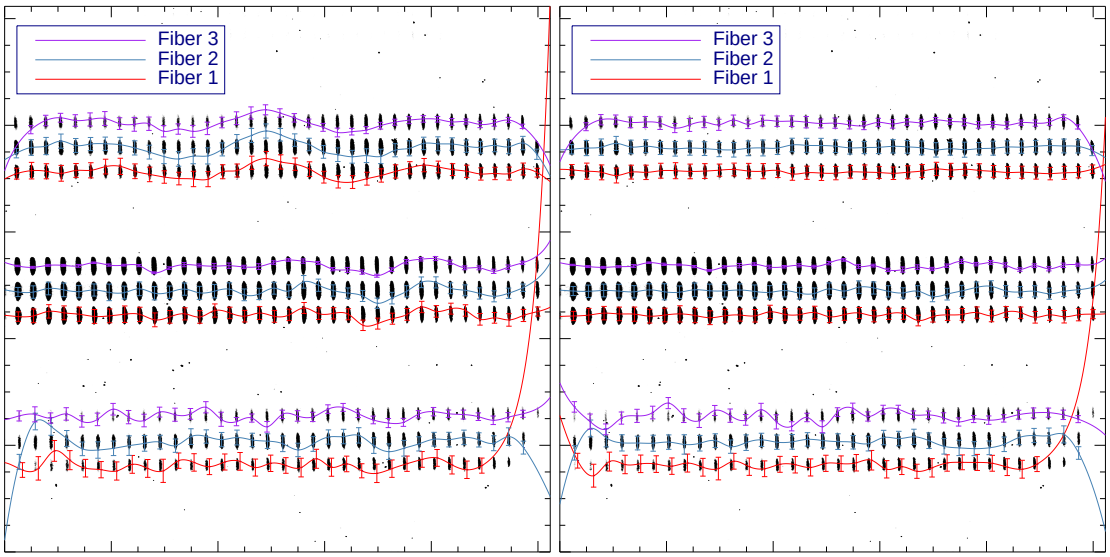

Fig. 4.20 During the August 2010 run, we inadvertently discovered that the detector array elements showed systematic residuals. **Left:** The (approximate) position of each comb line has been overplotted with an associated error bar that shows the relative amplitude of the mean and standard deviations of the comb line from a fifth-order polynomial fit to the dispersion solution (the deviations and errors have been scaled up by a factor of 3000). Each set of fiber comb residuals was fit with a cubic spline (of the same color). Since similar offsets appear in all three fibers, they must either be associated with the comb lines, or they must vary slowly over the array. The deviations in the bottom order (37) show the largest amount of scatter, which we attribute to the achromat. Since similar deviations appear in the top and middle orders (39 and 38, respectively), we suspect that these residuals result from defects on the array. **Right:** After adjusting the wavelength of each comb line by the residual amounts, and re-solving the dispersion solutions, the deviations are greatly reduced.

types and magnitudes are taken from Simbad database[4]. While we initially targeted M dwarfs, the S/N of these observations severely limited the precision we were able to obtain, and in the last two trimesters we limited our targets to the brightest RV standards and planet-bearing stars we could observe. The extracted stellar spectra and radial velocity plots for each of these targets are presented later in this chapter.

HET Target Spectral Characteristics								
Star	Spectral	Magnitudes						
	Type	B	V	R	I	J	H	K
GJ 273	M3.5	11.42	9.89	9	8.2	5.71	5.52	4.857
τ Boo	F6IV C	4.98	4.5	4.2	4	3.62	3.55	3.51
GJ 406	M6.5Ve	15.54	13.54	12.1		7.09	6.482	6.084
GJ 412 A	M2V	10.22	8.68	7.9	7.1	5.54	5	4.77
GJ 436	M2.5	12.2	10.68	9.58	8.24	6.9	6.319	6.073
Gl 699	M4Ve	11.28	9.54	8.7	7.9	5.24	4.83	4.52
HD 106714	G8III	5.876	4.938			3.380	2.911	2.697
σ Dra	K0V	5.47	4.70	4.2	3.8	3.42	3.04	2.90
η Cas	G3V	4.03	3.45	3.1	2.8	2.109	2.086	1.988
υ And	F9V	4.63	4.09	3.8	3.5	3.17	2.96	2.86
HD 168723	K0III	4.20	3.26			1.490	1.037	1.050

Table 4.1 The stellar targets for our 2010 HET observations. Horizontal lines divide the targets generally into the three HET runs, although τ Boo was observed in the first two runs, and σ Dra was observed in the last two runs.

4.4.1 PSU10-1-019: 2010 March 27 — April 2

During this run, we focused on a handful of faint M dwarfs and τ Boo, using uranium neon as our calibration source in the Y band. All science exposures were set to be 600 seconds long, to maintain a consistent cadence throughout our observing run, and avoid the ramp-down effect described in § 2.1.6. An example dark-subtracted science exposure using this configuration is shown in Figure 4.21.

The Pathfinder dewar was significantly damaged during transit, and we had to open the dewar while on-site in order to rectify the compromised vacuum seal and the liquid nitrogen vessel, which was leaning against the radiation shield, causing severe coolant consumption due to loss of thermal insulation. Some of this damage can be seen in the photos in Figure 4.22. Rectifying these mechanical problems consumed our preparation time at the telescope, and we had to compromise on some aspects of the setup at the telescope, most notably the fiber agitator, which we did not have

[4] `http://simbad.u-strasbg.fr/simbad/index.html`

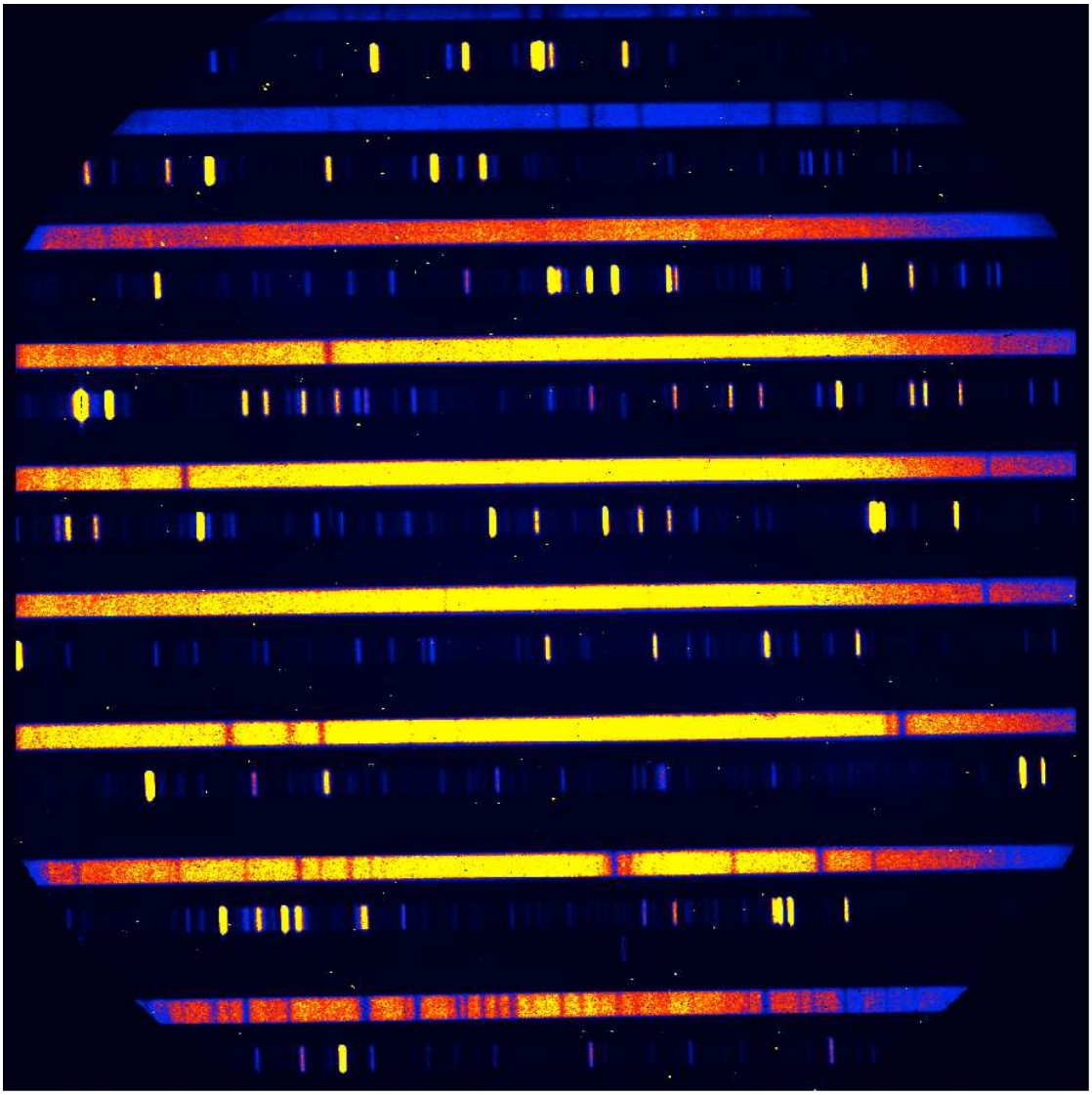

Fig. 4.21 An example science exposure using uranium neon as a calibration source. This exposure of σ Dra is from PSU10-2-017, but had approximately the same configuration as our observations during PSU10-1-019. Many fainter uranium calibration lines are not visible at this scale.

time to implement. The lack of this agitator likely led to increased modal noise in our observations.

4.4.2 PSU10-2-017: 2010 May 2 — 11

During our second run at the HET, we chose to limit our observations to three stars — τ Boo, σ Dra, and HD 106714, all of which are bright in the Y (I $\approx$ 4) and have well-established radial velocities. As in our first run, we used uranium-neon as a calibration source, and set our exposures to be 600 seconds long to maintain a consistent cadence throughout our observing run. We used our preparation time during this run to set up the fiber agitator.

4.4.3 PSU10-3-012: 2010 August 2 — 12

Our third run was by far our riskiest, since August is the rainy season in west Texas, the control room was being constructed, and we were coupling two instruments that had never been used together. We again limited our targets primarily to three stars — η Cas, υ And, and HD 168723, all of which are bright in H (magnitudes of 2, 3, and 1, respectively), and have well-known radial velocity patterns. During this run, we teamed up with Dr. Scott Diddams, Dr. Steve Osterman, and Gabe Ycas from CU/NIST to use an H-band frequency comb as our calibration source (see § 3.5.2). In order to access the H band, we had to perform a filter swap on-site at the HET, which does not have a clean room. Despite this increased risk, we successfully changed the filters, and linked the frequency comb to our spectrograph.

Based on my spectrograph model, we carefully selected two echelle and cross disperser angles to optimize the observed spectral region. The selected region is shown in Figure 4.23. Each of the main atmospheric telluric spectra are overplotted in these panels, highlighting the relative lack of telluric features in order 37, and the strong CO_2 bands in order 38. ThAn example science exposure is shown in Figure 4.24. Note the even spacing and amplitude of the frequency comb calibration lines in comparison to the uranium-neon calibration lines shown in Figure 4.21.

4.5 Extracted Spectra and Radial Velocity Measurements

The extracted spectra presented in the following subsections are flux-weighted averages of the observed stellar spectra, and thus are of higher quality than would be expected from any individual observation of the star.

4.5.1 GJ 273

GJ 273 is a mid-M dwarf (M3.5) with a very low vsin i ($\approx$ 1 km/s) (Reiners 2007), and for this reason is useful for vsin i measurements of other stars. The extracted spectrum of GJ 273 can be seen in Figure 4.25.

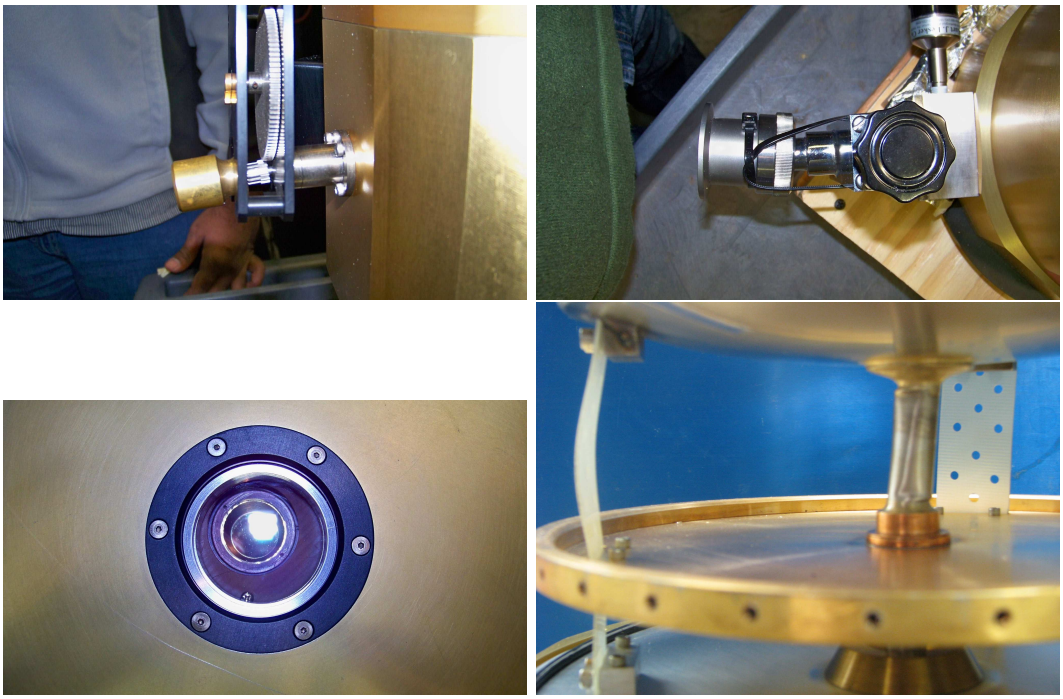

Fig. 4.22 Some of the damage sustained to the dewar during shipment to the HET. **Top-left:** A bent filter changer (not used by us). **Top-right:** The vacuum valve. The seal to this was substantially damaged and had to be machined to fit flush against the dewar. **Bottom-left:** The filter holder and PK-50, as seen through the CaF window. The two were significantly mis-aligned because the liquid nitrogen vessel inside the dewar was no longer centered. **Bottom-right:** The support system for the liquid nitrogen vessel, showing the bend and twist responsible for the mis-alignment mentioned above.

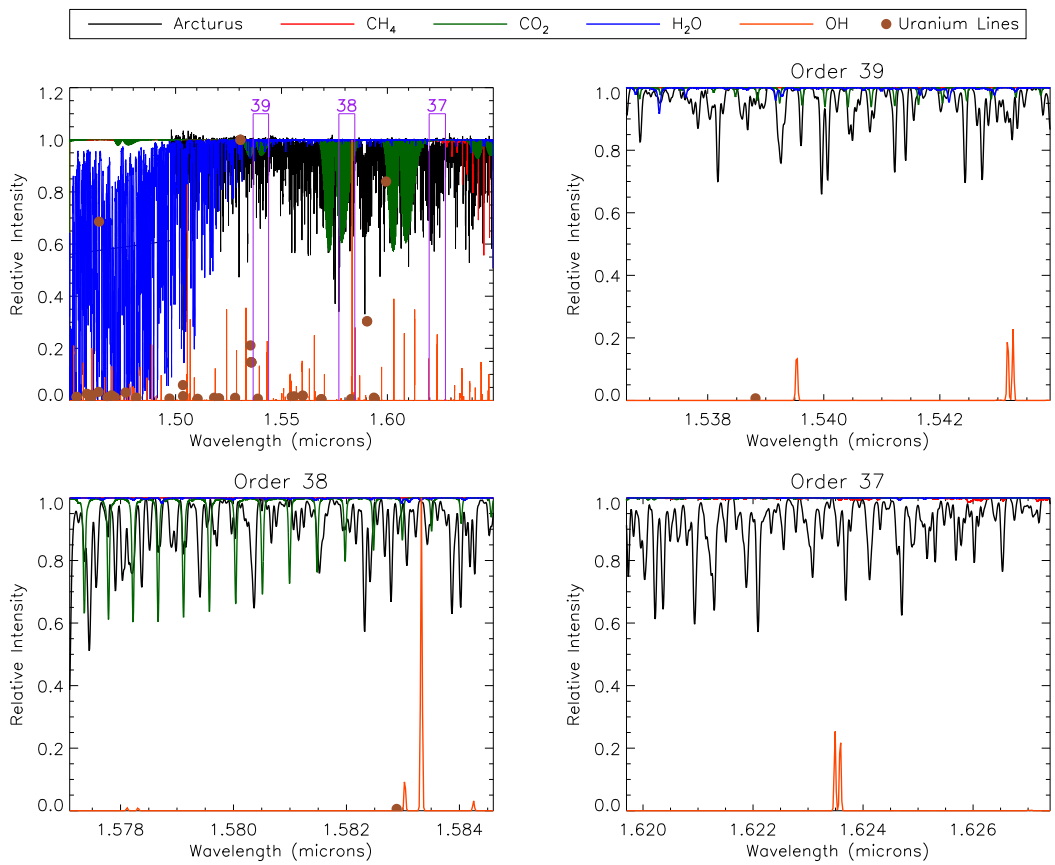

Fig. 4.23 The model of the selected spectral region for our H-band observations. The top-left panel shows most of the H-band, including the many overlapping contributions to the spectrum — the Arcturus spectrum in black, the telluric water lines in blue, the CO_2 bands in green, the methane bands in red, and the OH sky lines in orange. Also plotted are the approximate locations of the brightest uranium lines in these regions. The purple rectangles indicate the expected order ranges of each of the three orders visible on the array in the H band. These regions are magnified in the other three panels.

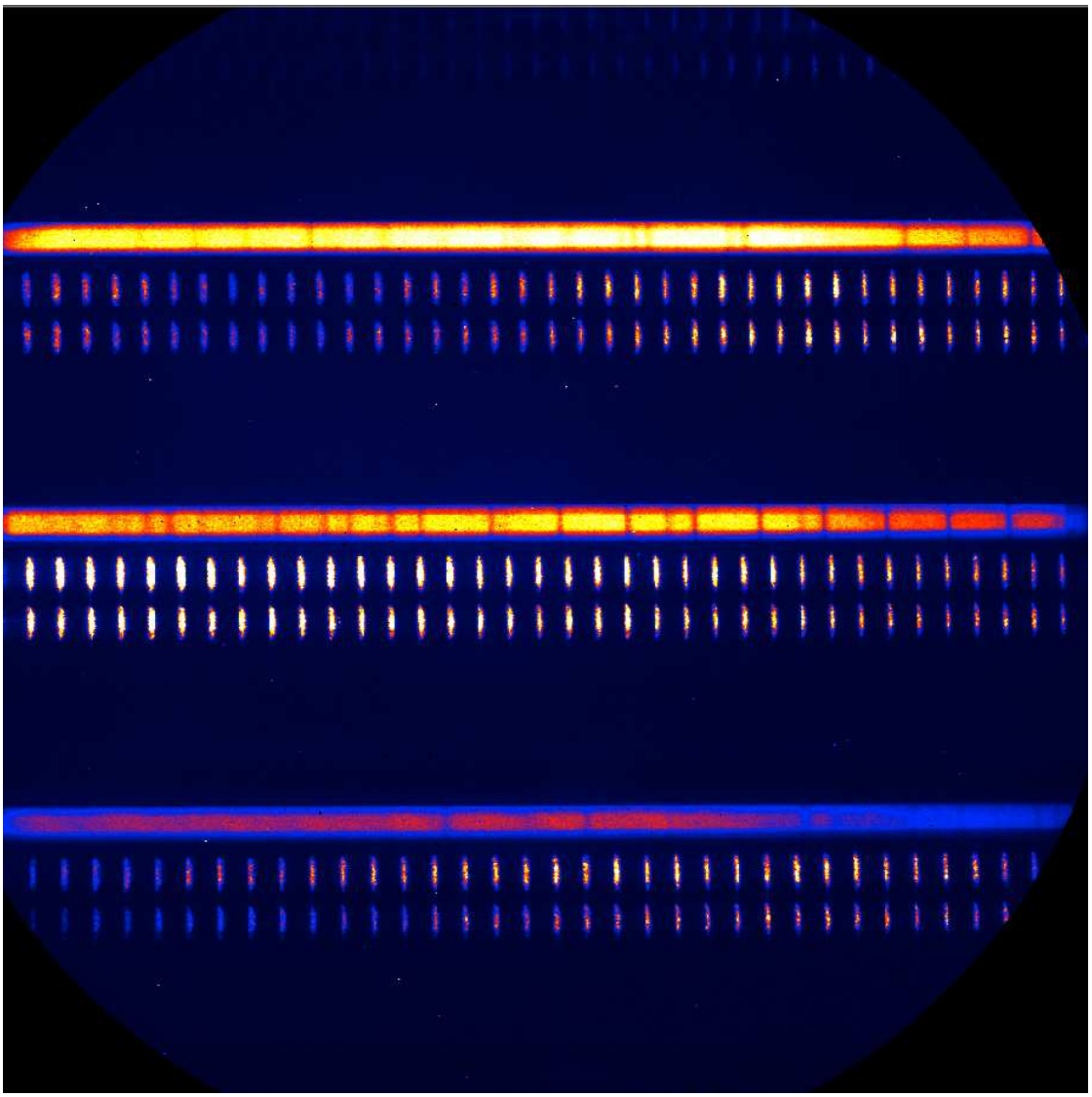

Fig. 4.24 An example science exposure using the CU/NIST laser frequency comb as a calibration source. This exposure of η Cas shows many deep CO_2 telluric lines in the middle order. In comparison to the uranium neon lines shown in Figure 4.21, the laser frequency comb calibration lines are evenly spaced and approximately the same amplitude over the entire image.

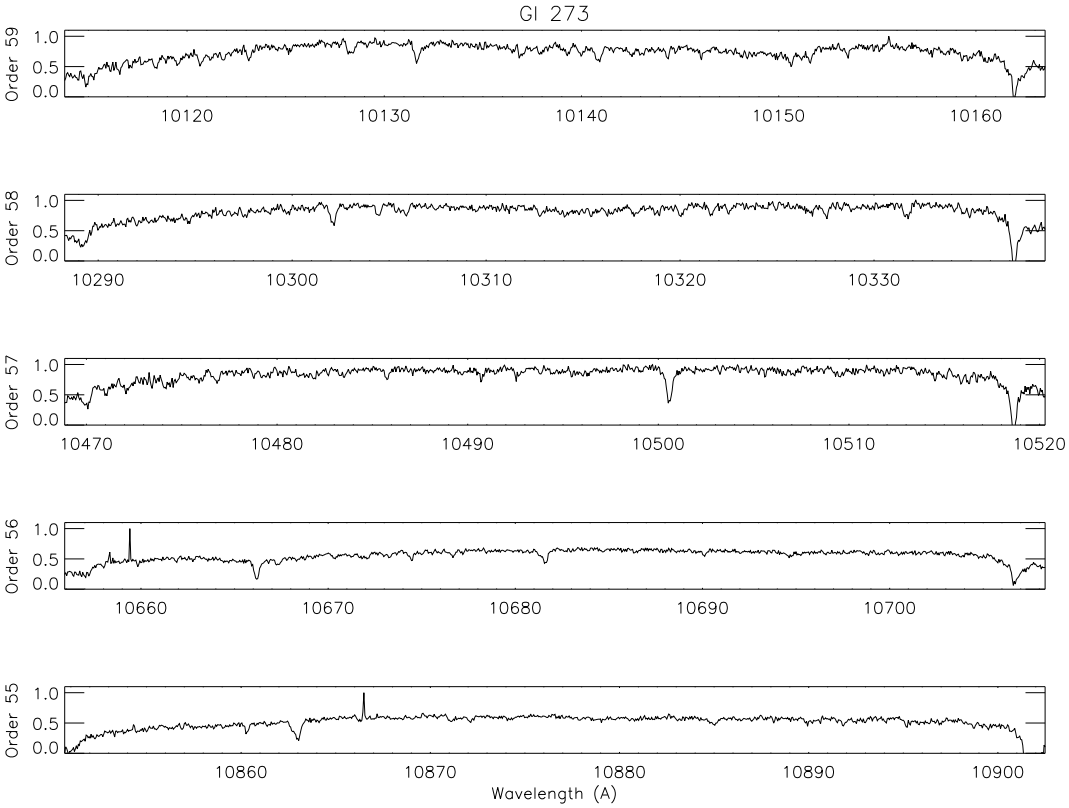

Fig. 4.25 The extracted spectrum of GJ 273. This M3.5V star has a very low vsin i, and thus very sharp spectral features.

4.5.2 τ Boo

τ Boo is a very bright, hot-jupiter hosting star with a large rotational velocity of 15.0 ± 0.5 km/s, which broadens the stellar lines and increases our precision limitation. τ Boo b has a mass of 4.1 $M_{♃}$ and orbits this star at 0.048 AU, inducing a velocity semi-amplitude of 461 ± 7.6 m/s[5]. The stellar jitter of this star is ≈ 15 m/s (Butler et al. 2006). The extracted spectrum fo τ Boo can be seen in Figure 4.26, and our measurements of the RV curves, using orders 56—59, are presented in Figure 4.27.

Ryan Terrian has measured the Q factors for these orders, and found that, on our best night of observations, the RV precision (including thermal background and read noise) was 14.8 m/s. This is roughly consistent with the RV curves that we measured (especially considering that the S/N was sometimes only half that on our best night). It is also not too surprising that our first run has a larger RMS, since we were not agitating the fiber during this run, and the modal noise should be slightly worse.

4.5.3 GJ 406

GJ 406 is the closest late M dwarf (M6.5Ve) to the Sun, but was still our faintest target. Note that this is the same star that was presented in Pavlenko et al. (2006). All but two of our observations of this star were taken without simultaneous calibrations, since the very small amount of scattered light from our uranium-neon lamp drowned out the stellar spectrum. Such a problem could be fixed with a variable neutral density filter. Figure 4.28 shows a dark-subtracted average of our GJ 406 science frames. As expected, the NIR spectrum of this late M dwarf is rich with spectral features. The extracted spectrum of GJ 406 can be seen in Figure 4.29. The stellar information content of this star is clearly superior to the Solar-like stars in our sample, but the S/N is much, much lower.

4.5.4 GJ 412 A

GJ 412 A is a M2V star 4.8 pc away, with a measured velocity RMS of 6.9 m/s (Endl et al. 2006). The extracted spectrum of GJ 412 A is presented in Figure 4.30.

4.5.5 GJ 436

GJ 436 hosts a Neptune-sized planet with a 2.64 day period and a velocity amplitude of 18.3 m/s. Discovered by Butler et al. (2004), they were able to achieve an RMS precision of 5.26 m/s with an iodine cell. The extracted spectrum of GJ 436 can be seen in Figure 4.31.

4.5.6 Gl 699

Although the existence of a planet around Barnard's Star has been proposed in the past, this high-proper motion mid-M dwarf is a decent radial velocity standard, as it is inactive and has a very low intrinsic velocity RMS of 3.4 m/s (Endl et al. 2006). The

[5] `http://exoplanets.org/oneup/?tau_Boo_b`

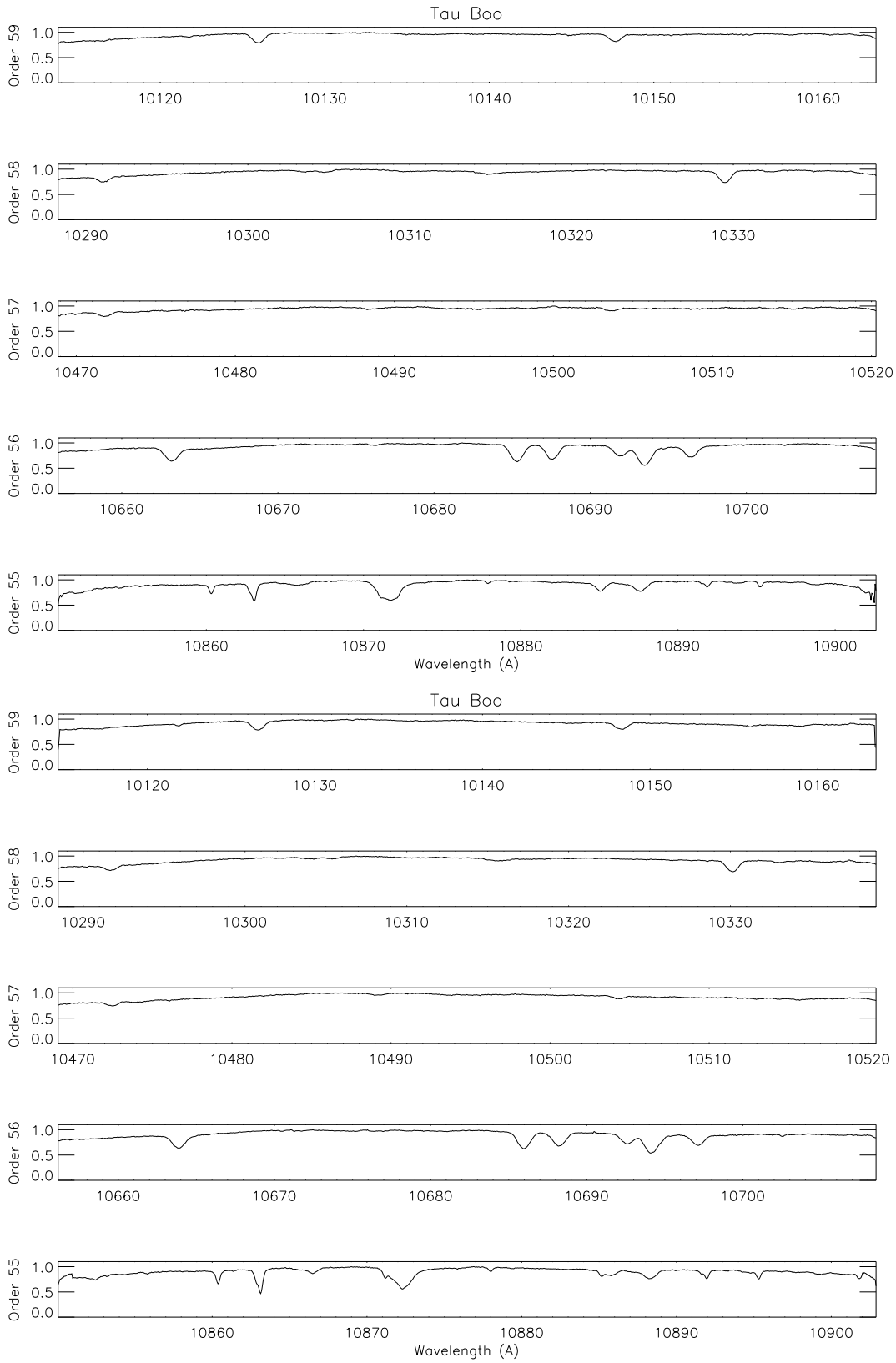

Fig. 4.26 The extracted spectrum of τ Boo, as seen during our first two on-sky observations at the HET.

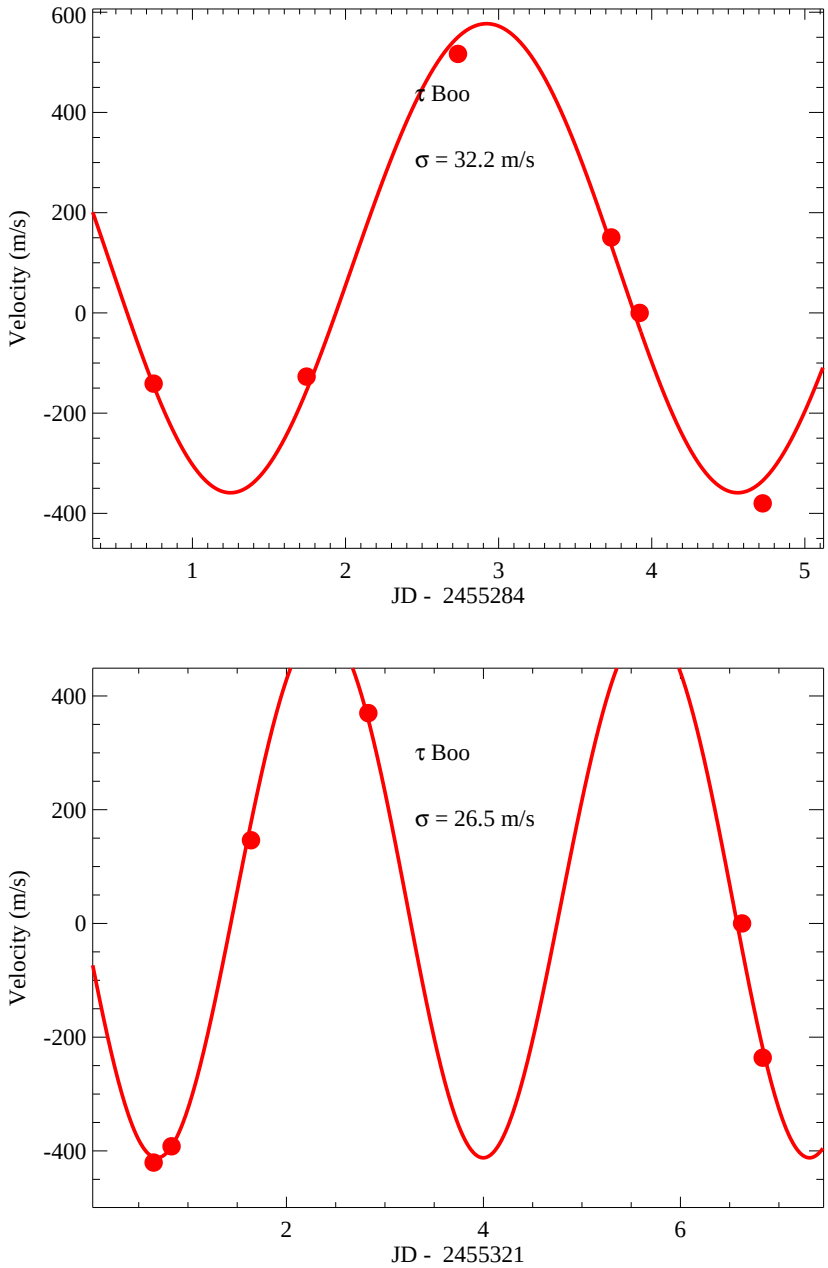

Fig. 4.27 The RV curve of τ Boötes, as measured by the Pathfinder spectrograph during the March (top) and May (bottom) 2010 runs at the HET. Error bars are 14.8 m/s, smaller than the points, and representative of the photon-limited noise floor of our brightest observation.

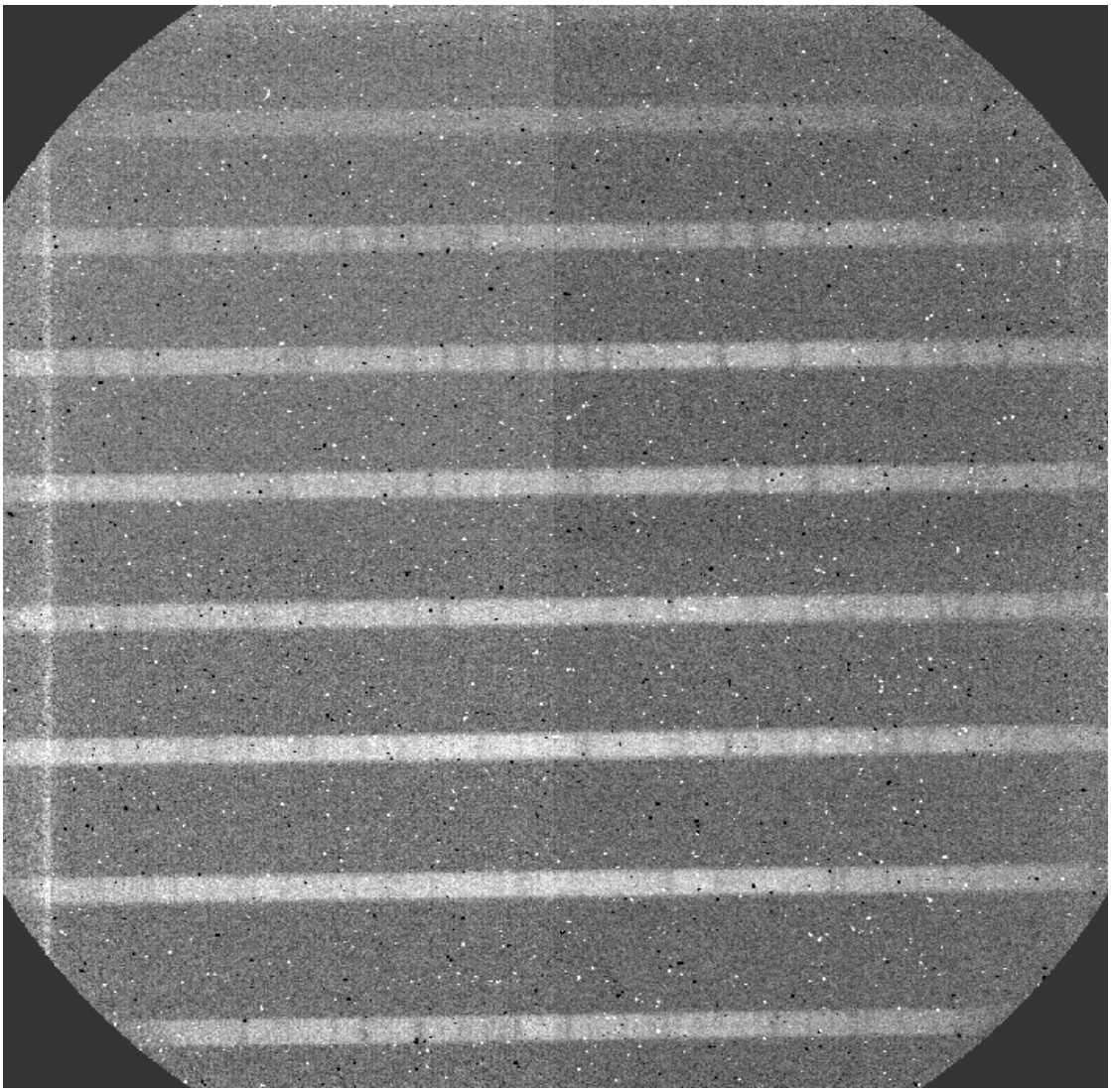

Fig. 4.28 The average dark-subtracted science exposure of GJ 406, our faintest target and latest M dwarf. We chose not to illuminate the detector with simultaneous calibration light, since the small amount of scattered light from the uranium-neon lamp is brighter than the stellar spectrum. This problem could be addressed with a variable neutral density filter in future implementations.

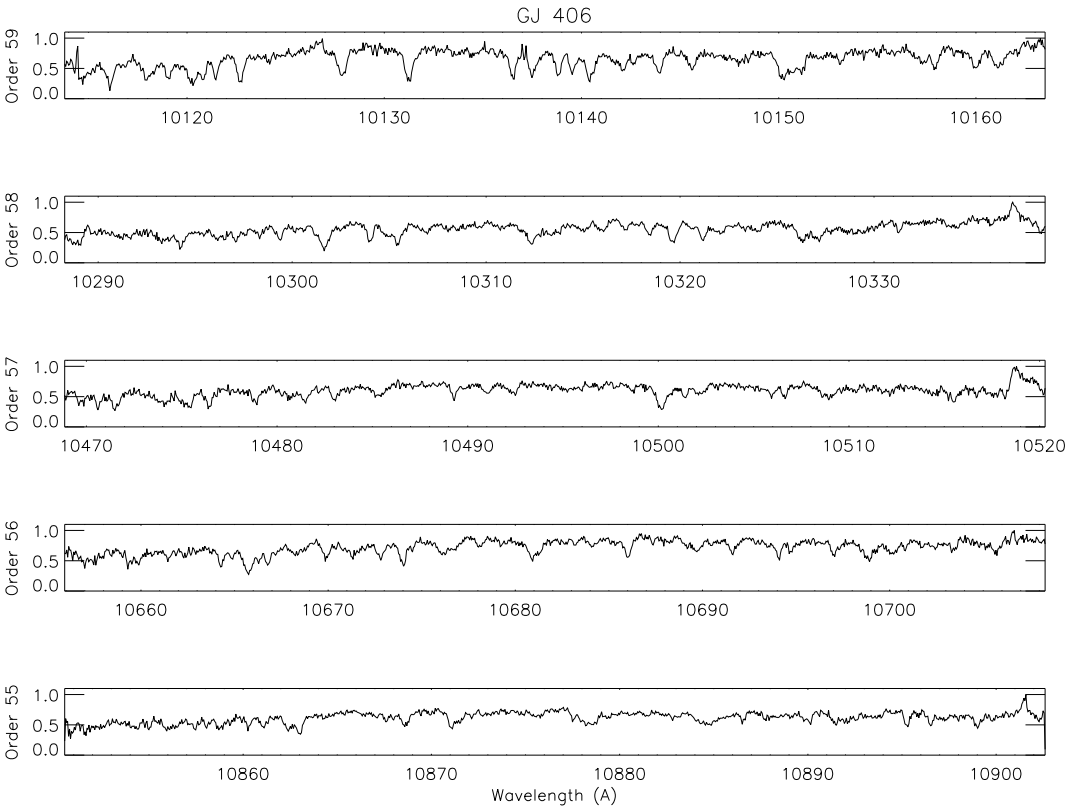

Fig. 4.29 The extracted spectrum of GJ 406. The latest M dwarf (M6.5Ve) in our sample, this stellar spectrum shows the extreme density of spectral content expected in late M dwarfs. This target was so faint that we chose not to contaminate the stellar spectrum with the small amount of scattered light from our uranium-neon calibration lamp.

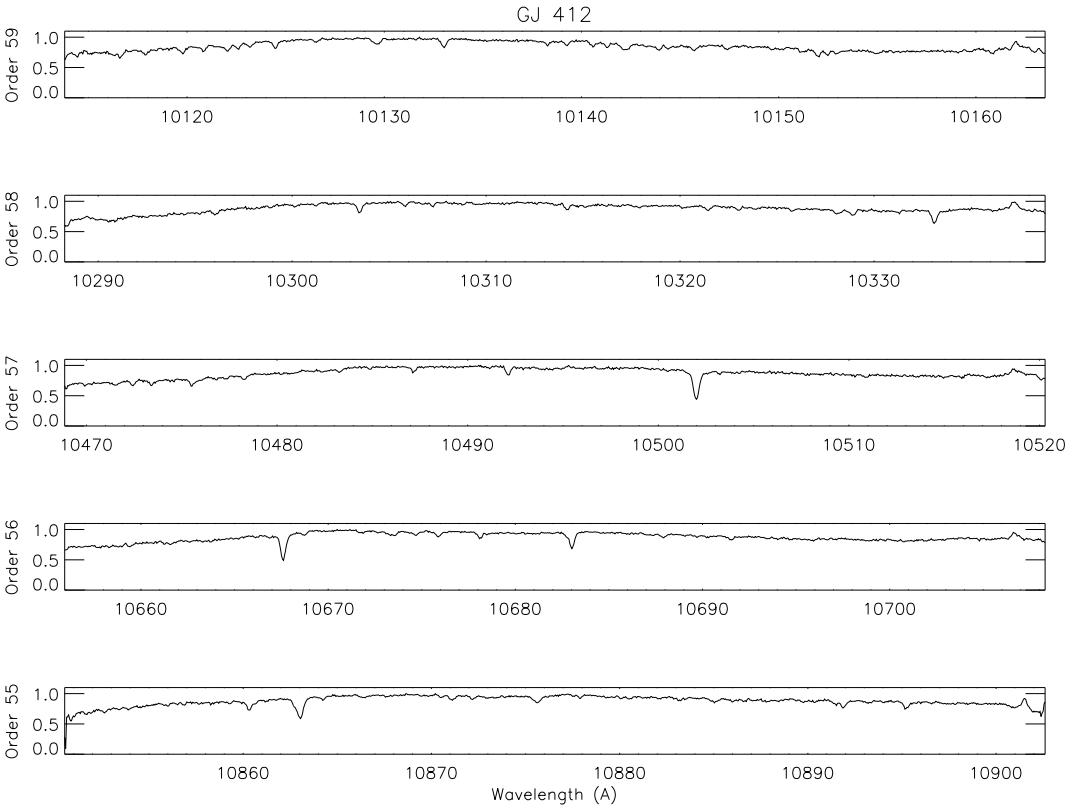

Fig. 4.30 The extracted spectrum of GJ 412 A.

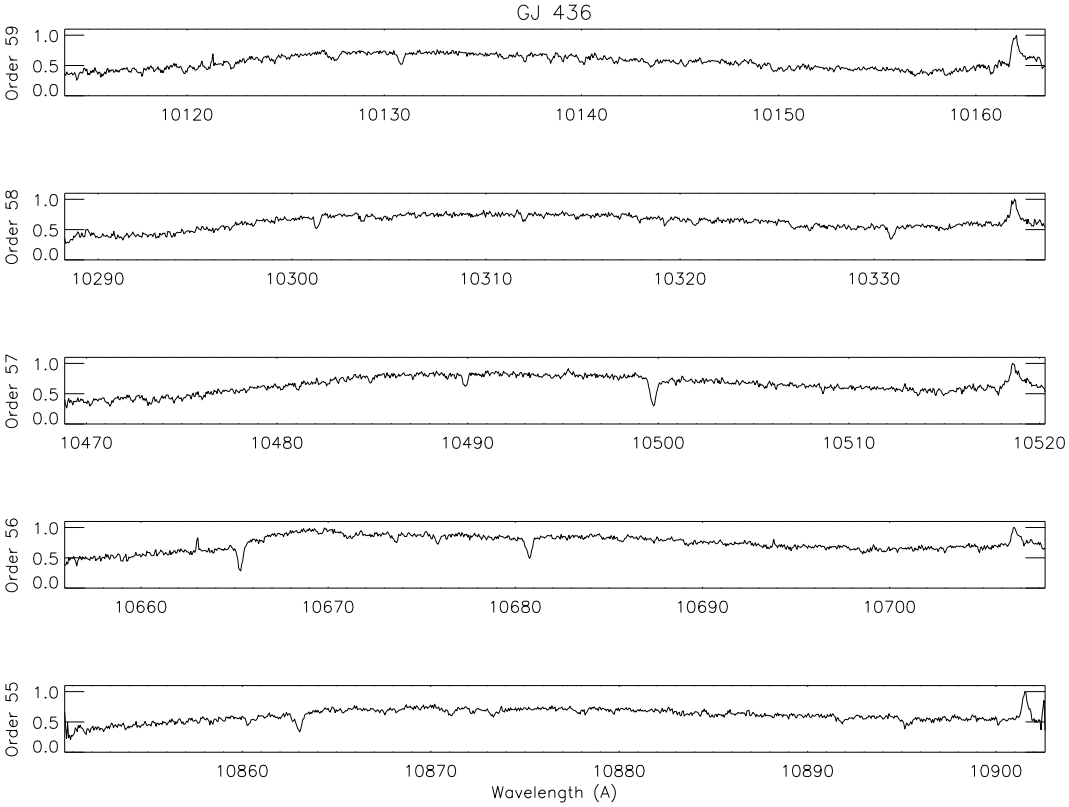

Fig. 4.31 The extracted spectrum of GJ 436.

extracted spectrum of Barnard's Star can be seen in Figure 4.32. Recovering the radial velocities with the mask cross-correlation technique is particularly tricky on this star, since there are no good M dwarf atmospheric models to help us identify the wavelengths of the observed stellar lines. This is a problem that will also impact HZPF, and we may be forced to utilize something besides the mask cross-correlation technique on these stars.

4.5.7 HD 106714

HD 106714 is a stable G, with a known long-term precision of 11.1 m/s (Hekker et al. 2006). The extracted spectrum of HD 106714 can be seen in Figure 4.33.

4.5.8 σ Draconis

σ Draconis is one of the most precise RV targets in the night sky, and shows amplitude variations of less than 5 m/s (McMillan et al. 1994). We were unable to track the velocities of this star to that level of precision, most likely because of uncertainties in our dispersion solution, but possibly because of the way σ Dra under-fills the pupil of the HET. As the telescope tracks this star, the SRF is constantly changing, and these changes could induce apparent velocity shifts of the sort we see in our RV measurements. The extracted spectrum of σ Dra can be seen in Figure 4.35.

4.5.9 η Cas

η Cas is a known stable star with a measured RMS on the order of 6 m/s (Mahadevan et al. 2008b,a). The extracted spectrum of η Cas can be seen in Figure 4.37.

4.5.10 υ And

υ And hosts three known exoplanets, including a hot Jupiter with a 4.6 day orbit, just within our observing timeframe while at the HET. Since the other two planets reside at much larger semi-major axes (0.83 and 2.52 AU), their impact on the observed RV curve over a week is ignorable. The extracted spectrum of υ Andromeda can be seen in Figure 4.39.

4.5.11 HD 168723

Hekker et al. (2006) measured a standard deviation in 18 radial velocity measurements of HD 168723 over 1876 days, making it one of their 34 stable giant stars. The stellar spectrum of HD 168723 is not well-matched by the solar spectrum, the latter of which has many fewer lines in the H band. HD 168723 has an stellar RV of 8.90 ± 0.07 km/s (Barbier-Brossat & Figon 2000). The velocities of this star are dominated by stellar oscillations with a 2.4-hour period and ≈ 10 m/s amplitude (Barban et al. 2004). It also has a very low vsini of 0.4 km/s, making its spectral lines very sharp, and thus giving it a very high Q factor and low intrinsic velocity uncertainty. Estimates of the Q factor in our H-band observations by Ryan Terrian indicate an attainable velocity precision of

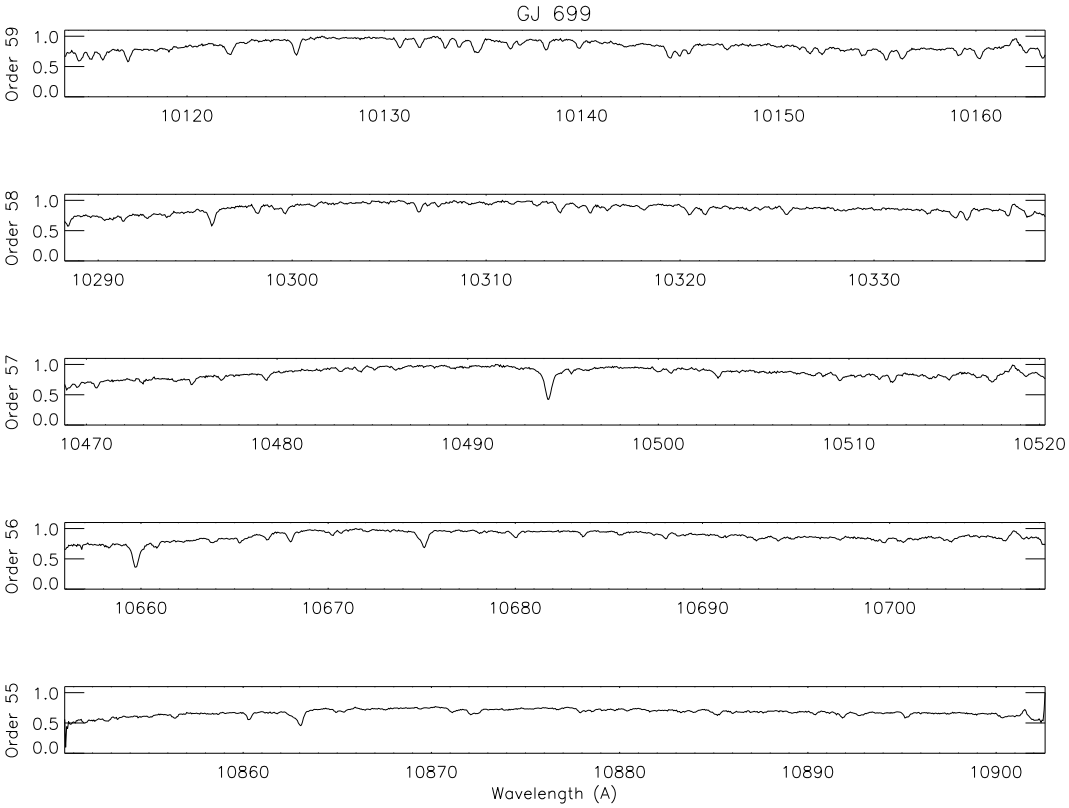

Fig. 4.32 The extracted spectrum of GJ 699 (Barnard's Star).

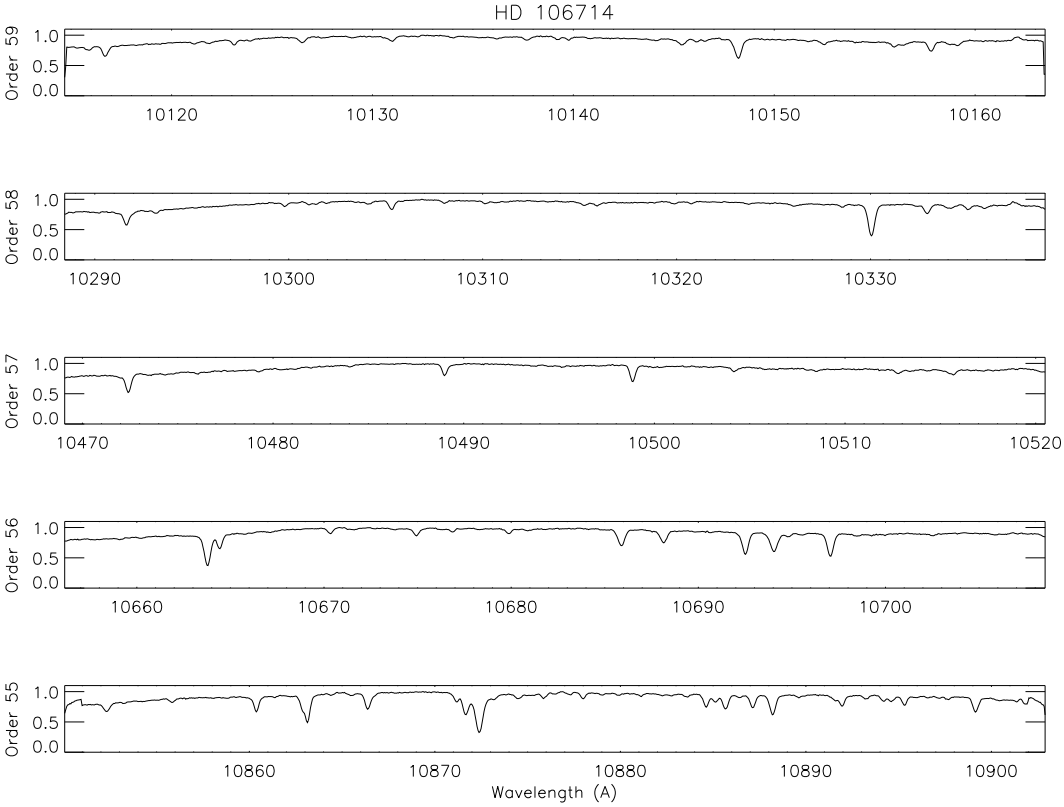

Fig. 4.33 The extracted spectrum of HD 106714.

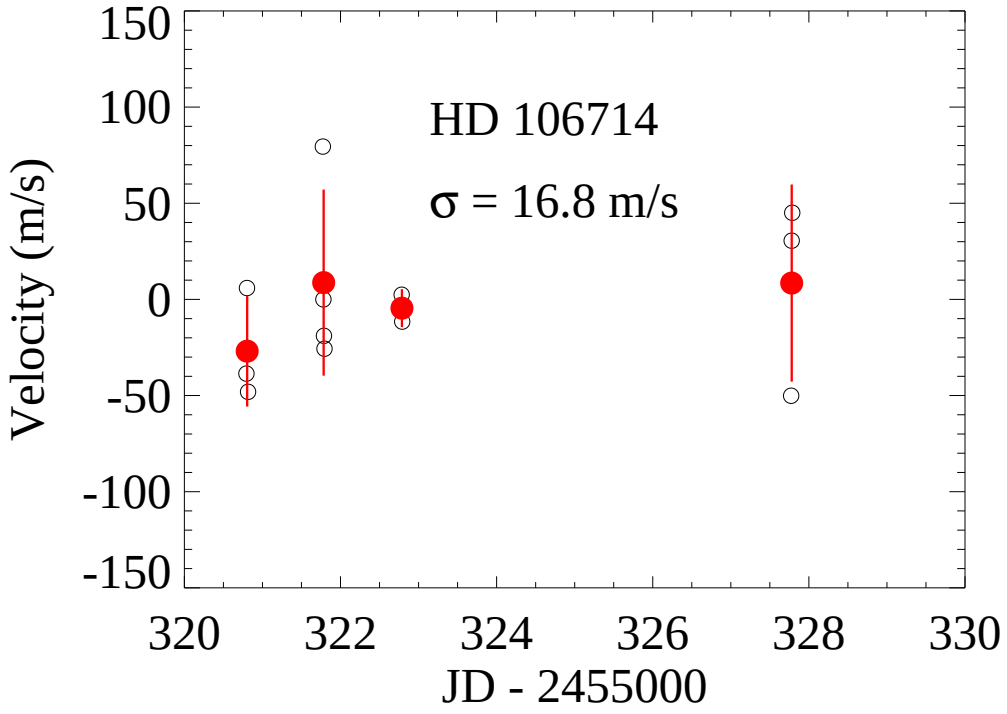

Fig. 4.34 The RV curve of HD106714, as measured by the Pathfinder spectrograph during our May 2010 run at the HET.

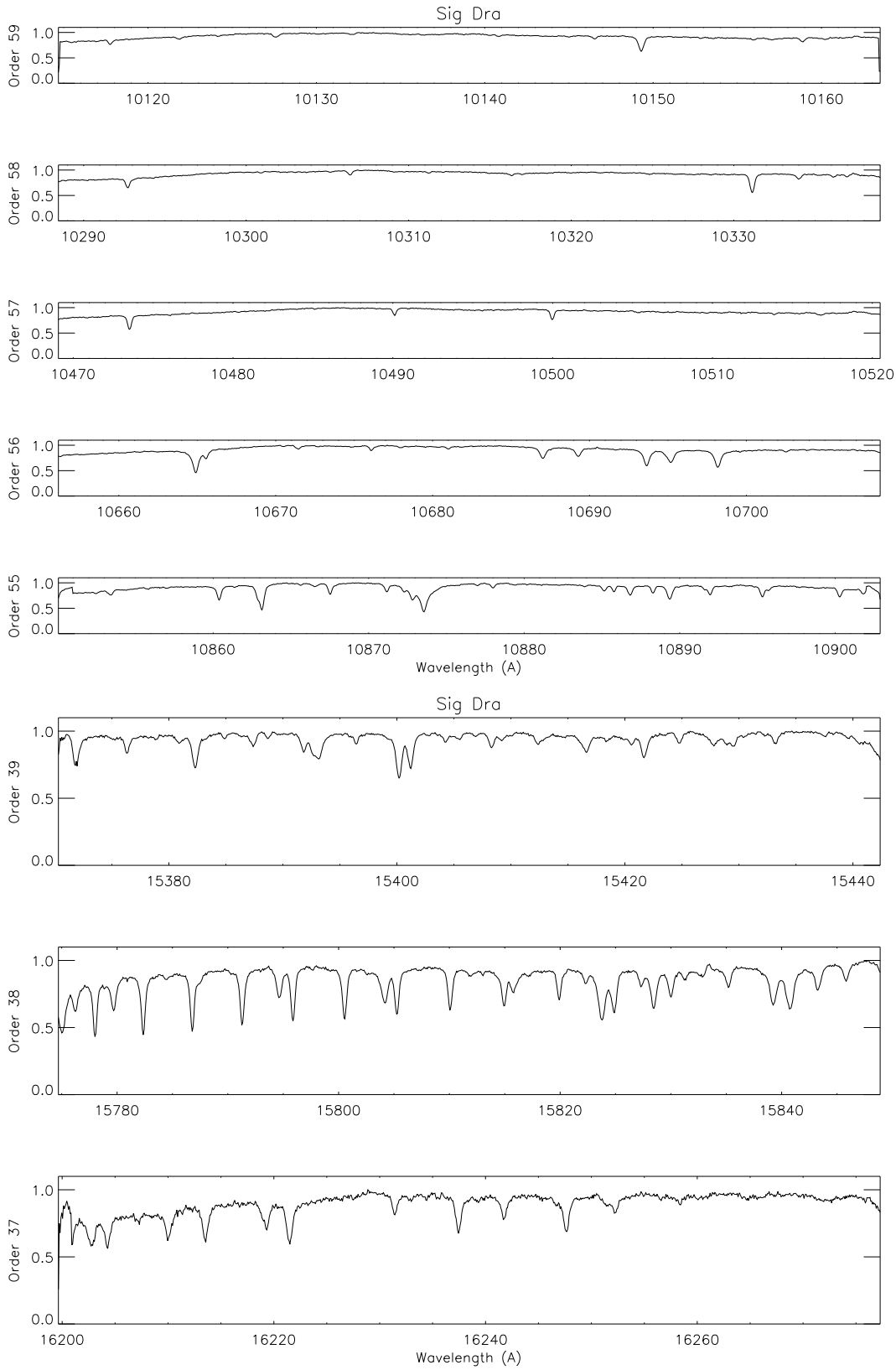

Fig. 4.35 The extracted spectrum of σ Draconis, as seen in the Y and H bands.

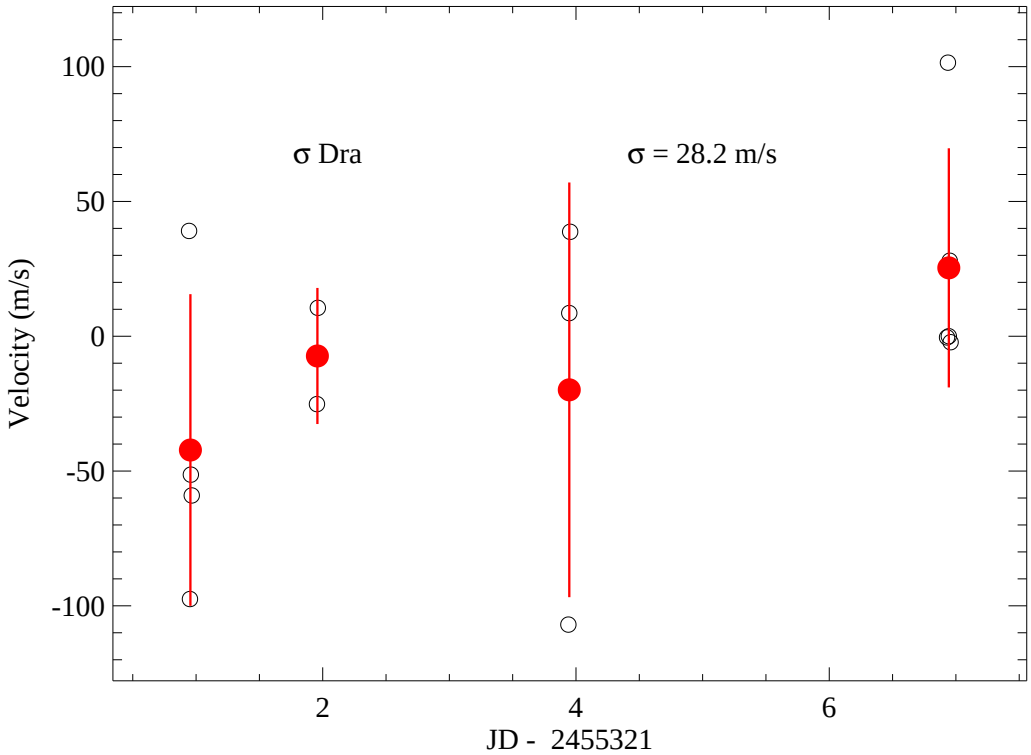

Fig. 4.36 The RV curve of σ Draconis, as measured by the Pathfinder spectrograph during our May 2010 run at the HET.

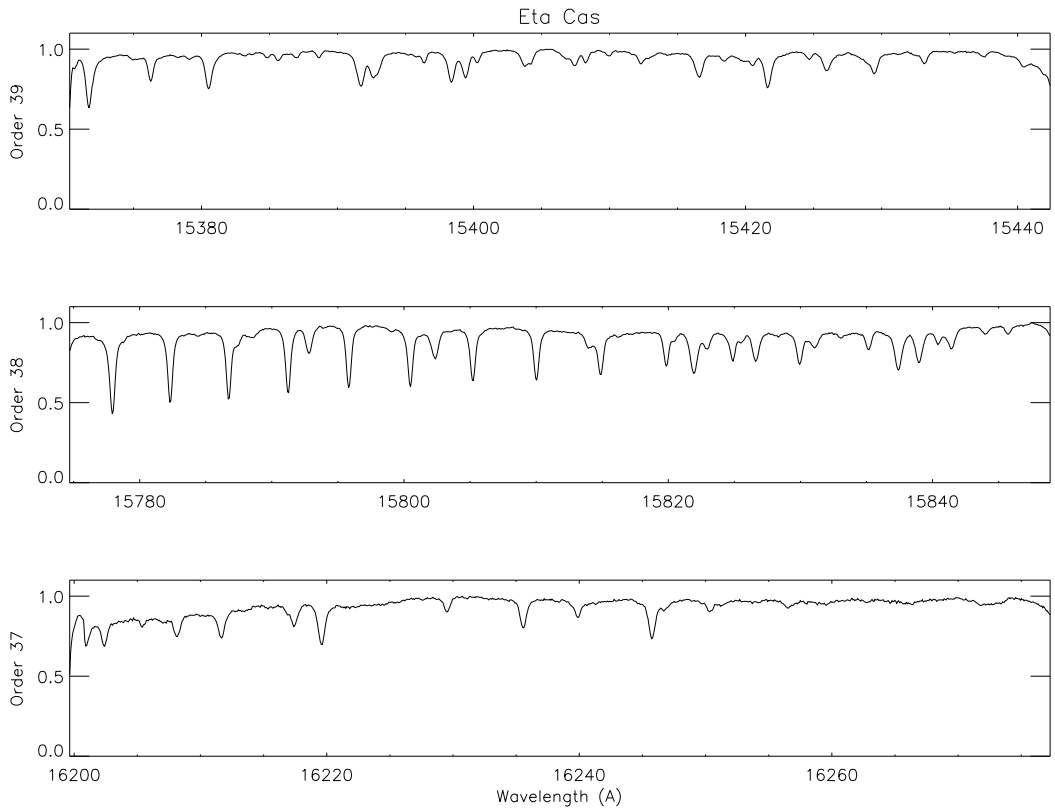

Fig. 4.37 The extracted spectrum of η Cas.

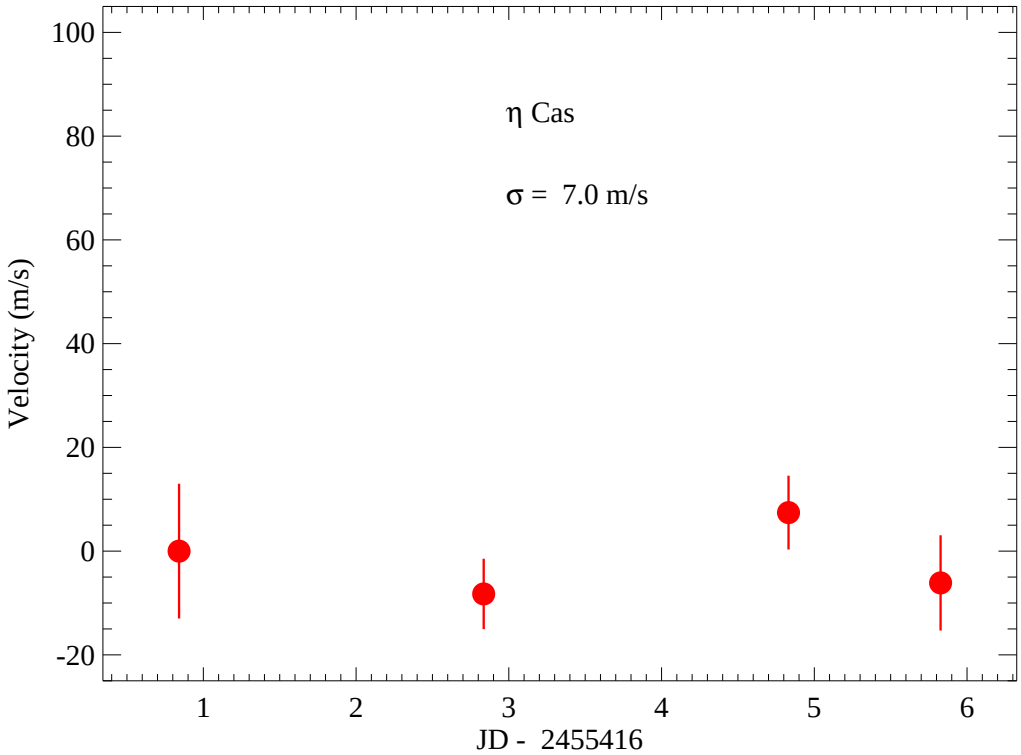

Fig. 4.38 The RV curve of η Cas, as measured by the Pathfinder spectrograph during our August 2010 run at the HET.

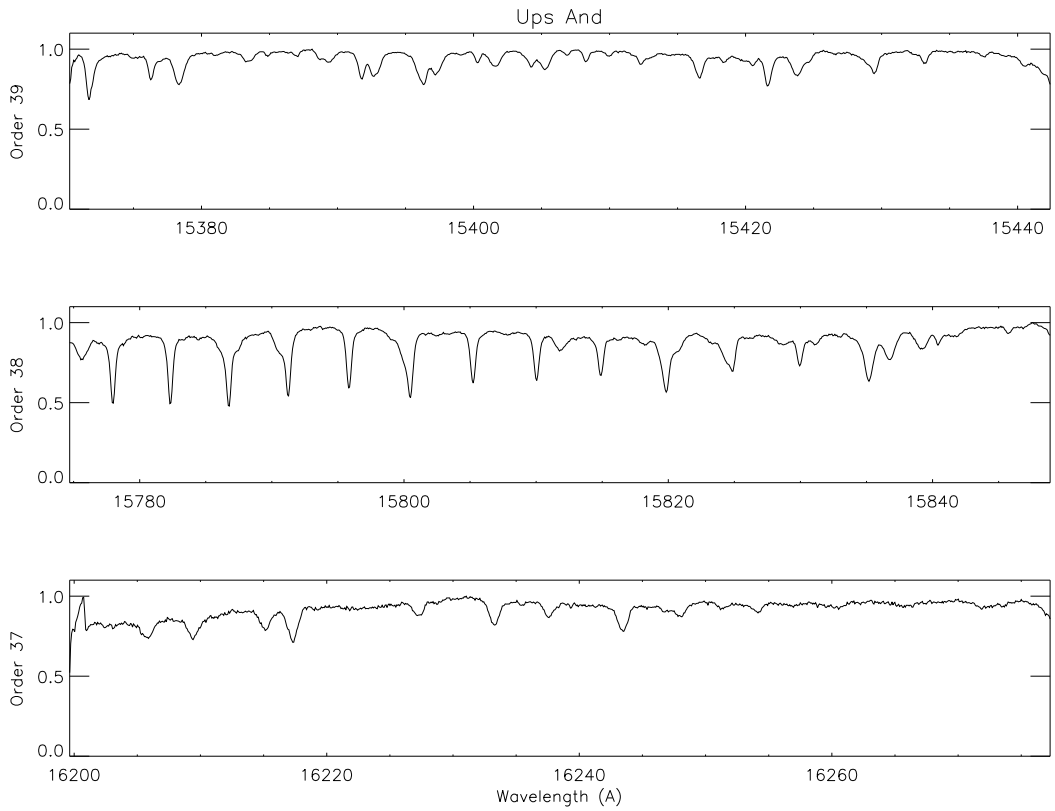

Fig. 4.39 The extracted spectrum of υ And.

1.5 m/s from our August observations. The extracted spectrum of HD 168723 can be seen in Figure 4.40.

4.5.12 CO_2 Band

Atmospheric lines are usually a hinderance to stellar observations, but ro-vibrational lines of CO_2 in the H band are sharp, abundant, deep, and show radial velocity shifts that are much more stable than the atmospheric motion of other species, most notably water. The wavelengths of these lines are known from molecular physics at the 5—50 m/s level, and have been used to measure instrumental precision limitations on CRIRES, where Figueira et al. (2010) achieved a precision of less than 10 m/s on HD 108309 (a radial velocity standard star). Based on a Q-factor analysis (see § 1.1.2) conducted by Ryan Terrian, the achievable precision on a single observation of these CO_2 lines is 5 m/s.

These CO_2 lines were particularly insightful, because they provide an independent reference frame in which to track changes in the dispersion solution, at least at the 10 m/s level. While we did not anticipate the laser frequency comb wavelengths changing at all, the comb frequencies did jump by a mode on the night of August 10th. In theory, since the components of the frequency comb equation were tracked during this time, the dispersion solution should have been tracked perfectly. However, our measurements of the CO_2 line velocities indicate that the dispersion solution is still off by about 50 m/s on the night of the 10th. While this shift cannot be explained by an unknown shift of a mode (which would translate to a shift of about 400 m/s), such a shift might be explained by a difference in f_{ceo}, the frequency of the carrier envelope offset. Since these velocities were derived from observations of η Cas, we might hypothesize that the shift is due to changes in the stellar spectrum. However, this hypothesis can be rejected, since the same shift is seen in the CO_2 lines of Vega, our telluric standard star for the third HET run (see Figure 4.42). The Vega spectra have problems of their own — the spectra were all partial exposures, so the frequency comb comparison spectra were always under-exposed, and the dispersion solutions slightly more uncertain — but the fact that the same shift shows up in both RV plots strongly suggests that the source of this shift is intrinsic to a system error that night. Ignoring the night of 10 August, and the partial exposures of Vega and η Cas, we were able to obtain an RMS on our velocities of 1.7 m/s (see Figure 4.43).

We also hypothesized that the shift on 10 August might be due to telluric water lines, which can very over the course of several minutes, and change dramatically from night to night. To test this hypothesis, Brandon Botzer used TERRASPEC (Bender in preparation) to measure the precipital water vapor column, which was then subtracted from the telluric spectrum of Vega. Subsequent measurement of the radial velocities of these water-corrected CO_2 lines yielded negligible changes in the previously-mentioned RV measurements.

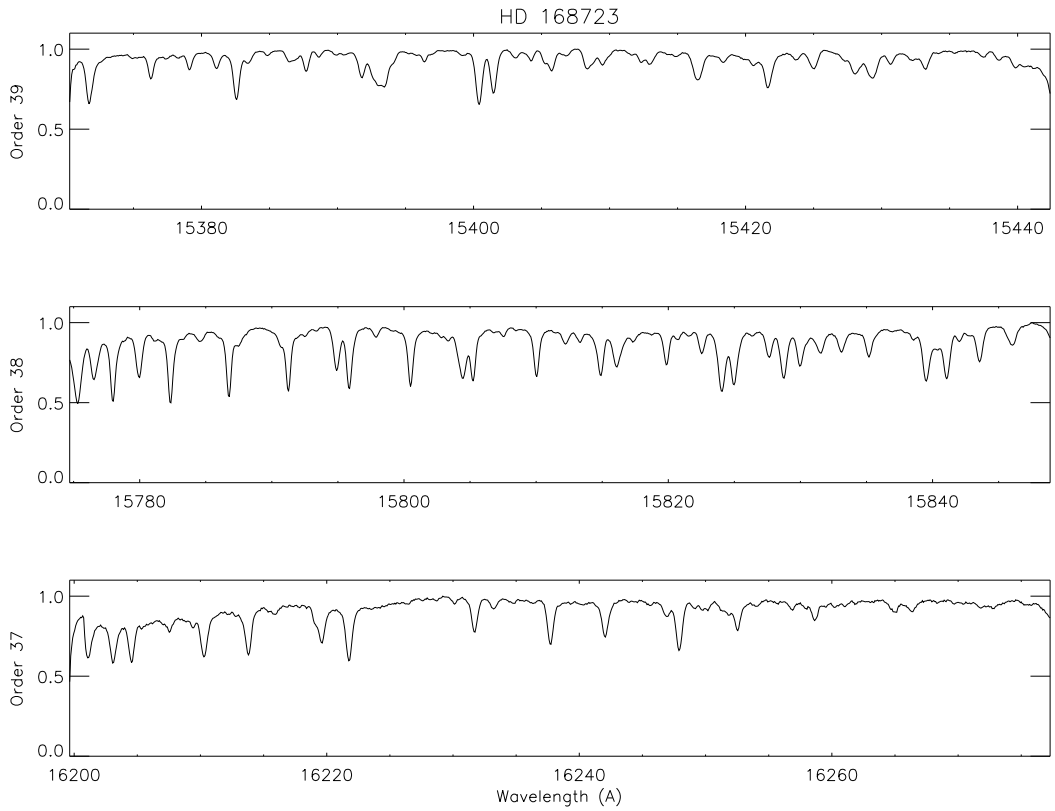

Fig. 4.40 The extracted spectrum of HD 168723.

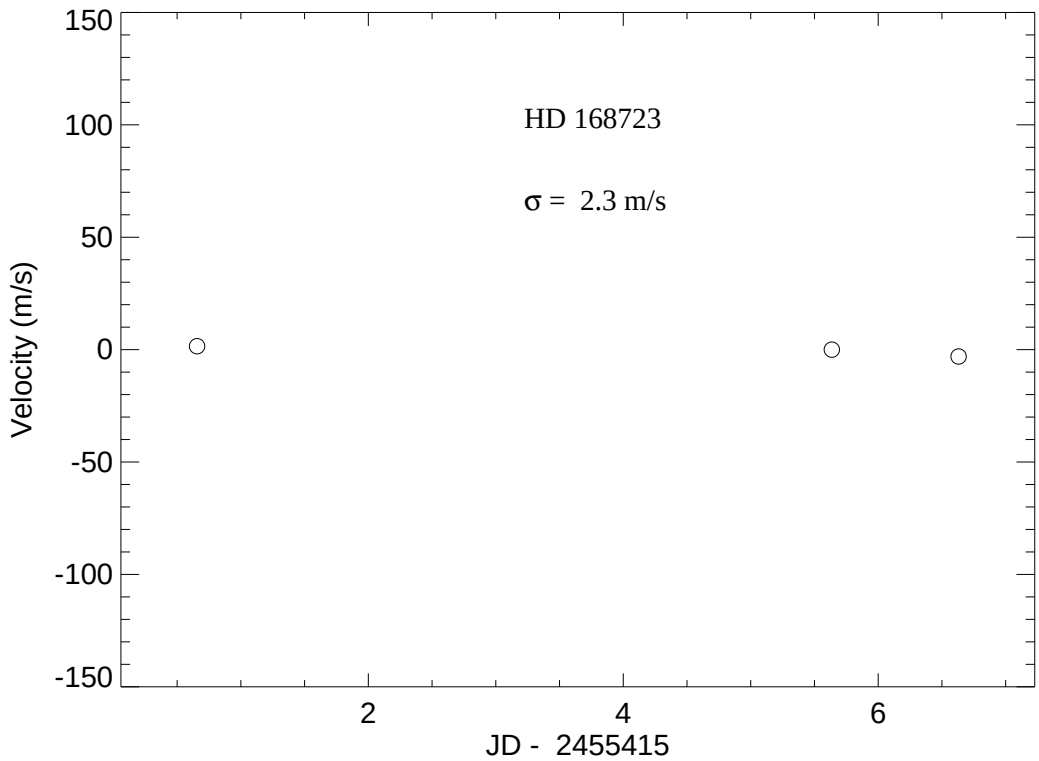

Fig. 4.41 The RV curve of HD 168723, as measured by the Pathfinder spectrograph during our August 2010 run at the HET.

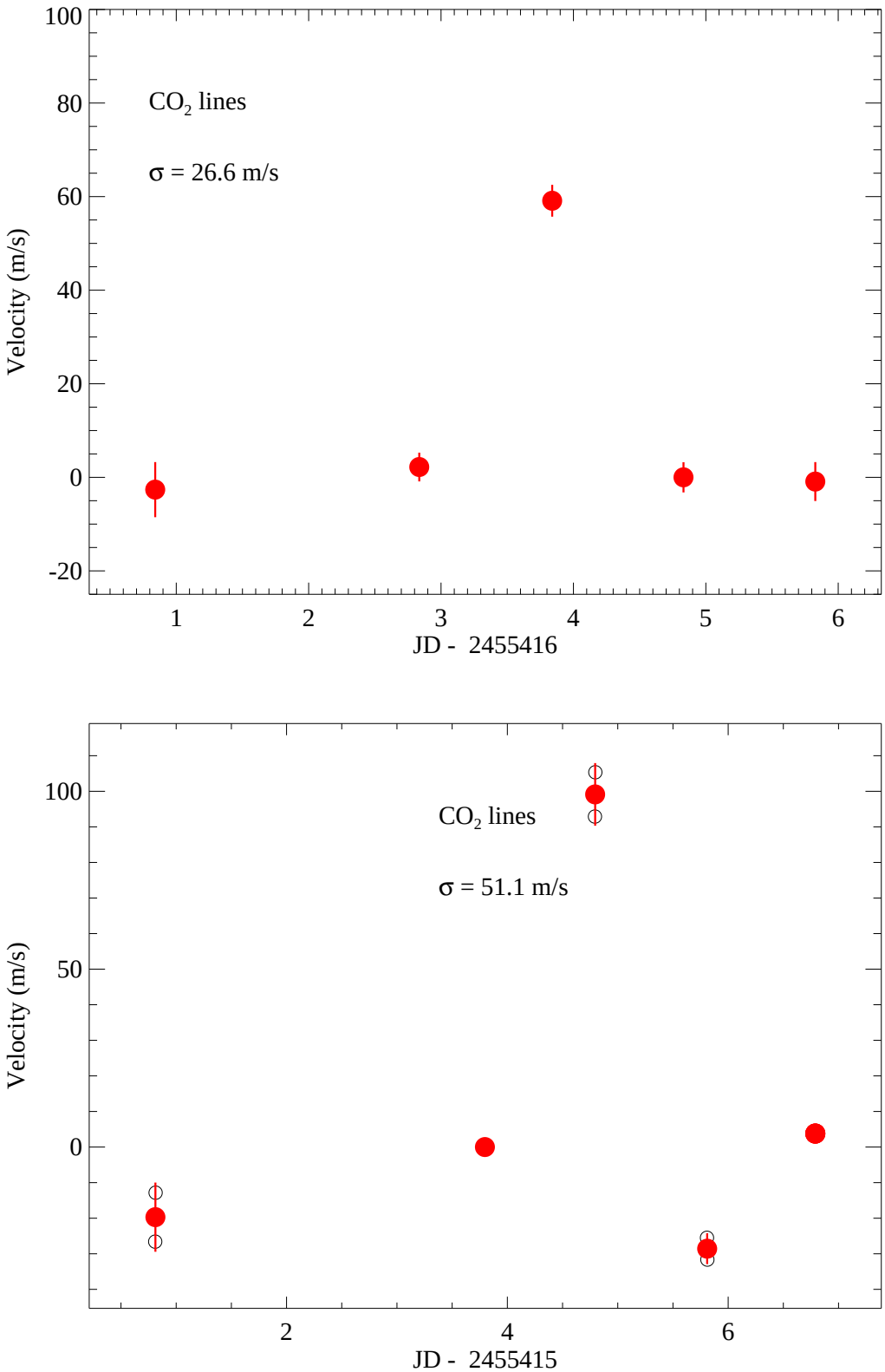

Fig. 4.42 Radial velocity measurements of the CO_2 lines of order 38 in η Cas (Top) and Vega (Bottom). Both spectra show the same ≈ 100 m/s jump in the measured velocities on 10 August (JD 2455420). The Vega points are all one or two partial exposures, reducing the counts in the comb spectrum, and leaving the dispersion solution vulnerable

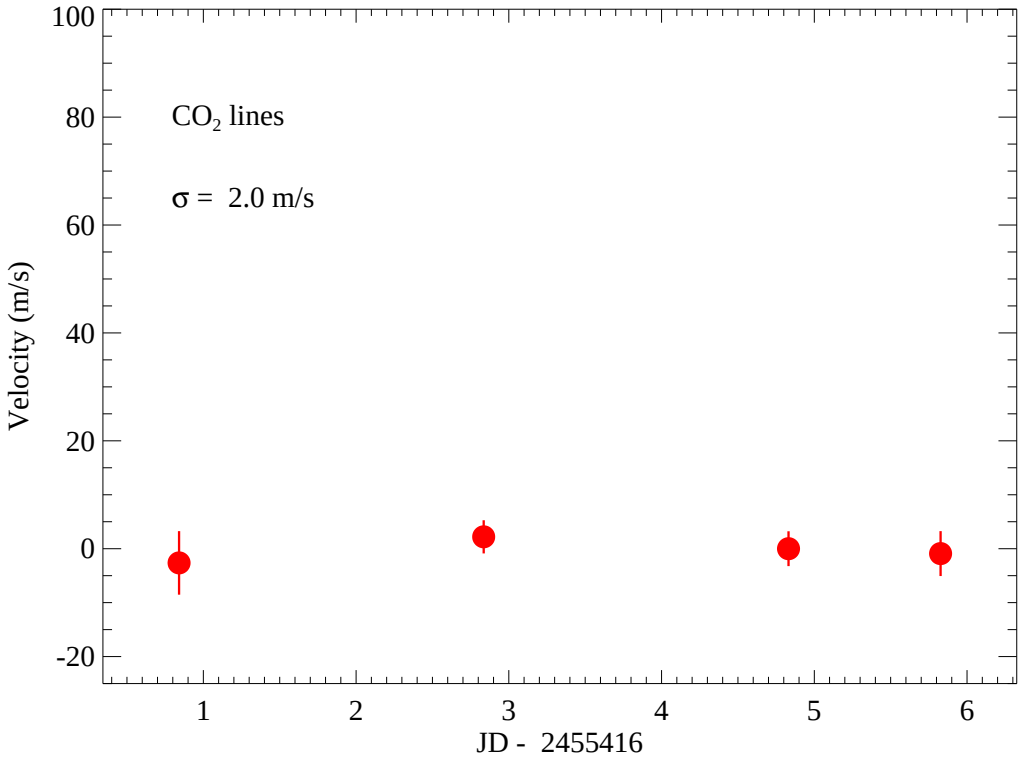

Fig. 4.43 Radial velocity measurements of the CO_2 lines of order 38 in η Cas, after excluding the night of 10 August (JD 2455420). This RMS precision is below the photon-limited precision, and therefore due in part to the chance alignment of these points.

4.6 Limitations to the Precision of Pathfinder

It is perhaps not too surprising that we were unable to attain our photon-limited radial velocity precisions for most of our targets, but it is worth discussing the various limits to our precision, and their possible solutions for the HZPF. First, the dispersion solutions with uranium neon, while adequate at the 20 m/s level, are not as good as the dispersion solutions provided by the frequency comb. This is not a surprise — the frequency comb lines vary only by a factor of a few in intensity, and are equally spaced in frequency, whereas the uranium lines vary by orders of magnitude, and are blended in ways that cannot be measured without the use of a much higher-resolution instrument, such as an FTS. A comb that covers the Y-, J-, and H-bands is quite desirable for the HZPF, but such a comb does not yet exist. A stabilized fabry-perot would also be sufficient, if its spectrum were stable and well-characterized at the sub-m/s level.

Second, the stars we observed exhibit many fewer lines than the number of expected lines in late M dwarfs, our ultimate targets, and thus less radial velocity information content (see § 1.1.2). On the other hand, the mask technique requires a precise knowledge of each individual spectral line, which will require high-quality models of late M dwarf spectra.

Third, the throughput of Pathfinder is very low, $\approx 0.35\%$. Future upgrades to the instrument will yield substantial increases. For example, the echelle is currently underfilled. Replacing it with a larger echelle would improve our throughput by a factor of 2-3. The current filter set is not quite optimal — a different selection of filters would gain us another factor of ≈ 2.5. Finally, a lot of light is lost at the slit; a fiber slicer or image slicer could gain us a factor of 4. In all, these changes would improve our throughput by a factor of 25, so getting to 5% throughput will not be exceptionally challenging.

Chapter 5

Conclusions and Future Work

Precision radial velocities in the NIR have lagged behind those of the optical for several years now, and this work brings the possibility of a high-resolution, NIR spectrograph a little closer to fruition. We have learned a great deal since the solar experiments presented in Chapter 2. In particular, the calibration source is paramount to the achievable precision. Our on-sky Y-band RV measurements were limited primarily by our ability to successfully measure the dispersion solution with the uranium-neon spectrum. Our H-band velocities were approximately four times as precise, despite the larger modal noise higher thermal background, and smaller wavelength coverage.

While frequency combs will ultimately prove to be the most precise calibration source currently in existence, their cost and technological challenges make them inaccessible to most research groups. Hollow cathode lamps are a relatively inexpensive calibration source that can be used to provide simultaneous wavelength calibration in fiber-fed spectrographs. The list of uranium lines I have compiled for the near Infrared are useful not just for exoplanet RV purposes, but for a variety of astrophysical applications.

Pathfinder is currently the most precise spectrograph for the Y band in the world, and the team continues to make improvements to the instrument. We were recently awarded funding for a new HAWAII 2K array, which offers several advantages over its previous generation, including a larger detector size, faster read times, reduced persistence and crosstalk, and minimized glow from electroluminescence (Hodapp et al. 2004). The upcoming HETDEX project will put the HET out of commission for several months, but in the meantime, we are preparing for the next set of on-sky experiments. For these, we are collaborating with the CU/NIST team, who has agreed to develop a frequency comb for the Y band. Pending the necessary funding, the most important upgrades to Pathfinder include a vacuum vessel, a double scrambler (Hunter & Ramsey 1992), and better thermal control.

The demand for a spectrograph such as the HZPF continues to grow. Kepler has already yielded several hundred transiting exoplanet candidates (only a handful of which are M dwarfs), and these will require follow-up radial velocity work to confirm. Similarly, the MEarth Project (Irwin et al. 2009) is expected to yield many M dwarf targets. With this work, we have clearly demonstrated that precision measurements can be made in the NIR. If it is funded, HZPF and instruments like it will improve our ability to confirm and discover habitable Earth-mass planets in the local neighborhood in the years to come.

I have been awarded an NRC fellowship to explore alternative NIR calibration sources at NIST with an FTS. My work at NIST will include developing calibration sources for the NIR, including better calibrations of thorium and uranium lines, careful

characterizations of frequency combs, and characterizing gas cells such as iodine and heavy methane for exoplanet RV groups. Frequency combs will eventually be the best possible calibration source for NIR observations, but for now they are expensive and notoriously difficult to maintain. Until these issues are resolved, cheaper, off-the-shelf hollow cathode lamps with sources such as ThAr and UNe will provide the astrophysical community with precise wavelength standards.

Appendix

The UNe H-band Spectrum

The following figures show the extracted H-band spectrum of Uranium Neon, calibrated with a frequency comb (see Figure 3.10). Each bottom panel shows the lowest 5% of the top panel, to emphasize the fainter Uranium lines. Both scales are normalized to the brightest line in the H band, a Neon line at 15234.87Å. A few Uranium lines are marked in blue, and all Neon lines have been marked with red lines. The Uranium wavelengths were measured independently with historical FTS data (see § 3.1), and the Neon wavelengths are from Sansonetti et al. (2004). More detail on this map can be found in § 3.5. An up-to-date version of this figure can be found in Redman et al. (in preparationb).

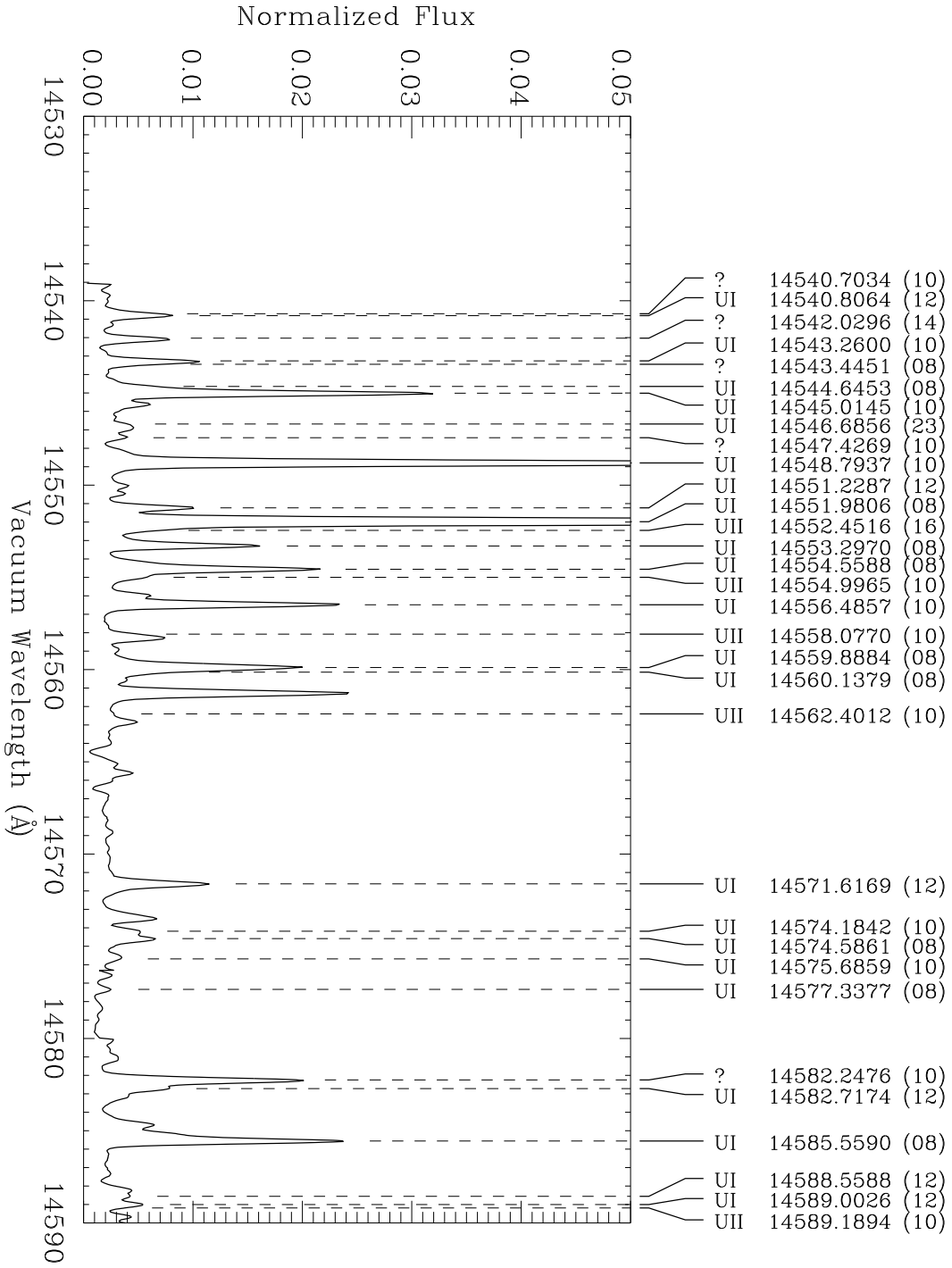
Normalized Flux
0.00
0.01
0.02
0.03
0.04
0.05
14530
14540
14550
14560
14570
14580
14590
Vacuum Wavelength (Å)
? 14540.7034 (10)
UI 14540.8064 (12)
? 14542.0296 (14)
UI 14543.2600 (10)
? 14543.4451 (08)
UI 14544.6453 (08)
UI 14545.0145 (10)
UI 14546.6856 (23)
? 14547.4269 (10)
UI 14548.7937 (10)
UI 14551.2287 (12)
UI 14551.9806 (08)
UII 14552.4516 (16)
UI 14553.2970 (08)
UI 14554.5588 (08)
UII 14554.9965 (10)
UI 14556.4857 (10)
UII 14558.0770 (10)
UI 14559.8884 (08)
UI 14560.1379 (08)
UII 14562.4012 (10)
UI 14571.6169 (12)
UI 14574.1842 (10)
UI 14574.5861 (08)
UI 14575.6859 (10)
UI 14577.3377 (08)
? 14582.2476 (10)
UI 14582.7174 (12)
UI 14585.5590 (08)
UI 14588.5588 (12)
UI 14589.0026 (12)
UII 14589.1894 (10)

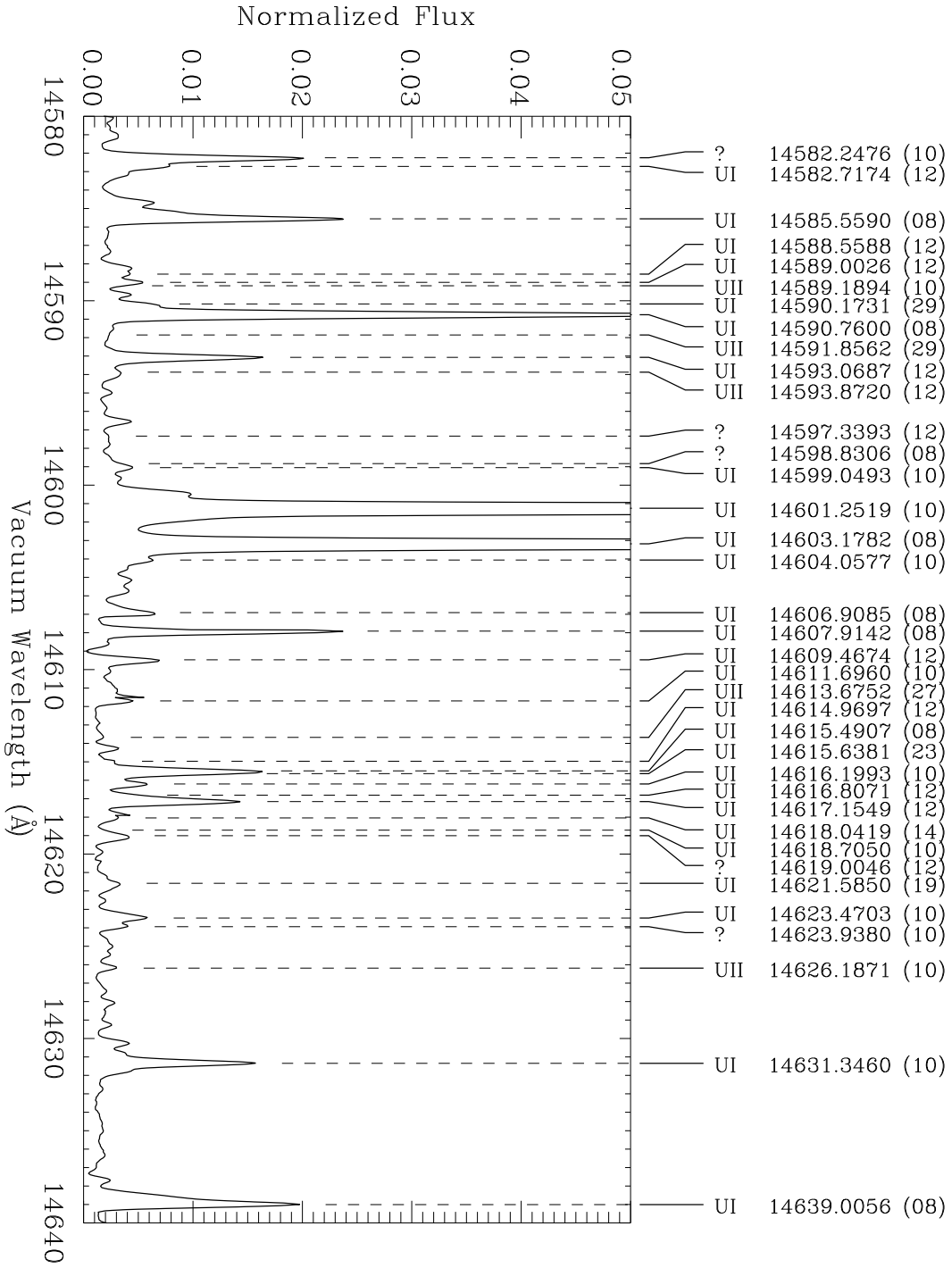
Normalized Flux
0.00
0.01
0.02
0.03
0.04
0.05
14580
14590
14600
14610
14620
14630
14640
Vacuum Wavelength (Å)
? 14582.2476 (10)
UI 14582.7174 (12)
UI 14585.5590 (08)
UI 14588.5588 (12)
UI 14589.0026 (12)
UII 14589.1894 (10)
UI 14590.1731 (29)
UI 14590.7600 (08)
UII 14591.8562 (29)
UI 14593.0687 (12)
UII 14593.8720 (12)
? 14597.3393 (12)
? 14598.8306 (08)
UI 14599.0493 (10)
UI 14601.2519 (10)
UI 14603.1782 (08)
UI 14604.0577 (10)
UI 14606.9085 (08)
UI 14607.9142 (08)
UI 14609.4674 (12)
UI 14611.6960 (10)
UII 14613.6752 (27)
UI 14614.9697 (12)
UI 14615.4907 (08)
UI 14615.6381 (23)
UI 14616.1993 (10)
UI 14616.8071 (12)
UI 14617.1549 (12)
UI 14618.0419 (14)
UI 14618.7050 (10)
? 14619.0046 (12)
UI 14621.5850 (19)
UI 14623.4703 (10)
? 14623.9380 (10)
UII 14626.1871 (10)
UI 14631.3460 (10)
UI 14639.0056 (08)

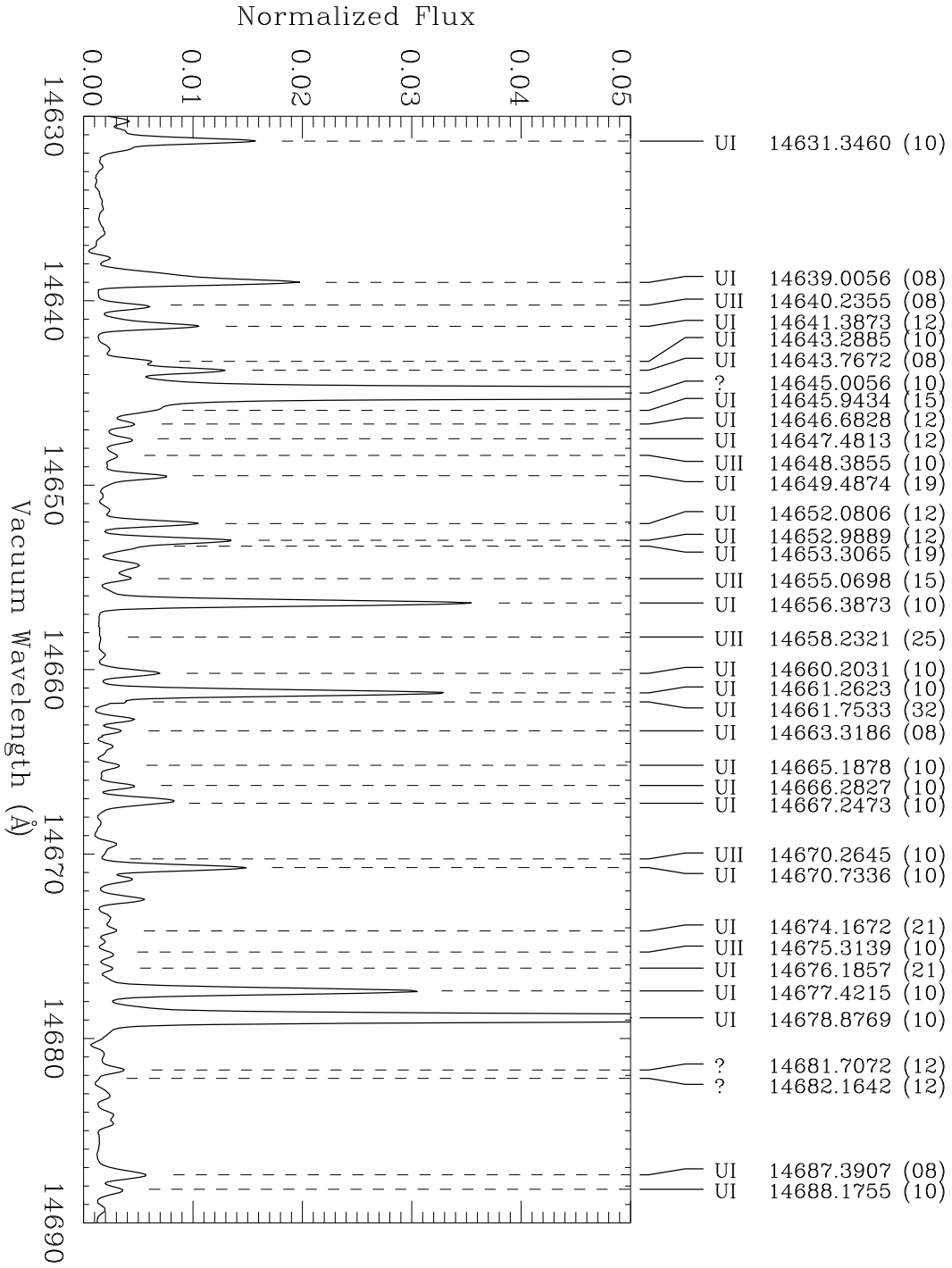
Normalized Flux
0.00
0.01
0.02
0.03
0.04
0.05
14630
14640
14650
14660
14670
14680
14690
Vacuum Wavelength (Å)
UI 14631.3460 (10)
UI 14639.0056 (08)
UII 14640.2355 (08)
UI 14641.3873 (12)
UI 14643.2885 (10)
UI 14643.7672 (08)
? 14645.0056 (10)
UI 14645.9434 (15)
UI 14646.6828 (12)
UI 14647.4813 (12)
UII 14648.3855 (10)
UI 14649.4874 (19)
UI 14652.0806 (12)
UI 14652.9889 (12)
UI 14653.3065 (19)
UII 14655.0698 (15)
UI 14656.3873 (10)
UII 14658.2321 (25)
UI 14660.2031 (10)
UI 14661.2623 (10)
UI 14661.7533 (32)
UI 14663.3186 (08)
UI 14665.1878 (10)
UI 14666.2827 (10)
UI 14667.2473 (10)
UII 14670.2645 (10)
UI 14670.7336 (10)
UI 14674.1672 (21)
UII 14675.3139 (10)
UI 14676.1857 (21)
UI 14677.4215 (10)
UI 14678.8769 (10)
? 14681.7072 (12)
? 14682.1642 (12)
UI 14687.3907 (08)
UI 14688.1755 (10)

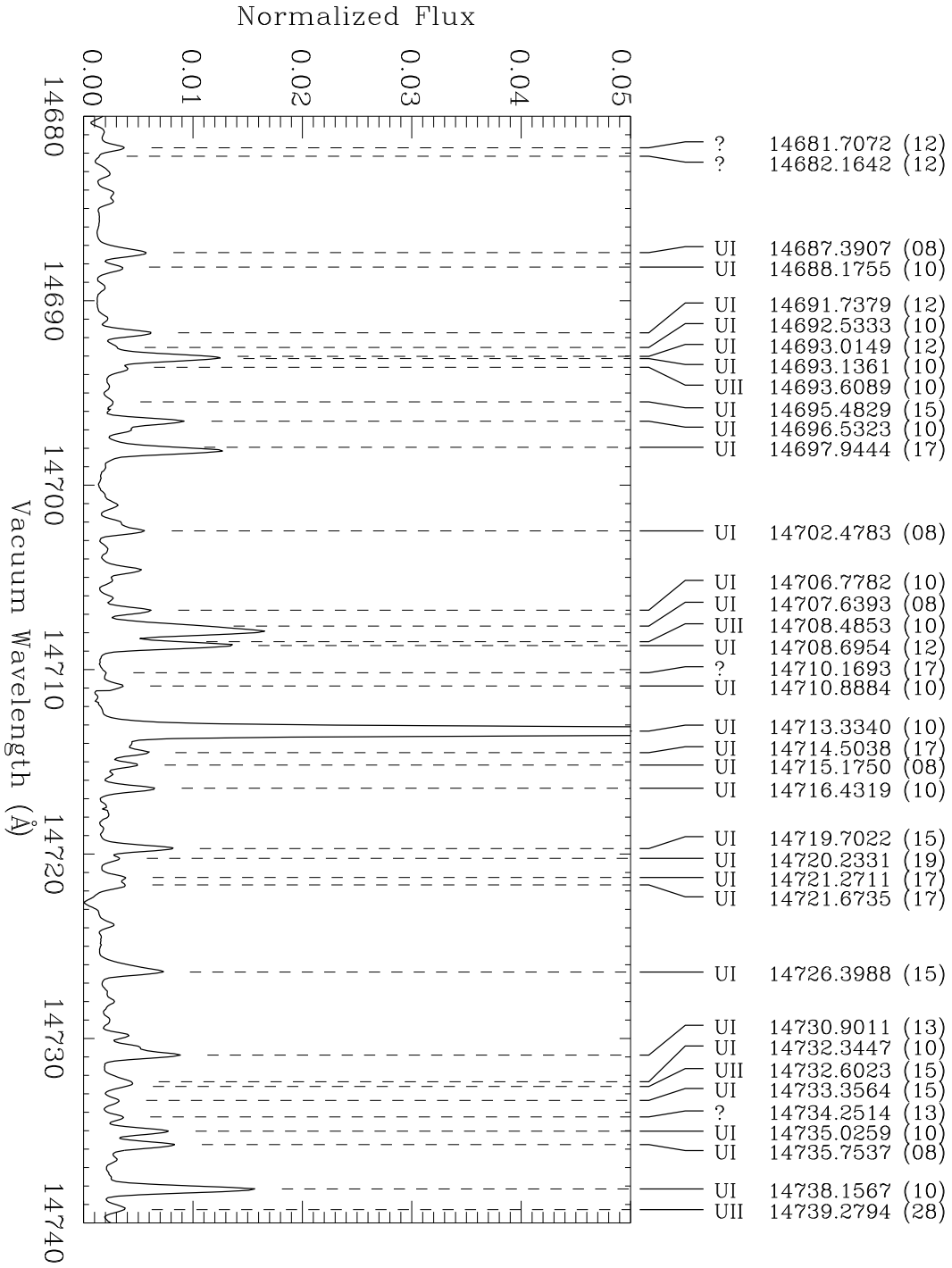
Normalized Flux
0.00
0.01
0.02
0.03
0.04
0.05
14680
14690
14700
14710
14720
14730
14740
Vacuum Wavelength (Å)
? 14681.7072 (12)
? 14682.1642 (12)
UI 14687.3907 (08)
UI 14688.1755 (10)
UI 14691.7379 (12)
UI 14692.5333 (10)
UI 14693.0149 (12)
UI 14693.1361 (10)
UII 14693.6089 (10)
UI 14695.4829 (15)
UI 14696.5323 (10)
UI 14697.9444 (17)
UI 14702.4783 (08)
UI 14706.7782 (10)
UI 14707.6393 (08)
UII 14708.4853 (10)
UI 14708.6954 (12)
? 14710.1693 (17)
UI 14710.8884 (10)
UI 14713.3340 (10)
UI 14714.5038 (17)
UI 14715.1750 (08)
UI 14716.4319 (10)
UI 14719.7022 (15)
UI 14720.2331 (19)
UI 14721.2711 (17)
UI 14721.6735 (17)
UI 14726.3988 (15)
UI 14730.9011 (13)
UI 14732.3447 (10)
UII 14732.6023 (15)
UI 14733.3564 (15)
? 14734.2514 (13)
UI 14735.0259 (10)
UI 14735.7537 (08)
UI 14738.1567 (10)
UII 14739.2794 (28)

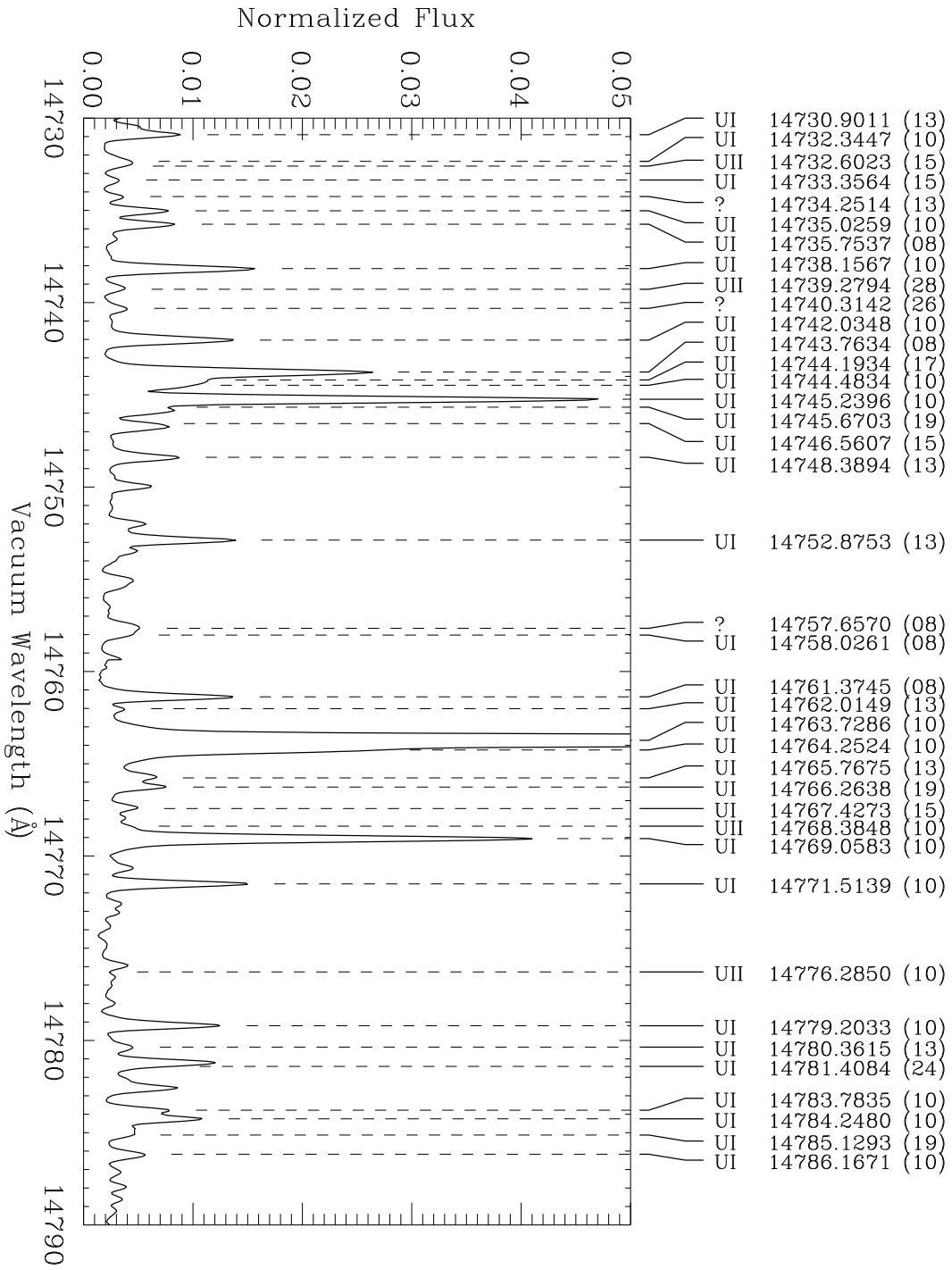
Normalized Flux
0.00
0.01
0.02
0.03
0.04
0.05
14730
14740
14750
14760
14770
14780
14790
Vacuum Wavelength (Å)
UI 14730.9011 (13)
UI 14732.3447 (10)
UII 14732.6023 (15)
UI 14733.3564 (15)
? 14734.2514 (13)
UI 14735.0259 (10)
UI 14735.7537 (08)
UI 14738.1567 (10)
UII 14739.2794 (28)
? 14740.3142 (26)
UI 14742.0348 (10)
UI 14743.7634 (08)
UI 14744.1934 (17)
UI 14744.4834 (10)
UI 14745.2396 (10)
UI 14745.6703 (19)
UI 14746.5607 (15)
UI 14748.3894 (13)
UI 14752.8753 (13)
? 14757.6570 (08)
UI 14758.0261 (08)
UI 14761.3745 (08)
UI 14762.0149 (13)
UI 14763.7286 (10)
UI 14764.2524 (10)
UI 14765.7675 (13)
UI 14766.2638 (19)
UI 14767.4273 (15)
UII 14768.3848 (10)
UI 14769.0583 (10)
UI 14771.5139 (10)
UII 14776.2850 (10)
UI 14779.2033 (10)
UI 14780.3615 (13)
UI 14781.4084 (24)
UI 14783.7835 (10)
UI 14784.2480 (10)
UI 14785.1293 (19)
UI 14786.1671 (10)

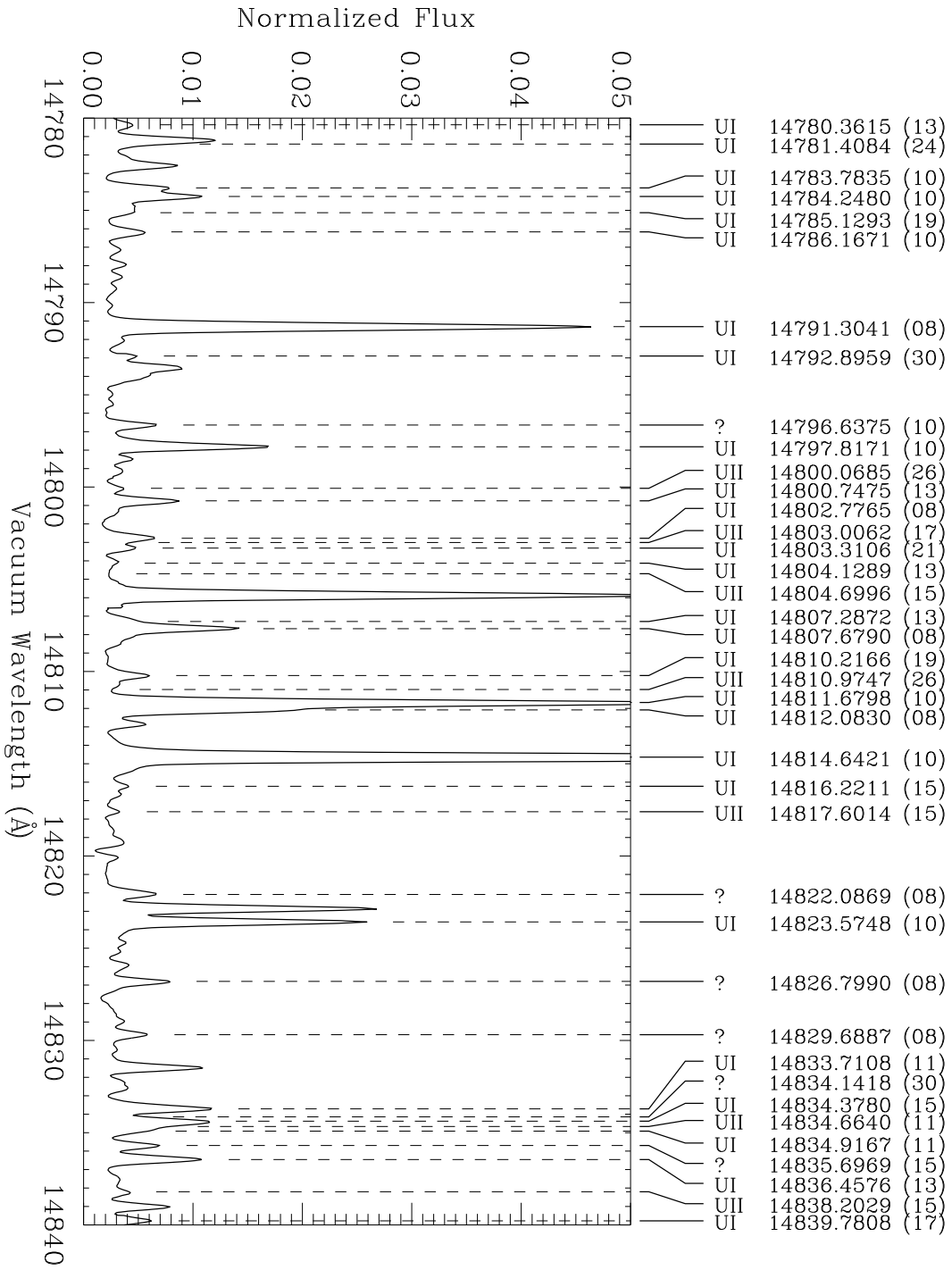
Normalized Flux
0.00
0.01
0.02
0.03
0.04
0.05
14780
14790
14800
14810
14820
14830
14840
Vacuum Wavelength (Å)
UI 14780.3615 (13)
UI 14781.4084 (24)
UI 14783.7835 (10)
UI 14784.2480 (10)
UI 14785.1293 (19)
UI 14786.1671 (10)
UI 14791.3041 (08)
UI 14792.8959 (30)
? 14796.6375 (10)
UI 14797.8171 (10)
UII 14800.0685 (26)
UI 14800.7475 (13)
UI 14802.7765 (08)
UII 14803.0062 (17)
UI 14803.3106 (21)
UI 14804.1289 (13)
UII 14804.6996 (15)
UI 14807.2872 (13)
UI 14807.6790 (08)
UI 14810.2166 (19)
UII 14810.9747 (26)
UI 14811.6798 (10)
UI 14812.0830 (08)
UI 14814.6421 (10)
UI 14816.2211 (15)
UII 14817.6014 (15)
? 14822.0869 (08)
UI 14823.5748 (10)
? 14826.7990 (08)
? 14829.6887 (08)
UI 14833.7108 (11)
? 14834.1418 (30)
UI 14834.3780 (15)
UII 14834.6640 (11)
UI 14834.9167 (11)
? 14835.6969 (15)
UI 14836.4576 (13)
UII 14838.2029 (15)
UI 14839.7808 (17)

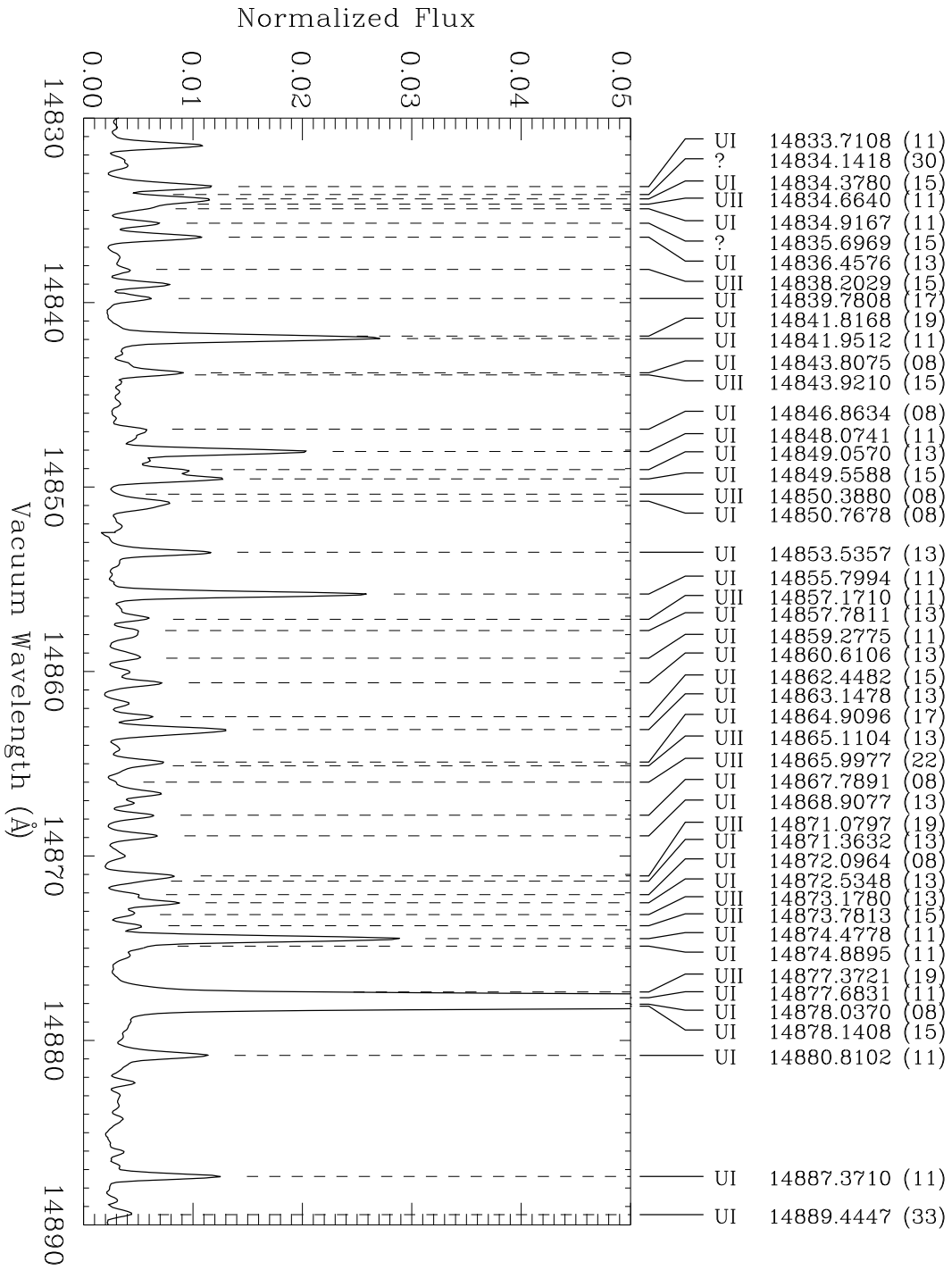
Normalized Flux
0.00
0.01
0.02
0.03
0.04
0.05
14830
14840
14850
14860
14870
14880
14890
Vacuum Wavelength (Å)
UI 14833.7108 (11)
? 14834.1418 (30)
UI 14834.3780 (15)
UII 14834.6640 (11)
UI 14834.9167 (11)
? 14835.6969 (15)
UI 14836.4576 (13)
UII 14838.2029 (15)
UI 14839.7808 (17)
UI 14841.8168 (19)
UI 14841.9512 (11)
UI 14843.8075 (08)
UII 14843.9210 (15)
UI 14846.8634 (08)
UI 14848.0741 (11)
UI 14849.0570 (13)
UI 14849.5588 (15)
UII 14850.3880 (08)
UI 14850.7678 (08)
UI 14853.5357 (13)
UI 14855.7994 (11)
UII 14857.1710 (11)
UI 14857.7811 (13)
UI 14859.2775 (11)
UI 14860.6106 (13)
UI 14862.4482 (15)
UI 14863.1478 (13)
UI 14864.9096 (17)
UII 14865.1104 (13)
UII 14865.9977 (22)
UI 14867.7891 (08)
UI 14868.9077 (13)
UII 14871.0797 (19)
UI 14871.3632 (13)
UI 14872.0964 (08)
UI 14872.5348 (13)
UII 14873.1780 (13)
UII 14873.7813 (15)
UI 14874.4778 (11)
UI 14874.8895 (11)
UII 14877.3721 (19)
UI 14877.6831 (11)
UI 14878.0370 (08)
UI 14878.1408 (15)
UI 14880.8102 (11)
UI 14887.3710 (11)
UI 14889.4447 (33)

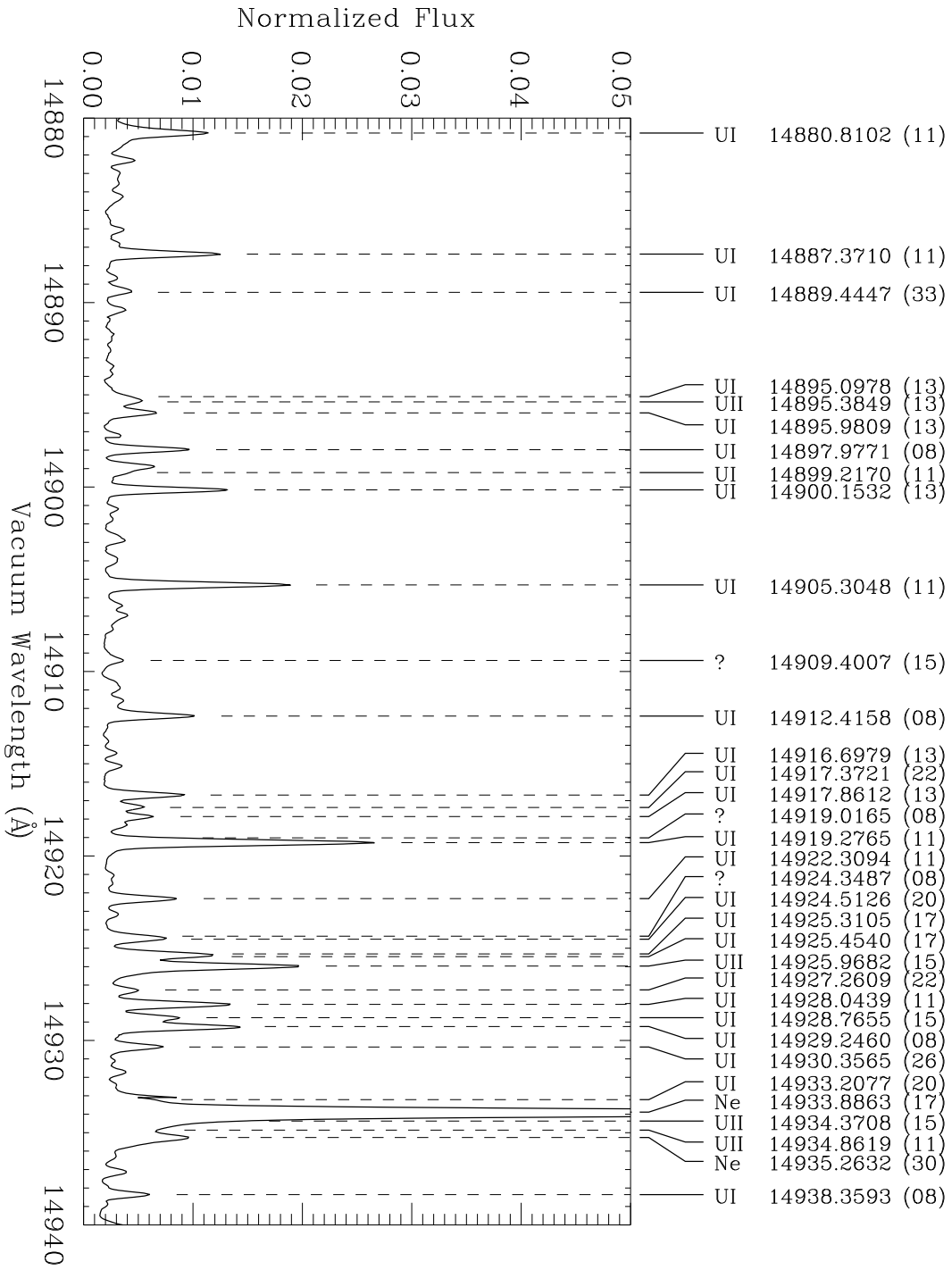
Normalized Flux
0.00
0.01
0.02
0.03
0.04
0.05
14880
14890
14900
14910
14920
14930
14940
Vacuum Wavelength (Å)
UI 14880.8102 (11)
UI 14887.3710 (11)
UI 14889.4447 (33)
UI 14895.0978 (13)
UII 14895.3849 (13)
UI 14895.9809 (13)
UI 14897.9771 (08)
UI 14899.2170 (11)
UI 14900.1532 (13)
UI 14905.3048 (11)
? 14909.4007 (15)
UI 14912.4158 (08)
UI 14916.6979 (13)
UI 14917.3721 (22)
UI 14917.8612 (13)
? 14919.0165 (08)
UI 14919.2765 (11)
UI 14922.3094 (11)
? 14924.3487 (08)
UI 14924.5126 (20)
UI 14925.3105 (17)
UI 14925.4540 (17)
UII 14925.9682 (15)
UI 14927.2609 (22)
UI 14928.0439 (11)
UI 14928.7655 (15)
UI 14929.2460 (08)
UI 14930.3565 (26)
UI 14933.2077 (20)
Ne 14933.8863 (17)
UII 14934.3708 (15)
UII 14934.8619 (11)
Ne 14935.2632 (30)
UI 14938.3593 (08)

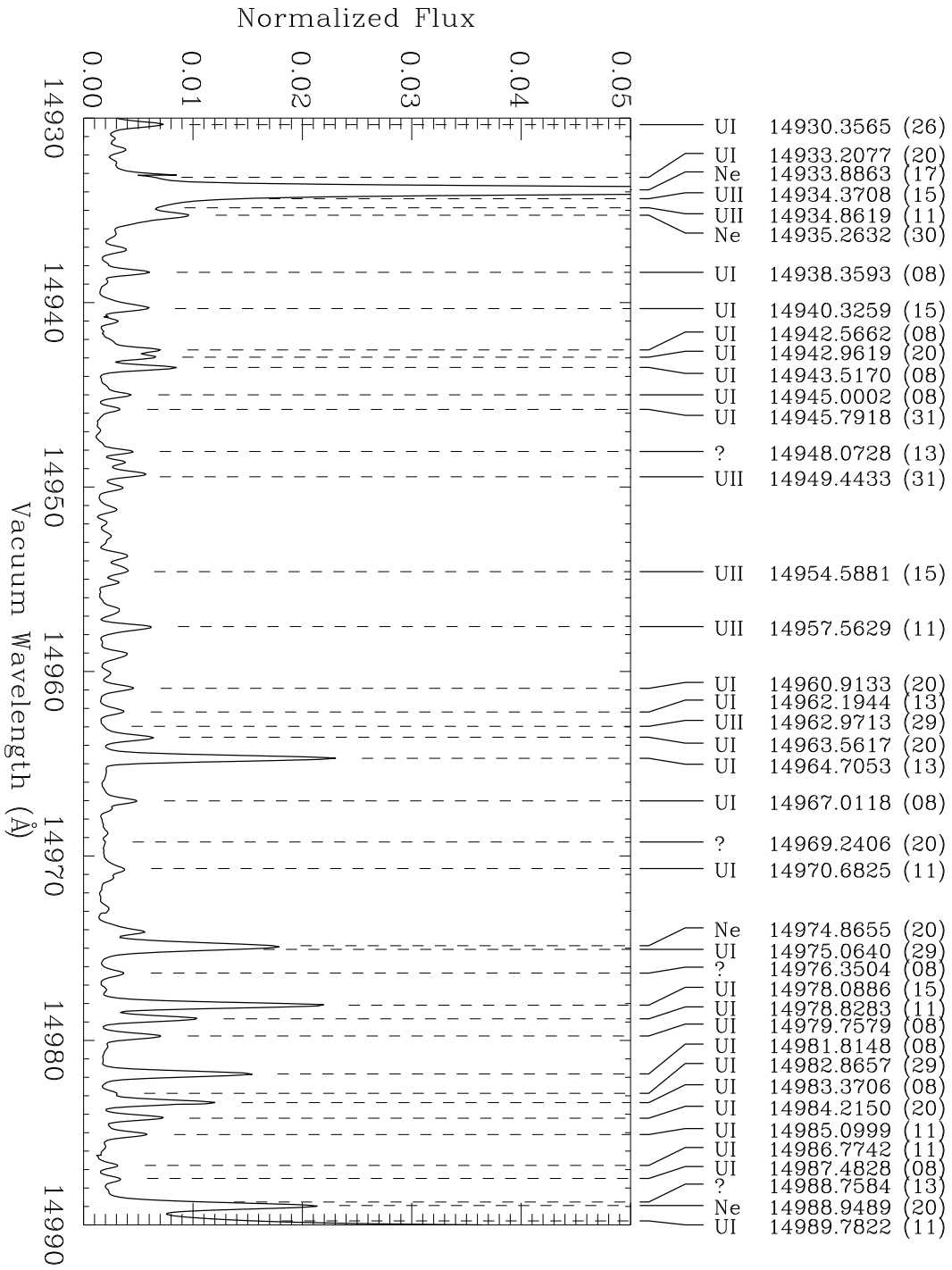
Normalized Flux
0.00
0.01
0.02
0.03
0.04
0.05
14930
14940
14950
14960
14970
14980
14990
Vacuum Wavelength (Å)
UI 14930.3565 (26)
UI 14933.2077 (20)
Ne 14933.8863 (17)
UII 14934.3708 (15)
UII 14934.8619 (11)
Ne 14935.2632 (30)
UI 14938.3593 (08)
UI 14940.3259 (15)
UI 14942.5662 (08)
UI 14942.9619 (20)
UI 14943.5170 (08)
UI 14945.0002 (08)
UI 14945.7918 (31)
? 14948.0728 (13)
UII 14949.4433 (31)
UII 14954.5881 (15)
UII 14957.5629 (11)
UI 14960.9133 (20)
UI 14962.1944 (13)
UII 14962.9713 (29)
UI 14963.5617 (20)
UI 14964.7053 (13)
UI 14967.0118 (08)
? 14969.2406 (20)
UI 14970.6825 (11)
Ne 14974.8655 (20)
UI 14975.0640 (29)
? 14976.3504 (08)
UI 14978.0886 (15)
UI 14978.8283 (11)
UI 14979.7579 (08)
UI 14981.8148 (08)
UI 14982.8657 (29)
UI 14983.3706 (08)
UI 14984.2150 (20)
UI 14985.0999 (11)
UI 14986.7742 (11)
UI 14987.4828 (08)
? 14988.7584 (13)
Ne 14988.9489 (20)
UI 14989.7822 (11)

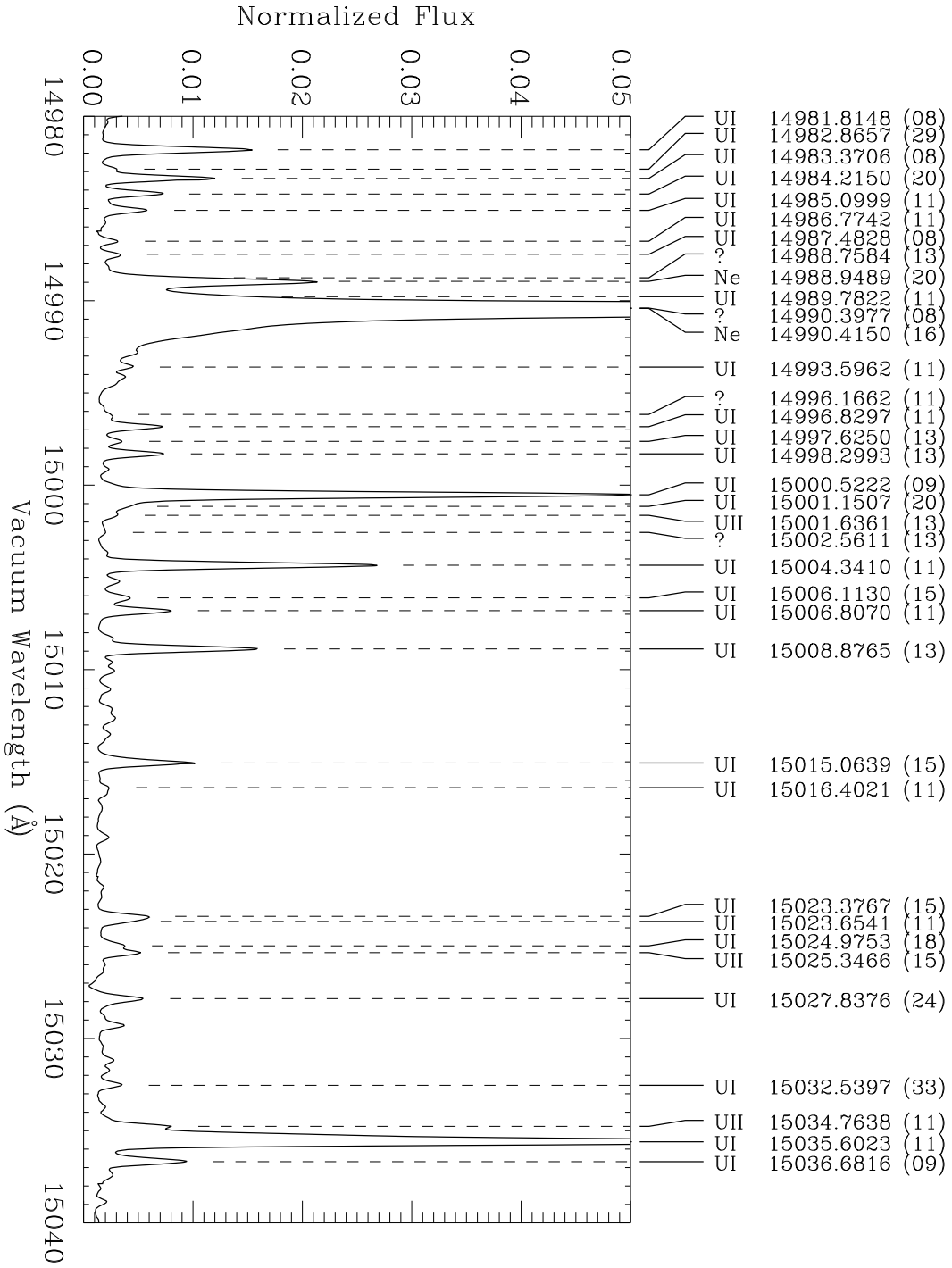
Normalized Flux
0.00
0.01
0.02
0.03
0.04
0.05
14980
14990
15000
15010
15020
15030
15040
Vacuum Wavelength (Å)
UI 14981.8148 (08)
UI 14982.8657 (29)
UI 14983.3706 (08)
UI 14984.2150 (20)
UI 14985.0999 (11)
UI 14986.7742 (11)
UI 14987.4828 (08)
? 14988.7584 (13)
Ne 14988.9489 (20)
UI 14989.7822 (11)
? 14990.3977 (08)
Ne 14990.4150 (16)
UI 14993.5962 (11)
? 14996.1662 (11)
UI 14996.8297 (11)
UI 14997.6250 (13)
UI 14998.2993 (13)
UI 15000.5222 (09)
UI 15001.1507 (20)
UII 15001.6361 (13)
? 15002.5611 (13)
UI 15004.3410 (11)
UI 15006.1130 (15)
UI 15006.8070 (11)
UI 15008.8765 (13)
UI 15015.0639 (15)
UI 15016.4021 (11)
UI 15023.3767 (15)
UI 15023.6541 (11)
UI 15024.9753 (18)
UII 15025.3466 (15)
UI 15027.8376 (24)
UI 15032.5397 (33)
UII 15034.7638 (11)
UI 15035.6023 (11)
UI 15036.6816 (09)

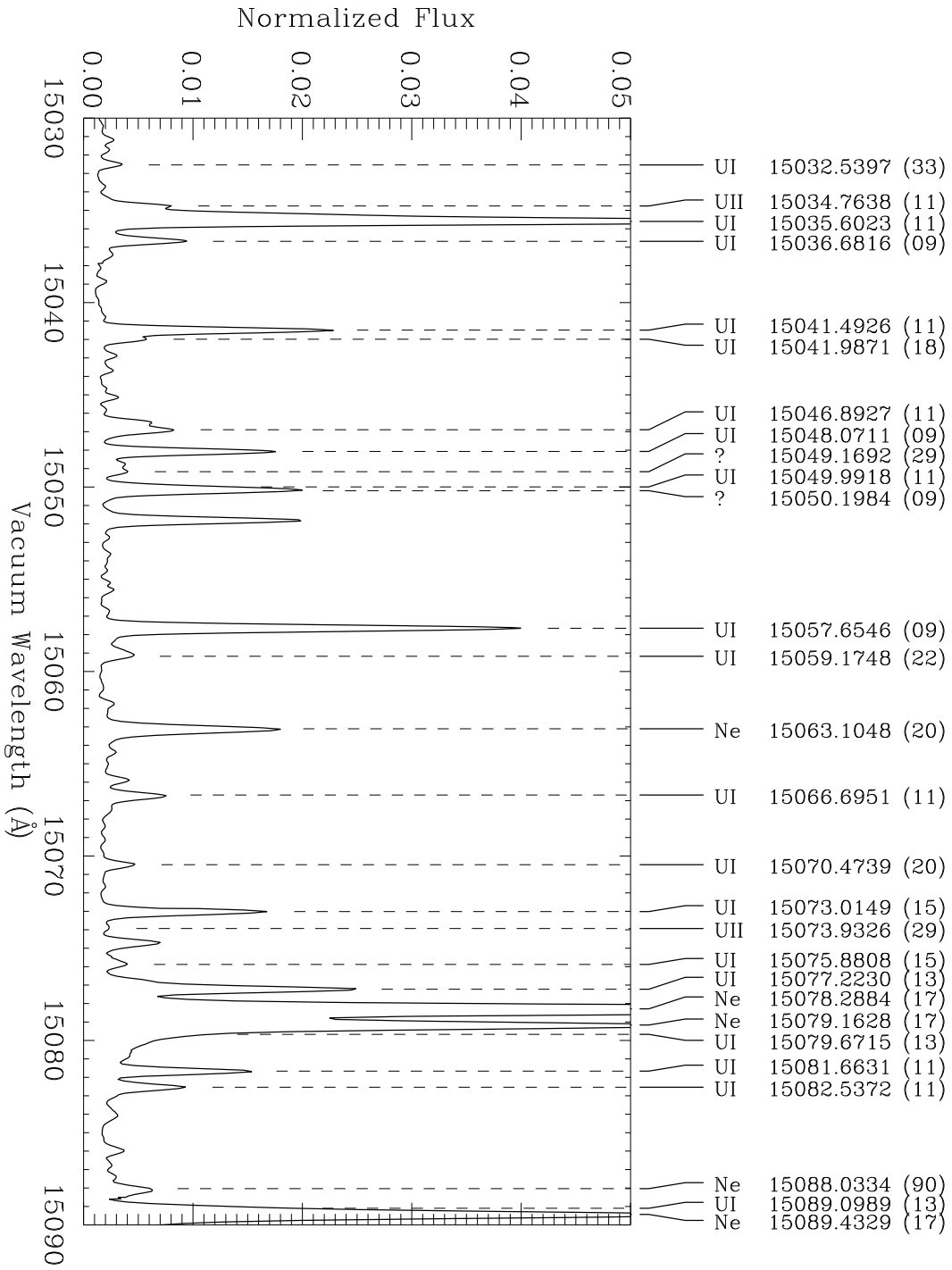
Normalized Flux
0.00
0.01
0.02
0.03
0.04
0.05
15030
15040
15050
15060
15070
15080
15090
Vacuum Wavelength (Å)
UI 15032.5397 (33)
UII 15034.7638 (11)
UI 15035.6023 (11)
UI 15036.6816 (09)
UI 15041.4926 (11)
UI 15041.9871 (18)
UI 15046.8927 (11)
UI 15048.0711 (09)
? 15049.1692 (29)
UI 15049.9918 (11)
? 15050.1984 (09)
UI 15057.6546 (09)
UI 15059.1748 (22)
Ne 15063.1048 (20)
UI 15066.6951 (11)
UI 15070.4739 (20)
UI 15073.0149 (15)
UII 15073.9326 (29)
UI 15075.8808 (15)
UI 15077.2230 (13)
Ne 15078.2884 (17)
Ne 15079.1628 (17)
UI 15079.6715 (13)
UI 15081.6631 (11)
UI 15082.5372 (11)
Ne 15088.0334 (90)
UI 15089.0989 (13)
Ne 15089.4329 (17)

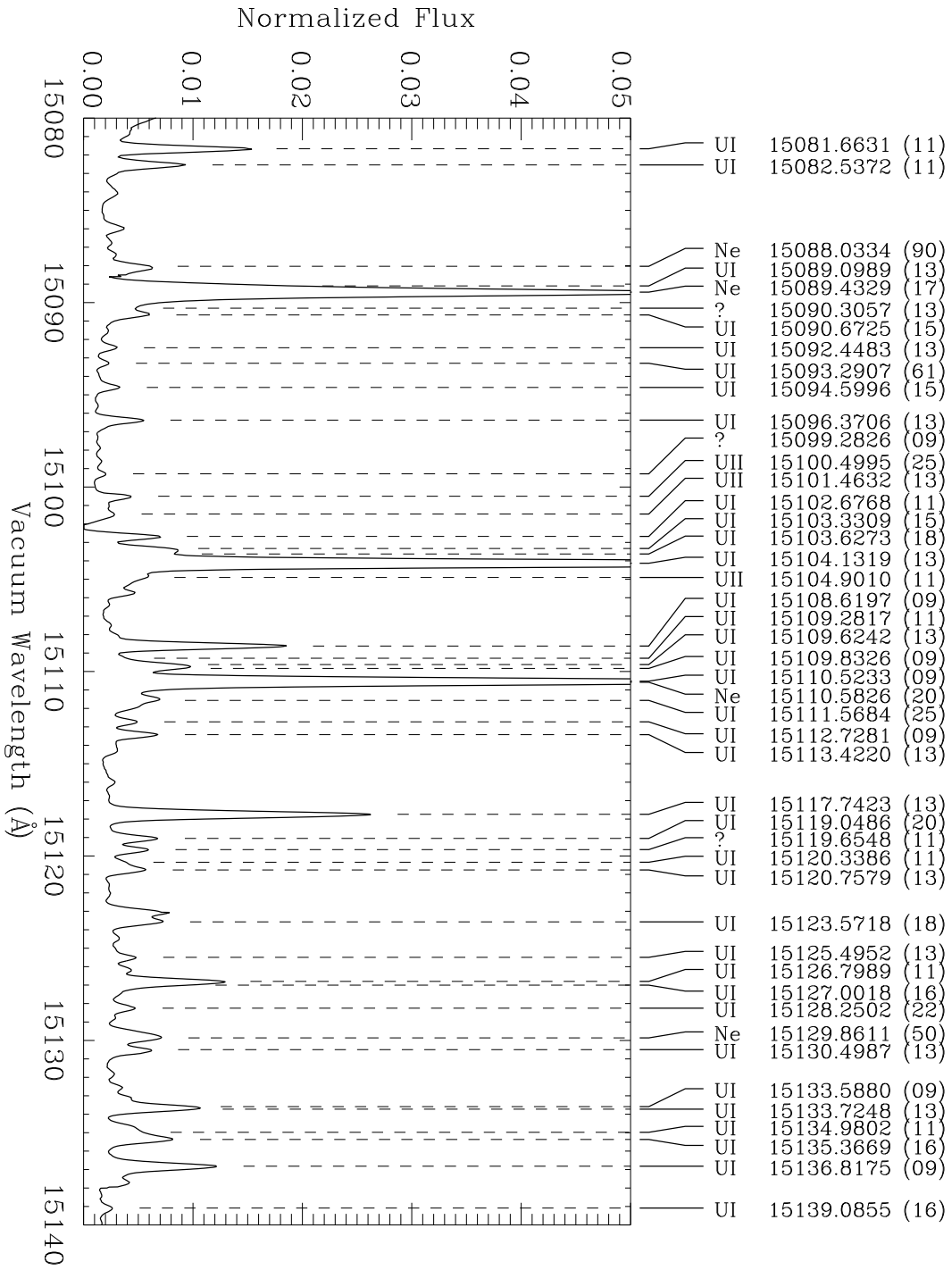
Normalized Flux
0.00
0.01
0.02
0.03
0.04
0.05
15080
15090
15100
15110
15120
15130
15140
Vacuum Wavelength (Å)
UI 15081.6631 (11)
UI 15082.5372 (11)
Ne 15088.0334 (90)
UI 15089.0989 (13)
Ne 15089.4329 (17)
? 15090.3057 (13)
UI 15090.6725 (15)
UI 15092.4483 (13)
UI 15093.2907 (61)
UI 15094.5996 (15)
UI 15096.3706 (13)
? 15099.2826 (09)
UII 15100.4995 (25)
UII 15101.4632 (13)
UI 15102.6768 (11)
UI 15103.3309 (15)
UI 15103.6273 (18)
UI 15104.1319 (13)
UII 15104.9010 (11)
UI 15108.6197 (09)
UI 15109.2817 (11)
UI 15109.6242 (13)
UI 15109.8326 (09)
UI 15110.5233 (09)
Ne 15110.5826 (20)
UI 15111.5684 (25)
UI 15112.7281 (09)
UI 15113.4220 (13)
UI 15117.7423 (13)
UI 15119.0486 (20)
? 15119.6548 (11)
UI 15120.3386 (11)
UI 15120.7579 (13)
UI 15123.5718 (18)
UI 15125.4952 (13)
UI 15126.7989 (11)
UI 15127.0018 (16)
UI 15128.2502 (22)
Ne 15129.8611 (50)
UI 15130.4987 (13)
UI 15133.5880 (09)
UI 15133.7248 (13)
UI 15134.9802 (11)
UI 15135.3669 (16)
UI 15136.8175 (09)
UI 15139.0855 (16)

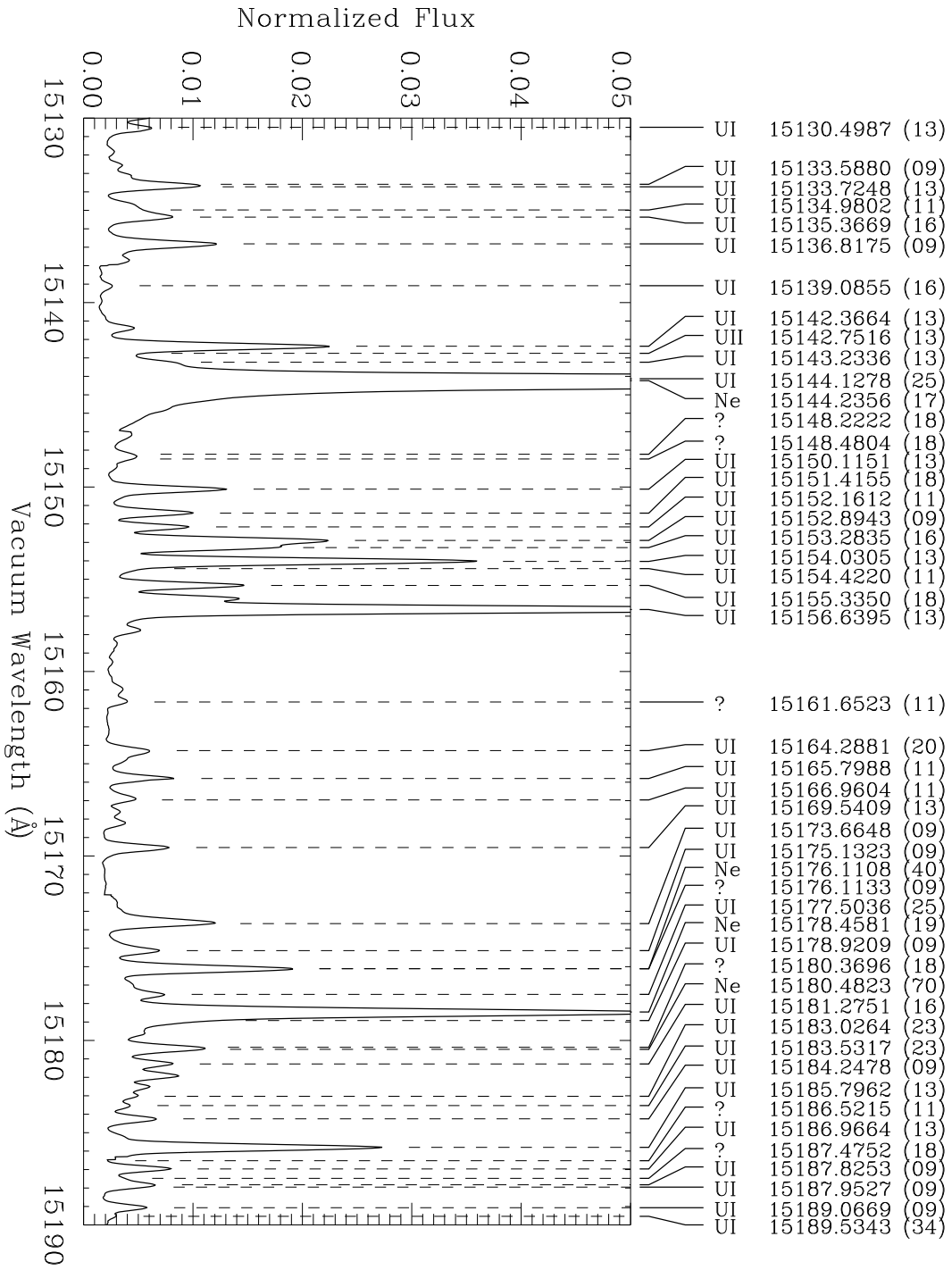
Normalized Flux
0.00
0.01
0.02
0.03
0.04
0.05
15130
15140
15150
15160
15170
15180
15190
Vacuum Wavelength (Å)
UI 15130.4987 (13)
UI 15133.5880 (09)
UI 15133.7248 (13)
UI 15134.9802 (11)
UI 15135.3669 (16)
UI 15136.8175 (09)
UI 15139.0855 (16)
UI 15142.3664 (13)
UII 15142.7516 (13)
UI 15143.2336 (13)
UI 15144.1278 (25)
Ne 15144.2356 (17)
? 15148.2222 (18)
? 15148.4804 (18)
UI 15150.1151 (13)
UI 15151.4155 (18)
UI 15152.1612 (11)
UI 15152.8943 (09)
UI 15153.2835 (16)
UI 15154.0305 (13)
UI 15154.4220 (11)
UI 15155.3350 (18)
UI 15156.6395 (13)
? 15161.6523 (11)
UI 15164.2881 (20)
UI 15165.7988 (11)
UI 15166.9604 (11)
UI 15169.5409 (13)
UI 15173.6648 (09)
UI 15175.1323 (09)
Ne 15176.1108 (40)
? 15176.1133 (09)
UI 15177.5036 (25)
Ne 15178.4581 (19)
UI 15178.9209 (09)
? 15180.3696 (18)
Ne 15180.4823 (70)
UI 15181.2751 (16)
UI 15183.0264 (23)
UI 15183.5317 (23)
UI 15184.2478 (09)
UI 15185.7962 (13)
? 15186.5215 (11)
UI 15186.9664 (13)
? 15187.4752 (18)
UI 15187.8253 (09)
UI 15187.9527 (09)
UI 15189.0669 (09)
UI 15189.5343 (34)

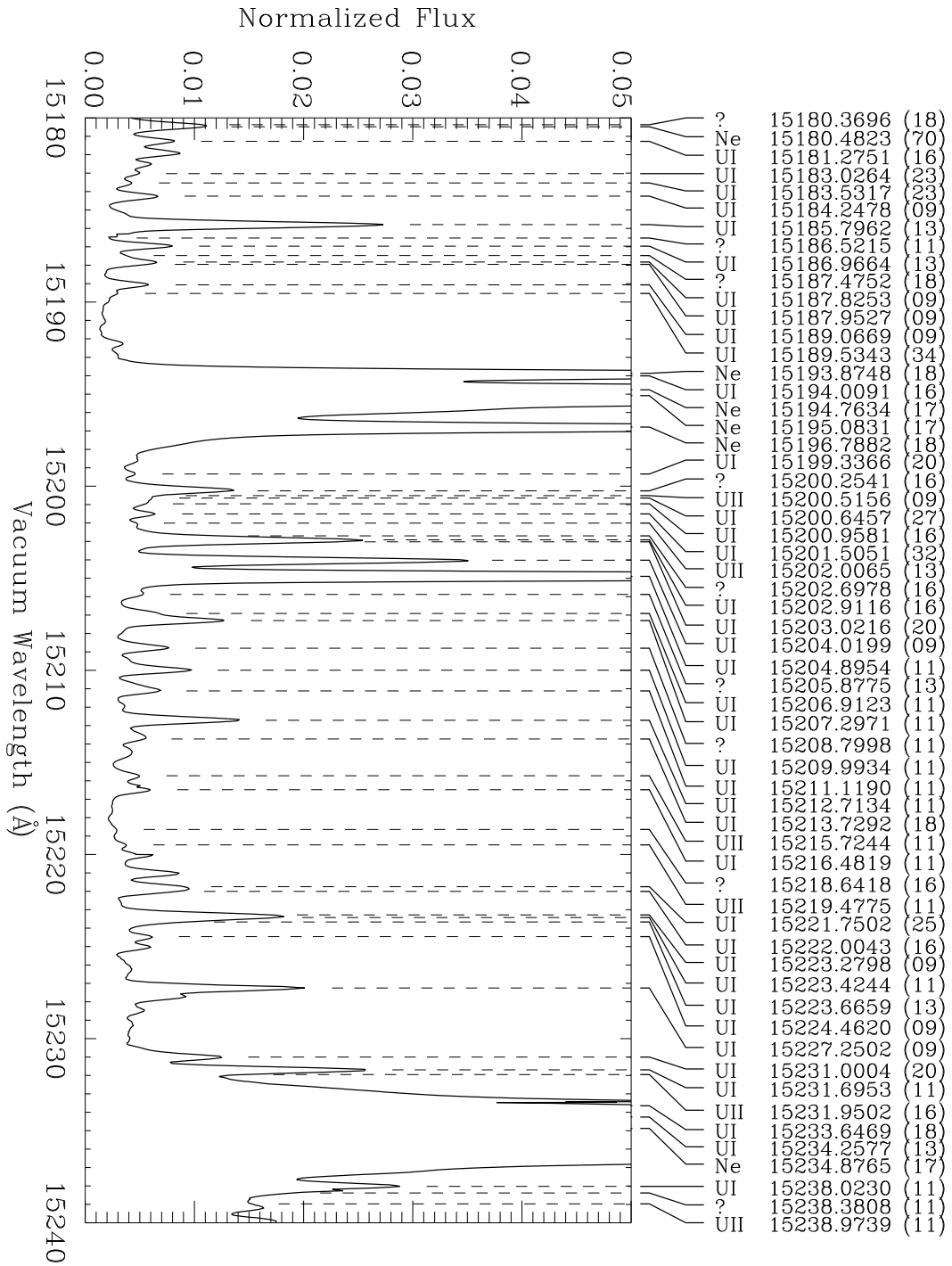
Normalized Flux
0.00
0.01
0.02
0.03
0.04
0.05
15180
15190
15200
15210
15220
15230
15240
Vacuum Wavelength (Å)
? 15180.3696 (18)
Ne 15180.4823 (70)
UI 15181.2751 (16)
UI 15183.0264 (23)
UI 15183.5317 (23)
UI 15184.2478 (09)
UI 15185.7962 (13)
? 15186.5215 (11)
UI 15186.9664 (13)
? 15187.4752 (18)
UI 15187.8253 (09)
UI 15187.9527 (09)
UI 15189.0669 (09)
UI 15189.5343 (34)
Ne 15193.8748 (18)
UI 15194.0091 (16)
Ne 15194.7634 (17)
Ne 15195.0831 (17)
Ne 15196.7882 (18)
UI 15199.3366 (20)
? 15200.2541 (16)
UII 15200.5156 (09)
UI 15200.6457 (27)
UI 15200.9581 (16)
UI 15201.5051 (32)
UII 15202.0065 (13)
? 15202.6978 (16)
UI 15202.9116 (16)
UI 15203.0216 (20)
UI 15204.0199 (09)
UI 15204.8954 (11)
? 15205.8775 (13)
UI 15206.9123 (11)
UI 15207.2971 (11)
? 15208.7998 (11)
UI 15209.9934 (11)
UI 15211.1190 (11)
UI 15212.7134 (11)
UI 15213.7292 (18)
UII 15215.7244 (11)
UI 15216.4819 (11)
? 15218.6418 (16)
UII 15219.4775 (11)
UI 15221.7502 (25)
UI 15222.0043 (16)
UI 15223.2798 (09)
UI 15223.4244 (11)
UI 15223.6659 (13)
UI 15224.4620 (09)
UI 15227.2502 (09)
UI 15231.0004 (20)
UI 15231.6953 (11)
UII 15231.9502 (16)
UI 15233.6469 (18)
UI 15234.2577 (13)
Ne 15234.8765 (17)
UI 15238.0230 (11)
? 15238.3808 (11)
UII 15238.9739 (11)

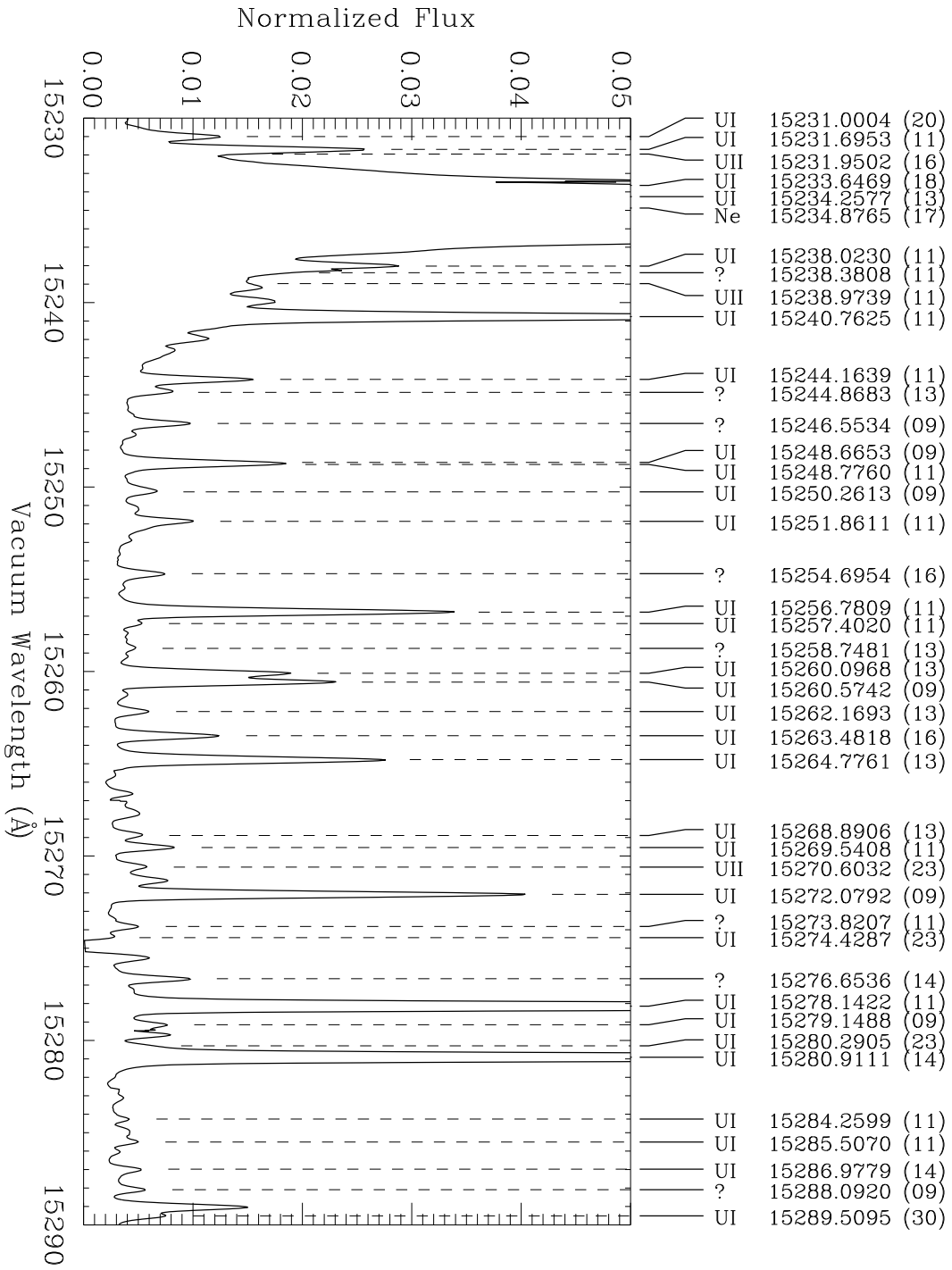
Normalized Flux
0.00
0.01
0.02
0.03
0.04
0.05
15230
15240
15250
15260
15270
15280
15290
Vacuum Wavelength (Å)
UI 15231.0004 (20)
UI 15231.6953 (11)
UII 15231.9502 (16)
UI 15233.6469 (18)
UI 15234.2577 (13)
Ne 15234.8765 (17)
UI 15238.0230 (11)
? 15238.3808 (11)
UII 15238.9739 (11)
UI 15240.7625 (11)
UI 15244.1639 (11)
? 15244.8683 (13)
? 15246.5534 (09)
UI 15248.6653 (09)
UI 15248.7760 (11)
UI 15250.2613 (09)
UI 15251.8611 (11)
? 15254.6954 (16)
UI 15256.7809 (11)
UI 15257.4020 (11)
? 15258.7481 (13)
UI 15260.0968 (13)
UI 15260.5742 (09)
UI 15262.1693 (13)
UI 15263.4818 (16)
UI 15264.7761 (13)
UI 15268.8906 (13)
UI 15269.5408 (11)
UII 15270.6032 (23)
UI 15272.0792 (09)
? 15273.8207 (11)
UI 15274.4287 (23)
? 15276.6536 (14)
UI 15278.1422 (11)
UI 15279.1488 (09)
UI 15280.2905 (23)
UI 15280.9111 (14)
UI 15284.2599 (11)
UI 15285.5070 (11)
UI 15286.9779 (14)
? 15288.0920 (09)
UI 15289.5095 (30)

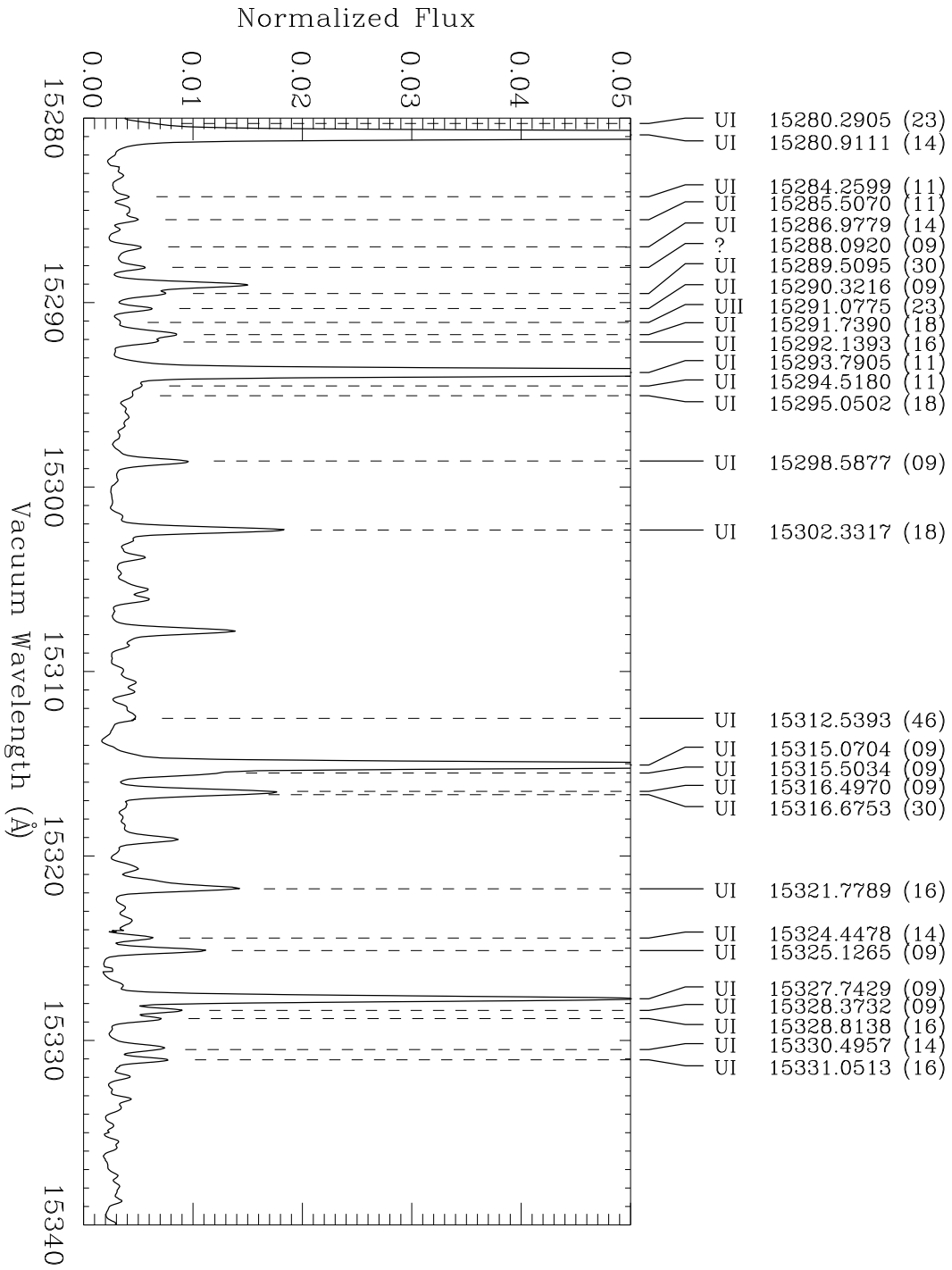
Normalized Flux
0.00
0.01
0.02
0.03
0.04
0.05
15280
15290
15300
15310
15320
15330
15340
Vacuum Wavelength (Å)
UI 15280.2905 (23)
UI 15280.9111 (14)
UI 15284.2599 (11)
UI 15285.5070 (11)
UI 15286.9779 (14)
? 15288.0920 (09)
UI 15289.5095 (30)
UI 15290.3216 (09)
UII 15291.0775 (23)
UI 15291.7390 (18)
UI 15292.1393 (16)
UI 15293.7905 (11)
UI 15294.5180 (11)
UI 15295.0502 (18)
UI 15298.5877 (09)
UI 15302.3317 (18)
UI 15312.5393 (46)
UI 15315.0704 (09)
UI 15315.5034 (09)
UI 15316.4970 (09)
UI 15316.6753 (30)
UI 15321.7789 (16)
UI 15324.4478 (14)
UI 15325.1265 (09)
UI 15327.7429 (09)
UI 15328.3732 (09)
UI 15328.8138 (16)
UI 15330.4957 (14)
UI 15331.0513 (16)

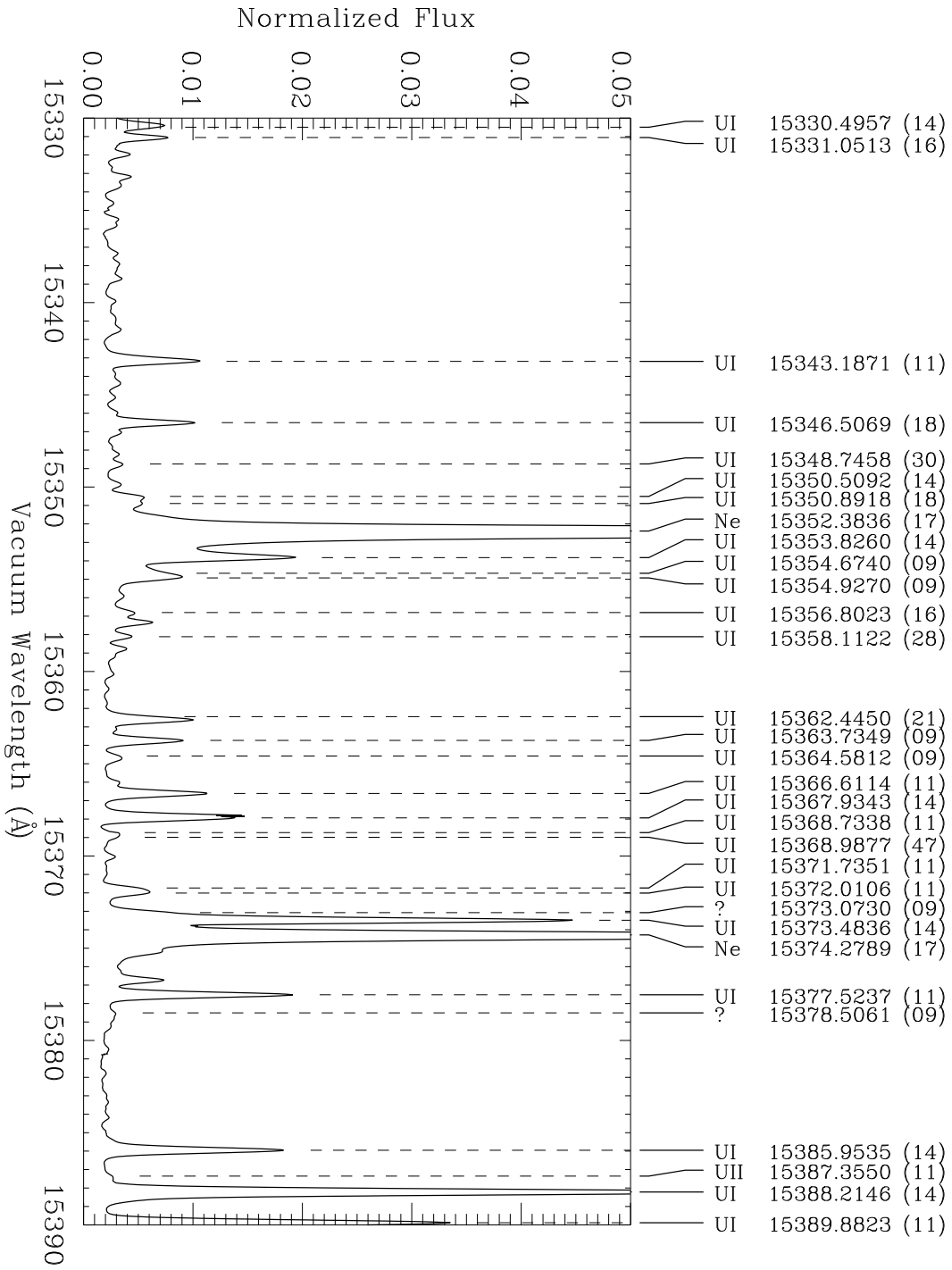
Normalized Flux
0.00
0.01
0.02
0.03
0.04
0.05
15330
15340
15350
15360
15370
15380
15390
Vacuum Wavelength (Å)
UI 15330.4957 (14)
UI 15331.0513 (16)
UI 15343.1871 (11)
UI 15346.5069 (18)
UI 15348.7458 (30)
UI 15350.5092 (14)
UI 15350.8918 (18)
Ne 15352.3836 (17)
UI 15353.8260 (14)
UI 15354.6740 (09)
UI 15354.9270 (09)
UI 15356.8023 (16)
UI 15358.1122 (28)
UI 15362.4450 (21)
UI 15363.7349 (09)
UI 15364.5812 (09)
UI 15366.6114 (11)
UI 15367.9343 (14)
UI 15368.7338 (11)
UI 15368.9877 (47)
UI 15371.7351 (11)
UI 15372.0106 (11)
? 15373.0730 (09)
UI 15373.4836 (14)
Ne 15374.2789 (17)
UI 15377.5237 (11)
? 15378.5061 (09)
UI 15385.9535 (14)
UII 15387.3550 (11)
UI 15388.2146 (14)
UI 15389.8823 (11)

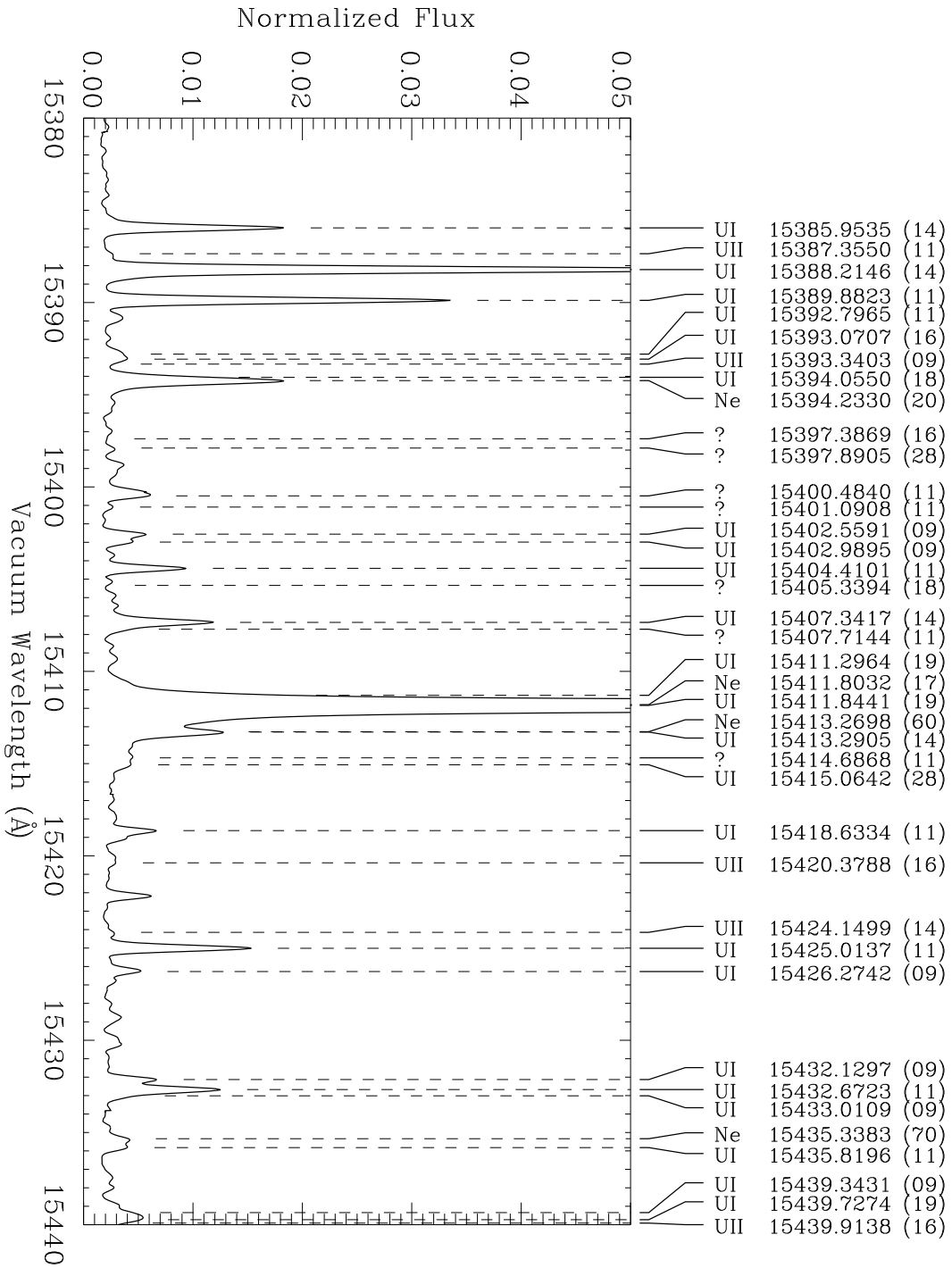
Normalized Flux
0.00
0.01
0.02
0.03
0.04
0.05
15380
15390
15400
15410
15420
15430
15440
Vacuum Wavelength (Å)
UI 15385.9535 (14)
UII 15387.3550 (11)
UI 15388.2146 (14)
UI 15389.8823 (11)
UI 15392.7965 (11)
UI 15393.0707 (16)
UII 15393.3403 (09)
UI 15394.0550 (18)
Ne 15394.2330 (20)
? 15397.3869 (16)
? 15397.8905 (28)
? 15400.4840 (11)
? 15401.0908 (11)
UI 15402.5591 (09)
UI 15402.9895 (09)
UI 15404.4101 (11)
? 15405.3394 (18)
UI 15407.3417 (14)
? 15407.7144 (11)
UI 15411.2964 (19)
Ne 15411.8032 (17)
UI 15411.8441 (19)
Ne 15413.2698 (60)
UI 15413.2905 (14)
? 15414.6868 (11)
UI 15415.0642 (28)
UI 15418.6334 (11)
UII 15420.3788 (16)
UII 15424.1499 (14)
UI 15425.0137 (11)
UI 15426.2742 (09)
UI 15432.1297 (09)
UI 15432.6723 (11)
UI 15433.0109 (09)
Ne 15435.3383 (70)
UI 15435.8196 (11)
UI 15439.3431 (09)
UI 15439.7274 (19)
UII 15439.9138 (16)

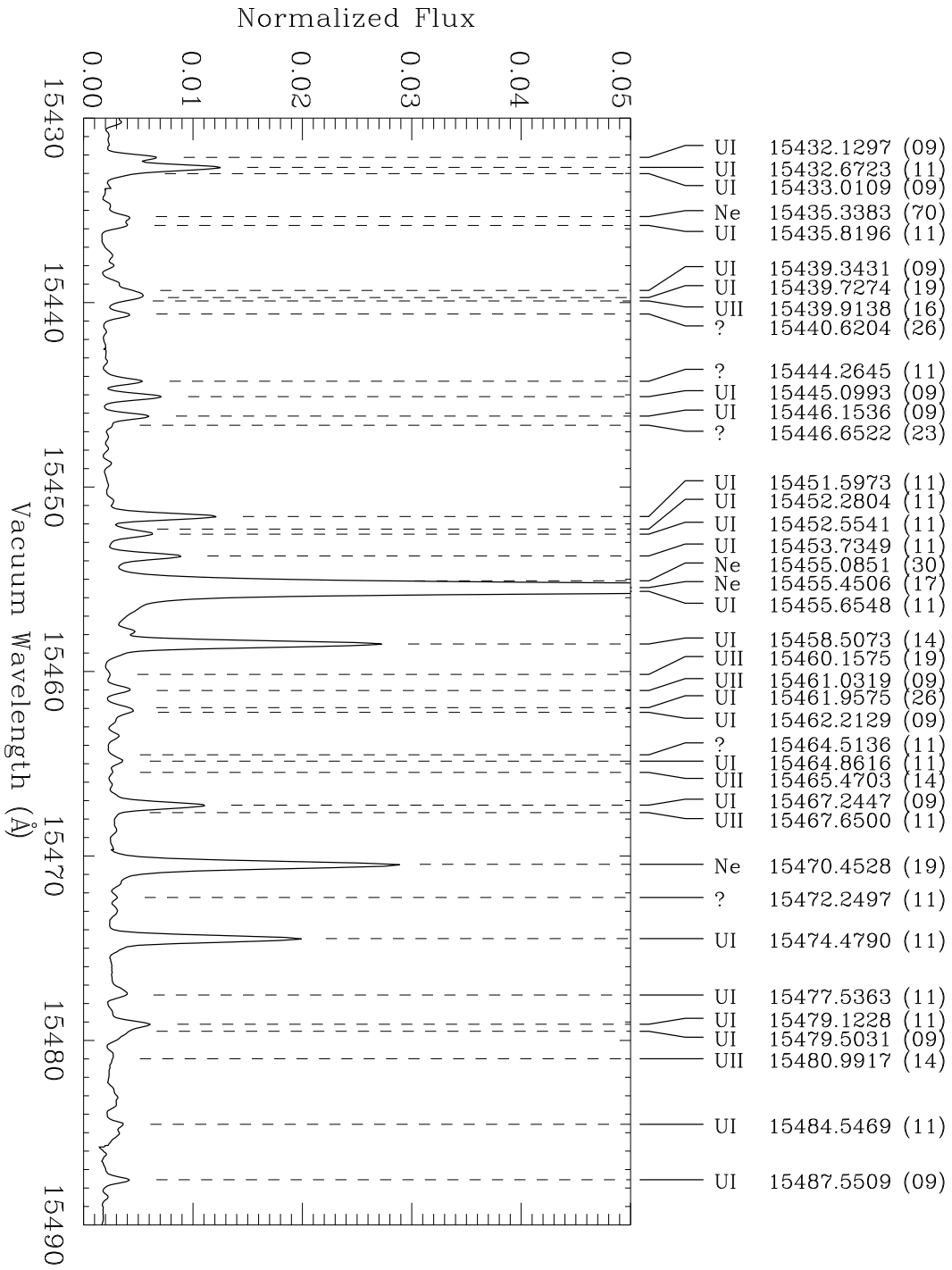
Normalized Flux
0.00
0.01
0.02
0.03
0.04
0.05
15430
15440
15450
15460
15470
15480
15490
Vacuum Wavelength (Å)
UI 15432.1297 (09)
UI 15432.6723 (11)
UI 15433.0109 (09)
Ne 15435.3383 (70)
UI 15435.8196 (11)
UI 15439.3431 (09)
UI 15439.7274 (19)
UII 15439.9138 (16)
? 15440.6204 (26)
? 15444.2645 (11)
UI 15445.0993 (09)
UI 15446.1536 (09)
? 15446.6522 (23)
UI 15451.5973 (11)
UI 15452.2804 (11)
UI 15452.5541 (11)
UI 15453.7349 (11)
Ne 15455.0851 (30)
Ne 15455.4506 (17)
UI 15455.6548 (11)
UI 15458.5073 (14)
UII 15460.1575 (19)
UII 15461.0319 (09)
UI 15461.9575 (26)
UI 15462.2129 (09)
? 15464.5136 (11)
UI 15464.8616 (11)
UII 15465.4703 (14)
UI 15467.2447 (09)
UII 15467.6500 (11)
Ne 15470.4528 (19)
? 15472.2497 (11)
UI 15474.4790 (11)
UI 15477.5363 (11)
UI 15479.1228 (11)
UI 15479.5031 (09)
UII 15480.9917 (14)
UI 15484.5469 (11)
UI 15487.5509 (09)

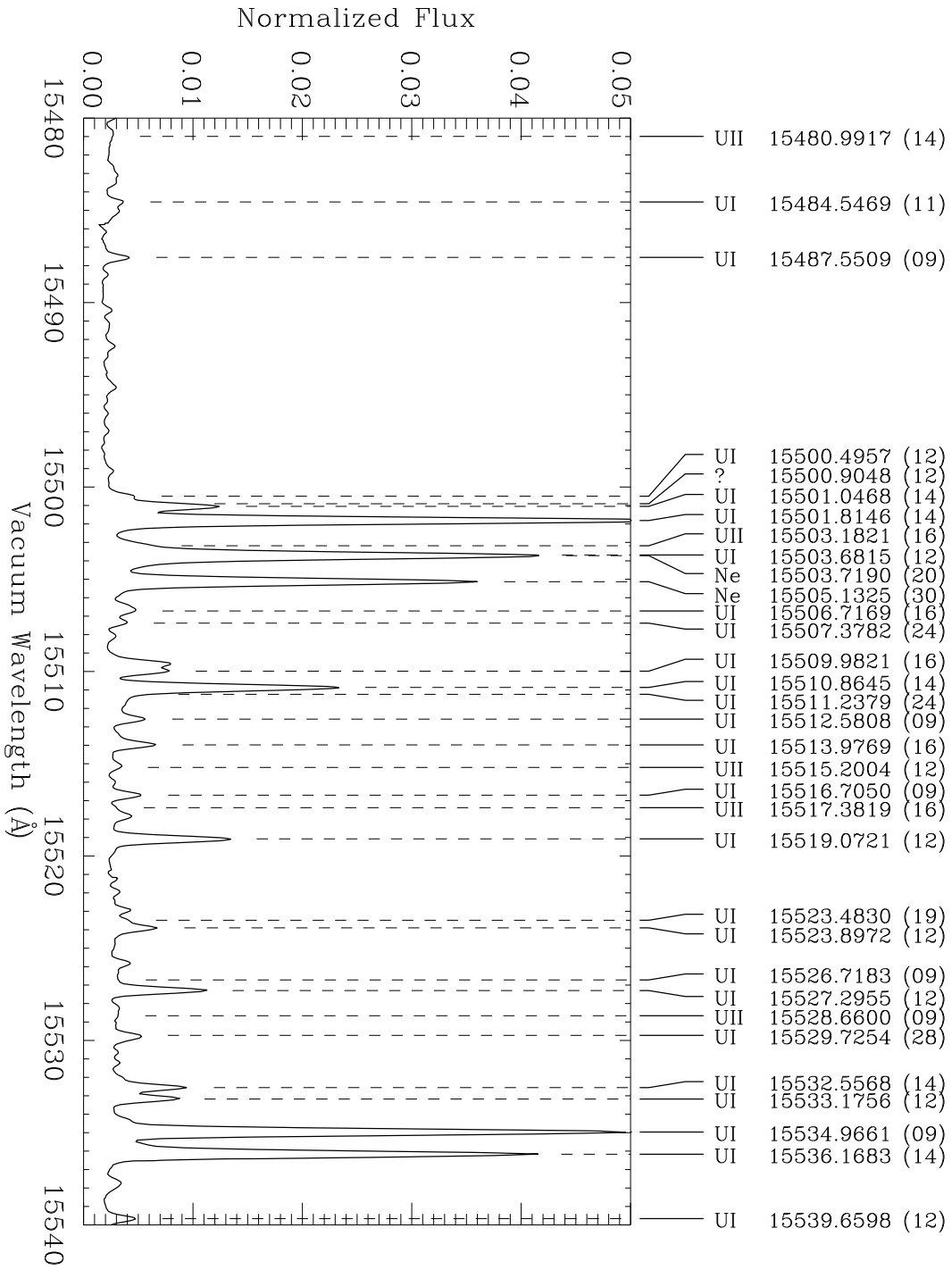
Normalized Flux
0.00
0.01
0.02
0.03
0.04
0.05
15480
15490
15500
15510
15520
15530
15540
Vacuum Wavelength (Å)
UII 15480.9917 (14)
UI 15484.5469 (11)
UI 15487.5509 (09)
UI 15500.4957 (12)
? 15500.9048 (12)
UI 15501.0468 (14)
UI 15501.8146 (14)
UII 15503.1821 (16)
UI 15503.6815 (12)
Ne 15503.7190 (20)
Ne 15505.1325 (30)
UI 15506.7169 (16)
UI 15507.3782 (24)
UI 15509.9821 (16)
UI 15510.8645 (14)
UI 15511.2379 (24)
UI 15512.5808 (09)
UI 15513.9769 (16)
UII 15515.2004 (12)
UI 15516.7050 (09)
UII 15517.3819 (16)
UI 15519.0721 (12)
UI 15523.4830 (19)
UI 15523.8972 (12)
UI 15526.7183 (09)
UI 15527.2955 (12)
UII 15528.6600 (09)
UI 15529.7254 (28)
UI 15532.5568 (14)
UI 15533.1756 (12)
UI 15534.9661 (09)
UI 15536.1683 (14)
UI 15539.6598 (12)

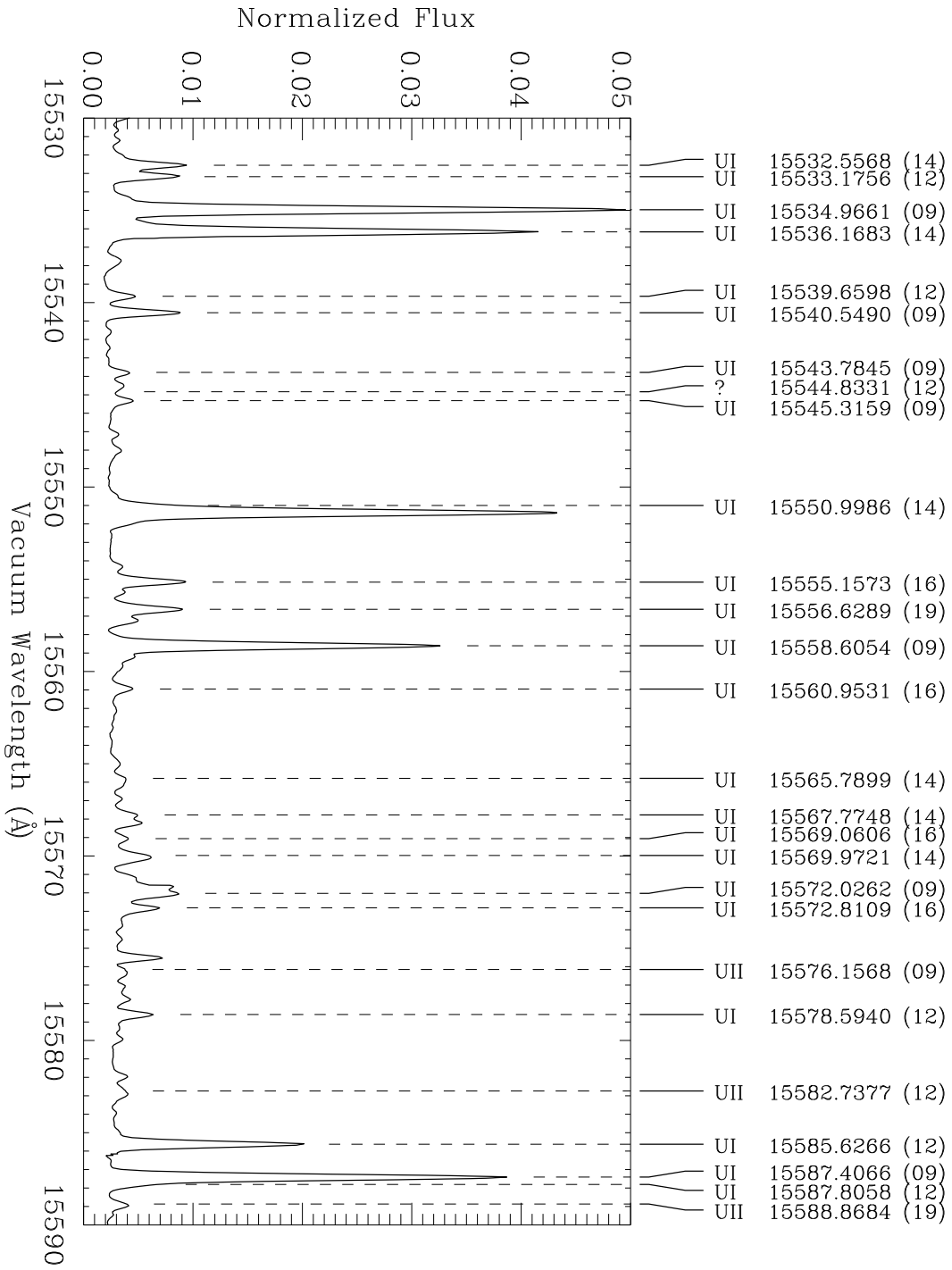
Normalized Flux
0.00
0.01
0.02
0.03
0.04
0.05
15530
15540
15550
15560
15570
15580
15590
Vacuum Wavelength (Å)
UI 15532.5568 (14)
UI 15533.1756 (12)
UI 15534.9661 (09)
UI 15536.1683 (14)
UI 15539.6598 (12)
UI 15540.5490 (09)
UI 15543.7845 (09)
? 15544.8331 (12)
UI 15545.3159 (09)
UI 15550.9986 (14)
UI 15555.1573 (16)
UI 15556.6289 (19)
UI 15558.6054 (09)
UI 15560.9531 (16)
UI 15565.7899 (14)
UI 15567.7748 (14)
UI 15569.0606 (16)
UI 15569.9721 (14)
UI 15572.0262 (09)
UI 15572.8109 (16)
UII 15576.1568 (09)
UI 15578.5940 (12)
UII 15582.7377 (12)
UI 15585.6266 (12)
UI 15587.4066 (09)
UI 15587.8058 (12)
UII 15588.8684 (19)

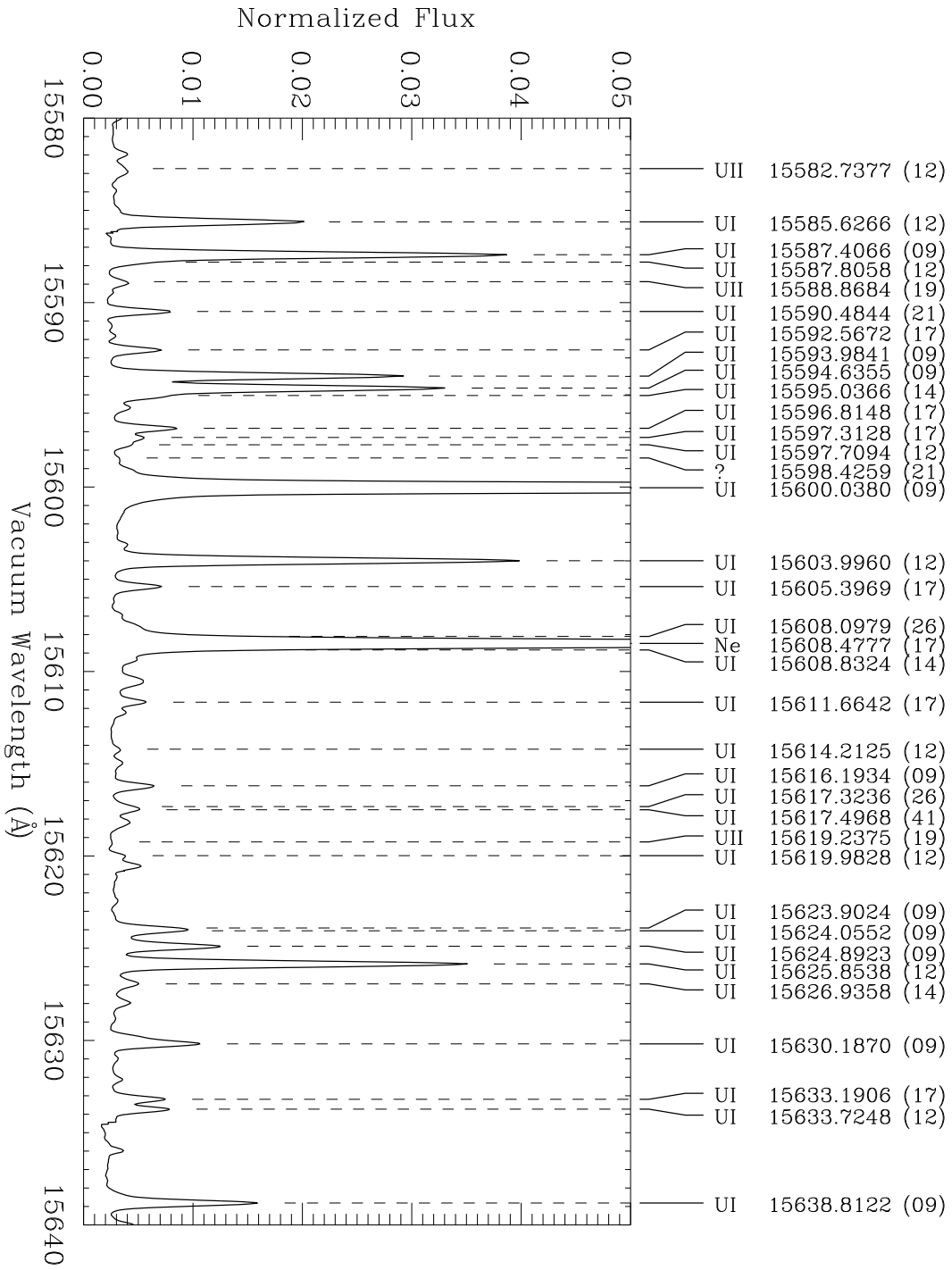
Normalized Flux
0.00
0.01
0.02
0.03
0.04
0.05
15580
15590
15600
15610
15620
15630
15640
Vacuum Wavelength (Å)
UII 15582.7377 (12)
UI 15585.6266 (12)
UI 15587.4066 (09)
UI 15587.8058 (12)
UII 15588.8684 (19)
UI 15590.4844 (21)
UI 15592.5672 (17)
UI 15593.9841 (09)
UI 15594.6355 (09)
UI 15595.0366 (14)
UI 15596.8148 (17)
UI 15597.3128 (17)
UI 15597.7094 (12)
? 15598.4259 (21)
UI 15600.0380 (09)
UI 15603.9960 (12)
UI 15605.3969 (17)
UI 15608.0979 (26)
Ne 15608.4777 (17)
UI 15608.8324 (14)
UI 15611.6642 (17)
UI 15614.2125 (12)
UI 15616.1934 (09)
UI 15617.3236 (26)
UI 15617.4968 (41)
UII 15619.2375 (19)
UI 15619.9828 (12)
UI 15623.9024 (09)
UI 15624.0552 (09)
UI 15624.8923 (09)
UI 15625.8538 (12)
UI 15626.9358 (14)
UI 15630.1870 (09)
UI 15633.1906 (17)
UI 15633.7248 (12)
UI 15638.8122 (09)

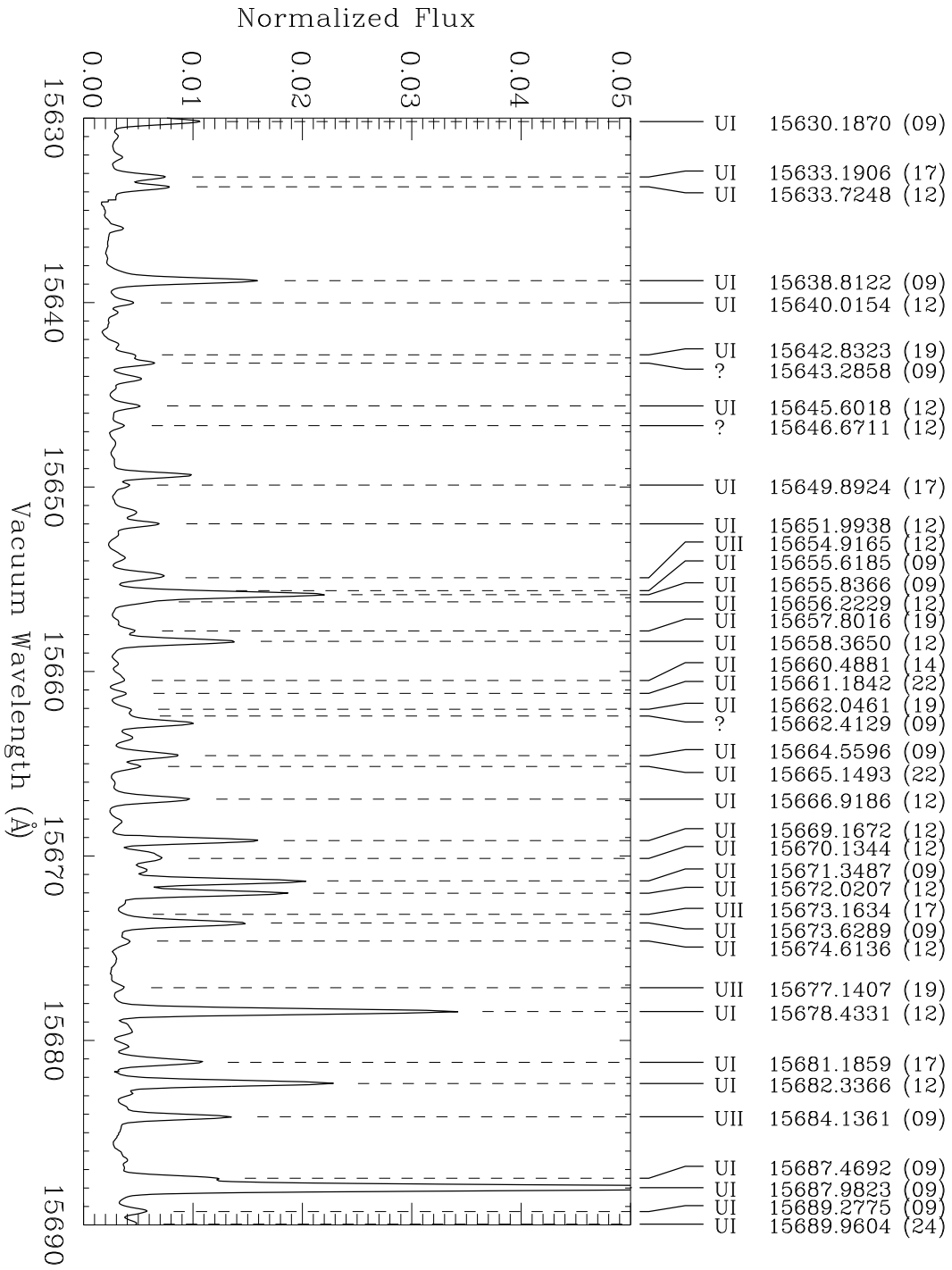
Normalized Flux
0.00
0.01
0.02
0.03
0.04
0.05
15630
15640
15650
15660
15670
15680
15690
Vacuum Wavelength (Å)
UI 15630.1870 (09)
UI 15633.1906 (17)
UI 15633.7248 (12)
UI 15638.8122 (09)
UI 15640.0154 (12)
UI 15642.8323 (19)
? 15643.2858 (09)
UI 15645.6018 (12)
? 15646.6711 (12)
UI 15649.8924 (17)
UI 15651.9938 (12)
UII 15654.9165 (12)
UI 15655.6185 (09)
UI 15655.8366 (09)
UI 15656.2229 (12)
UI 15657.8016 (19)
UI 15658.3650 (12)
UI 15660.4881 (14)
UI 15661.1842 (22)
UI 15662.0461 (19)
? 15662.4129 (09)
UI 15664.5596 (09)
UI 15665.1493 (22)
UI 15666.9186 (12)
UI 15669.1672 (12)
UI 15670.1344 (12)
UI 15671.3487 (09)
UI 15672.0207 (12)
UII 15673.1634 (17)
UI 15673.6289 (09)
UI 15674.6136 (12)
UII 15677.1407 (19)
UI 15678.4331 (12)
UI 15681.1859 (17)
UI 15682.3366 (12)
UII 15684.1361 (09)
UI 15687.4692 (09)
UI 15687.9823 (09)
UI 15689.2775 (09)
UI 15689.9604 (24)

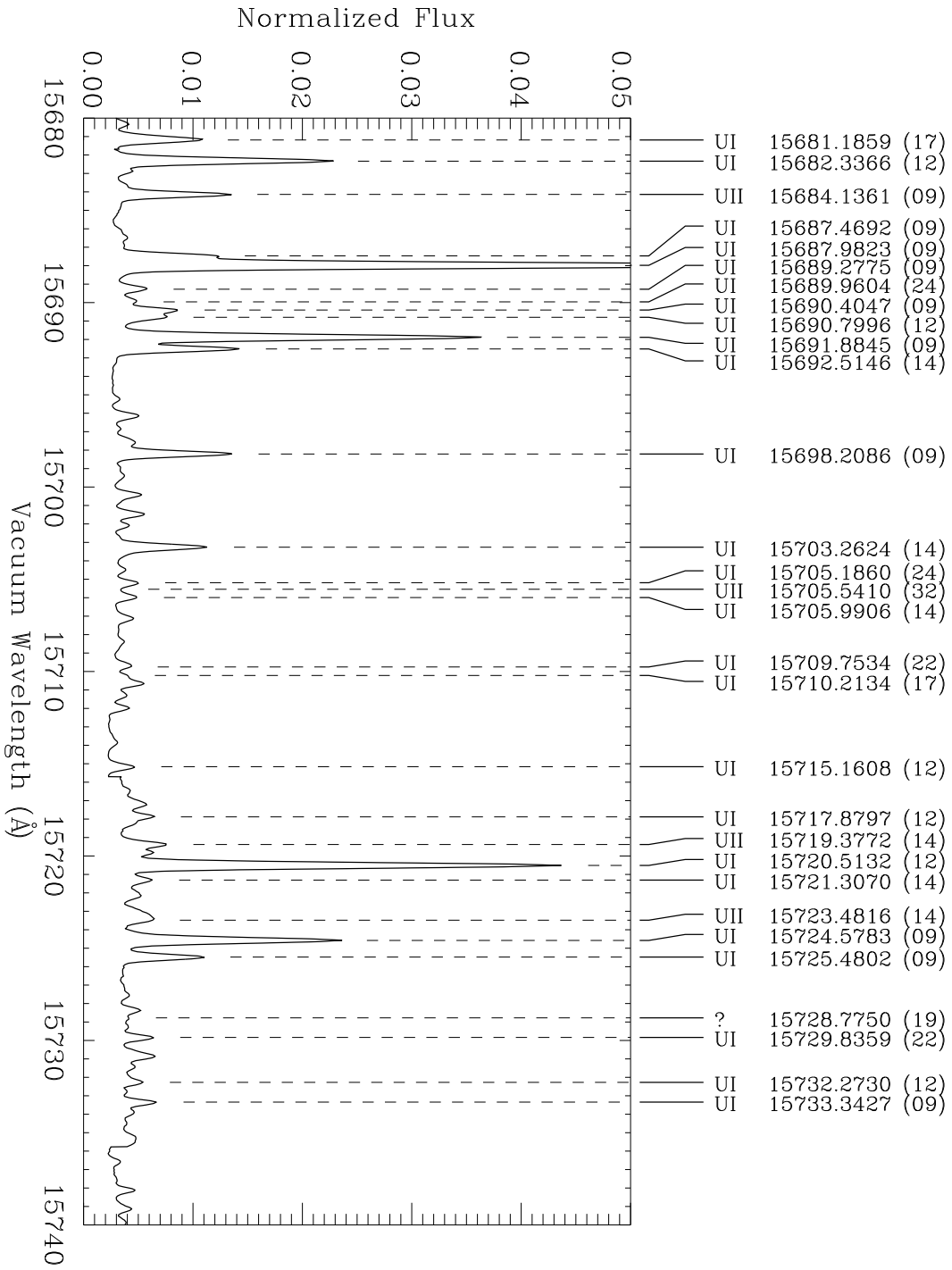
Normalized Flux
0.00
0.01
0.02
0.03
0.04
0.05
15680
15690
15700
15710
15720
15730
15740
Vacuum Wavelength (Å)
UI 15681.1859 (17)
UI 15682.3366 (12)
UII 15684.1361 (09)
UI 15687.4692 (09)
UI 15687.9823 (09)
UI 15689.2775 (09)
UI 15689.9604 (24)
UI 15690.4047 (09)
UI 15690.7996 (12)
UI 15691.8845 (09)
UI 15692.5146 (14)
UI 15698.2086 (09)
UI 15703.2624 (14)
UI 15705.1860 (24)
UII 15705.5410 (32)
UI 15705.9906 (14)
UI 15709.7534 (22)
UI 15710.2134 (17)
UI 15715.1608 (12)
UI 15717.8797 (12)
UII 15719.3772 (14)
UI 15720.5132 (12)
UI 15721.3070 (14)
UII 15723.4816 (14)
UI 15724.5783 (09)
UI 15725.4802 (09)
? 15728.7750 (19)
UI 15729.8359 (22)
UI 15732.2730 (12)
UI 15733.3427 (09)

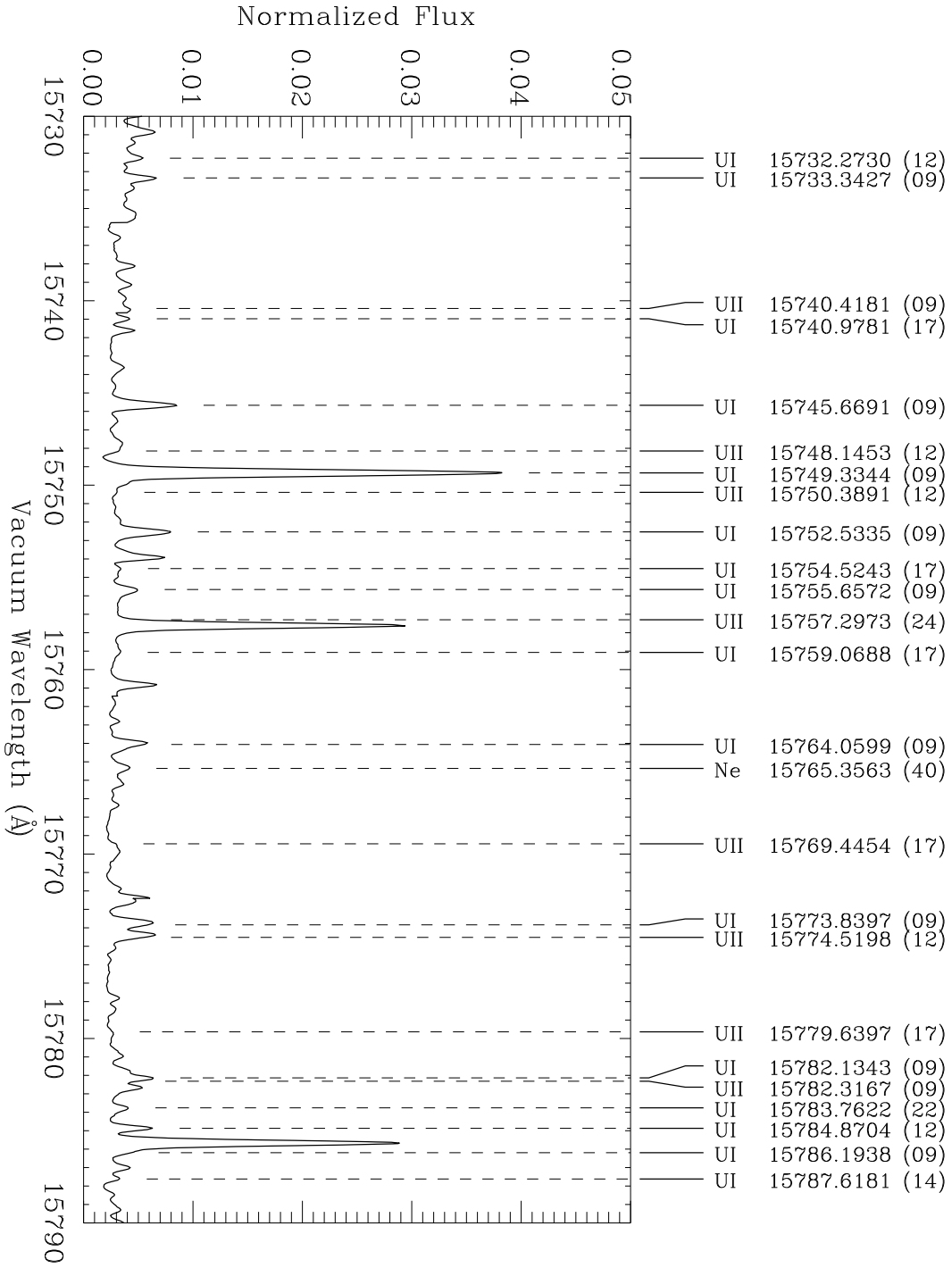
Normalized Flux
0.00
0.01
0.02
0.03
0.04
0.05
15730
15740
15750
15760
15770
15780
15790
Vacuum Wavelength (Å)
UI 15732.2730 (12)
UI 15733.3427 (09)
UII 15740.4181 (09)
UI 15740.9781 (17)
UI 15745.6691 (09)
UII 15748.1453 (12)
UI 15749.3344 (09)
UII 15750.3891 (12)
UI 15752.5335 (09)
UI 15754.5243 (17)
UI 15755.6572 (09)
UII 15757.2973 (24)
UI 15759.0688 (17)
UI 15764.0599 (09)
Ne 15765.3563 (40)
UII 15769.4454 (17)
UI 15773.8397 (09)
UII 15774.5198 (12)
UII 15779.6397 (17)
UI 15782.1343 (09)
UII 15782.3167 (09)
UI 15783.7622 (22)
UI 15784.8704 (12)
UI 15786.1938 (09)
UI 15787.6181 (14)

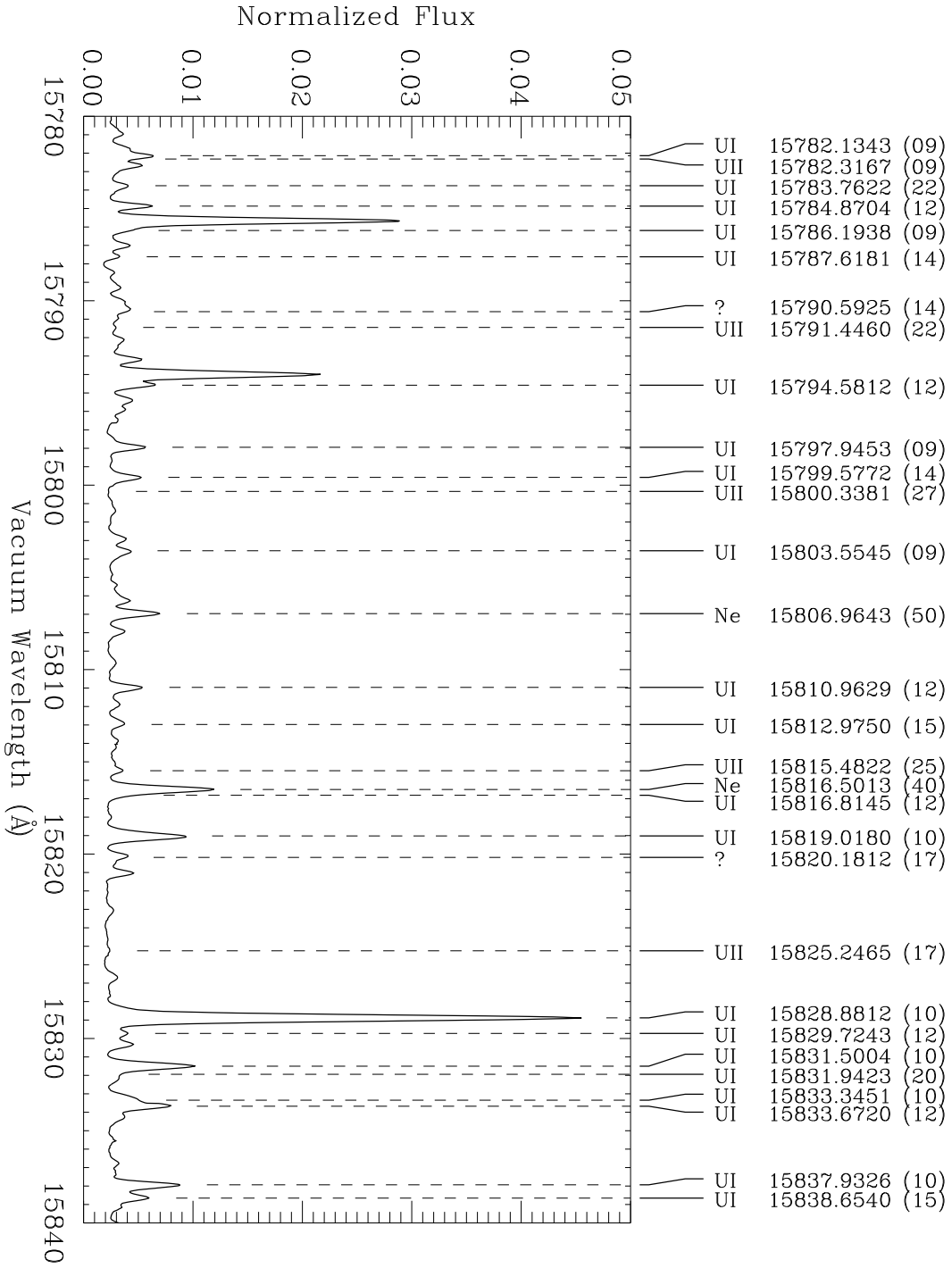
Normalized Flux
0.00
0.01
0.02
0.03
0.04
0.05
15780
15790
15800
15810
15820
15830
15840
Vacuum Wavelength (Å)
UI 15782.1343 (09)
UII 15782.3167 (09)
UI 15783.7622 (22)
UI 15784.8704 (12)
UI 15786.1938 (09)
UI 15787.6181 (14)
? 15790.5925 (14)
UII 15791.4460 (22)
UI 15794.5812 (12)
UI 15797.9453 (09)
UI 15799.5772 (14)
UII 15800.3381 (27)
UI 15803.5545 (09)
Ne 15806.9643 (50)
UI 15810.9629 (12)
UI 15812.9750 (15)
UII 15815.4822 (25)
Ne 15816.5013 (40)
UI 15816.8145 (12)
UI 15819.0180 (10)
? 15820.1812 (17)
UII 15825.2465 (17)
UI 15828.8812 (10)
UI 15829.7243 (12)
UI 15831.5004 (10)
UI 15831.9423 (20)
UI 15833.3451 (10)
UI 15833.6720 (12)
UI 15837.9326 (10)
UI 15838.6540 (15)

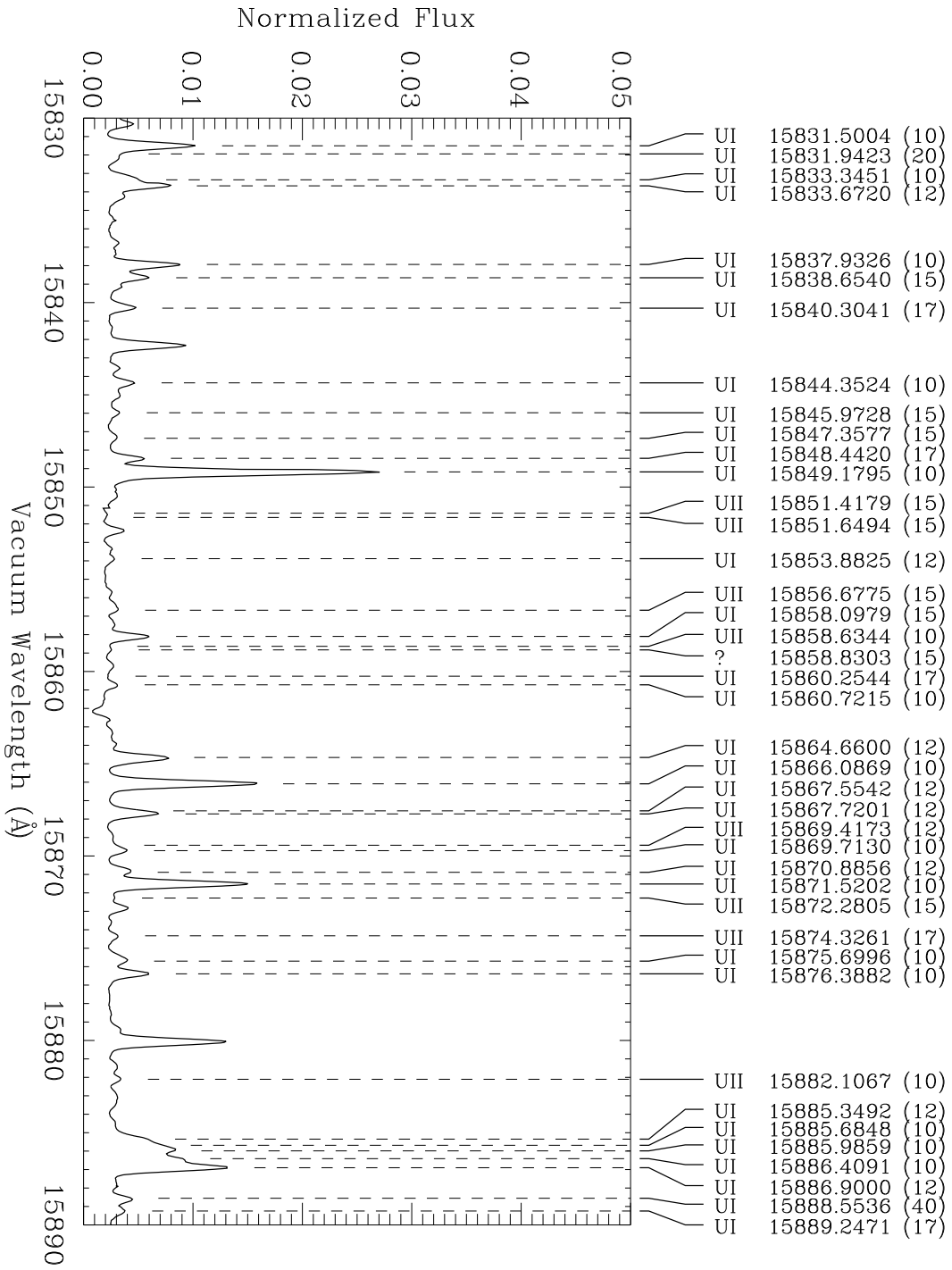
Normalized Flux
0.00
0.01
0.02
0.03
0.04
0.05
15830
15840
15850
15860
15870
15880
15890
Vacuum Wavelength (Å)
UI 15831.5004 (10)
UI 15831.9423 (20)
UI 15833.3451 (10)
UI 15833.6720 (12)
UI 15837.9326 (10)
UI 15838.6540 (15)
UI 15840.3041 (17)
UI 15844.3524 (10)
UI 15845.9728 (15)
UI 15847.3577 (15)
UI 15848.4420 (17)
UI 15849.1795 (10)
UII 15851.4179 (15)
UII 15851.6494 (15)
UI 15853.8825 (12)
UII 15856.6775 (15)
UI 15858.0979 (15)
UII 15858.6344 (10)
? 15858.8303 (15)
UI 15860.2544 (17)
UI 15860.7215 (10)
UI 15864.6600 (12)
UI 15866.0869 (10)
UI 15867.5542 (12)
UI 15867.7201 (12)
UII 15869.4173 (12)
UI 15869.7130 (10)
UI 15870.8856 (12)
UI 15871.5202 (10)
UII 15872.2805 (15)
UII 15874.3261 (17)
UI 15875.6996 (10)
UI 15876.3882 (10)
UII 15882.1067 (10)
UI 15885.3492 (12)
UI 15885.6848 (10)
UI 15885.9859 (10)
UI 15886.4091 (10)
UI 15886.9000 (12)
UI 15888.5536 (40)
UI 15889.2471 (17)

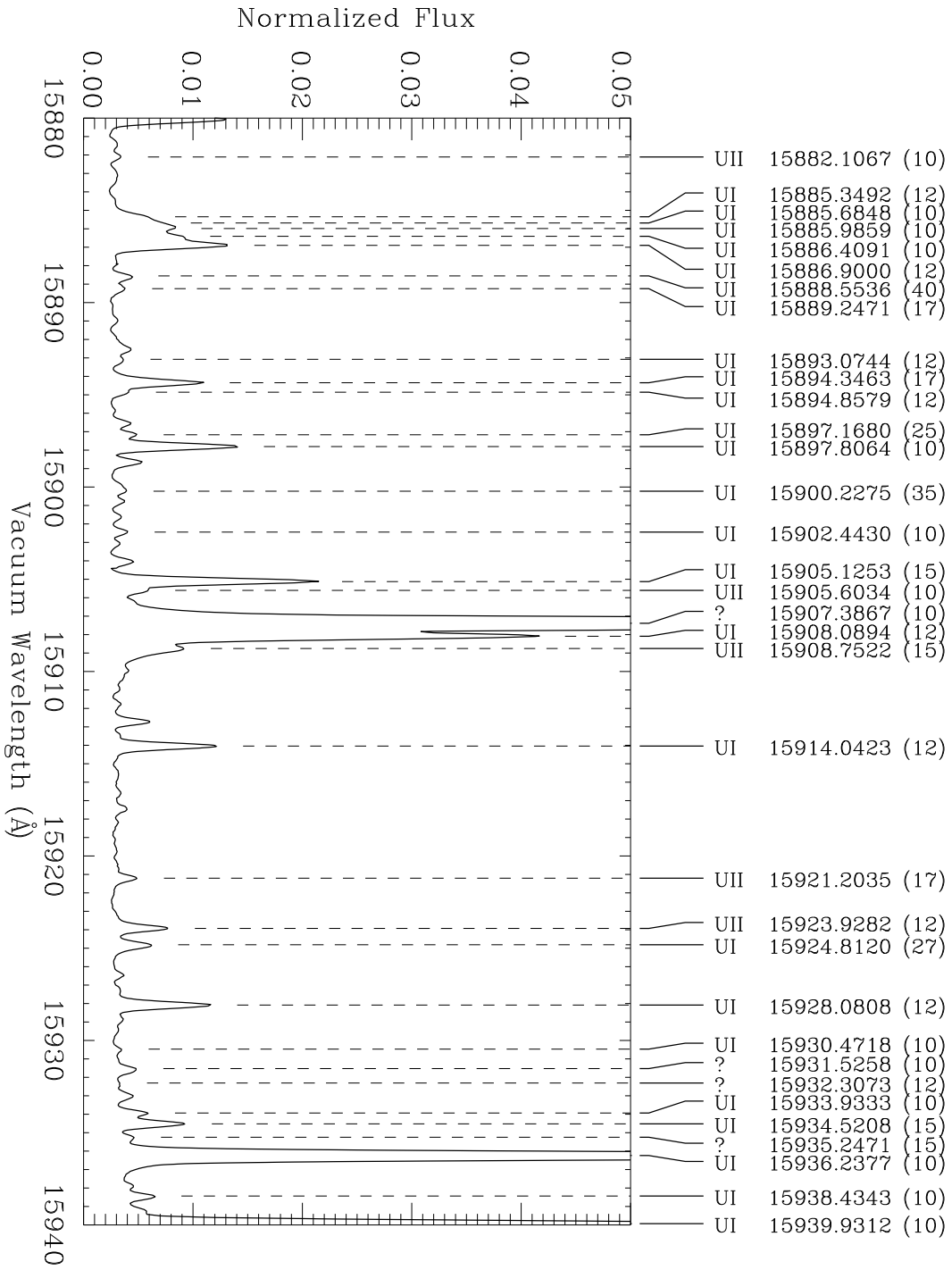
Normalized Flux
0.00
0.01
0.02
0.03
0.04
0.05
15880
15890
15900
15910
15920
15930
15940
Vacuum Wavelength (Å)
UII 15882.1067 (10)
UI 15885.3492 (12)
UI 15885.6848 (10)
UI 15885.9859 (10)
UI 15886.4091 (10)
UI 15886.9000 (12)
UI 15888.5536 (40)
UI 15889.2471 (17)
UI 15893.0744 (12)
UI 15894.3463 (17)
UI 15894.8579 (12)
UI 15897.1680 (25)
UI 15897.8064 (10)
UI 15900.2275 (35)
UI 15902.4430 (10)
UI 15905.1253 (15)
UII 15905.6034 (10)
? 15907.3867 (10)
UI 15908.0894 (12)
UII 15908.7522 (15)
UI 15914.0423 (12)
UII 15921.2035 (17)
UII 15923.9282 (12)
UI 15924.8120 (27)
UI 15928.0808 (12)
UI 15930.4718 (10)
? 15931.5258 (10)
? 15932.3073 (12)
UI 15933.9333 (10)
UI 15934.5208 (15)
? 15935.2471 (15)
UI 15936.2377 (10)
UI 15938.4343 (10)
UI 15939.9312 (10)

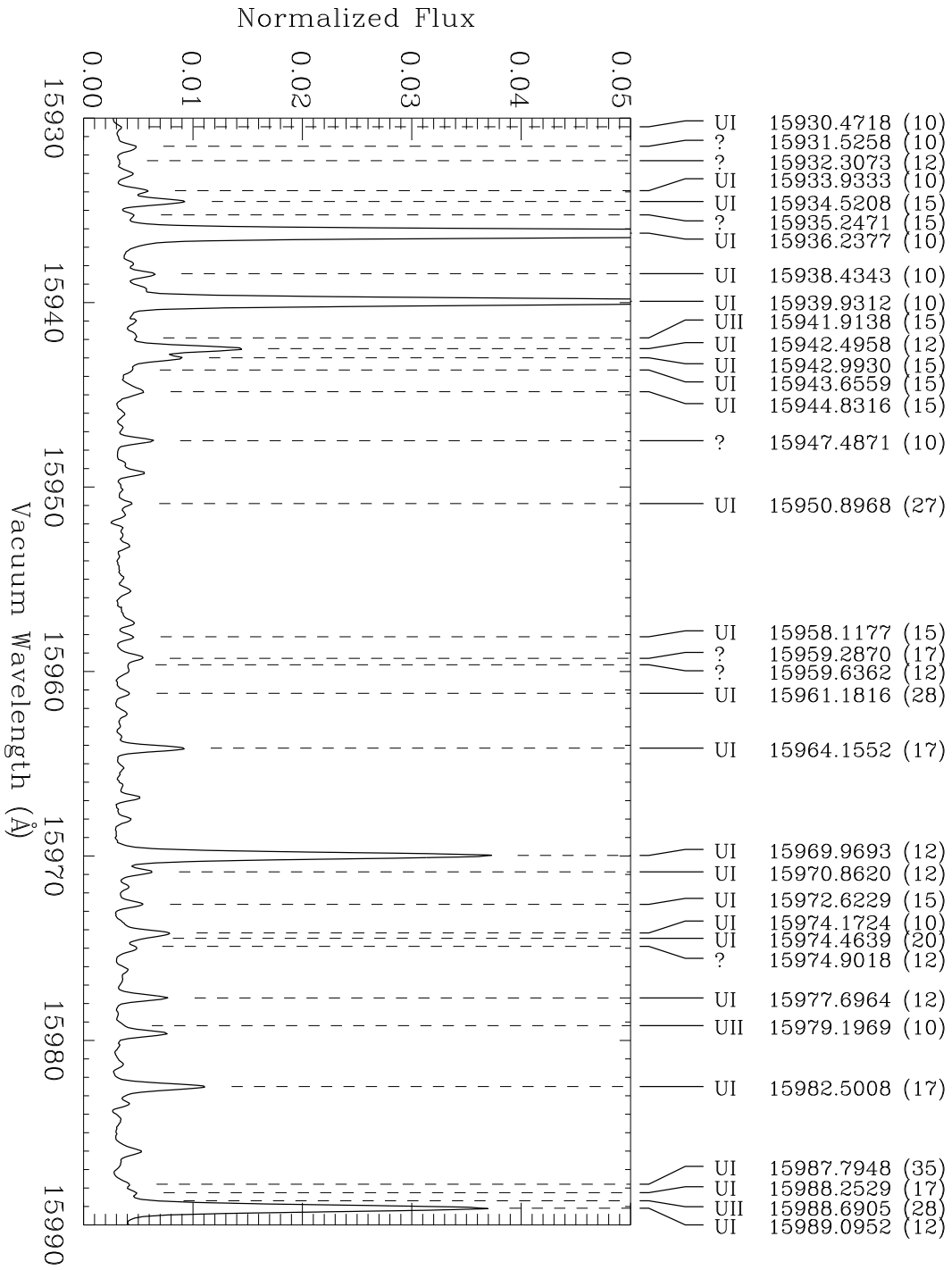
Normalized Flux
0.00
0.01
0.02
0.03
0.04
0.05
15930
15940
15950
15960
15970
15980
15990
Vacuum Wavelength (Å)
UI 15930.4718 (10)
? 15931.5258 (10)
? 15932.3073 (12)
UI 15933.9333 (10)
UI 15934.5208 (15)
? 15935.2471 (15)
UI 15936.2377 (10)
UI 15938.4343 (10)
UI 15939.9312 (10)
UII 15941.9138 (15)
UI 15942.4958 (12)
UI 15942.9930 (15)
UI 15943.6559 (15)
UI 15944.8316 (15)
? 15947.4871 (10)
UI 15950.8968 (27)
UI 15958.1177 (15)
? 15959.2870 (17)
? 15959.6362 (12)
UI 15961.1816 (28)
UI 15964.1552 (17)
UI 15969.9693 (12)
UI 15970.8620 (12)
UI 15972.6229 (15)
UI 15974.1724 (10)
UI 15974.4639 (20)
? 15974.9018 (12)
UI 15977.6964 (12)
UII 15979.1969 (10)
UI 15982.5008 (17)
UI 15987.7948 (35)
UI 15988.2529 (17)
UII 15988.6905 (28)
UI 15989.0952 (12)

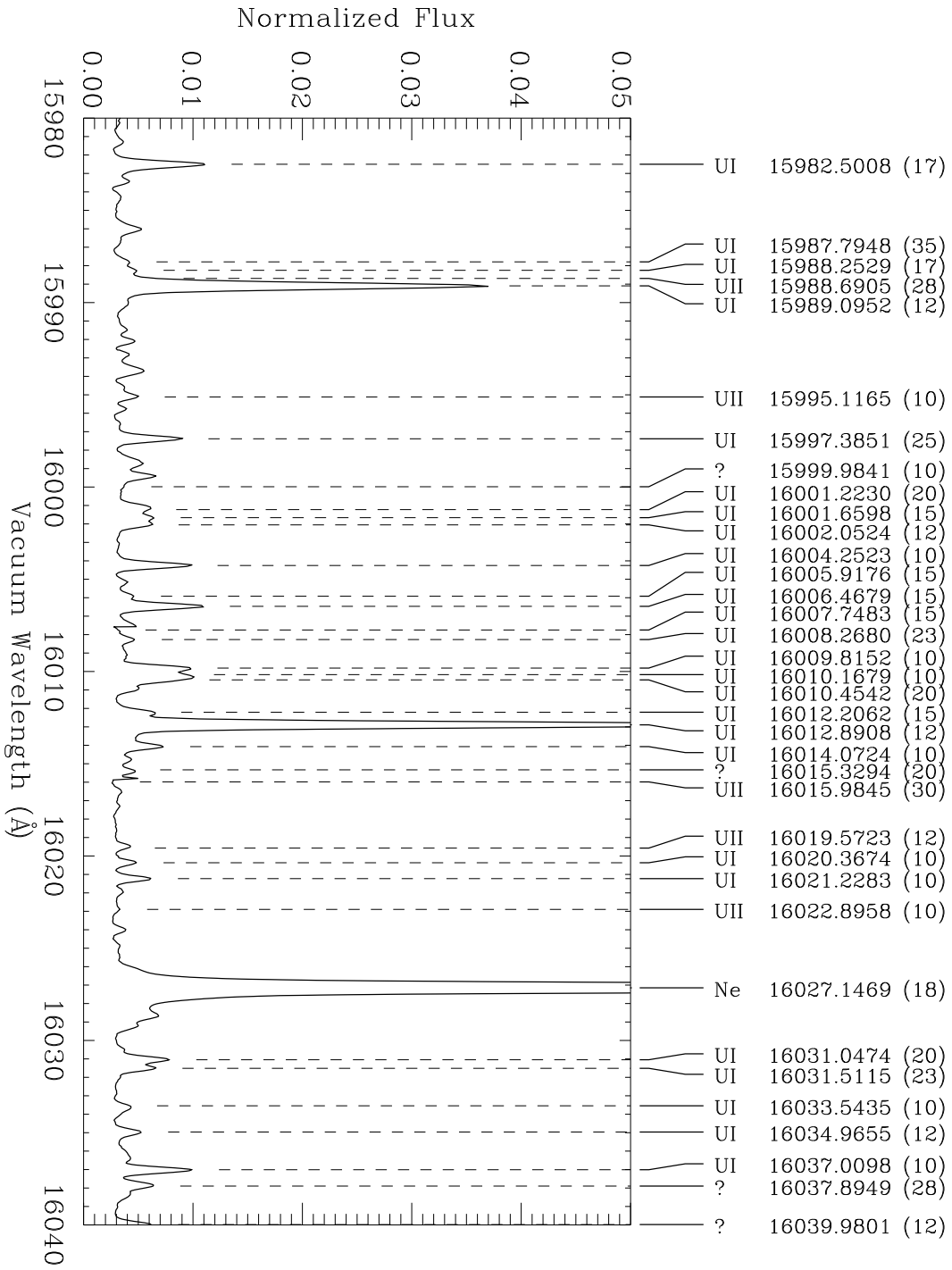
Normalized Flux
0.00
0.01
0.02
0.03
0.04
0.05
15980
15990
16000
16010
16020
16030
16040
Vacuum Wavelength (Å)
UI 15982.5008 (17)
UI 15987.7948 (35)
UI 15988.2529 (17)
UII 15988.6905 (28)
UI 15989.0952 (12)
UII 15995.1165 (10)
UI 15997.3851 (25)
? 15999.9841 (10)
UI 16001.2230 (20)
UI 16001.6598 (15)
UI 16002.0524 (12)
UI 16004.2523 (10)
UI 16005.9176 (15)
UI 16006.4679 (15)
UI 16007.7483 (15)
UI 16008.2680 (23)
UI 16009.8152 (10)
UI 16010.1679 (10)
UI 16010.4542 (20)
UI 16012.2062 (15)
UI 16012.8908 (12)
UI 16014.0724 (10)
? 16015.3294 (20)
UII 16015.9845 (30)
UII 16019.5723 (12)
UI 16020.3674 (10)
UI 16021.2283 (10)
UII 16022.8958 (10)
Ne 16027.1469 (18)
UI 16031.0474 (20)
UI 16031.5115 (23)
UI 16033.5435 (10)
UI 16034.9655 (12)
UI 16037.0098 (10)
? 16037.8949 (28)
? 16039.9801 (12)

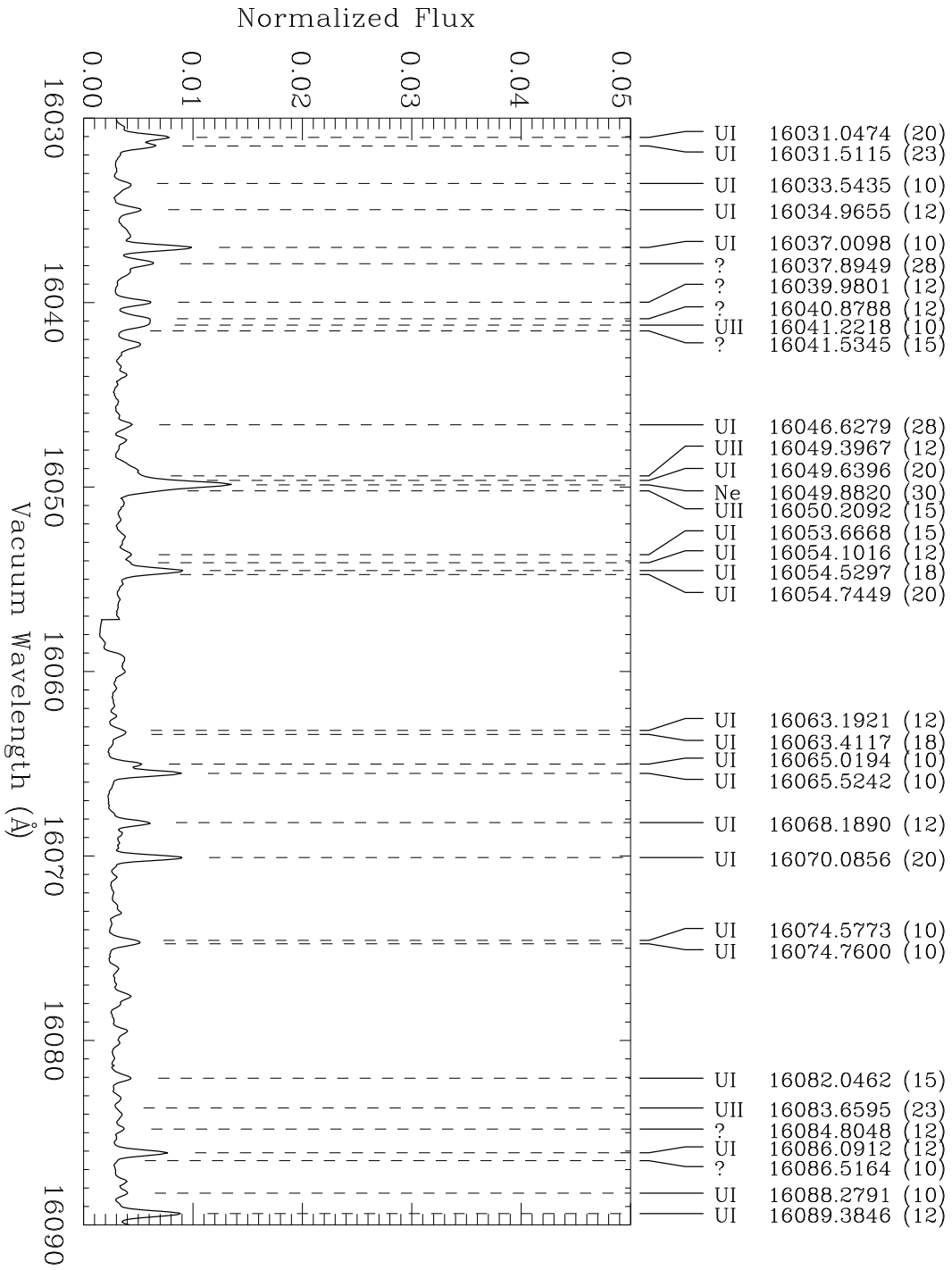
Normalized Flux
0.00
0.01
0.02
0.03
0.04
0.05
16030
16040
16050
16060
16070
16080
16090
Vacuum Wavelength (Å)
UI 16031.0474 (20)
UI 16031.5115 (23)
UI 16033.5435 (10)
UI 16034.9655 (12)
UI 16037.0098 (10)
? 16037.8949 (28)
? 16039.9801 (12)
? 16040.8788 (12)
UII 16041.2218 (10)
? 16041.5345 (15)
UI 16046.6279 (28)
UII 16049.3967 (12)
UI 16049.6396 (20)
Ne 16049.8820 (30)
UII 16050.2092 (15)
UI 16053.6668 (15)
UI 16054.1016 (12)
UI 16054.5297 (18)
UI 16054.7449 (20)
UI 16063.1921 (12)
UI 16063.4117 (18)
UI 16065.0194 (10)
UI 16065.5242 (10)
UI 16068.1890 (12)
UI 16070.0856 (20)
UI 16074.5773 (10)
UI 16074.7600 (10)
UI 16082.0462 (15)
UII 16083.6595 (23)
? 16084.8048 (12)
UI 16086.0912 (12)
? 16086.5164 (10)
UI 16088.2791 (10)
UI 16089.3846 (12)

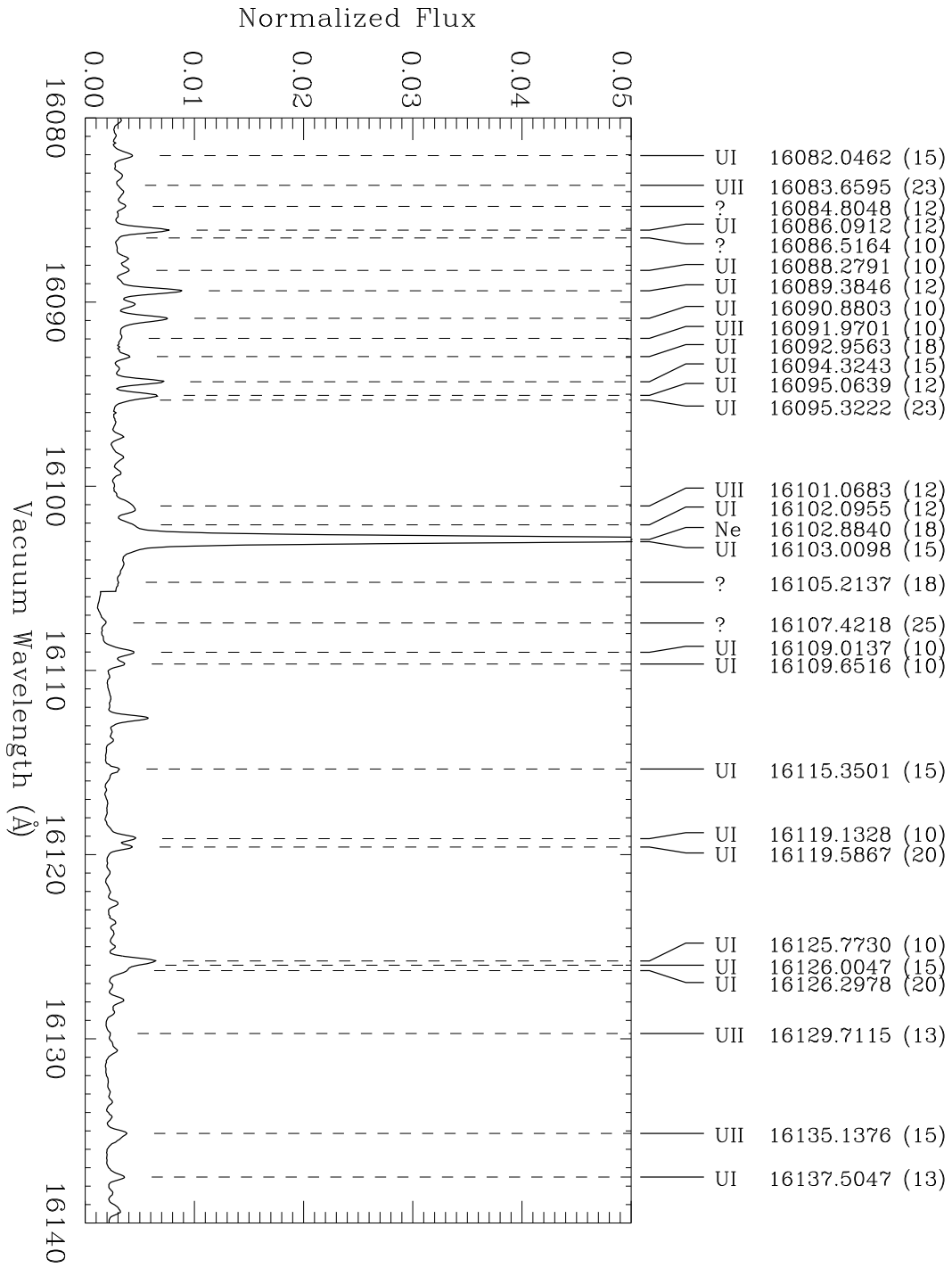
Normalized Flux
0.00
0.01
0.02
0.03
0.04
0.05
16080
16090
16100
16110
16120
16130
16140
Vacuum Wavelength (Å)
UI 16082.0462 (15)
UII 16083.6595 (23)
? 16084.8048 (12)
UI 16086.0912 (12)
? 16086.5164 (10)
UI 16088.2791 (10)
UI 16089.3846 (12)
UI 16090.8803 (10)
UII 16091.9701 (10)
UI 16092.9563 (18)
UI 16094.3243 (15)
UI 16095.0639 (12)
UI 16095.3222 (23)
UII 16101.0683 (12)
UI 16102.0955 (12)
Ne 16102.8840 (18)
UI 16103.0098 (15)
? 16105.2137 (18)
? 16107.4218 (25)
UI 16109.0137 (10)
UI 16109.6516 (10)
UI 16115.3501 (15)
UI 16119.1328 (10)
UI 16119.5867 (20)
UI 16125.7730 (10)
UI 16126.0047 (15)
UI 16126.2978 (20)
UII 16129.7115 (13)
UII 16135.1376 (15)
UI 16137.5047 (13)

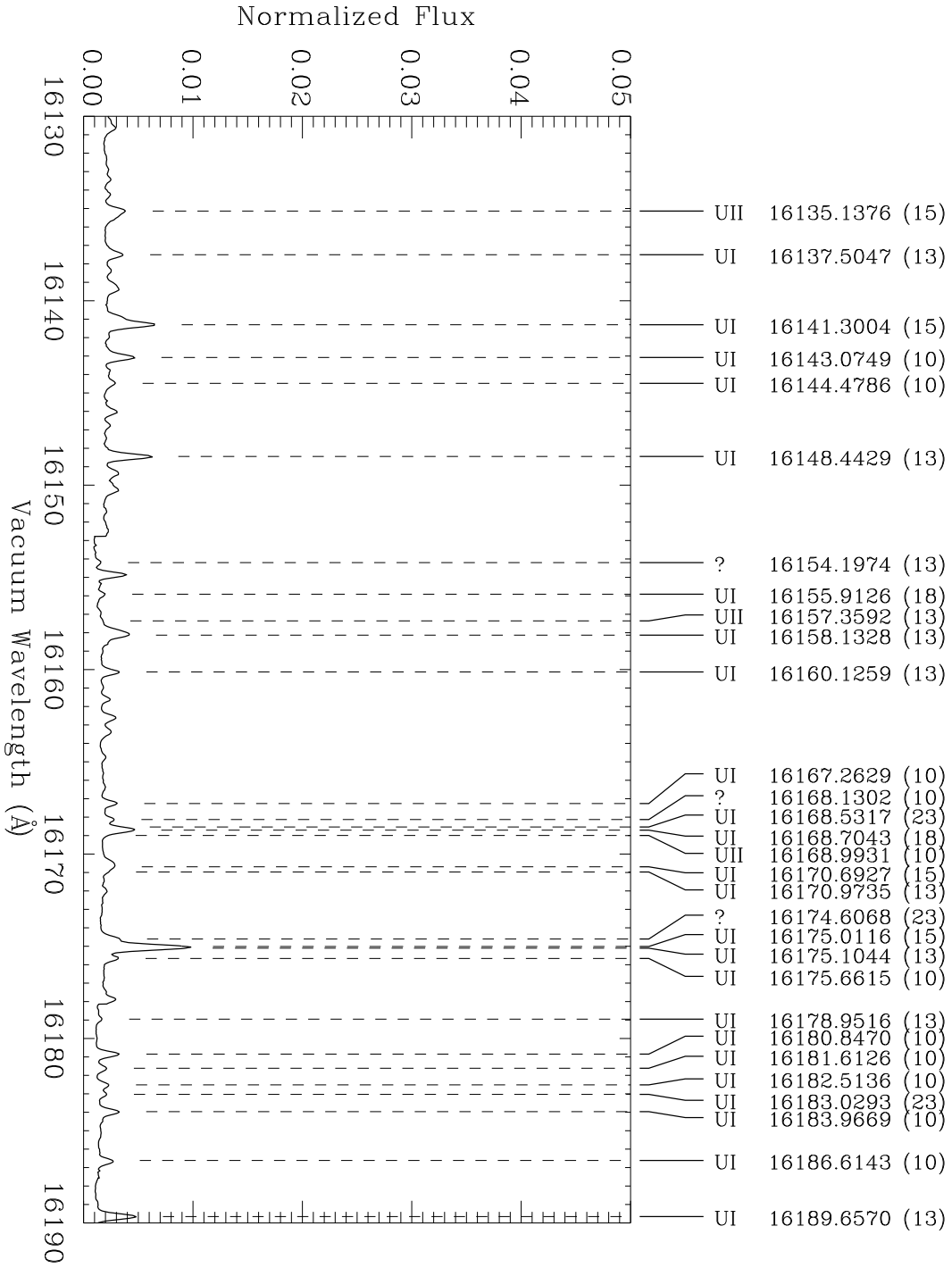
Normalized Flux
0.00
0.01
0.02
0.03
0.04
0.05
16130
16140
16150
16160
16170
16180
16190
Vacuum Wavelength (Å)
UII 16135.1376 (15)
UI 16137.5047 (13)
UI 16141.3004 (15)
UI 16143.0749 (10)
UI 16144.4786 (10)
UI 16148.4429 (13)
? 16154.1974 (13)
UI 16155.9126 (18)
UII 16157.3592 (13)
UI 16158.1328 (13)
UI 16160.1259 (13)
UI 16167.2629 (10)
? 16168.1302 (10)
UI 16168.5317 (23)
UI 16168.7043 (18)
UII 16168.9931 (10)
UI 16170.6927 (15)
UI 16170.9735 (13)
? 16174.6068 (23)
UI 16175.0116 (15)
UI 16175.1044 (13)
UI 16175.6615 (10)
UI 16178.9516 (13)
UI 16180.8470 (10)
UI 16181.6126 (10)
UI 16182.5136 (10)
UI 16183.0293 (23)
UI 16183.9669 (10)
UI 16186.6143 (10)
UI 16189.6570 (13)

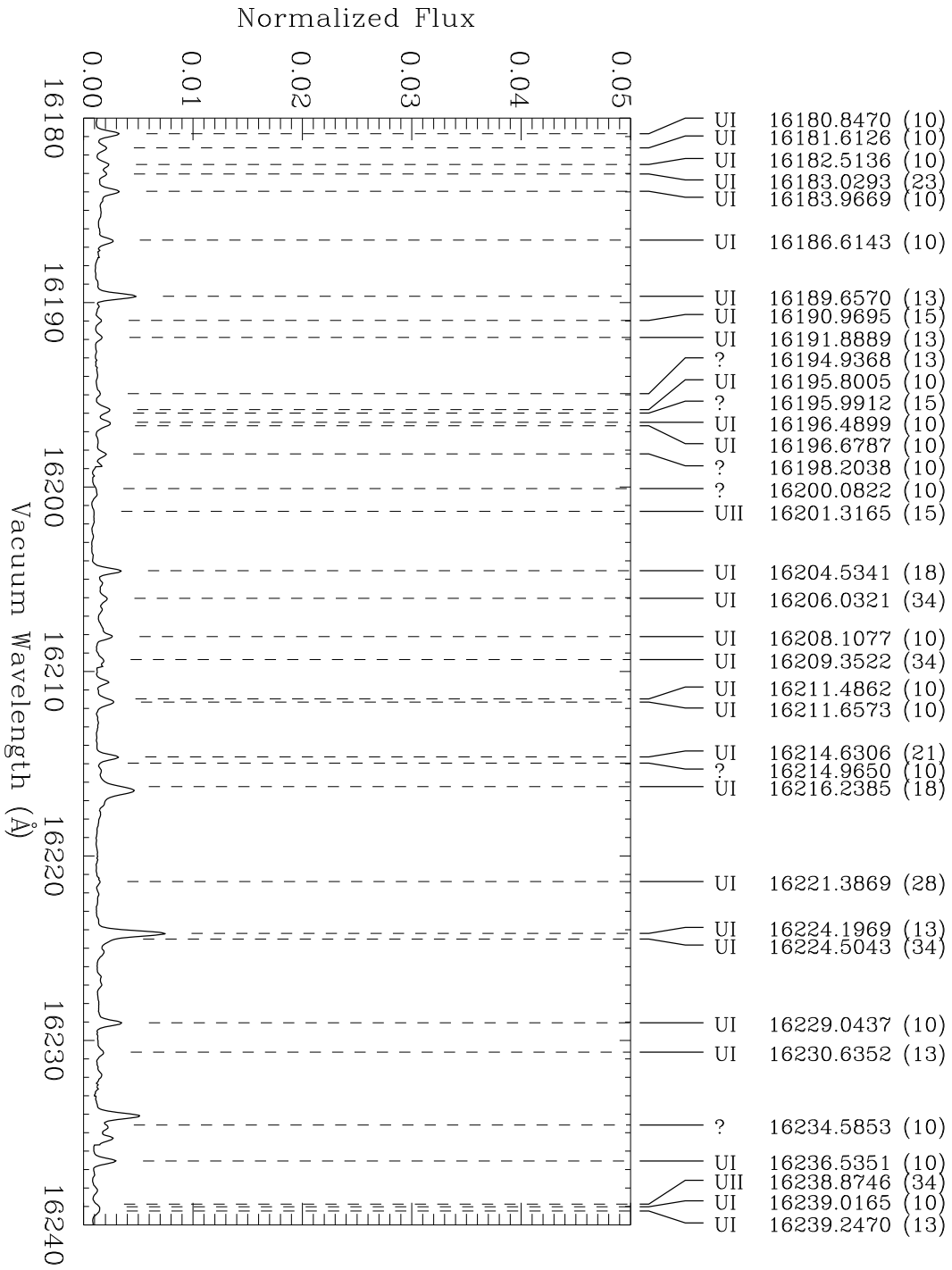
Normalized Flux
0.00
0.01
0.02
0.03
0.04
0.05
16180
16190
16200
16210
16220
16230
16240
Vacuum Wavelength (Å)
UI 16180.8470 (10)
UI 16181.6126 (10)
UI 16182.5136 (10)
UI 16183.0293 (23)
UI 16183.9669 (10)
UI 16186.6143 (10)
UI 16189.6570 (13)
UI 16190.9695 (15)
UI 16191.8889 (13)
? 16194.9368 (13)
UI 16195.8005 (10)
? 16195.9912 (15)
UI 16196.4899 (10)
UI 16196.6787 (10)
? 16198.2038 (10)
? 16200.0822 (10)
UII 16201.3165 (15)
UI 16204.5341 (18)
UI 16206.0321 (34)
UI 16208.1077 (10)
UI 16209.3522 (34)
UI 16211.4862 (10)
UI 16211.6573 (10)
UI 16214.6306 (21)
? 16214.9650 (10)
UI 16216.2385 (18)
UI 16221.3869 (28)
UI 16224.1969 (13)
UI 16224.5043 (34)
UI 16229.0437 (10)
UI 16230.6352 (13)
? 16234.5853 (10)
UI 16236.5351 (10)
UII 16238.8746 (34)
UI 16239.0165 (10)
UI 16239.2470 (13)

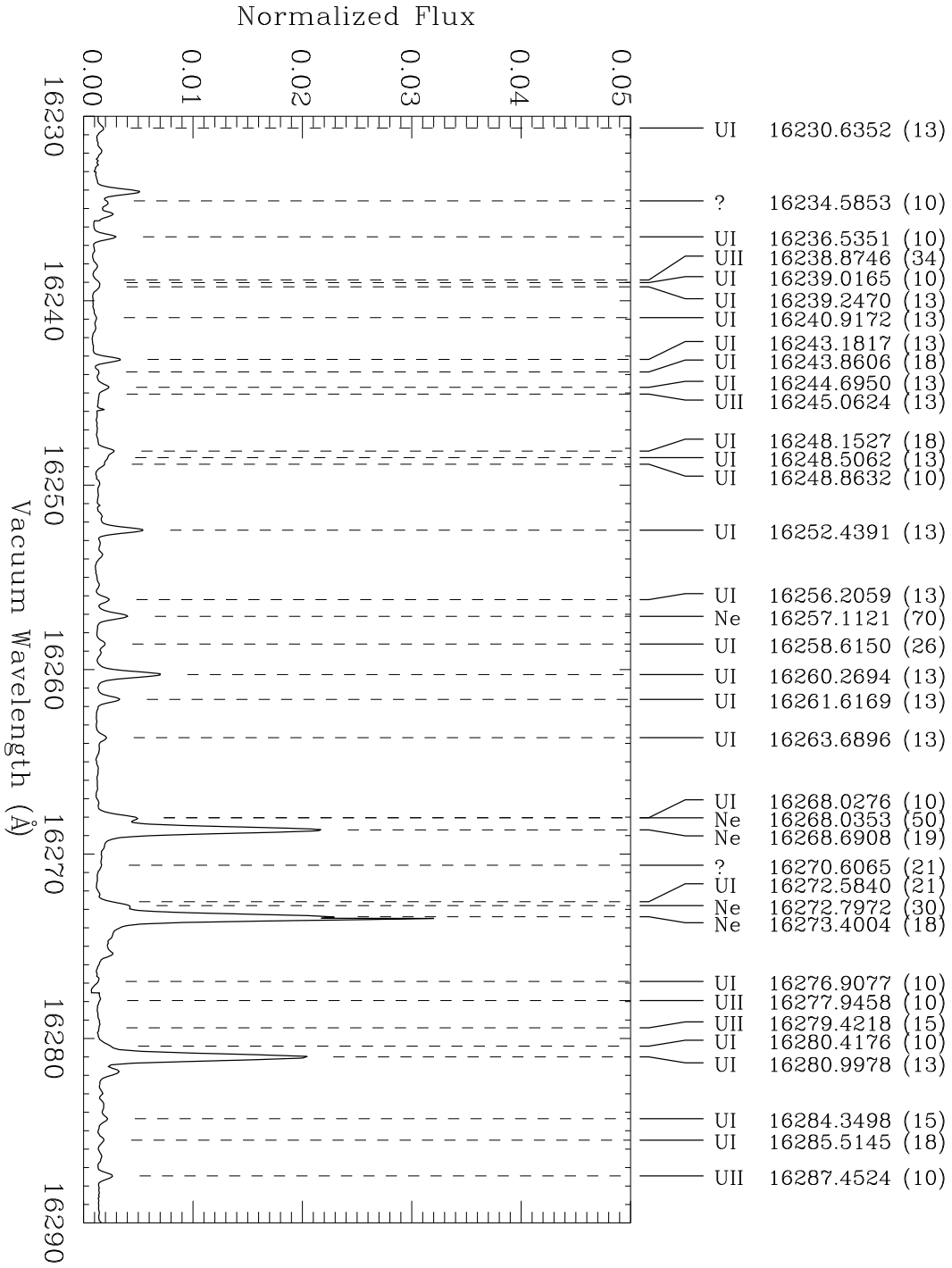
Normalized Flux
0.00
0.01
0.02
0.03
0.04
0.05
16230
16240
16250
16260
16270
16280
16290
Vacuum Wavelength (Å)
UI 16230.6352 (13)
? 16234.5853 (10)
UI 16236.5351 (10)
UII 16238.8746 (34)
UI 16239.0165 (10)
UI 16239.2470 (13)
UI 16240.9172 (13)
UI 16243.1817 (13)
UI 16243.8606 (18)
UI 16244.6950 (13)
UII 16245.0624 (13)
UI 16248.1527 (18)
UI 16248.5062 (13)
UI 16248.8632 (10)
UI 16252.4391 (13)
UI 16256.2059 (13)
Ne 16257.1121 (70)
UI 16258.6150 (26)
UI 16260.2694 (13)
UI 16261.6169 (13)
UI 16263.6896 (13)
UI 16268.0276 (10)
Ne 16268.0353 (50)
Ne 16268.6908 (19)
? 16270.6065 (21)
UI 16272.5840 (21)
Ne 16272.7972 (30)
Ne 16273.4004 (18)
UI 16276.9077 (10)
UII 16277.9458 (10)
UII 16279.4218 (15)
UI 16280.4176 (10)
UI 16280.9978 (13)
UI 16284.3498 (15)
UI 16285.5145 (18)
UII 16287.4524 (10)

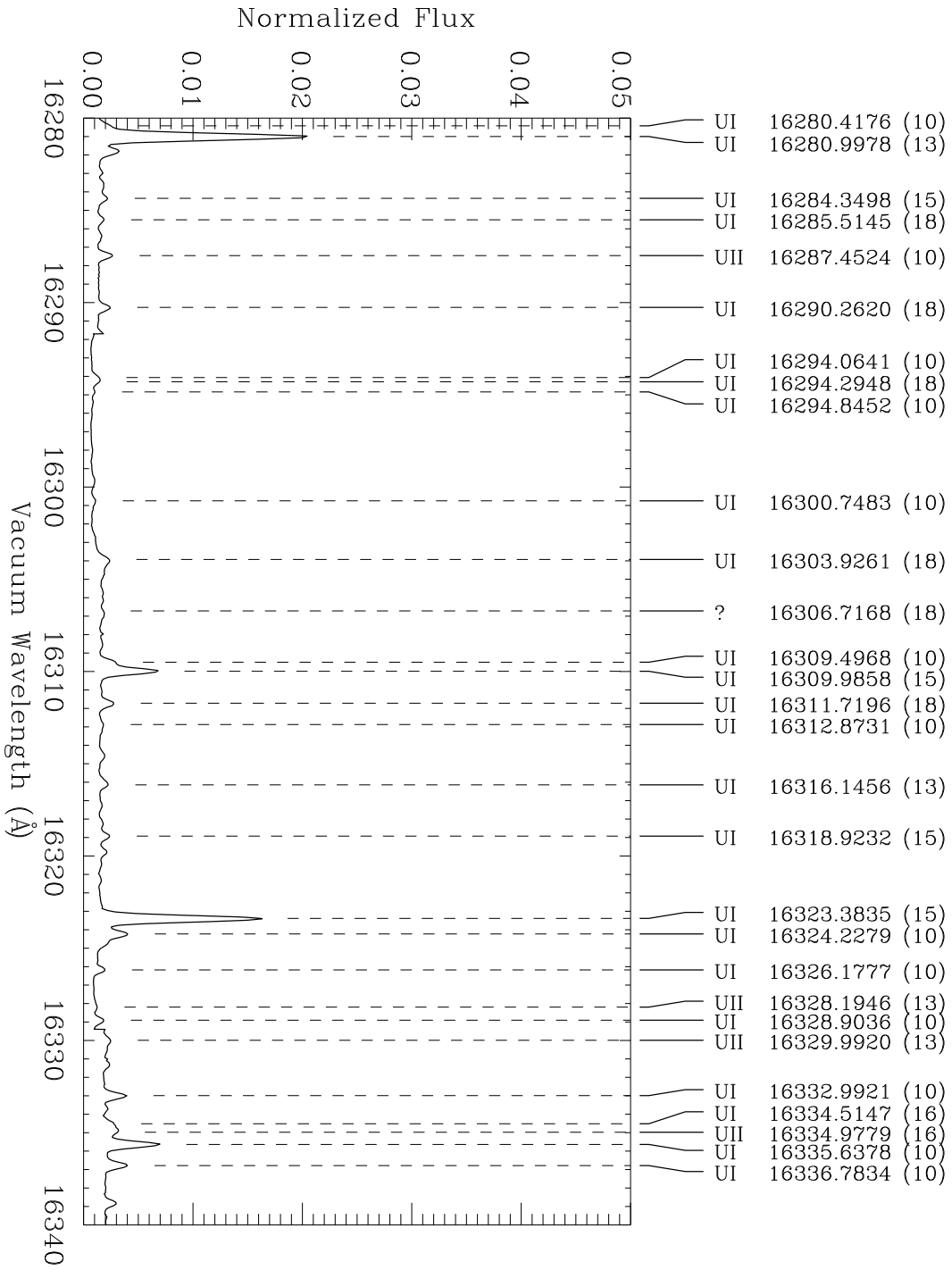
Normalized Flux
0.00
0.01
0.02
0.03
0.04
0.05
16280
16290
16300
16310
16320
16330
16340
Vacuum Wavelength (Å)
UI 16280.4176 (10)
UI 16280.9978 (13)
UI 16284.3498 (15)
UI 16285.5145 (18)
UII 16287.4524 (10)
UI 16290.2620 (18)
UI 16294.0641 (10)
UI 16294.2948 (18)
UI 16294.8452 (10)
UI 16300.7483 (10)
UI 16303.9261 (18)
? 16306.7168 (18)
UI 16309.4968 (10)
UI 16309.9858 (15)
UI 16311.7196 (18)
UI 16312.8731 (10)
UI 16316.1456 (13)
UI 16318.9232 (15)
UI 16323.3835 (15)
UI 16324.2279 (10)
UI 16326.1777 (10)
UII 16328.1946 (13)
UI 16328.9036 (10)
UII 16329.9920 (13)
UI 16332.9921 (10)
UI 16334.5147 (16)
UII 16334.9779 (16)
UI 16335.6378 (10)
UI 16336.7834 (10)

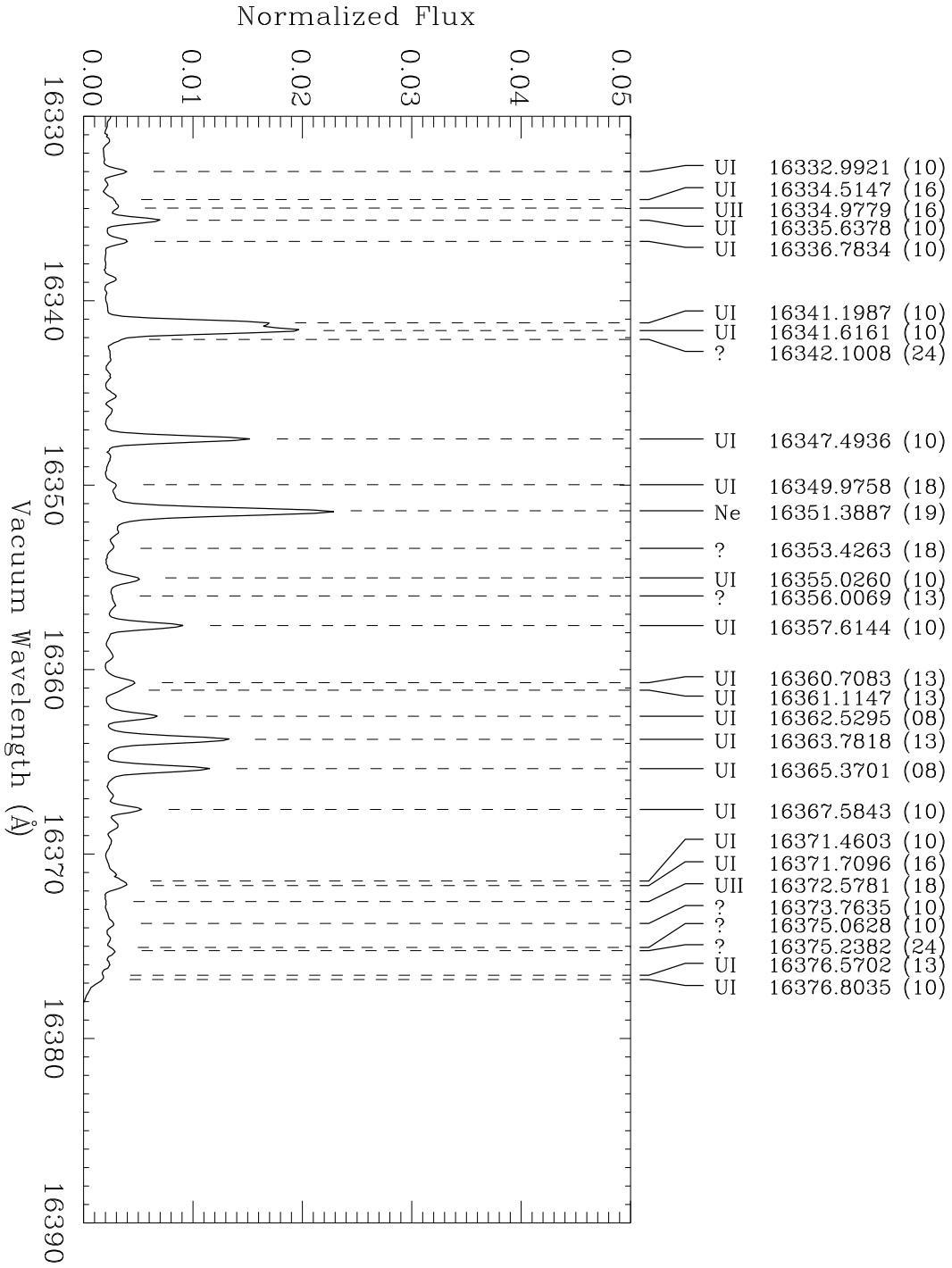
Normalized Flux
0.00
0.01
0.02
0.03
0.04
0.05
16330
16340
16350
16360
16370
16380
16390
Vacuum Wavelength (Å)
UI 16332.9921 (10)
UI 16334.5147 (16)
UII 16334.9779 (16)
UI 16335.6378 (10)
UI 16336.7834 (10)
UI 16341.1987 (10)
UI 16341.6161 (10)
? 16342.1008 (24)
UI 16347.4936 (10)
UI 16349.9758 (18)
Ne 16351.3887 (19)
? 16353.4263 (18)
UI 16355.0260 (10)
? 16356.0069 (13)
UI 16357.6144 (10)
UI 16360.7083 (13)
UI 16361.1147 (13)
UI 16362.5295 (08)
UI 16363.7818 (13)
UI 16365.3701 (08)
UI 16367.5843 (10)
UI 16371.4603 (10)
UI 16371.7096 (16)
UII 16372.5781 (18)
? 16373.7635 (10)
? 16375.0628 (10)
? 16375.2382 (24)
UI 16376.5702 (13)
UI 16376.8035 (10)

Bibliography

Adams, F. C. & Laughlin, G. 1997, Reviews of Modern Physics, 69, 337

Alibert, Y., Mordasini, C., Benz, W., & Winisdoerffer, C. 2005, A&A , 434, 343

Allen, C. W. 1973, Astrophysical quantities (London: University of London, Athlone Press, —c1973, 3rd ed.)

Barban, C., De Ridder, J., Mazumdar, A., Carrier, F., Eggenberger, P., De Ruyter, S., Vanautgaerden, J., Bouchy, F., & Aerts, C. 2004, in ESA Special Publication, Vol. 559, SOHO 14 Helio- and Asteroseismology: Towards a Golden Future, ed. D. Danesy, 113–+

Barbier-Brossat, M. & Figon, P. 2000, A&AS, 142, 217

Baudrand, J. & Walker, G. A. H. 2001, PASP , 113, 851

Bean, J. L., Seifahrt, A., Hartman, H., Nilsson, H., Wiedemann, G., Reiners, A., Dreizler, S., & Henry, T. J. 2010, ApJ , 713, 410

Bender, C. in preparation

Blaise, J. & Radziemski, Jr., L. J. 1976, Journal of the Optical Society of America (1917-1983), 66, 644

Blaise, J., Wyart, J., Vergès, J., Engleman, Jr., R., Palmer, B. A., & Radziemski, L. J. 1994, Journal of the Optical Society of America B Optical Physics, 11, 1897

Blake, C., Charbonneau, D., White, R., Torres, G., Marley, M., & Saumon, D. 2008, The Astrophysical Journal Letters, 678, L125

Blake, C. H., Charbonneau, D., & White, R. J. 2010, ApJ , 723, 684

Borucki, W. J., Koch, D., Basri, G., Batalha, N., Brown, T., Caldwell, D., Caldwell, J., Christensen-Dalsgaard, J., Cochran, W. D., DeVore, E., Dunham, E. W., Dupree, A. K., Gautier, T. N., Geary, J. C., Gilliland, R., Gould, A., Howell, S. B., Jenkins, J. M., Kondo, Y., Latham, D. W., Marcy, G. W., Meibom, S., Kjeldsen, H., Lissauer, J. J., Monet, D. G., Morrison, D., Sasselov, D., Tarter, J., Boss, A., Brownlee, D., Owen, T., Buzasi, D., Charbonneau, D., Doyle, L., Fortney, J., Ford, E. B., Holman, M. J., Seager, S., Steffen, J. H., Welsh, W. F., Rowe, J., Anderson, H., Buchhave, L., Ciardi, D., Walkowicz, L., Sherry, W., Horch, E., Isaacson, H., Everett, M. E., Fischer, D., Torres, G., Johnson, J. A., Endl, M., MacQueen, P., Bryson, S. T., Dotson, J., Haas, M., Kolodziejczak, J., Van Cleve, J., Chandrasekaran, H., Twicken, J. D., Quintana, E. V., Clarke, B. D., Allen, C., Li, J., Wu, H., Tenenbaum, P., Verner, E., Bruhweiler, F., Barnes, J., & Prsa, A. 2010, Science, 327, 977

Borucki, W. J., Koch, D. G., Basri, G., Batalha, N., Brown, T. M., Bryson, S. T., Caldwell, D., Christensen-Dalsgaard, J., Cochran, W. D., DeVore, E., Dunham, E. W., Gautier, III, T. N., Geary, J. C., Gilliland, R., Gould, A., Howell, S. B., Jenkins, J. M., Latham, D. W., Lissauer, J. J., Marcy, G. W., Rowe, J., Sasselov, D., Boss, A., Charbonneau, D., Ciardi, D., Doyle, L., Dupree, A. K., Ford, E. B., Fortney, J., Holman, M. J., Seager, S., Steffen, J. H., Tarter, J., Welsh, W. F., Allen, C., Buchhave, L. A., Christiansen, J. L., Clarke, B. D., Désert, J., Endl, M., Fabrycky, D., Fressin, F., Haas, M., Horch, E., Howard, A., Isaacson, H., Kjeldsen, H., Kolodziejczak, J., Kulesa, C., Li, J., Machalek, P., McCarthy, D., MacQueen, P., Meibom, S., Miquel, T., Prsa, A., Quinn, S. N., Quintana, E. V., Ragozzine, D., Sherry, W., Shporer, A., Tenenbaum, P., Torres, G., Twicken, J. D., Van Cleve, J., & Walkowicz, L. 2011, ArXiv e-prints

Borucki, W. J. & the Kepler Team. 2010, ArXiv e-prints

Boss, A. 1997, Science, 276, 1836

Bouchy, F., Pepe, F., & Queloz, D. 2001, A&A , 374, 733

Braje, D. A., Kirchner, M. S., Osterman, S., Fortier, T., & Diddams, S. A. 2008, Eur. Phys. J. D, 48, 57

Brault, J. & Abrams, M. 1989, OSA Technical Digest Series (Washington: Optical Society of America), 6, 110

Brown, T. M. 1990, in Astronomical Society of the Pacific Conference Series, Vol. 8, CCDs in astronomy, ed. G. H. Jacoby, 335–344

Butler, R. P., Vogt, S. S., Marcy, G. W., Fischer, D. A., Wright, J. T., Henry, G. W., Laughlin, G., & Lissauer, J. J. 2004, ApJ , 617, 580

Butler, R. P., Wright, J. T., Marcy, G. W., Fischer, D. A., Vogt, S. S., Tinney, C. G., Jones, H. R. A., Carter, B. D., Johnson, J. A., McCarthy, C., & Penny, A. J. 2006, ApJ , 646, 505

Campbell, B. & Walker, G. A. H. 1979, PASP , 91, 540

Campbell, B., Yang, S., Irwin, A. W., & Walker, G. A. H. 1991, in Lecture Notes in Physics, Berlin Springer Verlag, Vol. 390, Bioastronomy: The Search for Extraterrestial Life — The Exploration Broadens, ed. J. Heidmann & M. J. Klein, 19–20

Campbell, R. D. & Thompson, D. J. 2006, in Scientific Detectors for Astronomy 2005, ed. J. E. Beletic, J. W. Beletic, & P. Amico, 507–+

Chen, J., Sickler, J. W., Fendel, P., Ippen, E. P., Kärtner, F. X., Wilken, T., Holzwarth, R., & Hänsch, T. W. 2008, Opt. Lett., 33, 959

Connes, P. 1985, APSS , 110, 211

Conway, J. G. & Worden, E. F. 1984, Journal of the Optical Society of America B Optical Physics, 1, 788

Davis, S., Abrams, M., & Brault, J. 2001, Fourier Transform Spectrometry (Academic, New York, 2001)

Degraffenreid, W. & Sansonetti, C. J. 2002, Journal of the Optical Society of America B Optical Physics, 19, 1711

Edelstein, J., Muterspaugh, M. W., Erskine, D. J., Feuerstein, W. M., Marckwordt, M., Wishnow, E., Lloyd, J. P., Herter, T., Muirhead, P., Gull, G. E., Henderson, C., & Parshley, S. C. 2007, in Presented at the Society of Photo-Optical Instrumentation Engineers (SPIE) Conference, Vol. 6693, Society of Photo-Optical Instrumentation Engineers (SPIE) Conference Series

Edlén, B. 1966, Metrologia, 2, 71

Endl, M., Cochran, W. D., Kürster, M., Paulson, D. B., Wittenmyer, R. A., MacQueen, P. J., & Tull, R. G. 2006, ApJ , 649, 436

Engleman, Jr., R. 2003, JQSRT , 78, 1

Figueira, P., Pepe, F., Melo, C. H. F., Santos, N. C., Lovis, C., Mayor, M., Queloz, D., Smette, A., & Udry, S. 2010, A&A , 511, A55+

Fitzpatrick, M. J. 1993, in Astronomical Society of the Pacific Conference Series, Vol. 52, Astronomical Data Analysis Software and Systems II, ed. R. J. Hanisch, R. J. V. Brissenden, & J. Barnes, 472–+

Gatewood, G. & Eichhorn, H. 1973, AJ , 78, 769

Gettel, S. 2008

Goody, R. M. & Yung, Y. L. 1989, Atmospheric radiation : theoretical basis (Atmospheric radiation : theoretical basis, 2nd ed., by Richard M. Goody and Y.L. Yung. New York, NY: Oxford University Press, 1989)

Gray, D. F. & Brown, K. I. T. 2006, PASP , 118, 399

Greene, T. P., Tokunaga, A. T., Toomey, D. W., & Carr, J. B. 1993, in Society of Photo-Optical Instrumentation Engineers (SPIE) Conference Series, Vol. 1946, Society of Photo-Optical Instrumentation Engineers (SPIE) Conference Series, ed. A. M. Fowler, 313–324

Grupp, F. 2003, A&A , 412, 897

Hall, J. L. 2006, Reviews of Modern Physics, 78, 1279

Hänsch, T. W. 2006, Reviews of Modern Physics, 78, 1297

Hatzes, A. P. 1999, in Astronomical Society of the Pacific Conference Series, Vol. 185, IAU Colloq. 170: Precise Stellar Radial Velocities, ed. J. B. Hearnshaw & C. D. Scarfe, 259–+

Hatzes, A. P., Cochran, W. D., & Endl, M. Observational Techniques: Precise Stellar Radial Velocity Measurements (Unpublished)

Hatzes, A. P., Cochran, W. D., & Endl, M. 2010, in Astrophysics and Space Science Library, Vol. 366, Astrophysics and Space Science Library, ed. N. Haghighipour, 51–76

Hébrard, G., Bouchy, F., Pont, F., Loeillet, B., Rabus, M., Bonfils, X., Moutou, C., Boisse, I., Delfosse, X., Desort, M., Eggenberger, A., Ehrenreich, D., Forveille, T., Lagrange, A., Lovis, C., Mayor, M., Pepe, F., Perrier, C., Queloz, D., Santos, N. C., Ségransan, D., Udry, S., & Vidal-Madjar, A. 2008, A&A , 488, 763

Hekker, S., Reffert, S., Quirrenbach, A., Mitchell, D. S., Fischer, D. A., Marcy, G. W., & Butler, R. P. 2006, A&A , 454, 943

Hershey, J. L. 1973, AJ , 78, 421

Hodapp, K.-W., Hora, J. L., Hall, D. N. B., Cowie, L. L., Metzger, M., Irwin, E., Vural, K., Kozlowski, L. J., Cabelli, S. A., Chen, C. Y., Cooper, D. E., Bostrup, G. L., Bailey, R. B., & Kleinhans, W. E. 1996, New Astronomy, 1, 177

Hodapp, K. W., Kuhn, J., Thornton, R., Irwin, E., Yamada, H., Waterson, M., Kozlowski, L., Montroy, J. T., Haas, A., Vural, K., & Cabelli, C. 2004, in Astrophysics and Space Science Library, Vol. 300, Scientific Detectors for Astronomy, The Beginning of a New Era, ed. P. Amico, J. W. Beletic, & J. E. Belectic, 501–509

Hodapp, K.-W., Rayner, J., & Irwin, E. 1992, PASP , 104, 441

Horne, K. 1986, PASP , 98, 609

Howard, A. W., Marcy, G. W., Johnson, J. A., Fischer, D. A., Wright, J. T., Isaacson, H., Valenti, J. A., Anderson, J., Lin, D. N. C., & Ida, S. 2010, Science, 330, 653

Huélamo, N., Figueira, P., Bonfils, X., Santos, N. C., Pepe, F., Gillon, M., Azevedo, R., Barman, T., Fernández, M., di Folco, E., Guenther, E. W., Lovis, C., Melo, C. H. F., Queloz, D., & Udry, S. 2008, A&A , 489, L9

Hunter, T. R. & Ramsey, L. W. 1992, PASP , 104, 1244

Irwin, J., Charbonneau, D., Nutzman, P., & Falco, E. 2009, in American Institute of Physics Conference Series, Vol. 1094, American Institute of Physics Conference Series, ed. E. Stempels, 445–448

Jenkins, J. S., Ramsey, L. W., Jones, H. R. A., Pavlenko, Y., Gallardo, J., Barnes, J. R., & Pinfield, D. J. 2009, ApJ , 704, 975

Johnson, H. L. & Morgan, W. W. 1953, ApJ , 117, 313

Jones, H., Rayner, J., & Lunney, D. 2006

Joshi, M. 2003, Astrobiology, 3, 415

Joshi, M. M., Haberle, R. M., & Reynolds, R. T. 1997, Icarus, 129, 450

Kasting, J. F., Whitmire, D. P., & Reynolds, R. T. 1993, Icarus, 101, 108

Kerber, F., Nave, G., & Sansonetti, C. 2008, The Astrophysical Journal Supplement Series, 178, 374

Kirchner, M. S., Braje, D. A., Fortier, T. M., Weiner, A. M., Hollberg, L., & Diddams, S. A. 2009, Opt. Lett., 34, 872

Kirkpatrick, J. D., Henry, T. J., & McCarthy, Jr., D. W. 1991, The Astrophysical Journal Supplement Series, 77, 417

Laughlin, G., Bodenheimer, P., & Adams, F. C. 1997, ApJ , 482, 420

—. 2004, ApJL , 612, L73

Lawson, P., Traub, W., & Unwin, S. 2009

Learner, R. C. M., Thorne, A. P., Wynne-Jones, I., Brault, J. W., & Abrams, M. C. 1995, Journal of the Optical Society of America A, 12, 2165

Li, C., Benedick, A. J., Fendel, P., Glenday, A. G., Kärtner, F. X., Phillips, D. F., Sasselov, D., Szentgyorgyi, A., & Walsworth, R. L. 2008, NAT , 452, 610

Libbrecht, K. G. 1988, in IAU Symposium, Vol. 132, The Impact of Very High S/N Spectroscopy on Stellar Physics, ed. G. Cayrel de Strobel & M. Spite, 83–+

López-Alonso, J. M., Alda, J., & Bernabéu, E. 2002, AO , 41, 320

Lovis, C. & Pepe, F. 2007, A&A , 468, 1115

Lovis, C., Pepe, F., Bouchy, F., Lo Curto, G., Mayor, M., Pasquini, L., Queloz, D., Rupprecht, G., Udry, S., & Zucker, S. 2006, in Presented at the Society of Photo-Optical Instrumentation Engineers (SPIE) Conference, Vol. 6269, Ground-based and Airborne Instrumentation for Astronomy. Edited by McLean, Ian S.; Iye, Masanori. Proceedings of the SPIE, Volume 6269, pp. 62690P (2006).

Luhman, K. L., Lada, C. J., Hartmann, L., Muench, A. A., Megeath, S. T., Allen, L. E., Myers, P. C., Muzerolle, J., Young, E., & Fazio, G. G. 2005, ApJL , 631, L69

Lunine, J. I., Fischer, D., Hammel, H. B., Henning, T., Hillenbrand, L., Kasting, J., Laughlin, G., Macintosh, B., Marley, M., Melnick, G., Monet, D., Noecker, C., Peale, S., Quirrenbach, A., Seager, S., & Winn, J. N. 2008, Astrobiology, 8, 875

Mahadevan, S. & Ge, J. 2009, ApJ , 692, 1590

Mahadevan, S., Ge, J., Fleming, S. W., Wan, X., DeWitt, C., van Eyken, J. C., & McDavitt, D. 2008a, PASP , 120, 1001

Mahadevan, S., Ramsey, L., Wolszczan, A., Wright, J., Endl, M., & Redman, S. 2010, in American Astronomical Society Meeting Abstracts, Vol. 215

Mahadevan, S., van Eyken, J., Ge, J., DeWitt, C., Fleming, S. W., Cohen, R., Crepp, J., & Vanden Heuvel, A. 2008b, ApJ , 678, 1505

Marcy, G. W. & Butler, R. P. 1992, PASP , 104, 270

Markwardt, C. B. 2009, in Astronomical Society of the Pacific Conference Series, Vol. 411, Astronomical Society of the Pacific Conference Series, ed. D. A. Bohlender, D. Durand, & P. Dowler, 251–+

Mayor, M., Bonfils, X., Forveille, T., Delfosse, X., Udry, S., Bertaux, J., Beust, H., Bouchy, F., Lovis, C., Pepe, F., Perrier, C., Queloz, D., & Santos, N. C. 2009, A&A , 507, 487

Mayor, M. & Queloz, D. 1995, NAT , 378, 355

McLean, I. S., Becklin, E. E., Bendiksen, O., Brims, G., Canfield, J., Figer, D. F., Graham, J. R., Hare, J., Lacayanga, F., Larkin, J. E., Larson, S. B., Levenson, N., Magnone, N., Teplitz, H., & Wong, W. 1998, in Presented at the Society of Photo-Optical Instrumentation Engineers (SPIE) Conference, Vol. 3354, Society of Photo-Optical Instrumentation Engineers (SPIE) Conference Series, ed. A. M. Fowler, 566–578

McLean, I. S., McGovern, M. R., Burgasser, A. J., Kirkpatrick, J. D., Prato, L., & Kim, S. S. 2003, ApJ , 596, 561

McMillan, R. S., Moore, T. L., Perry, M. L., & Smith, P. H. 1994, APSS , 212, 271

Mizuno, H. 1980, Progress of Theoretical Physics, 64, 544

Mohanty, S. & Basri, G. 2003, ApJ , 583, 451

Morgan, W. W., Keenan, P. C., & Kellman, E. 1943, An atlas of stellar spectra, with an outline of spectral classification, ed. Morgan, W. W., Keenan, P. C., & Kellman, E.

Muirhead, P., Edelstein, J., Erskine, D. J., Hamren, K. M., Covey, K. R., & Lloyd, J. P. 2011, in American Astronomical Society Meeting Abstracts, Vol. 217, American Astronomical Society Meeting Abstracts

Murphy, M. T., Udem, T., Holzwarth, R., Sizmann, A., Pasquini, L., Araujo-Hauck, C., Dekker, H., D'Odorico, S., Fischer, M., Hänsch, T. W., & Manescau, A. 2007, MNRAS , 380, 839

Nave, G., Sansonetti, C., & Griesmann, U. 1997, Fourier Transform Spectroscopy: Methods and Applications, 3, 38

Nelder, J. & Mead, R. 1965, Computer Journal, 7, 5

Omerbashich, M. 2008, ArXiv e-prints

Osterman, S., Diddams, S., Beasley, M., Froning, C., Hollberg, L., MacQueen, P., Mbele, V., & Weiner, A. 2007, in Society of Photo-Optical Instrumentation Engineers (SPIE) Conference Series, Vol. 6693, Society of Photo-Optical Instrumentation Engineers (SPIE) Conference Series

Palmer, B., Keller, R., & Engleman Jr, R. 1980, Atlas of uranium emission intensities in a hollow cathode discharge, Tech. rep., LA-8251-MS, Los Alamos Scientific Lab., NM (USA)

Pavlenko, Y. V., Jones, H. R. A., Lyubchik, Y., Tennyson, J., & Pinfield, D. J. 2006, A&A , 447, 709

Peale, S. J. 1977, in IAU Colloq. 28: Planetary Satellites, ed. J. A. Burns, 87–111

Pepe, F., Mayor, M., Delabre, B., Kohler, D., Lacroix, D., Queloz, D., Udry, S., Benz, W., Bertaux, J.-L., & Sivan, J.-P. 2000, in Presented at the Society of Photo-Optical Instrumentation Engineers (SPIE) Conference, Vol. 4008, Proc. SPIE Vol. 4008, p. 582-592, Optical and IR Telescope Instrumentation and Detectors, Masanori Iye; Alan F. Moorwood; Eds., ed. M. Iye & A. F. Moorwood, 582–592

Pepe, F. A. & Lovis, C. 2008, Physica Scripta Volume T, 130, 014007

Piskunov, N. E. & Valenti, J. A. 2002, A&A , 385, 1095

Pollack, J. B., Hubickyj, O., Bodenheimer, P., Lissauer, J. J., Podolak, M., & Greenzweig, Y. 1996, Icarus, 124, 62

Prato, L., Huerta, M., Johns-Krull, C., Mahmud, N., Jaffe, D., & Hartigan, P. 2008, The Astrophysical Journal Letters, 687, L103

Quinlan, F., Ycas, G., Osterman, S., & Diddams, S. A. 2010, Rev. Sci. Instrum., 81, 063105

Quirrenbach, A., Amado, P. J., Mandel, H., Caballero, J. A., Mundt, R., Ribas, I., Reiners, A., Abril, M., Aceituno, J., Afonso, C., Barrado Y Navascues, D., Bean, J. L., Béjar, V. J. S., Becerril, S., Böhm, A., Cárdenas, M. C., Claret, A., Colomé, J., Costillo, L. P., Dreizler, S., Fernández, M., Francisco, X., Galadí, D., Garrido, R., González Hernández, J. I., Guàrdia, J., Guenther, E. W., Gutiérrez-Soto, F., Joergens, V., Hatzes, A. P., Helmling, J., Henning, T., Herrero, E., Kürster, M., Laun, W., Lenzen, R., Mall, U., Martin, E. L., Martín-Ruiz, S., Mirabet, E., Montes, D., Morales, J. C., Morales Muñoz, R., Moya, A., Naranjo, V., Rabaza, O., Ramón, A., Rebolo, R., Reffert, S., Rodler, F., Rodríguez, E., Rodríguez Trinidad, A., Rohloff, R. R., Sánchez Carrasco, M. A., Schmidt, C., Seifert, W., Setiawan, J., Solano, E., Stahl, O., Storz, C., Suárez, J. C., Thiele, U., Wagner, K., Wiedemann, G., Zapatero Osorio, M. R., Del Burgo, C., Sánchez-Blanco, E., & Xu, W. 2010, in Society of Photo-Optical Instrumentation Engineers (SPIE) Conference Series, Vol. 7735, Society of Photo-Optical Instrumentation Engineers (SPIE) Conference Series

Ramsey, L., Barnes, J., Redman, S., Jones, H., Wolszczan, A., Bongiorno, S., Engel, L., & Jenkins, J. 2008, Publications of the Astronomical Society of the Pacific, 120, 887

Redman, S. L., Lawler, J. E., Nave, G., Ramsey, L. W., & Mahadevan, S. in preparationa

Redman, S. L., Ycas, G. G., Terrian, R., Mahadevan, S., Ramsey, L. W., Bender, C. F., Osterman, S. N., Diddams, S. A., Quinlan, F., Lawler, J. E., & Nave, G. in preparationb

Reid, I. N. & Hawley, S. L. 2005, New light on dark stars : red dwarfs, low-mass stars, brown dwarfs (New Light on Dark Stars Red Dwarfs, Low-Mass Stars, Brown Stars, by I.N. Reid and S.L. Hawley. Springer-Praxis books in astrophysics and astronomy. Praxis Publishing Ltd, 2005. ISBN 3-540-25124-3)

Reiners, A. 2007, A&A , 467, 259

Reiners, A., Bean, J. L., Huber, K. F., Dreizler, S., Seifahrt, A., & Czesla, S. 2010, ApJ , 710, 432

Rockenfeller, B., Bailer-Jones, C. A. L., & Mundt, R. 2006, A&A , 448, 1111

Saar, S. H. & Donahue, R. A. 1997, ApJ , 485, 319

Salomana, E. & Sansonetti, C. 2004, Journal of Physical and Chemical Reference Data, 33, 1113

Sansonetti, C. 2007, Journal of Research of the National Institute of Standards and Technology, 112

Sansonetti, C., Blackwell, M., & Saloman, E. 2004, JOURNAL OF RESEARCH-NATIONAL INSTITUTE OF STANDARDS AND TECHNOLOGY, 109, 371

Schroeder, D. 2000, Astronomical optics (Academic Pr)

Seifahrt, A. & Käufl, H. U. 2008, A&A , 491, 929

Selsis, F., Kasting, J. F., Levrard, B., Paillet, J., Ribas, I., & Delfosse, X. 2007, A&A , 476, 1373

Sizer, II, T. 1989, IEEE J. Quantum. Electron., 25, 97

Smith, R. M., Zavodny, M., Rahmer, G., & Bonati, M. 2008, in Presented at the Society of Photo-Optical Instrumentation Engineers (SPIE) Conference, Vol. 7021, Society of Photo-Optical Instrumentation Engineers (SPIE) Conference Series

Steinmetz, T., Wilken, T., Araujo-Hauck, C., Holzwarth, R., Hänsch, T., & Udem, T. 2009, Appl. Phys. B: Lasers Opt., 96, 251

Steinmetz, T., Wilken, T., Araujo-Hauck, C., Holzwarth, R., Hänsch, T. W., Pasquini, L., Manescau, A., D'Odorico, S., Murphy, M. T., Kentischer, T., Schmidt, W., & Udem, T. 2008, Science, 321, 1335

Szentgyorgyi, A., Cramer, C., Benedick, A., Glenday, A. G., Kaertner, F. X., Korzennik, S., Li, C., Ordway, M. P., Phillips, D. F., Sasselov, D., & Walsworth, R. L. 2008, in Society of Photo-Optical Instrumentation Engineers (SPIE) Conference Series, Vol. 7014, Society of Photo-Optical Instrumentation Engineers (SPIE) Conference Series

Ulrich Käufl, H. 2008, in Precision Spectroscopy in Astrophysics, ed. N. C. Santos, L. Pasquini, A. C. M. Correia, & M. Romaniello , 227–230

Valdivielso, L., Esparza, P., Martín, E. L., Maukonen, D., & Peale, R. E. 2010, ApJ , 715, 1366

Valencia, D., O'Connell, R. J., & Sasselov, D. D. 2007, ApJL , 670, L45

van de Kamp, P. 1963, AJ , 68, 515

Vogt, S. S., Butler, R. P., Rivera, E. J., Haghighipour, N., Henry, G. W., & Williamson, M. H. 2010, ApJ , 723, 954

West, A., Hawley, S., Bochanski, J., Covey, K., Reid, I., Dhital, S., Hilton, E., & Masuda, M. 2008, The Astronomical Journal, 135, 785

Wetherill, G. W. 1994, APSS , 212, 23

Whaling, W., Anderson, W., Carle, M., Brault, J., & Zarem, H. 2002, JOURNAL OF RESEARCH-NATIONAL INSTITUTE OF STANDARDS AND TECHNOLOGY, 107, 149

Wilken, T., Lovis, C., Manescau, A., Steinmetz, T., Pasquini, L., Lo Curto, G., Hänsch, T. W., Holzwarth, R., & Udem, T. 2010, MNRAS , 405, L16

Williams, D. M., Kasting, J. F., & Wade, R. A. 1997, NAT , 385, 234

Winn, J., Howard, A., Johnson, J., Marcy, G., Isaacson, H., Shporer, A., Bakos, G., Hartman, J., Holman, M., Albrecht, S., et al. 2011, The Astronomical Journal, 141, 63

Winn, J. N., Fabrycky, D., Albrecht, S., & Johnson, J. A. 2010, ApJL , 718, L145

Wolszczan, A. & Frail, D. A. 1992, NAT , 355, 145

Vita
Stephen L Redman

Education

The Pennsylvania State University State College, Pennsylvania 2005–2011
Ph.D. in Astronomy & Astrophysics, expected in (May) (2011)
Area of Specialization: Precision Radial Velocity Searches for Exoplanets

University of Vermont Burlington, VT 2001–2005
B.S. in Physics, *magna cum laude*

Awards and Honors

Downsborough Graduate Fellowship	2010
NASA Graduate Student Research Program Fellowship	2008–2010
Pennsylvania Space Grant Consortium Fellowship	2006–2010
Harold F. Martin Graduate Assistant Outstanding Teaching Award	2008
Braddock/Roberts Fellowship	2005

Research Experience

Doctoral Research The Pennsylvania State University 2006–Present
Dissertation Advisor: Prof. Lawrence W. Ramsey
Commissioned the PSU Pathfinder, a Near-Infrared spectrograph designed to explore the challenges associated with making precision radial velocities in the Y, J, and H bands. Created a line list for Uranium, a NIR calibration source.

Graduate Research The Pennsylvania State University 2008–2010
Research Advisor: Dr. Scott T. Miller
Co-wrote, co-starred, and co-edited 19 video demonstrations for an online astronomy course. Proved that these videos provided a statistically-significant advantage to students who viewed them, and that students are not good at judging what is and is not helpful.

Undergraduate Research University of Vermont 2003–2008
Research Advisor: Prof. Joanna Rankin
Discovered a pulsar with an unusual combination of mode changes, nulling, and drifting subpulses. Proved that pulsar nulling can be either random or non-random and varies from pulsar to pulsar.

Teaching Experience

Guest Lecturer The Pennsylvania State University 2007
Taught a summer section of Astronomy 001.

Teaching Assistant The Pennsylvania State University 2005-2007
Taught, improved, and designed eight lab sections over two years. Designed three new observing labs to teach non-major undergrads how to use telescopes.

Teaching Asstant University of Vermont, Burlington, VT 2004-2005
Taught two lab sections of Astronomy 006 to undergraduate non-majors.